Imperial College London

Department of Electrical and Electronic Engineering

# NEMS by Sidewall Transfer Lithography

Dixi Liu

September 2015

Supervised by Professor Richard R.A. Syms

Submitted to the Department of Electrical and Electronic Engineering of

Imperial College London

in fulfilment of the requirements for the degree of

Doctor of Philosophy

# Declaration of Originality

I herewith certify that all results reported in this thesis are primarily due to the author, except for background material which has been properly referenced and acknowledged.

# Copyright Declaration

# Acknowledgements

Firstly, I would like to show my sincere gratitude to my supervisor, Professor Richard Syms for his guidance and patience in this Ph.D. project. I learnt a lot of valuable things from him, among which the most important one was the way to think and the way to solve. I really appreciate the time he spent on this work, also showing me the fascination of research. It was my pleasure to work with him throughout my Ph.D.

Secondly, I would like to thank Dr Munir Ahmad, who has offered me a lot of kind help and suggestion in the cleanrooms since the first day of this project. Also I am particularly grateful to Dr Tom Tate and Dr Steve Wright, who have always been glad to help solving problems. The OSD group in EEE department is a harmonious and warm environment to work in. I would like to thank all my excellent colleagues who have supported me in different ways during the past four years, including Prof Andrew Holmes, Dr Hadri Mokhtar, Dr Kaushal Choonee, Dr Mario D'Auria, Dr Oleksiy Sydoruk, Ms Susan Brace, Dr Zahid Durrani, etc.

I would also like to thank all my dear friends I met in Imperial College. They are Bin Xu, Boli Chen, Chen Wang, Cheng Cheng, Chengyuan Liu, Fangjing Hu, Hao Jiang, Huafeng Liu, Jingye Sun, Mingyang Sun, Shuo Yang, Xiaoxin Liang, Yilun Zhou, Yuanqi Hu, Yujie Wu, Zhengwei Wang, Zongxiang Wu, etc. I will never forget the happy time we spent together which brought me the unique memories of all these four years. It was your company and support that gave me courage to be strong and move forward.

Finally, I would like to express the most sincere thanks to my parents. Thanks for your always support and selfless love since I was born. The joy of finishing this work must be shared with you. I love you forever mum and dad.

# Abstract

A batch fabrication process for nano-electro-mechanical systems (NEMS) based on sidewall transfer lithography (STL) is developed and demonstrated. The STL is used to form nanoscale flexible silicon suspensions entirely by conventional lithography. A two-step process is designed for single-layer STL to fabricate simple electrothermal actuators, while a three-step process is designed to allow nanoscale features intersecting with each other for more complicated device lay-outs. Fabricated nanoscale features has a minimum in-plane width of approx. 100nm and a high aspect ratio of $50 : 1$. Combined structures with microscale and nanoscale parts are transferred together into silicon by deep reactive etching (DRIE). Suspensions are achieved either by plasma undercut or HF vapour etch based on BSOI.

The STL processes are used to form nanoscale suspensions while conventional lithography is used to form localised microscale features such as anchors. A wide variety of demonstrator devices have been fabricated with high feature quality. Analytic models have been developed to compare with experimental characterization and finite element analysis (FEA) predictions. Lattice structures fabricated by multi-layer STL have also be investigated as a novel type of mechanical metamaterial. Thus, the process could allow low-cost and mass parallel fabrication of future NEMS with a wider range of potential applications.

# Contents

# List of Figures

# List of Tables

# Units and Symbols

## Symbols

Chapter 5

| | | |
|---|---|---|
| $L$ | Beam length | [m] |
| $h$ | Beam central offset | [m] |
| $W$ | Beam width | [m] |
| $D$ | Beam depth | [m] |
| $M(x)$ | Bending moment | $[\text{N} \cdot \text{m}]$ |
| $I$ | Second moment of area | $[\text{m}^4]$ |
| $E$ | Young's modulus | $[\text{N}/\text{m}^2]$ |
| $M_A$ | End moment | $[\text{N} \cdot \text{m}]$ |
| $F_0$ | Axial force | [N] |
| $F$ | Transverse force | [N] |
| $y_{00}(x)$ | Initial beam Shape | [m] |
| $y_0(x)$ | Deflected beam shape with axial force | [m] |
| $y(x)$ | Deflected beam shape with axial and transverse force | [m] |
| $d_{max0}$ | Midpoint deflection with axial force | [m] |
| $d_{max}$ | Midpoint deflection with axial and transverse force | [m] |
| $u_0(x)$ | Deflection with axial force | [m] |
| $u(x)$ | Deflection with axial and transverse force | [m] |

| | | |
|---|---|---|
| $\triangle L$ | Change in beam length | [m] |
| $\delta L$ | Defference from the horizontal length | [m] |
| $\frac{\triangle L}{L}$ | Fractional change in beam length | [Dimensionless] |
| $\triangle T_{avg}$ | Average temperature rise | [K] |
| $\alpha$ | Linear thermal expansion coefficient | [K$^{-1}$] |
| $k_T$ | Transverse stiffness | [N/m] |
| $\theta$ | Tilted beam angle | [rad] |
| $P$ | Drive power | [W] |
| $k_{th}$ | Thermal conductivity | [W/m$\cdot$K] |
| $\triangle T_{max}$ | Peak temperature rise | [K] |
| $F_{axial}$ | Net axial force | [N] |
| $S$ | Sensitivity of deflection to temperature change | [m/K] |
| $\sigma_{int}$ | Intrinsic stress | [N/m$^2$] |

## Acronyms

| | |
|---|---|
| NEMS | Nano-electro-mechanical Systems |
| STL | Sidewall Transfer Lithography |
| DRIE | Deep Reactive Ion Etching |
| HF | Hydrogen Fluoride |
| BSOI | Bonded Silicon-on-Insulator |
| FEA | Finite Element Analysis |
| IC | Integrated-circuit |
| MEMS | Micro-electro-mechanical Systems |

| | |
|---|---|
| SOI | Silicon-on-Insulator |
| HAR | High-aspect-ratio |
| LIGA | Lithographie Galvanoformung Abformung |
| UV | Ultra Violet |
| RIE | Reactive Ion Etching |
| ICP | Inductively Coupled Plasma |
| SEM | Scanning Electron Microscope |
| SMA | Shape Memory Alloy |
| EBL | Electron Beam Lithography |
| FIB | Focused Ion Beam |
| CVD | Chemical Vapour Deposition |
| NIL | Nanoimprint Lithography |
| SFIL | Step-and-flash Imprint Lithography |
| CNTs | Carbon Nano Tubes |
| SWCNTs | Single-walled Carbon Nano Tubes |
| CMOS | Complementary Metal–oxide–semiconductor |
| MESFETs | Metal–semiconductor Field-effect Transistors |
| MOSFETs | Metal–oxide–semiconductor Field-effect Transistors |
| PECVD | Plasma Enhanced Chemical Vapour Deposition |
| STS | Surface Technology Systems |
| CAD | Computer Aided Design |
| CF | Complementary Function |
| PI | Particular Integral |
| RHS | Right Hand Side |

LHS          Left Hand Side

# 1 Introduction

## 1.1 MEMS

Miniaturization has been an over-riding theme in the development of the integrated circuit (IC) and its associated manufacturing industry. Continuous investment in fabrication technology has driven device integration and performance, and resulted in a thriving global market. The newer field of Micro-electro-mechanical systems (MEMS) has developed rapidly in the past forty years, largely by adapting silicon (Si) based micromachining technology. Apart from economies of scale following from smaller device dimensions, reduced size contributes to improved electrical and mechanical performance, for example through lower power consumption and higher sensitivity, and also contributes to higher reliability and the ability to exploit new physical phenomena.

The history of MEMS is closely associated with the development of IC technology. Micromachining of semiconductors such as Si and Ge has received attention since the first generation of transistors in the late 1940s, which launched the era of micro-electronics. Almost from the start, there was an awareness of potential mechanical applications [1], and the first MEMS device - the resonant gate transistor - was demonstrated by Nathanson in 1967 [2]. Commercialization of MEMS began in the 1970s, and since then a wide variety of devices and potential applications have been investigated [3]. Improvements to bulk and surface micromachining techniques have been continual, allowing the integration of MEMS with ICs [4] as well as increases in system complexity (for example, by enabling 3D fabrication and assembly) [5]. Since the 1990s, advanced micromachining technology has greatly increased the possibilities for microstructure fabrication and reduced the associated manufacturing cost, leading to a boom in applications and an increasingly global MEMS market.

Microsystems have been successfully adapted to a wide diversity of physical domains, operating on mechanical, electrical, optical, thermal, fluidic, chemical, and biochemical principles.

The most common devices are miniaturized sensors and actuators, or complete analysis systems. However, many other miniaturized components such as displays and switches have been demonstrated and applications have been found in the automotive, aerospace, communications, consumer, defense, energy, general industrial, IT, medical and security sectors. Figure 1.1 shows a forecast of markets for different MEMS applications. The predicted market in 2019 will be approx. 24 billion US dollars, almost triple the 2010 market (Yole Development Inc., France) [6].

**MEMS market forecast (in B$)**

*(Source : Status of the MEMS Industry report, Yole Développement, July 2014)*
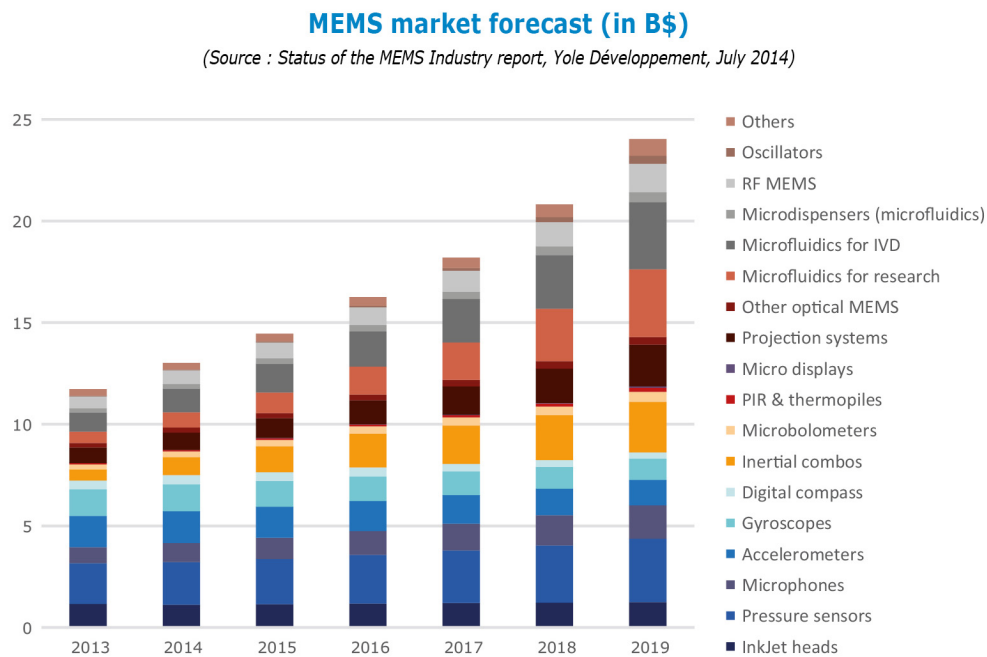


Figure 1.1: 2014 MEMS application market forecast by Yole Development.

## 1.1.1 MEMS fabrication

Most MEMS fabrication processes were initially inherited from the silicon IC industry, but have been substantially modified to allow fabrication of the three-dimensional structures needed for MEMS. In contrast to microelectronics, alternative materials such as glasses, ceramics, plastics, metals are also often required for specific application domains. Thus, MEMS fabrication has tended to diverge from microelectronics technology.

### 1.1.1.1 Photolithography

Photolithography (also known as optical lithography) is the most basic tool of mass parallel fabrication, and largely drove the semiconductor industry from its inception. The typical pattern resolution of contact photolithography is down to 2μm (limited by the wavelength of the radiation), which is usually used in research and developing prototype devices. However, the resolution has been continuously improved, and photolithography has been extended to feature size below 50nm by modern techniques such as excimer laser lithography, immersion lithography, multiple patterning, etc.

The process involves the transfer of a master pattern from a photomask to a target substrate using a thin layer of light-sensitive material or "photoresist". Figure 1.2 shows a typical process on silicon. The process starts with a clean substrate surface (1), typically a semiconductor wafer or a wafer coated with a metal or oxide, and a source pattern defined on a clear glass substrate as a set of opaque and clear areas, typically with micron-scale dimensions. The wafer is first coated with a uniform layer of photoresist (2), normally either positive (a) or negative (b) resist. The pattern is transferred to the resist layer by exposure to light of an appropriate wavelength, typically in the ultraviolet range. A developer is then used to remove either the exposed (positive) or the unexposed (negative) parts of the photoresist, due to the chemical reaction caused during illumination (4). Hence the original pattern is transferred to the resist, which can serve as a mask for later etching steps (a(5) and b(5)). The photoresist is then removed to leave a clean surface with patterned features (a(6) and b(6)). In the alternative lift-off process, a relatively thin layer of target material is deposited after development (c(5)). Removal of the resist then lifts off unwanted regions of the target material, resulting in a reversed pattern (c(6)).

### 1.1.1.2 Bulk micromachining

Bulk micromachining was one of the first processes developed for MEMS fabrication, and involves the formation of deep features on single crystal silicon substrates by wet etching. A patterned mask layer is first formed, and the substrate is then immersed in a specialised etching solution (such as potassium hydroxide, tetramethylammonium hydroxide, or ethylenediamine pyrocatechol). Conventional etch processes result in isotropic material removal. However, bulk micromachining exploits the different etching rates that can be obtained in different crystallographic directions due to variations of chemical bond densities. For example, in single crystal
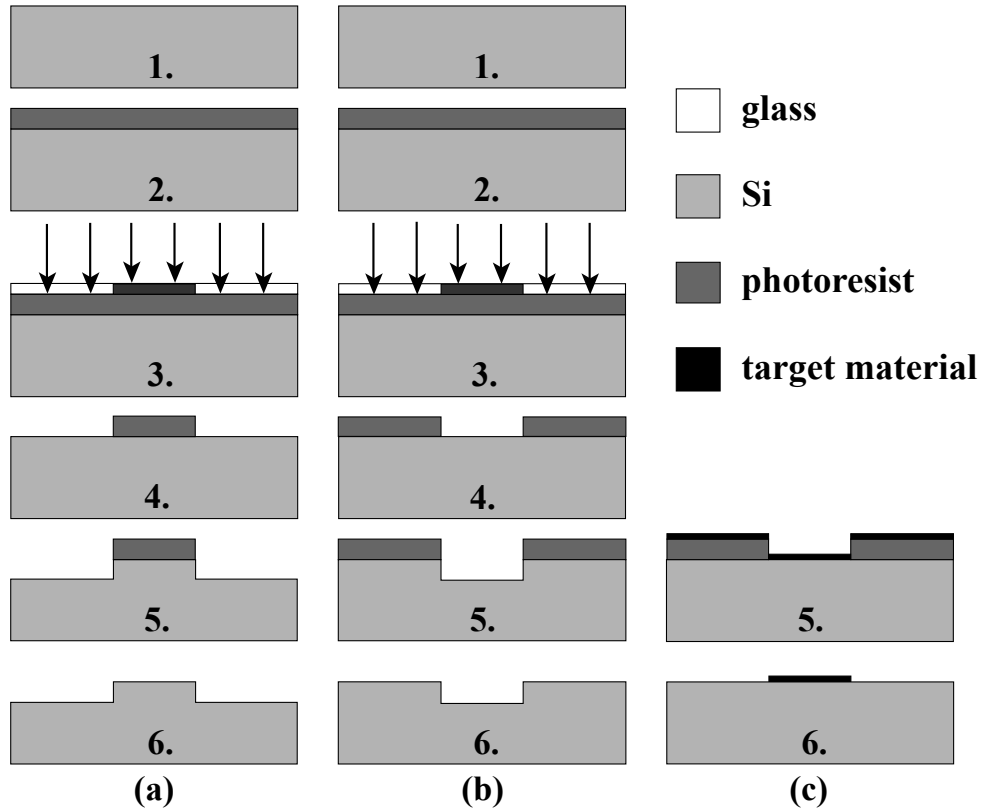
Figure 1.2: Schematic diagram of photolithography process on silicon.

silicon the etching rate on $< 100 >$ planes is the fastest, while etching of $< 111 >$ may be up to 100 times slower. As a result, deep features with sidewalls sloped at a fixed angle of $54.74°$, can easily be formed, including V-groves and inverted pyramids, and additional etch stop layers can be used to form suspended structures. However, despite its apparent simplicity, bulk micromachining is difficult to incorporate into a process flow, and can yield only a restricted set of features.

### 1.1.1.3 Surface micromachining

Surface micromachining was established to fabricate structures which are difficult or impossible to achieve by bulk machining. A broad definition of the surface micromachining process is the formation of microscale structures by depositing, patterning and etching thin layers of materials on the surface of the substrate wafers. The thickness of the deposited layer is typically from a fraction of a micron to a few microns. Surface micromachining can be a multi-layer process, and consequently allows precise definition especially on complex MEMS designs. Suspended structures can easily be achieved by undercutting mechanical parts through removal of sacrificial layers. Surface micromachining has largely replaced bulk micromachining because of its

flexibility and compatibility with IC fabrication.

A derivative and promising technique developed is the silicon-on-insulator (SOI) process. Here, device fabrication is based on multi-layer wafers containing an insulating interlayer (normally silicon dioxide or sapphire, which can also act as a sacrificial layer) between a silicon device layer and the substrate or handle layer. The thickness of the device layer and the interlayer can range from nanometers to micrometers depending on the application. Two main methods are used to manufacture SOI wafers, thermal wafer bonding and oxygen ion implantation; both allow the precise definition of each layer. SOI processes have been industrialized in the last ten years, opening more opportunities for applications.

Several processes have been developed to fabricate features with a much higher aspect ratio than surface micromachined structures. The first, additive, type involves a combination of thick resist patterning, electroplating and micromolding. Free-standing structures can also be formed, by removing a sacrificial layer from beneath the high-aspect-ratio (HAR) structure. Typical examples include LIGA (Lithographie Galvanoformung Abformung) and SU-8 patterning. LIGA requires an expensive synchrotron exposure tool, while SU-8 patterning can be carried out using a conventional ultraviolet (UV) source. A key restriction is that the structures are typically formed in electroplated metals or moulded plastics, and hence cannot easily be combined with electronics for sensing.

The second, subtractive process, deep reactive ion etching (DRIE), forms HAR features directly in silicon, and consequently is more useful. It is a cyclic dry etching process involving alternate reactive ion etching (RIE) and passivation steps that protect sidewall features while achieving highly vertical etching through the silicon device layer or handle layer. DRIE is carried out using relatively simple inductively coupled plasma (ICP) etching equipment, and can be easily adapted to bonded silicon-on-insulator (BSOI) wafers and other micromachining techniques such as micromolding, which also improves the process flexibility. As a result, it has had considerable industrial impact and is the fabrication technique of choice for many MEMS devices.

### 1.1.2 Mechanical MEMS

The core concept of MEMS devices is to achieve transduction between different types of signals. A wide range of signal types can be involved, including mechanical, electrical, magnetic, thermal, optical and chemical signals, as detailed in Table 1.1 [7]. However, it is also worth

noting that multiple mechanisms can be involved in a single system, for example using both electrical and mechanical signals as intermediate links.

| To / From | Electrical | Magnetic | Mechanical | Thermal | Chemical | Radiative |
|---|---|---|---|---|---|---|
| **Electrical** | | Ampereís Law | Electrostatics, Electrophoresis | Resistive Heating | Electrolysis, Ionization | EM Transmission |
| **Magnetic** | Hall Effect, Mag. Resistance | | Magnetostatics, Magnetostriction | Eddy Currents Hysteretic Loss | Magnetic Separation | Magneto-optics |
| **Mechanical** | Variable Cap. Piezoresistance Piezoelectricity | Magnetostriction | | Friction | Phase Change | Tribo-luminescence |
| **Thermal** | Thermoelectric | Curie Point | Thermal Expansion | | Reaction Rate Ignition | Thermal Radiation |
| **Chemical** | Electrochemical Potential | Chemomagnetic | Phase Change | Combustion | | Chemo-luminescence |
| **Radiative** | Photoconductor, EM Receiving | Magneto-optics | Radiation Hardening | Photothermal | Photochemical | |

Table 1.1: Table of common transduction mechanisms used in MEMS.

Mechanical MEMS were the earliest category to be developed. Most mechanical MEMS contain suspended micromachined structures (e.g. cantilevers, springs, thin films, etc.), and involve elastic effects such as stress and strain in their operation. The most common applications are mechanical microsensors and microactuators.

### 1.1.2.1 Mechanical microsensor

Mechanical microsensors detect the signal to be measured and convert it to an electrical signal via a suitable transduction mechanism. Such sensors can be subdivided into many groups based on their different motion modes (angular or linear), supporting structures (springs, cantilevers, torsional bars), transduction mechanism (capacitive, piezoresistive, piezoelectric, optical) and control mode (open or closed loop). Examples of typical mechanical microsensors are given as below.

Pressure sensors were first built by Honeywell Research Centre and the Bell Labs in 1960s, utilising the transverse and shear piezoresistance effects [8]. After that, other device types with different transduction mechanisms were quickly investigated, including capacitive and resonant force detection. Due to the advantages of mature manufacturing process, small size and high performance and price ratio, pressure sensors are the most widely used MEMS sensors. Performance usually depends on the measurement range, accuracy, linearity and operating temperature range. The main aim of future research on pressure sensors is to develop new materials for harsh environments.

Accelerometers represent another high-volume application for MEMS, and were originally developed for automotive safety applications. The main performance indicators include measurement range, resolution, scale factor stability and noise performance. Figure 1.3a shows the scanning electron microscope (SEM) image of a $400 \times 400 \mu m^2$ 3-axis MEMS accelerometer before capping [9]. MEMS accelerometers can easily be integrated with peripheral circuits to combine small size with low power consumption. The piezoresistive accelerometer by Amarasinghe is a representative of an ultra-small device [10]. As shown in Figure 1.3b, with a package size of $700 \mu m \times 700 \mu m \times 550 \mu m$, it can fully meet the requirements of low volume and weight in miniaturized applications such as biomedical sensors. Another typical example of ultra-low power consumption is the ADXL346 3-axis digital accelerometer by Analog Devices. With supply voltage of 2.75V, the supply current is as low as $23 \mu A$ in measurement mode and $0.2 \mu A$ in standby mode [11].

Thermal sensors are another important application of mechanical MEMS. Most devices exploit thermal deformation due to different expansion between multi-layers or HAR geometries to analyse heat transfer effects or environment temperature changes. MEMS thermal sensors can easily be fabricated in arrays, to form thermal imaging devices. Applications have been extended in recent years to include biomedical sensors. For example, a MEMS differential thermal biosensor with thermopiles was developed for sensitive metabolite measurements in microfluid flows by monitoring the heat produced in enzyme-catalyzed reactions [12].
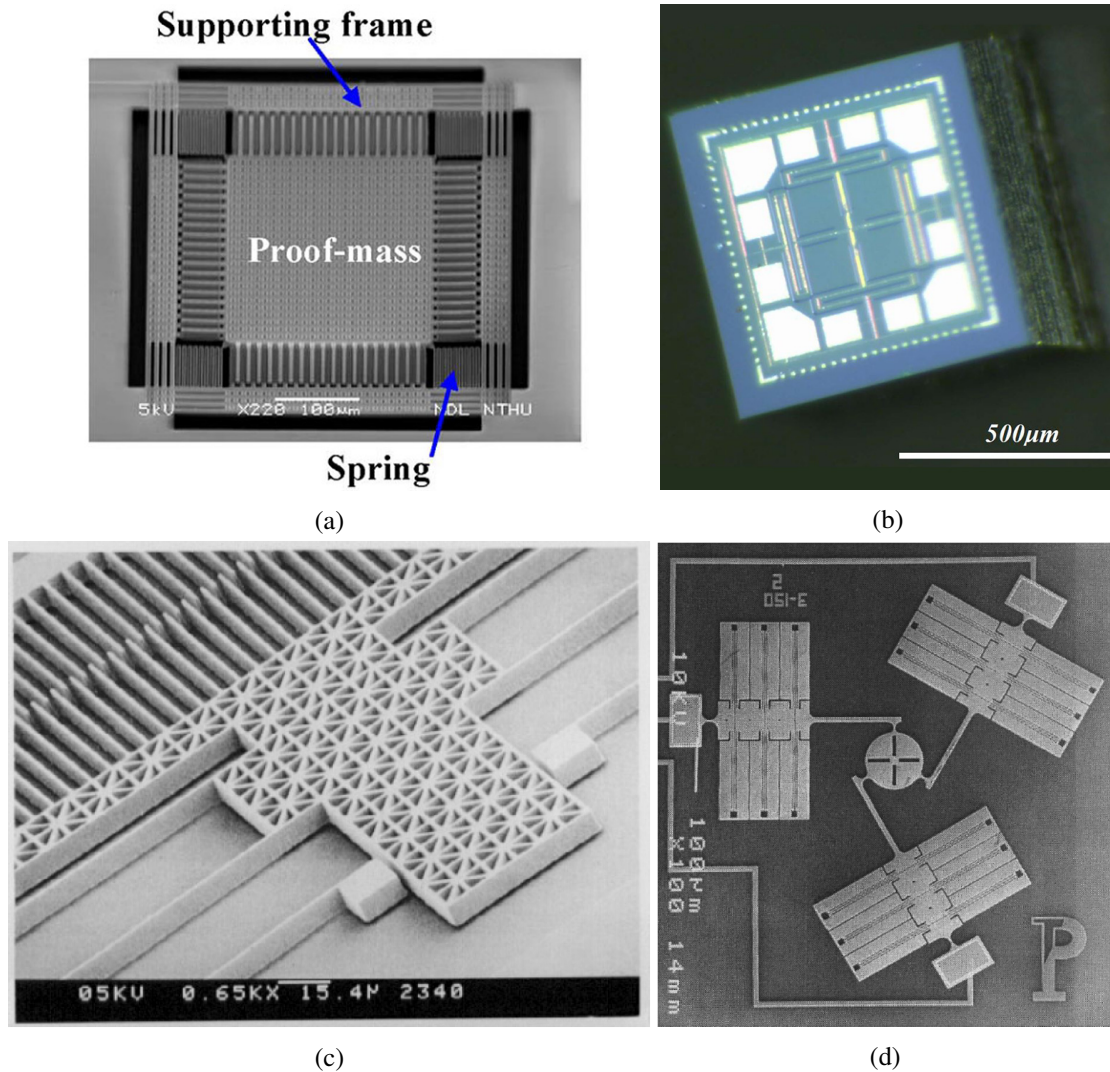
Figure 1.3: (a) SEM view of a $400 \times 400 \mu m^2$ 3-axis MEMS accelerometer before capping; (b) a fabricated miniature three-axis micro accelerometer; (c) close-up SEM view showing the comb-finger array and beam anchors of a comb-drive MEMS actuator; (d) SEM view of a planar three degree-of-freedom parallel micro-manipulator.

### 1.1.2.2 Mechanical microactuator

Microactuators may be needed to actuate a resonant sensing system, to tune a variable component such as filter or a beam deflector, or to self-test a miniaturized system. The general operation principle is to transform an input signal (ideally, electrical) into an output response in the form of a displacement or an actuation force. The most common operating principles are electrothermal, electrostatic, piezoelectric and electromagnetic actuators. All have different size scaling laws and consequently different applications.

Electrostatic utilise the attractive electrostatic force between positive and negative electrodes. The earliest designs used parallel plate electrodes, and suffered from an unfortunate snap-down

instability. Later designs used comb-drive [13] or interdigitated electrodes, which are intrinsically more stable. Figure 1.3c shows a close-up view of a comb-finger array and beam anchors [14]. Such designs have been developed into rotary motors [15], and used as drive units in complex microsystems. Other designs include scratch drive, inchworm [16], impact [17], repulsive [18], and curved [19] [20] actuators. The main disadvantage of all electrostatic actuators is their relatively large size, and the requirement of high drive voltage (around hundreds of volts), which makes it difficult to achieve on-chip integration with smaller movable structures.

MEMS Electrothermal actuators have been studied extensively with various designs and functions. Devices usually operate by differential thermal expansion between electrically heated parts of a suspended structure, and other unheated parts. The first-generation devices were suspended bimorphs, with different thermal expansion between different layers of materials [21] [22]. Later designs eliminated the need for multiple materials by using asymmetric beam layouts or arrangements for differential heating [23]. The common type of devices can be built by etching and undercutting a mechanical layer on the top of a sacrificial layer to form free-movable suspended structures [24]. In-plane or out-of-plane motion of the device is then achieved passing a current between anchors to form thermal heating. Figure 1.3d shows a planar three degree-of-freedom parallel micro-manipulator by using the non-uniform Joule heating and constrained thermal expansion of the device structures [25]. Recent development of thermal actuators has involved novel materials such as shape memory alloy (SMA), which can generate large force with a relatively small temperature change [26] [27]. Phase change materials such as paraffin, whose solid and liquid states have considerable volumetric difference, have also been explored recently due to their large actuation force [28].

The most common arrangements of electrothermal actuators are shape bimorph [29, 30]and buckling [31–33] actuators. In the former case, actuation is caused by differential thermal expansion between hot and cold arms, and in the latter between a hot arm and the substrate. Two well-known types of device designs have been developed and studied. One is known as a V-beam actuator, because the beams are initially shaped into a chevron layout, while the other has a raised cosine pre-buckle. The basis of actuation for both has been investigated using Euler buckling theory and finite element analysis (FEA), typically using a simplified single-beam model, as well as the thermal aspects [34, 35]. In addition, more complex arrangements have been developed, including cascaded, out-of-plane and feedback-controlled actuators, and actuators with in-built strain gauges. Such electrothermal actuators have a wide range of applications.

For example, V-beam actuators have been used as the basis of linear and rotary stepping motors. Other applications include optical alignment, micro-optical devices, devices for cell manipulation and movable neural microelectrode arrays.

### 1.1.3 Size scaling

Miniaturization involves size scaling effects in addition to a simple reduction of system dimensions. These effects typically involve changes to material properties, the alteration of the relative significance of different physical phenomena (for example, the relative effects of different forces), and the introduction of new phenomena.

Most MEMS devices are based on thin layers of deposited or etched materials, and their electrical and mechanical performance can therefore be significantly differently from equivalent macroscopic structures. The causes might lie in the processes used to form the thin films, or deviations from material homogeneity when the device dimension is approaching that of an individual material grain. For example, single crystal silicon is one of the mostly used materials in MEMS, and its defect distribution (point, line and plane defect) can normally be neglected under micro-mechanical analysis. However, the same is not true of deposited polycrystalline materials such as polysilicon and metals.

Studies of scaling effects have been carried out on a large range of MEMS materials, including metals (copper [36] and nickel [37]), composites [38], polymers [39] and polysilicon [40]. The material properties studied include Young's modulus (the ratio between stress and mechanical strain), Poisson's ratio, the yield stress, plastic deformation effects and the electrical and thermal conductivity. This work has confirmed that material properties can change dramatically with feature size, depending on the material. For example, in 1994, Fleck used tension and torsion experiments with copper wires to confirm that the strain gradient plasticity rose as the diameter fell from millimeter to micrometer scale [36]. Similarly, in 1998, Stolken and Evans observed that the strain gradient plasticity was increased in foil when its thickness was reduced from 50μm to 12.5μm [37].

Scaling effects are also reflected in the mechanical properties of MEMS due to their large surface-to-volume ratio. For example, scaling down of all linear dimensions by a factor of ten ($f = 10$) leads to a reduction in surface area ($S$) by a factor of a hundred and in volume ($V$) by a factor of a thousand. Other mechanical parameters such as mass ($m$) and mechanical stiffness ($k$) are reduced accordingly. For example, for a cantilever of length $L$, second moment of area $I$

and Young's modulus ($E$), we can obtain:

$$S \propto f^2$$
$$m = \rho V \propto f^3 \tag{1.1}$$
$$k = \frac{3EI}{L^3} \propto f$$

One obvious conclusion is that the reduction of mass (which determines the system inertia) is much larger (by a factor of 1000) than the reduction in stiffness. This means MEMS devices could maintain a good quality of mechanical strength with greatly reduced device mass. Benefiting from this, a large variety of MEMS inertial devices have been developed including accelerometers [41], gyroscopes [42], and seismometers [43]. Other obvious advantages include reduced shock sensitivity in inertial sensors, increased resonant frequency in signal processing devices, reduced drive power and voltage in actuators, and so on.

Another category of effects are new physical phenomena that may arise when device dimensions are reduced to the nanoscale. For example, quantum mechanical effects cannot be ignored when analysing very small electrothermal systems since both the electrons involved in the current flow and the phonons involved in the heat flow can no longer be understood in terms of classical physics; instead, both will be quantised [44]. Alternative physics could provide advantages in some applications and disadvantages in others. However, quantum effects lie beyond the scope of this thesis, which focuses instead on the classical benefits of size scaling.

## 1.2 NEMS

Nano-electro-mechanical systems (NEMS) are a further development of MEMS, which were first investigated in the 1990s. Since most NEMS are simply integrated electromechanical systems with nanoscale dimensions, many of the design, fabrication and characterisation techniques developed for MEMS can be adapted directly for NEMS. In many cases, the benefits of size scaling are performance improvements as described earlier. However, NEMS can also involve new physical phenomena, including small size effects, surface and boundary effects, quantum size effects and the macroscopic quantum tunnelling effect. NEMS devices can therefore have unique characteristics and functions that are impossible to achieve using microscale devices, such as ultra-high frequency, ultra-low energy consumption, ultra-high sensitivity, excellent surface quality control, high adsorption capacity and nanoscale control of actuation.

Often these advantages can be achieved using a combination of localized nanoscale features with a mainly microscale structure for readout. However, it will be difficult to exploit any potentially advantageous effects without appropriate methods of fabricating extremely small structures. Unfortunately, the low-cost, mass-parallel replication method - optical lithography - that powered the microelectronics revolution cannot be used to replicate features with dimensions significantly below the wavelength of UV light. This apparently innocuous limitation has very significant consequences: there are no industrial NEMS fabrication processes, no equivalent of a MEMS foundry for NEMS, and few if any NEMS devices in production.

### 1.2.1 NEMS fabrication

Just as it was in the IC industry, the existence of suitable patterning methods is likely to be a key determinant of the ultimate commercial success of the NEMS industry. Because of the difficulties involved, a number of very different approaches have been investigated, but none have been particularly successful. NEMS fabrication processes can be divided into two main categories: top-down and bottom-up. At the moment, most processes used for research purposes are top-down methods that allow the fabrication of one-off prototypes, but are far too costly for large-scale production. In contrast, bottom-up processes are much cheaper, but lack the flexibility to form general device layouts, and generally yield only periodic or random arrays of simple structures. As a result, there is a need (addressed as the main topic of this thesis) for processes that are flexible enough for low-cost fabrication of at least a subset of NEMS devices.

#### 1.2.1.1 Nanoscale lithography

In nanoscale lithography, the diffraction limit of the optical light source used for pattern transfer in microelectronics and MEMS is overcome by using a particle beam of much shorter wavelength, based on the theory of wave-particle duality. Examples of such processes include electron beam lithography (EBL) [45] and focused ion beam (FIB) lithography, both developed as fabrication techniques for two dimensional nanoscale structures with a planar resolution of a few nanometers [46] [47] [48]. Both methods rely on large, complex items of capital equipment and fabricate patterns by slow, serial writing. EBL uses an electron source based on a hot filament or a cold cathode to write on a specialized electron beam resist; FIB uses a liquid metal ion source, typically of a low-melting point metal such as In and Ga, to erode a surface directly. In each case, the field of view that can be addressed using electronic beam deflection is limited

to around $1mm^2$, and larger areas can only be written by moving between fields using a stepper-motor controlled table. As a result, while EBL and FIB are commonly used for definition or local modification of master patterns, they are simply too expensive for mass parallel fabrication of devices.

Recent approaches have involved a combination of direct writing with other common fabrication processes. One example is focused-ion-beam chemical-vapor-deposition (FIB-CVD) [49, 50], which combines FIB machining with chemical vapour deposition (CVD) to deposit patterned nanoscale structures with arbitrary 3D arrangements. For example, Figure 1.4a shows a SEM photograph of a microwine glass with 2.75μm external diameter and nanoscale wall thickness fabricated using FIB-CVD [51]. FIB can also be combined with a reactive gas to carry out directed nanoscale etching.

FIB lithography can also be used to achieve 3D nanoscale structures that self-assemble by directed stress release [52, 53]. The principle is to use FIB machining to introduce tensile stress in a suspended layer of material by producing a thin (usually < 100nm) damaged region. The strain thus generated can be used to power out-of-plane rotation of a set of patterned flat parts, and hence achieve a self-assembled 3D structure. Figure 1.4b shows a self-assembled nanoscale cubic frame fabricated with FIB-introduced stress [54].



(a)                                      (b)
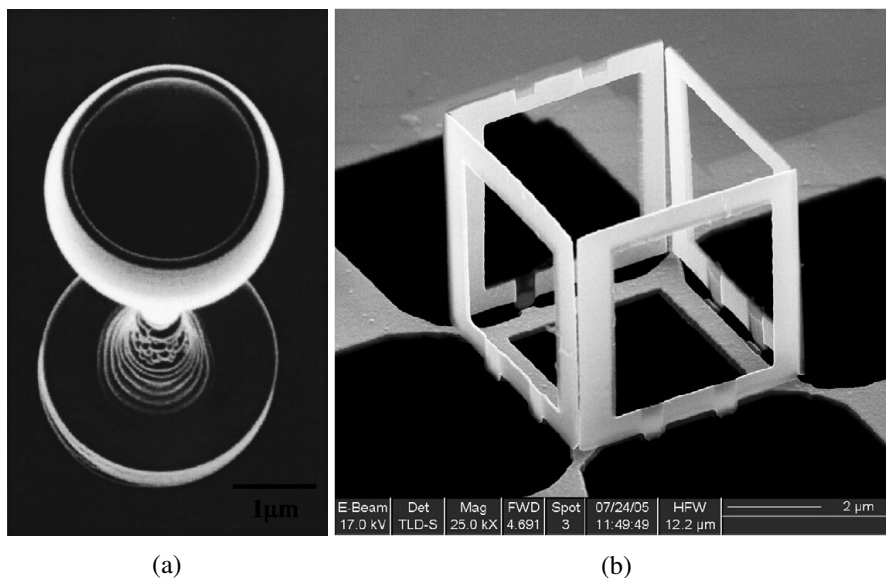
Figure 1.4: (a) Microwine glass with 2.75μm external diameter and 12μm height; (b) a stand-up 3D cubic frame fabricated using self-assembled FIB stress-introducing process.

Particle beam lithography methods represent the most common approaches to nanoscale patterning. Less common methods include dip-pen lithography and atomic force microscopy [55].

In each case, the advantages to researchers are very obvious, as they can define arbitrary arrangements of features with high resolution and precision. However, the slow speed, expense and unreliability of the equipment involved limit their use in mass production. What is required are methods that can easily replicate nanoscale patterns.

### 1.2.1.2 Nanoimprint

The most common nanoscale replication technology is nanoimprint lithography (NIL), initially proposed by Chou in 1996 [56]. The process involves replication of a master stamp (which must itself typically be formed by a combination of e-beam lithography and reactive ion etching, but which can be re-used many times) by embossing of a thin layer of resist. Figure 1.5a shows the process flow of a general NIL process. A thin layer of imprint resist is first coated on the substrate to be patterned [57]. A rigid stamp with pre-patterned nanoscale features is then pressed into the resist surface. The resist is then reshaped by mechanical force to follow the shape of the stamp. After removing the stamp, the nanoscale patterns generated in the imprint resist can easily be transferred to the substrate material by RIE.

Shortly after the publication of the initial process, a series of process variations were developed. For example, in thermoplastic NIL, the imprint resist is heated to a controlled temperature, reducing its viscosity and ensuring that it fully flows to fill in the mold [57]. In step-and-flash imprint lithography (SFIL), a liquid resist is embossed, and then cured by parallel exposure to UV light so that it cross-links and solidifies. In soft lithography [58], a poly-dimethyl-siloxane stamp is used to transfer an alkanethiol ink onto a gold-coated substrate. The thiol groups bind to the gold, leaving the tails of the molecules to form a self-assembled monolayer that can be used as a resist for further processing. However, the resist is relatively fragile and cannot withstand aggressive etches.

Figure 1.5b and 1.5c shows SEM photographs of imprinted patterns with feature sizes down to 25nm [59, 60]. However, current NIL processes can produce features with dimensions below 5nm [60]. Because replication does not involve series patterning, NIL has significantly higher throughput and lower cost than direct-write techniques. However, it clearly works best when the surface to be patterned is completely planar, and hence may be less suitable for fabrication of more general NEMS, when intermediate processing results in surface steps.
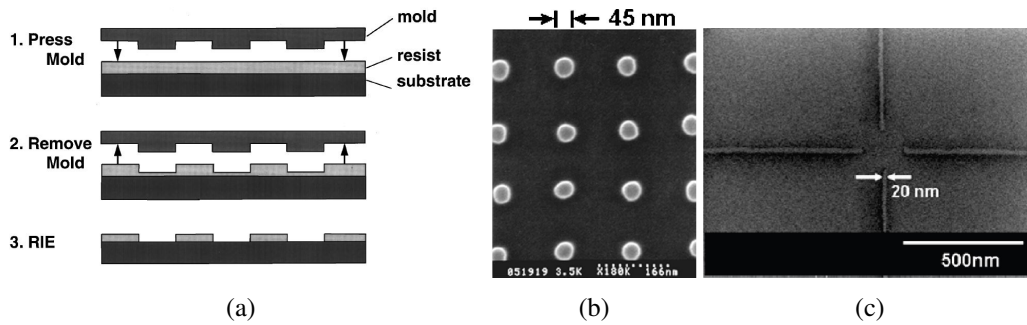
Figure 1.5: (a) Schematic diagram of nanoimprint lithography process; top SEM views of (b) imprinted PMMA mesas of 45nm and (b) a close-up grid pattern of 20nm.

### 1.2.1.3 Nanosphere lithography

An entirely different approach is offered by nanosphere lithography, a very simple parallel fabrication process for producing ordered nanoscale particle arrays [61]. The arrays are generated by spin coating a wafer with a solution containing suspended nanoscale spheres (typically, latex, with a size ranging from 100nm to 1μm), which are forced by a combination of convection and surface tension into close-packed hexagonal arrays. The arrays can then serve as masks for subsequent processing steps, including reactive ion etching and lift-off of a metal film, creating surfaces that can act as filters, textured surfaces for surface-enhanced Raman spectroscopy or periodic optical structures. Feature sizes below 100nm can be routinely achieved using very simple equipment [62], and nanosphere lithography can be used with terraced substrates to modify the periodic arrangement. However, its key restriction – its natural tendency to form close packed hexagonal arrays – cannot easily be overcome.

Although a wide variety of nanoscale fabrication process has been developed as mentioned above, industrialization of NEMS is still limited by the lack of an appropriate patterning process. Direct patterning processes including EBL and FIB lithography are too expensive and too slow. Undirected processes such as nanosphere lithography are cheap and parallel, but can only generate specific nanoscale features. Replication processes including nanoimprint lithography and soft lithography also provide possible approaches to nanoscale patterning. However, these methods are only marginally useful for mass production because of their own inherent restrictions.

Thus, for NEMS devices to be successful in commercial production, a key requirement is the development of an alternative nanoscale patterning process. Three main features are desirable: (1) a parallel process capable of mass production, (2) the ability to fabricate a wide range of

## 1.2.2 Mechanical NEMS devices

As defined earlier, many NEMS are miniature version of MEMS, again with electrical and mechanical functionality but with nanoscale dimensions. However, there is a common misunderstanding that NEMS are just miniaturized MEMS. As explained in Section 1.1.3, the size scaling effects after miniaturization should affect many aspects including material properties, physics of operation, and even introducing new phenomena at the nanoscale. These all provide considerable improvement on the system performance such as higher Q factors and reduced mass, as well higher frequency operation. This section will briefly review and highlight recent progress in mechanical NEMS research.

Using the nanoscale fabrication techniques described above, MEMS dimensions have already been pushed below the microscale. For example, Figure 1.6a shows doubly clamped nanoscale silicon beams released from BSOI substrates, which have been patterned by EBL [63]. The in-plane beam width varies from 0.16μm to 1.4μm. At such size scales, the techniques used for actuation mainly involve magneto-motive [64] and electrostatic actuation [65]. The former utilises the Lorentz force generated in the current-carrying structure in a magnetic field while the later uses the electrostatic force between charged capacitor plates. Existing work shows functional NEMS devices can operate at frequencies of 1GHz and 700MHz respectively, Other actuation techniques include electrothermal heating and piezoelectricity. However, compared with MEMS, the challenge of NEMS actuation is transducing excitation energy effectively to nano structures at high frequency.

In terms of operating functions, most current mechanical NEMS can be divided into two groups: (1) devices that benefit from the scaled dimension of the system to achieve improved performance from current sensors and actuators, and (2) devices that utilise the unique properties of NEMS materials and structures to exploit new features from existing MEMS devices.

NEMS resonators are typical representatives that belong to the first group. Research in NEMS resonators has attracted extensive attention due to unique structural and functional characteristics obtained at nanoscale dimensions. Improved device performance has been achieved by scaling down the size of core elements from micro- to nanoscale. In addition to improving the operating frequency, NEMS resonators show have improved quality factors than comparable microscale devices [66], which show significant potential in signal processing. Another typical

advantage of NEMS is the high sensitivity. As shown in Figure 1.3b, the electrometer developed by Cleland in 1998 achieved a much higher charge sensitivity of $0.1e\mathrm{Hz}^{-0.5}$ than conventional field-effect transistors, with additional advantages such as higher operating temperature and larger bandwidth [67].

NEMS inertial sensors benefit from small mass and high Q factors [68]. Analytic evaluation and numerical estimates of mass sensitivity indicate an enormous potential for mass sensing. For example, since nanoscale cantilevers typically have a cross-sectional dimension of 10nm, the active mass can be reduced to $10^{-18}$g, suitable for detecting extremely small additional masses. Devices based on NEMS resonator arrays have been able to detect the binding of individual DNA molecules [69] (Figure 1.6c). It is likely that similar devices may achieve a mass sensitivity of 1 Dalton (one twelfth of the mass of an unbound neutral atom of carbon-12) [68], almost reaching the boundary of conventional mass spectrometry.



| (a) | (b) | (c) |
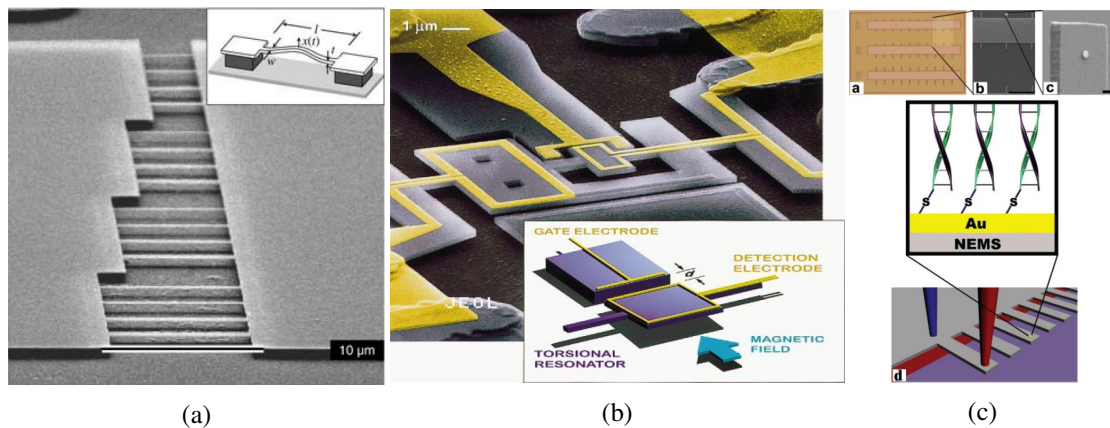
Figure 1.6: (a) SEM images of doubly clamped NEMS beams on BSOI patterned by EBL; (b) a nanometre-scale charge detector (the inset schematically depicts the torsional mechanical resonator, detection electrode and gate electrode); (c) Optical micrography, SEM images and schematic showing arrays of cantilevers to detect the binding of DNA molecules by NEMS oscillators.

NEMS devices that take advantages of carbon nano tubes (CNTs) could be typical examples in the second group. In recent research, CNTs have demonstrated promising mechanical and electrical properties: a great difference between axial and radial elasticity [70], tolerance of extremely large non-linear deflection and buckling [71], high current densities [72] and high thermal conductivity [73]. These properties may make CNTs appropriate for NEMS. Important applications of CNT based sensors are AFM probe tips, which reduces the effective tip radius down to 3nm [74, 75]. The lateral resolution is thus increased up to 70% compared with silicon tips. CNTs have also used in mechanical strain sensors [76, 77]. For example, in [76], single-

walled carbon nanotubes (SWCNTs) were embedded in a polymer substrate to make strain sensors, since the position of the D* Raman band strongly depends on the strain transferred from the substrate to the nanotubes . Other applications have involved chemical and biochemical CNT sensors [78]. The integration of CNTs offers many possibilities for future NEMS, however a key requirement will be to control their growth or assembly.

## 1.3 Sidewall transfer process

Sidewall transfer lithography (STL) (also known as edge-defined lithography or spacer lithography) is a type of self-aligned double patterning method that provides a low cost solution for nanoscale patterning (as illustrated in Figure 1.7). STL is designed to produce sub-micron features by utilising the transformation of thin-layer materials deposited on microscale moulds. Ultra-narrow lines can be defined by the thickness of the sidewall films. Due to its superior control of dimension and high production efficiency, STL has been investigated consistently in recent years, and the critical feature dimension has now been reduced below 10nm [79, 80].



(a)                                                      (b)
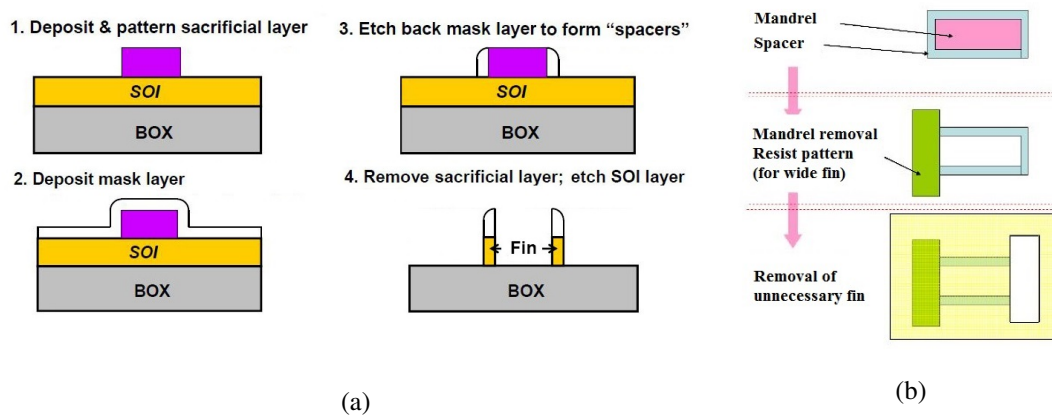
Figure 1.7: Schematic diagrams of (a) a typical STL process for FinFET fabrication; (b) STL process combined with additional lithography steps

STL was originally developed for CMOS (complementary metal–oxide–semiconductor) fabrication. In 1975, Nicholas et al. successfully defined edge features on existing mesas by controlling lateral diffusion in polysilicon [81]. The method was then developed to form polysilicon gate CMOS devices by selectively removing non-highly doped polysilicon [82]. Meanwhile, Jackson et al. fabricated GaAs MESFETS (metal–semiconductor field-effect transistors) using edge plated Au to define sub-micron (0.4μm) lines [83]. However, a more practicable method was developed by Hunter et al. in 1981, by conformal coating and anisotropic etching

of a polysilicon layer over original $SiO_2$ mesas. Sub-micron elements ($0.1 - 0.4\mu m$) were then defined by the polysilicon left by the sidewalls, which could be adjusted during the conformal coating [84]. Afterwards, the development of STL was driven in conjunction with thin film technology and surface micromachining. In recent years, STL has been widely used for FinFET fabrication [85–91].

In addition, STL has also been used for fabrication of nanowire arrays. Various materials have been investigated, including silicon [79], diamond [92], platinum [93,94], platinum silicide [95] and nickel silicide [96]. Corresponding applications range from sensors [92] to catalytic surfaces [97]. Further applications also include field emitters [98,99] and quantum dots [100–102]. Fabrication of silicon moulds has also been extensively investigated [103–105] combined with modern fabrication processes such DRIE and lift-off. STL processes have also been used to fabricate nanoimprint templates [106–109].

A typical STL process consists of the four main steps illustrated in Figure 1.7a [110]. Firstly, a sacrificial layer is deposited on the substrate and patterned to form a set of mesas or spacers (step 1). Secondly, a conformal layer of the material is coated over the whole surface, covering all the mesas (step 2). In the next step, the mask layer is anisotropically removed from all the horizontal surfaces, leaving only material on the vertical sidewalls of the mesas (step 3). Thus, the in-plane linewidth of the sidewall features is defined by the mask material thickness, which can easily be controlled to be sub-micron. Finally, the sacrificial layer is removed, and the sidewall pattern is transferred into the substrate by further etching (step 4). A variety of features can be transferred, including nanoscale ribs [111–115], slots [116–118] and vertically stacked multilayers [107, 119, 120].

Various techniques have been used to form sidewall masks in different materials, such as silylated resist [112], silicon nitride [111] and silicon oxide [108]. Smaller critical dimensions can be achieved by reducing the thickness of the mask layer. The spacing of final patterns is defined by width of mesas, which is normally limited by optical lithography. However, using a repeated sidewall process, this can be further reduced by replacing the sacrificial features with a previously-fabricated set of sidewall masks.

Although the basic STL features are closed paths following the perimeters of the sacrificial patterns, the process can be combined with additional conventional lithography steps to increase feature diversity. Figure 1.7b shows a process that uses additional lithography and etching steps to remove parts of the sidewall masks allowing open shapes [110]. Isolated paths can

then be combined with additional patterns for more complicated designs. For example, Figure 1-8 shows two types of thin-body MOSFETs (metal–oxide–semiconductor field-effect transistors) gate process (gate-first and gate-last), in which STL is used to form nanoscale fins [110].
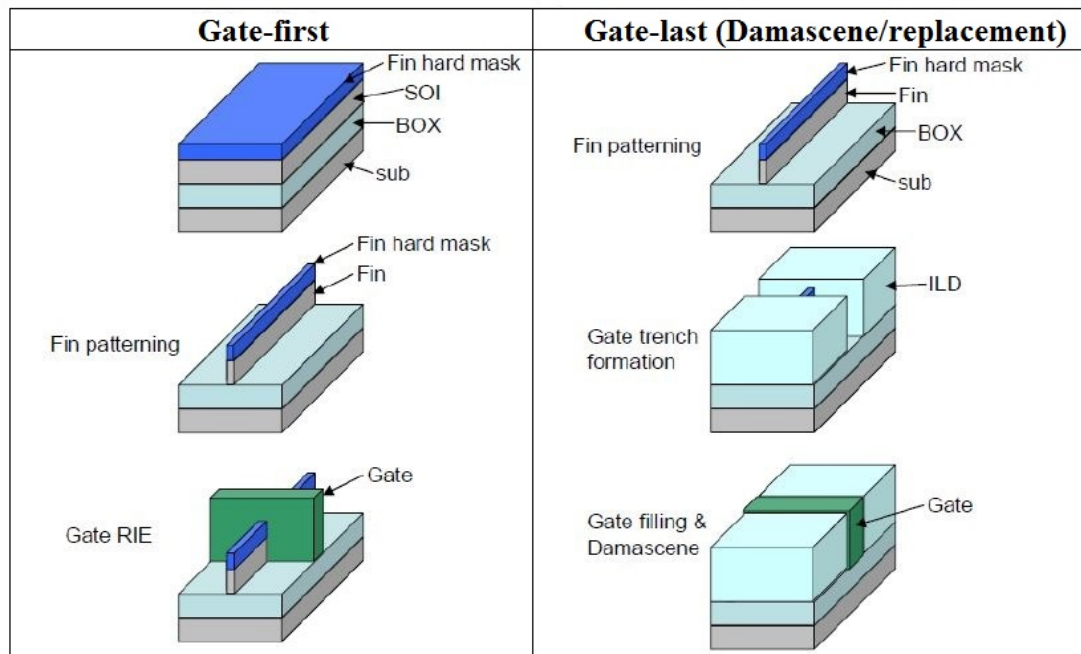


Figure 1.8: Schematic diagrams of (a) gate-first and (b) gate-last thin body MOSFET gate processes.

As a mass parallel nanoscale fabrication process, STL has received limited attention in more general 3D micromachining. The only applications which have been investigated are nanoscale needles [121] and channels [122]. However, it should be possible to adapt STL to low-cost NEMS fabrication. Ideally, it should be possible to achieve comparable in-plane feature sizes to those obtained in CMOS fabrication, although the minimum might be restricted by other micromachining process such as deep silicon etching. Combined with additional lithography steps, it should be possible to achieve a wide variety of pattern geometries and combine them with micro- and nanoscale parts. Developed processes should be applicable to either bulk silicon or BSOI wafers, however the later should offer more precise definition of vertical depth of structures. The aim of this thesis is to investigate exactly these possibilities.

## 1.4 Thesis plan

The structure of the remainder of the thesis is as follows. In Chapter 2, a STL NEMS process is introduced, together with the DRIE process needed to form and undercut HAR NEMS features. Elementary in-plane electrothermal actuators are then demonstrated in Chapter 3. Prototype devices in bulk and BSOI wafers are presented, and the new processing issues experienced are discussed. In Chapter 4, the mechanical and electrothermal performance of completed NEMS actuators is then characterised, and compared with the results of FEA. Because the latter is somewhat unsatisfactory, new analytic models for two specific NEMS electrothermal actuators (with chevron and raised cosine pre-buckle, respectively) are developed in Chapter 5. In Chapter 6, a multi-layer STL NEMS process is demonstrated as an extension of the single-layer process. The process is used to fabricate a wide range of different device layouts, and specific fabrication issues are again discussed. In Chapter 7, the 2D lattice fabricated by the multi-layer STL is further analysed theoretically and experimentally, which can be understood as a novel type of mechanical metamaterial. Reasonable agreement has been achieved between theory, experiments and FEA predictions, although accuracy of the last is limited by simulated device lay-outs. Finally, conclusions are drawn in Chapter 8, and possibilities for future work are introduced.

# 2 Sidewall transfer lithography

In this chapter, sidewall transfer lithography (STL) is introduced, together with the related fabrication processes used for general 3D micromachining. Section 2.1 gives a brief introduction to the STL process, and corresponding background information. The process is then detailed in a step-by-step fashion, based on the provided process flow in Section 2.2. Section 2.3 provides detailed information on the modified Bosch process for deep reactive ion etching (DRIE) to form nanoscale features. The standard Bosch process is now optimized to be compatible with NEMS fabrication. The etching rate is also calibrated to obtain suitable feature profiles, using experimental results. In Section 2.4, a novel technique of plasma undercut is introduced as an extension of the Bosch process to achieve dry release of both micro- and nano-scale suspensions. The technical essentials are explained, and the results of experimental fabrication trials are again described. Finally, the process constraints are discussed in Section 2.5, where a short conclusion is presented.

## 2.1 Introduction

Future nano-electro-mechanical systems will require low-cost, mass-parallel fabrication processes. However, many current fabrication techniques involve either an expensive atomic force microscope or dip-pen lithography or processes such as soft lithography, nanoimprint lithography that themselves require nanoscale masters as mentioned in Chapter 1. In each case, the cost, slow speed and complexity of the patterning step may prevent the translation of NEMS into practical use. However, many NEMS only require localized nanoscale parts surrounded by supporting microscale features. It is therefore highly desirable to develop cheap, parallel processes for fabricating nano-structures, which can be made compatible with most NEMS applications.

One possibility is sidewall transfer lithography, a set of processes that can transform the perimeter of a microscale feature into a nanoscale surface mask. The general approach is to coat an etched mesa with a conformal layer of material that may be selectively removed from

45

horizontal surfaces, leaving the vertical surfaces to provide a mask whose width is determined by the coating thickness. STL is a wafer-scale process entirely based on optical lithography and DRIE, and hence that can be carried out using much simpler equipment. It can also be used with either bulk silicon or bonded silicon-on-insulator (BSOI) wafers. The process effectively uses the techniques and equipment of conventional photolithography designed for microscale features to fabricate nanoscale features, thereby reducing the fabrication cost and increasing the yield rate.

Figure 2.1 outlines the range of possible STL processes. Figure 2.1a shows how sidewall processes may be used to form nanoscale ribs, by first forming a mesa, and coating it with a layer of material which is then etched except on the vertical perimeter. Figure 2.1b shows how it may be used to form slots, by using the nanoscale feature in Figure 2.1a as a mask in an additional lift-off process. If the coating is a multilayer, and one of the layers may be selectively removed from between the others, nanoscale separations between nanoscale parts may also be formed, as shown in Figure 2.1c. Generally, the patterns follow closed polygonal perimeters. However, additional etch steps may be used to remove parts of the pattern to leave separate lines as shown in Figure 2.1d, and selective etching of a multilayer sidewall allows a stepped variation in width in a nanoscale line as shown in 2.1e.
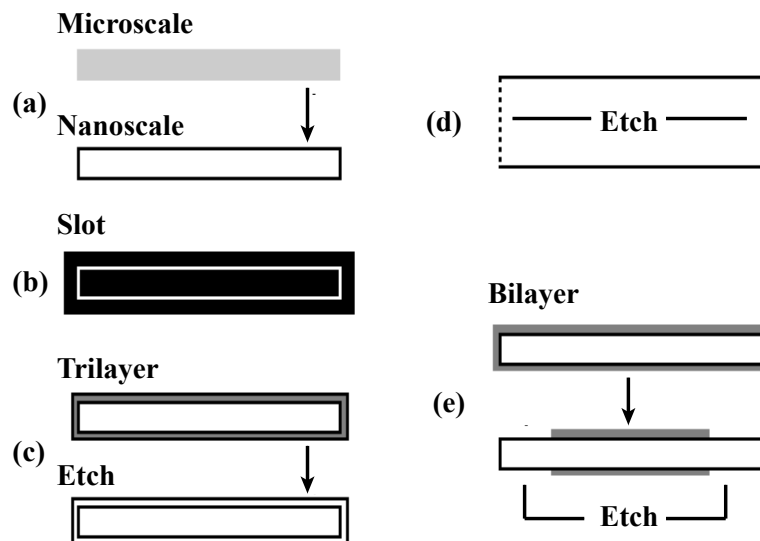


Figure 2.1: STL processes: (a) conventional; (b) reverse; (c) multiline; (d) interrupted; (e) variable width.

Applications for STL include microelectronics, optoelectronics, field emission devices, nanowires,

nanofluidics and nanoimprint templates. In each application demonstrated to date, the nanoscale features are one-dimensional; however, here we argue that the method has considerable potential for fabrication two-dimensional device lay-outs if suitably developed, as detailed in Chapter 6.

In this chapter, the basic principle of the STL process will be introduced, based on a single sidewall patterning step followed by a DRIE step to transfer the pattern into high-aspect-ratio (HAR) silicon features.

## 2.2 Process flow

Figure 2.2 illustrates the process flow of two different STL processes based on BSOI wafers. One uses the outer edges of mesas to form nanoscale features, while the other uses the inner edges of slots. Starting with bare wafers (step 1), optical lithography is first used to form an initial set of microscale patterns (step 2), which are then transferred into shallow silicon mesas (left) or slots (right) by an anisotropic etching process (step 3). After removing the photoresist mask (step 4), the whole surface is conformally coated using the sidewall mask material, to leave all the surface steps fully covered (step 5). The coated layer on the horizontal surface is then selectively etched, leaving only the vertical parts of the coating as a mask defining nanoscale beam arrays (step 6). The pattern is then transferred into the silicon substrate using DRIE, typically etching down to the oxide interlayer (step 7). Finally, the sidewall mask is removed to leave only the silicon features on a oxide substrate (step 8).

As shown above, the sidewall features follow any shallow steps patterned in the initial conventional lithography including both mesas and slots. Thus both positive and negative photoresist can be adapted to the process easily, with appropriate resolution. To form nanoscale suspended parts, an additional conventional lithography step can be added before transferring the combined pattern into the silicon substrate (i.e., before step 7), to define other microscale features such as anchors. The suspended parts can then be freed by etching of the sacrificial oxide interlayer beneath the nanoscale parts at the end (after step 8).

Previous work has also used photoresist as mesas. This method shows some advantages as it is then possible to remove the original mesa easily after the sidewall mask formation (after step 6). The two silicon surfaces on both sides of a single sidewall will then be at the same height for the following DRIE step. However, it is difficult to achieve vertical edges from photoresist
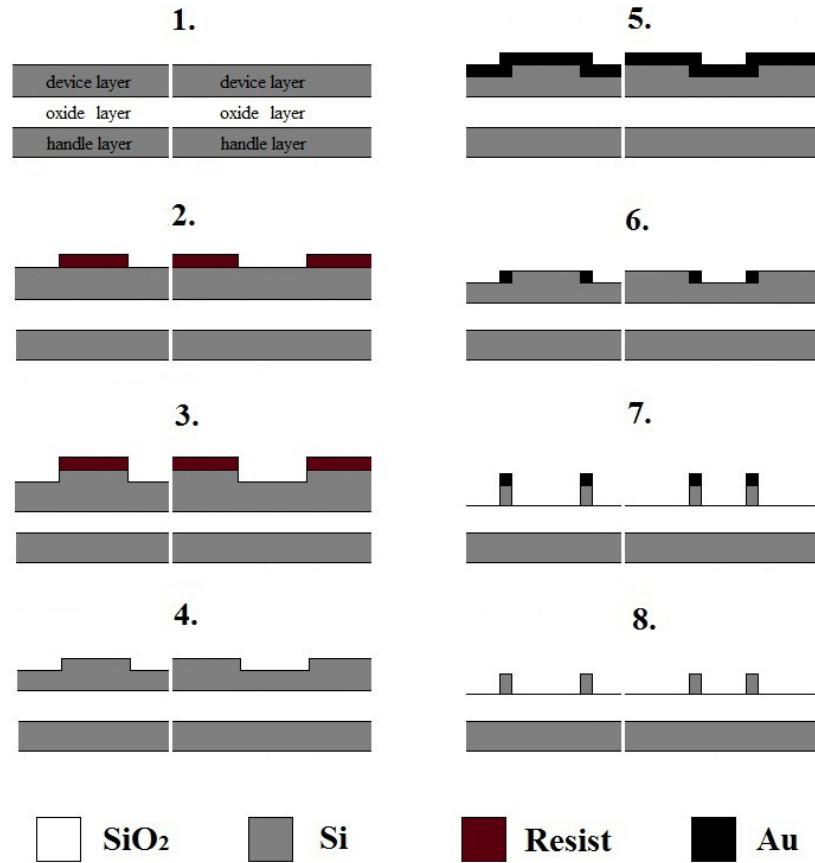
Figure 2.2: Process flow for BSOI STL: (1) starting BSOI wafers; (2) coat and pattern resist; (3) DRIE to form mesas and slots; (4) strip resist; (5) sputter coat Cr/Au; (6) selective sputter-etch Cr/Au; (7) DRIE to oxide interlayer; (8) remove sidewall masks.

mesas, which have curved corners in most cases. This aspect normally results in poor quality in the attached sidewall masks. Thus, silicon mesas were chosen for the highly vertical step features that can be formed using optimised DRIE.

The sidewall mask formation is the critical step in the STL process. A malleable material with low stress is the ideal choice for the sidewall material. However, there are also other factors to be considered: the material must a) be compatible with selective horizontal etching, b) have low intrinsic stress, c) have good adhesion and d) be easy to remove. After careful consideration, Au was chosen for preliminary tests, although other materials such as silica are easier to remove at the end of the process. The main reason for the choice was low stress. For example, in separate experiments, thermal oxide was proven to have good adhesion but very high intrinsic stress. However, low-temperature deposition methods such as plasma enhanced chemical vapour deposition (PECVD) would provide more compatible $SiO_2$ layers.

The width of the sidewall mask defines the critical feature size produced by the STL ($\leqslant$

100nm with current experimental results) which obviously shows a close connection with the thickness of the mask layer deposited in step 5. Details about the sidewall mask profile can be found in Chapter 3.

## 2.3 Nanoscale deep reactive ion etching

Deep reactive ion etching (DRIE) is a silicon etching process widely used in industrial MEMS fabrication. The Bosch DRIE process was originally developed by the German company Robert Bosch GmbH. It was subsequently licensed to STS (Surface Technology Systems), a UK manufacturer of ICP (inductively coupled plasma) DRIE systems. It is a cyclic process contains alternate $SF_6/O_2$ plasma etching and $C_4F_8$ passivation steps, and can operate with a dual frequency plasma to allow conventional deep silicon etching and stop-on-oxide. The Bosch process is the process most commonly used in MEMS fabrication, when HAR microscale structures are required.

### 2.3.1 Standard Bosch DRIE process

The standard Bosch STS ICP DRIE process offers great advantages compared with isotropic RIE in microscale silicon etching. It achieves high selectivity with the most common mask materials in microelectronics, including photoresist $(60:1)$ and $SiO_2$ $(100:1)$ typically. Consequently, much greater feature depth can be achieved (for example, etching right through a $500\mu m$ thick wafer). It can also achieve high verticality in the step profile of etched features, if the parameters of each process cycle are well chosen. As result, very deep beam structures can be fabricated, with well-defined mechanical properties.

Figure 2.3 shows a schematic diagram of the standard Bosch DRIE process. A mask layer is first patterned to define feature areas to be etched on the silicon substrate. Before each etching cycle, a $C_4F_8$ polymer passivation layer is deposited on the whole surface. In the next etching step, a $SF_6/O_2$ plasma is used to etch the silicon substrate almost in a vertical direction, punching through the horizontal surface and etching away the silicon at the bottom of the window. However, some lateral etching inevitably occurs, so that small scallop-shaped features are generated as well. A passivation layer is then deposited, and the cycle of etching and passivation is repeated. The presence of passivation on the sidewalls protects vertical features from lateral over etching. Using this general operating principle, the Bosch DRIE process can easily form

macroscale HAR features, but generally suffers from periodic scallops in the sidewall, with a typical scallop size of approx. 0.4μm.
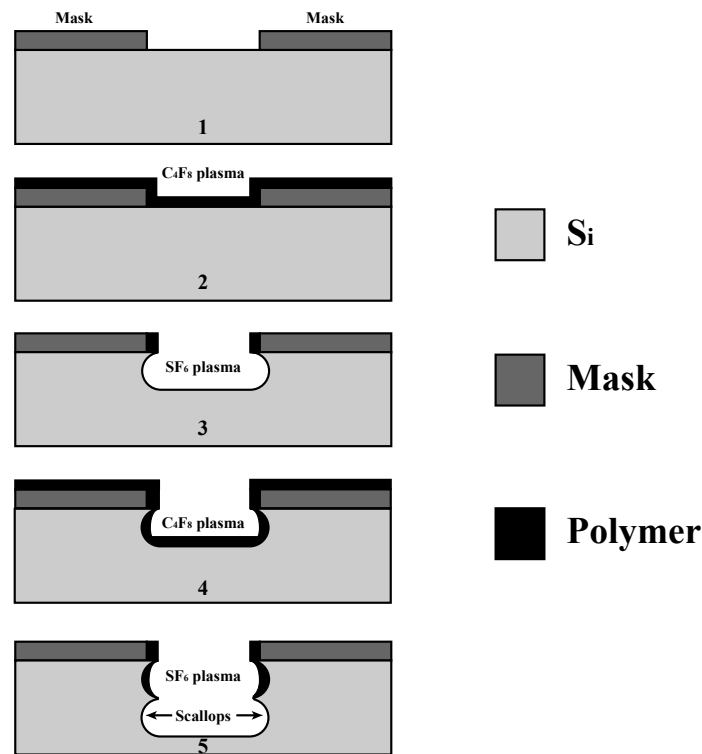


Figure 2.3: Schematic diagram of standard Bosch DRIE process.

## 2.3.2 Compatible Bosch process for NEMS

Although the standard Bosch DRIE process works very well for MEMS fabrication, it must be further investigated and optimized for HAR nanostructures. This work and all subsequent etching were carried out using a STS Single-Chamber Multiplex ICP DRIE at Imperial College. As the critical feature size is determined by the scalloping inherent in cyclic etching, most of the effort was devoted to minimizing the scallop size and ensuring that the scallops did not destroy the nanoscale features. Particularly, erosion of any 100nm wide beam must occur when the scallop size rises above 50nm, since the scalloping must occur on both sides.

Figure 2.4 shows SEM views of experimental features etched with different scallop sizes. In each case, the nanoscale features are defined by a Cr/Au sidewall mask (approx. 200nm in width) and etched using DRIE. In Figure 2.4a, severe erosion can be observed on the silicon walls, which have clearly collapsed in some places. The remaining features show a series of scallop-shaped indentations in the walls inherent from the cyclic process. Figure 2.4b shows

the result of a modified etching process, with the same sidewall mask. Here, the duration of the etch cycle (and consequently the scallop size) has been reduced. The horizontal traces on the nanoscale beam show that it has survived multiple cycles of etching. Although there are some signs of erosion at the base of the beam, the etching is uniform and highly anisotropic even near the joints between micro- and nano-scale features. Figure 2.4c shows a cross-sectional view obtained by cleaving the nanoscale beam. Scallops can now be seen clearly on the silicon wall, with sizes gradually decreasing from the top down. Despite this, the beam width is also decreasing. Consequently, erosion can then be predicted if etching goes further, which explains wall damage at the bottom in Figure 2.4b. Figure 2.4d shows the upper part of a structure etched with much larger scallops. Here the sidewall mask (the feature with much smaller scallops) has been completely undercut. As a result, there can be no nanoscale beam formation if the etching is carried any further.



(a)  (b)  (c)  (d)
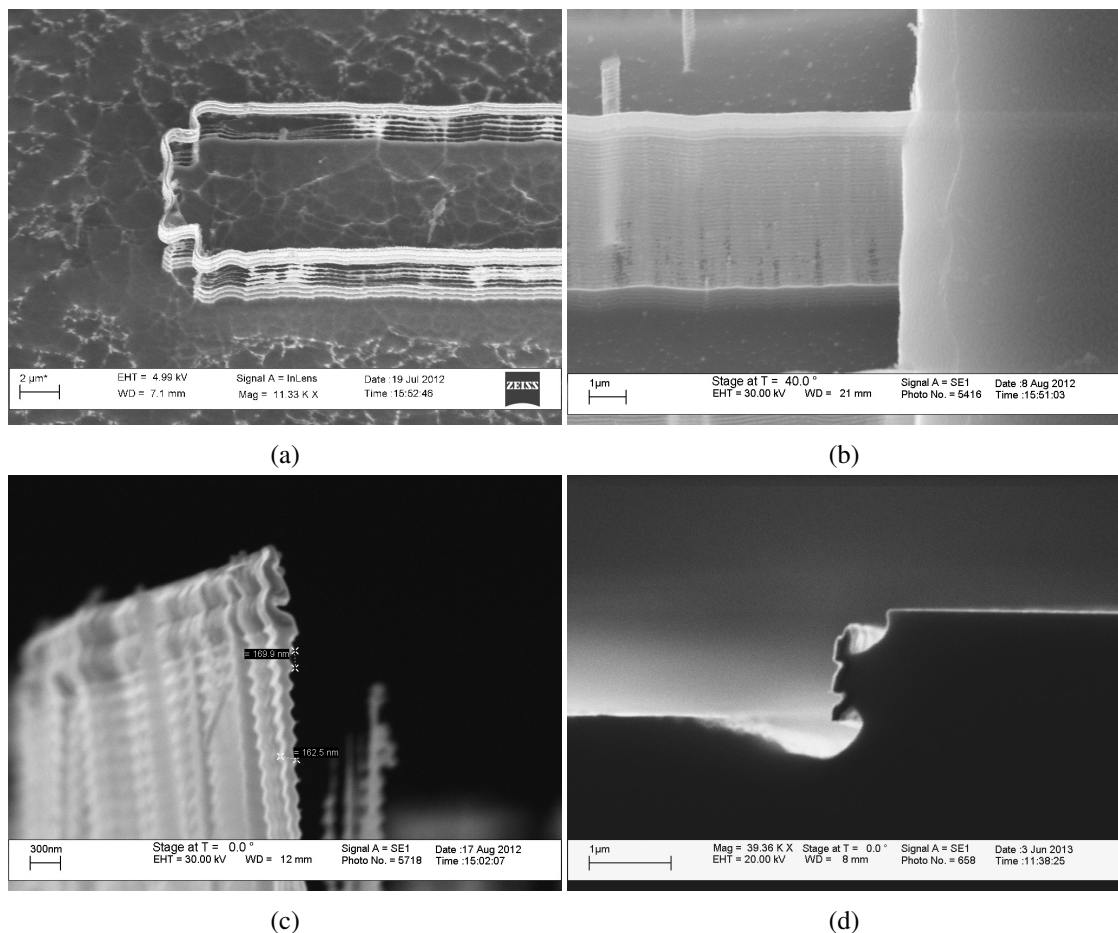
Figure 2.4: SEM views of (a) and (b) etched nanoscale features with different scallop sizes; (c) cross-sectional view of nanoscale beam; (d) sidewall mask undercut by large scallops.

The DRIE parameters must therefore be chosen to minimize the scallop sizes in order to

prevent erosion and achieve uniformity in nanoscale etching. Table 2.1 shows the parameters of two comparable process, one giving large scallops and suitable for microscale etching, the other giving much smaller scallops for nanoscale etching. As can be seen, the etching power and the duration of each etching cycle must be greatly reduced to obtain a process with small scallops. Experimental results show that only the lowest values yield etched features compatible with nanoscale structuring. The corresponding parameters for the passivation cycles must also be changed to achieve an appropriate ratio between the etching and passivation cycle times, and hence to prevent grass formation due to over-passivation. The scallop size of the nanoscale etch process (LCD-350) is approx. 35nm compared with 420nm in a typical microscale process (LCD-1), a 12-fold reduction.

| Recipe | RF Power (W) | | Cycle time (s) | | Gass flow (sccm) | | Pressure (mtorr) | | Scallop size |
| | Coil | Platen | Etch | Passivation | $SF_6$, $O_2$ | $C_4F_8$ | Etch | Passivation | (nm) |
|---|---|---|---|---|---|---|---|---|---|
| LCD-1 | 600 | 15 | 13.8 | 9 | 130, 13 | 110 | 20 | 15 | 420 |
| LCD-350 | 350 | 11 | 10 | 5.2 | 50, 5 | 80 | 6.2 | 7.3 | 35-40 |

Table 2.1: Different parameters of two DRIE process for (a) microscale and (b) nanoscale features.

Figure 2.5 shows the variation of scallop size with the duration of each etch cycle for the two different RF powers (350W and 600W). These data were extracted from SEM photographs of etched samples experimentally, assuming a semi-circular scallop profile, which can be overestimated in practice. These data confirm the results of Table 2.1, namely low power and short etch cycles are required for successful nanoscale etching.
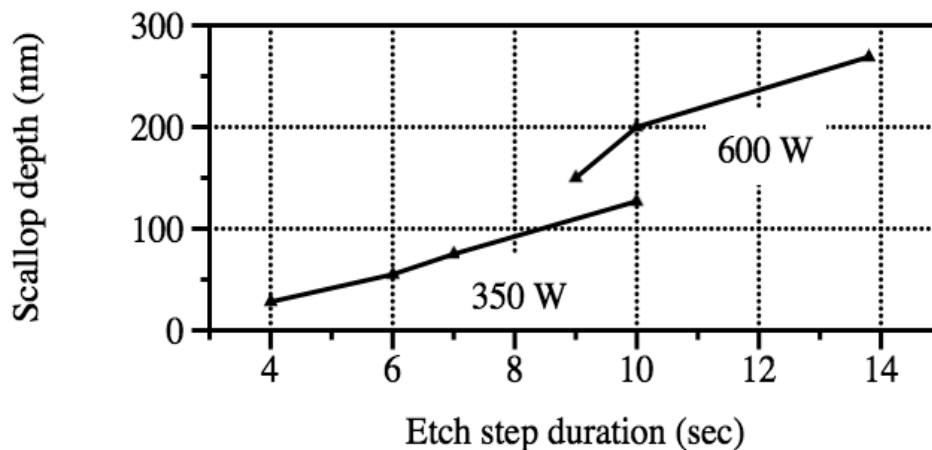


Figure 2.5: Variation of scallop depth with etch step duration, at different RF powers.

Figure 2.6 shows SEM views of silicon features obtained after optimization of the DRIE

process parameters. The cross-sectional views are obtained by cleaving the structures to evaluate the wall profiles. Figure 2.6a shows a nanoscale beam with a high ($> 35:1$) aspect ratio and only minor variations in thickness after a deep etching. The scallop is minimized and almost invisible, thus preventing the lateral erosion effectively. The modified process can also be used to improve the etching of the original mesa features, and hence improve the profile of the sidewall mask. Figure 2.6b shows a silicon mesa with 10μm width, which has been etched to a depth of 6.5μm with minimal scallops. A highly vertical sidewall is now achieved, with a very smooth surface. Although this result is generally useful in shallow, microscale etching, it is specially promising for the STL process as the profile of the mesa edge will affect the sidewall mask attaching to it. Hence, the optimised DRIE process can now be used to etch both microscale (Figure 2.2, step 3) and nanoscale (Figure 2.2, step 7) patterns in the STL process.



(a)                                    (b)
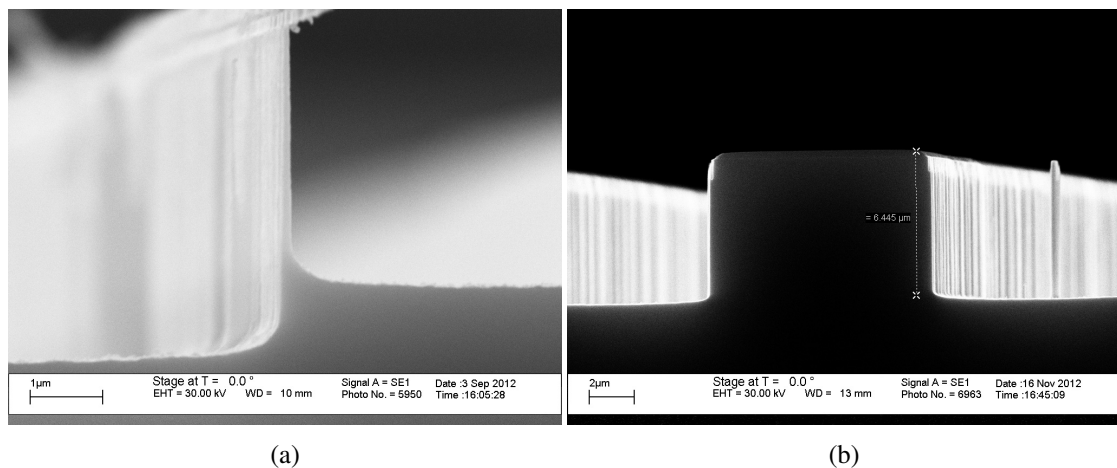
Figure 2.6: Cross-sectional SEM views of (a) nanoscale and (b) microscale silicon features etched by optimised DRIE process.

The optimised DRIE process was then calibrated to achieve appropriate etch depths. For example, Figure 2.7aa shows the variation of the etch depth with the number of etch cycles, for the etching recipe LCD-350 in Table 2.1. With an RF power of 350W and duration of 4s in each etching cycle, a etching depth of 4.5μm was achieved after 60 cycles, with an almost linear etching rate (approx. 75nm/min). Some over-etching is necessary to remove the additional silicon in the mesa regions and to compensate for any variation in the device layer thickness when using BSOI wafers. However, because of the low RF power used, it was found to be unnecessary to use low-frequency plasma (normally required to prevent charge build-up) to stop on the oxide interlayer.

The DRIE process was then adjusted further to control the beam profile. Figure 2.7b compares

the variation of beam width with depth for beams etched with two different processes. These data were extracted from SEM photographs of cleaved test specimens. Trace A shows the variation for an etching recipe with excessive passivation. Starting from an initial value of 150nm (which is over-large due, to excessive scalloping of the mesa as shown in Figure 2.4a), the beam width clearly increases significantly with depth, to approx. 300nm at its base. One possible explanation is that it takes longer for the reactive ions in a plasma to arrive at the reaction surface as etching proceeds. If the duration of the etching cycle is kept constant, the etch cycle may fail to consume all of the passivation layer in a deep trench. Any passivation remaining at the feet of sidewalls then causes gradually increasing sidewall dimensions. To avoid this effect, the duration of both the etching and passivation cycles should be adjusted to maintain feature quality as etching goes deeper. Trace B shows the variation that can be achieved with an optimised recipe; here, the beam width is close to 100nm throughout, with a high aspect ratio (40 : 1).
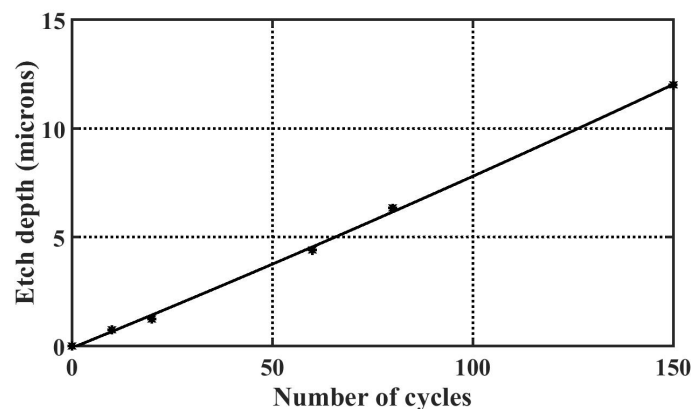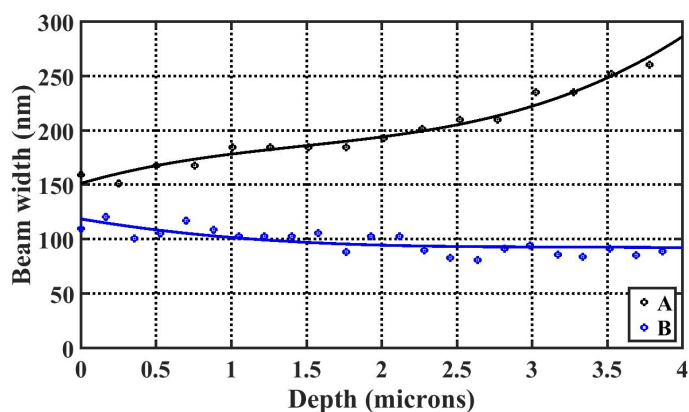


Figure 2.7: Variation of (a) etch depth with number of etching cycles, and (b) beam width with depth, for different process schedules.

## 2.4 Plasma undercut

Plasma undercut is a novel and promising extension of the Bosch DRIE process. Undercut was previously presented as a flaw in etched features (for example, as shown in Figure 2.4d). However, it is always more interesting to turn waste into wealth. Figure 2.8 shows a dry release process, based on the use of an isotropic $SF_6$ plasma RIE step after deep etching of HAR silicon features to form suspended nanoscale structures. Before undercut, sufficient passivation must be be deposited to prevent lateral erosion of the suspended parts. Microscale features such as anchors will also be undercut; however, these will not be released, due to their significantly larger size.
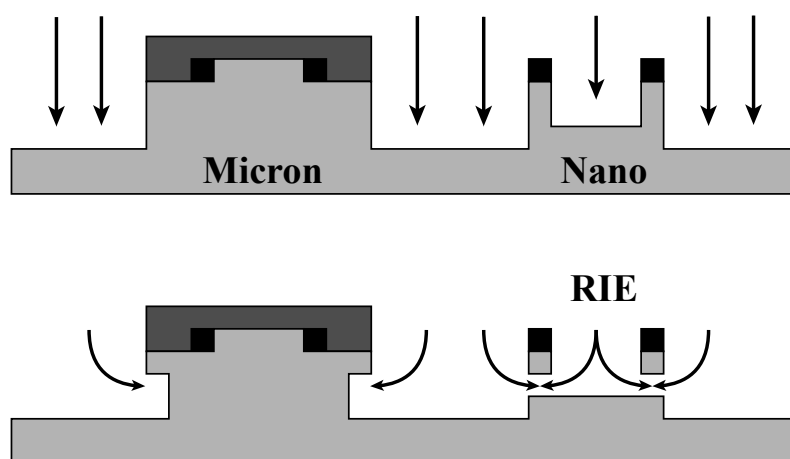


Figure 2.8: Schematic diagram of a dry releasing process using plasma undercut.

It was found that different processes are needed to undercut structures with different dimensions. For nanoscale features, the best solution is to utilize the modified cyclic Bosch DRIE process with much larger scallop sizes. As described earlier, since it is possible to control the scallop size precisely by adjusting the etching parameters, appreciate processes can be developed to undercut nanoscale features in a wide range of sizes, up to a few hundred nanometres. Figure 2.9a shows a nanoscale silicon beam during undercut. Two large semi-circular scallops are formed at the bottom of each side of the silicon wall. They are vertically staggered because of the original height variation introduced by the silicon mesa structure. Hence, the scallop radius needed for undercut is almost the same as the beam width, as the entire beam must be

undercut by a single scallop.

A relative complex process is needed to undercut microscale features, since it is very easy to damage any nearby nanostructures using a highly isotropic etch. A polymer layer of $C_4F_8$ must be deposited prior to etching, to provide sufficient protection of the whole structure, followed by a short but highly vertically $SF_6/O_2$ plasma to punch through the horizontal parts of the passivation layer. This step is extremely important to avoid any footing effect from the residual polymer. It is then safe to undercut the features with a much stronger isotropic RIE process. As the final RIE step is usually quite rapid and aggressive, special care must be taken to prevent erosion, by adjusting the amount of passivation. However, with practice, microscale features up to 5μm may be successfully undercut using the above techniques. Figure 2.9b shows a series of microscale beams that are partly undercut, with only a very small width of silicon at the bottom still connected to the substrate. Because these microscale parts are not formed using a mask derived from a mesa structure, undercut occurs from both sides of the beam at the same height, so the scallop depth needed for undercut is only half of the beam width.



(a)          (b)
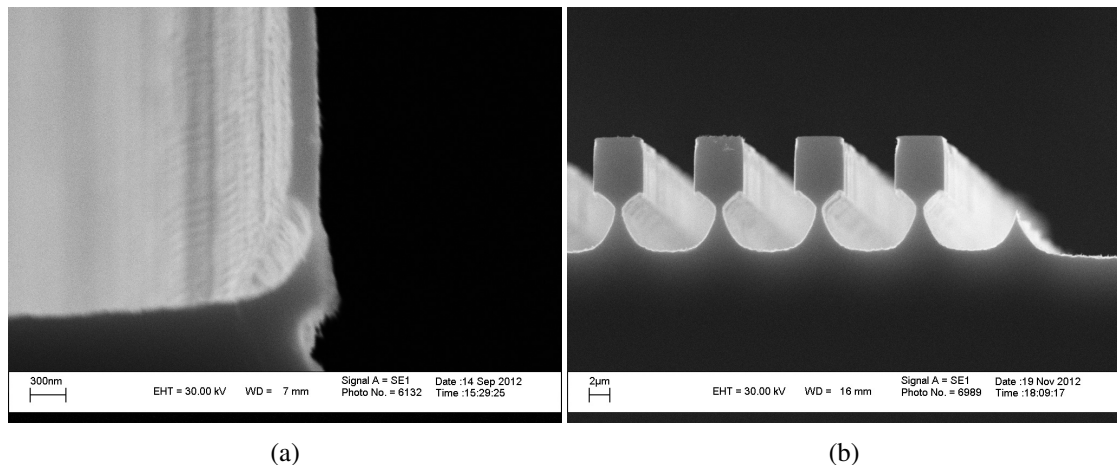
Figure 2.9: SEM views of (a) nanoscale and (b) microscale silicon features undercut by $SF_6/O_2$ plasma.

Etched features were further investigated to obtain a better understanding of the undercut process. Figure 2.10 shows the bottom of the silicon beam after full undercut of both nanoscale (Figure 2.10a) and microscale (Figure 2.10b) features. In Figure 2.10a, a small hole can be seen near the bottom in the middle of the beam. Since the beam should have been protected by passivation on both sides, and that the etching mask should still remain at the top, it is reasonable to deduce that the beam must have been slightly over-etched by isotropic etching from the bottom up. Figure 2.10b shows a close-up of the bottom profile of an over-turned

microscale beam after undercut. As predicted in Figure 2.9b, the bottom shows a multiply-curved profile resulting from attack by the isotropic plasma etch in several directions.
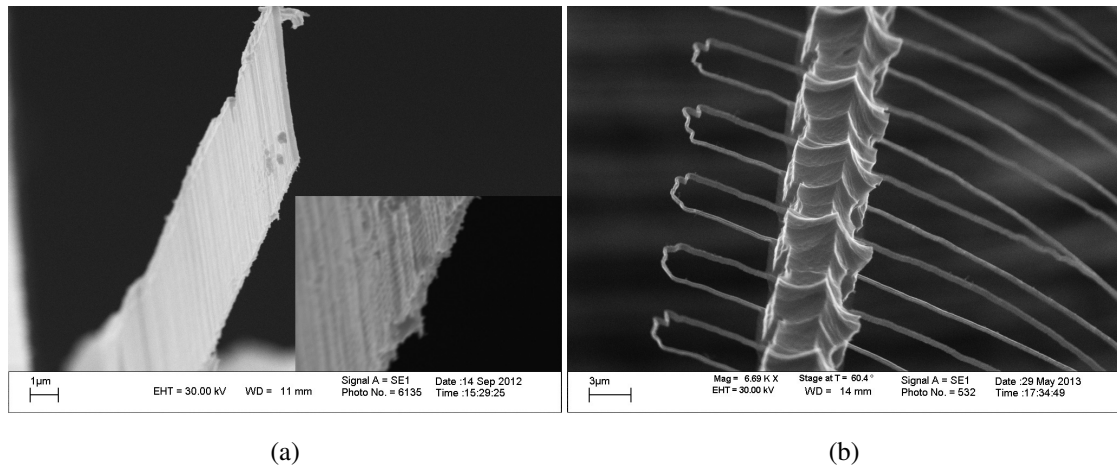


Figure 2.10: SEM views of bottom profiles obtained from (a) nanoscale and (b) microscale undercut silicon beams.

Such all-in-one process can simplify fabrication, by accomplishing multiple steps without the need to remove the wafer from the deep etching plant. This approach greatly improves the reliability and feasibility of the whole STL NEMS process. With this technique, it is possible to form combined micro- and nanoscale suspensions on bulk silicon wafers instead of BSOI, which should lower the process cost. More importantly, dry release can greatly improve MEMS fabrication yields, since it eliminates the surface tension collapse that often occurs in the drying step that must immediately follow a wet release process.

## 2.5 Discussion

Geometric constraints are more fundamental. For example, all the nanoscale features must follow the perimeters of closed polygons. This makes the STL well suited to the formation of multiple built-in beams (as here) but will present a significant limitation for other designs. For example, it is not possible to form single cantilevers using the process in Figure 2.2. However, it is simple to envisage additional patterning steps that interrupt polygons to allow cantilevers, or overlay polygons to generate more complex designs such as intersecting suspensions.

Similarly, all nanoscale features must have constant width. However, it would be possible to employ additional sidewall layers, which are removed over part of the perimeter by patterning and differential etching, to yield nanoscale features with variable width. This approach might be used (for example) to construct shape bimorphs, but clearly requires additional deposition,

57

lithography and etching steps.

Finally, it is not simple to introduce nanoscale separations; typically, STL yields nanoscale features or slots, but not both at the same time. The use of multilayer sidewalls based on alternating materials should allow at least the formation of parallel beams with nanoscale gaps. Other post-processes such thermal, surface tension or electrostatic actuation might be used to adjust structures after release. However, it is hard to see how some components that are common in MEMS (for example, electrostatic comb drives) could be formed with both nanoscale parts and nanoscale gaps. Thus, the method does have significant constraints.

Such processes are potentially attractive for mass production of NEMS, since they allow wafer-scale fabrication using widely available, low-cost equipment. However, they suffer from key topological constraints, and overcoming these limitations should extend the range of applications.

# 3 Single-layer NEMS actuators

In this chapter, the design of a series of NEMS electrothermal actuators is introduced, fabrication processes suitable for bulk silicon and bonded silicon-on-insulator (BSOI) materials are developed and the results of initial processing are described. In Section 3.1, the designs of double- and single-ended actuators are described, together with the corresponding mask layouts. The fabrication results obtained using processes based on sidewall transfer lithography for bulk Si and BSOI are then described in Section 3.1 and Section 3.3 respectively. In each case, the results of lithography and etching are discussed and complete prototype devices are demonstrated. In Section 3.4, a number of residual processing issues are discussed and conclusions are drawn in Section 3.5.

## 3.1 Device concept and design

Using the STL process introduced in Chapter 2, two well-known designs of electrothermal actuators have been fabricated to prove the process concept. As shown in Figure 3.1, a combination of micro- and nanoscale structures was adapted to demonstrate the compatibility of the STL. Specific dimensions were chosen to highlight particular aspects of processing, especially the stress effect.

The lay-out of a double-ended buckling actuator of V-beam or chevron shape is shown in Figure 3.1a [33, 35]. A set of parallel beams patterned by STL layer 1 defines the nanoscale beams. Microscale anchors at both ends are patterned using STL layer 2, as well as a central crossbeam to tie all the nanoscale beams together. When the beams are heated electrically, by passing a current between the anchors, an in-plane motion of the crossbeam is generated due to differential thermal expansion of the pre-buckled shape. Detailed analysis of the thermo-mechanical response of a V-beam actuator in Chapter 5 shows that the motion is quasi-linear. Clearly, the crossbeam ties the entire nanobeam array together, and constrains the motion to collective deflection in the pre-buckling direction. The occurrence of higher-order buckling

modes is thus minimized.

Figure 3.1b shows an alternative design of single-ended thermal actuator based on a folded V-beam shape [123, 124]. The actuator consists of sets of cold and hot beam arrays, which are tied together at their free ends by a crossbeam. At the fixed ends, anchors are subdivided for each set of beams to allow a heater current to be passed through the hot arms. The cold arms then serve as tethers, so that in plane motion due to differential thermal expansion of the hot beam array is constrained in the direction shown.
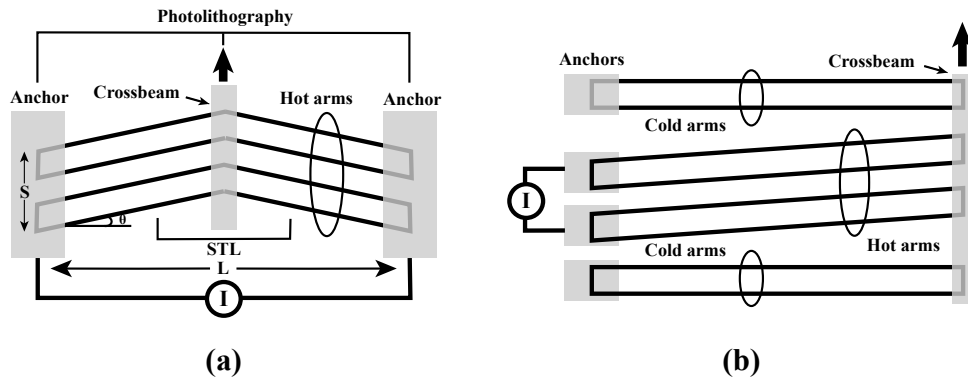


Figure 3.1: Lay-out of (a) a double-ended and (b) single-ended V-beam actuators designed based on STL process.

A mask set containing both types of electrothermal micro actuators was then designed, for 100mm diameter wafers. For all devices, the total beam length was 1mm, with two different beam separations of 5μm and 10μm. In both cases, the number of hot beams was much larger than those shown in Figure 3.1, up to 58 for the folded V-beam actuator and 116 for the single-ended actuator. All the hot arms were designed with a slope angle of $\theta = 0.01$rad. For the single-ended device, 4 parallel cold beams were provided at each end to constrain the displacement direction. The width of the crossbeam was 2μm and 10μm of crossbeam projected beyond the beam array ends. The total number of dies on the whole wafer was 2420, and a mixture of various designs was included in each block of dies. The overall design was based on fabrication of 100nm nanoscale beams on BSOI wafers with 5μm device layer thickness, so that the aspect ratio of the resulting nanobeams was approximately 50 : 1. The corresponding ratio of out-of-plane to in-plane stiffness of a single beam is 2500 : 1.

## 3.2 NEMS actuators on bulk silicon wafers

Demonstrator devices were firstly fabricated in 100mm diameter bulk silicon wafers (P-type, $< 100 >$ crystal oriented, resistivity $1 - 5\Omega \cdot \text{cm}$) as shown in Figure 3.2a. The fabrication process was designed for both bulk silicon and BSOI wafers. Obviously, BSOI wafers provide more accurate definition of the device layer. However, bulk silicon wafers were used to test the process and discover potential fabrication issues, thus improving the yield and reducing cost.

Prototype devices were fabricated based on the CAD lay-outs shown in Figure 3.1. Figure 3.2 shows the top view of complete devices in bulk Si. For both double-ended V-beam (Figure 3.2b) and single-ended (Figure 3.2c) actuators, the overall die size is $1400\mu\text{m} \times 640\mu\text{m}$. All devices were released from the silicon substrate by isotropic plasma undercut.



(a)  (b)  (c)
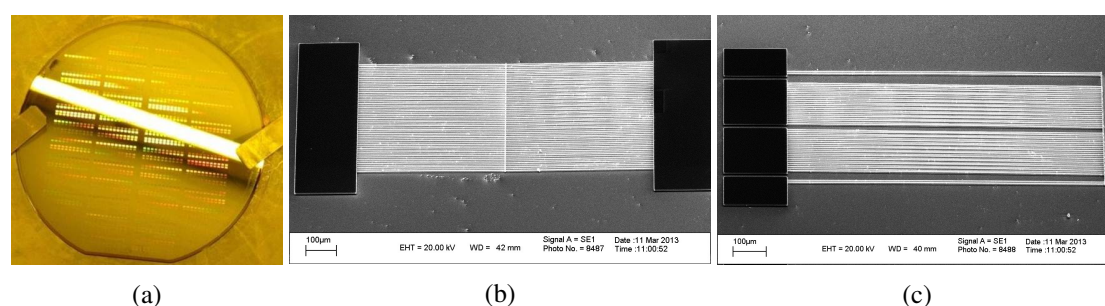
Figure 3.2: (a)Demonstrator NEMS actuators fabricated on a 4-inch silicon wafer; top SEM views of (b) double-ended and (c) single-ended NEMS V-beam actuators on bulk silicon.

### 3.2.1 Fabrication steps

Fabrication was based on a set of processes developed from the elementary STL process introduced in Chapter 2. Figure 3.3 shows the process steps for bulk silicon wafers. Conventional lithography is firstly used to form the initial microscale pattern using an optical resist and a mask that defines the nanoscale features (step 1). The pattern is then transferred into the silicon substrate by DRIE to form a set of shallow mesas (step 2). The resist is stripped off and the silicon surface is thoroughly cleaned (step 3). A semi-conformal metal coating is then deposited over the whole wafer by RF sputtering (step 4). The horizontal surfaces of this layer are then selectively removed to leave only the sidewall features following the perimeter of the initial mesa pattern as masks for the nanoscale features such as suspension beams (step 5). A second conventional lithography step is then used to pattern microscale features such as anchors (step 6), and the combined pattern is then transferred simultaneously into the silicon by DRIE to form

all structures including joints between micro- and nano-scale structures (step 7). An isotropic plasma etching step is then used to release the nanoscale suspensions while the microscale features remaining in place as anchors (step 8). The resist is stripped in an oxygen plasma asher (step 9), and a thin aluminium layer is deposited over the entire structure (step 10), providing electrical contact for subsequent characterization.
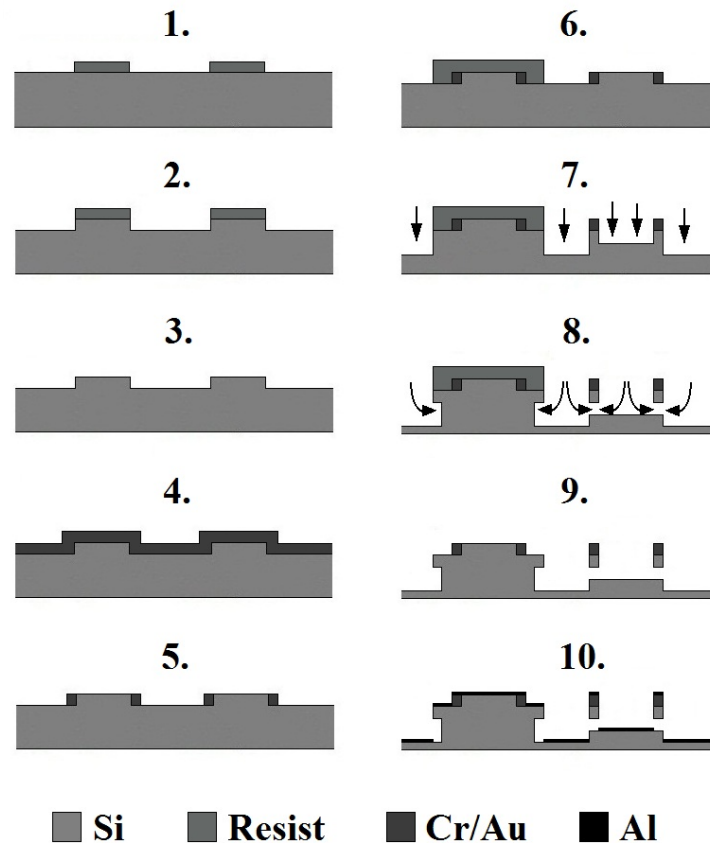
Figure 3.3: Schematic diagram of bulk STL process developed for NEMS.

The mask set was a low-cost chrome-on-glass set manufactured by laser writing at Delta Mask B.V., Enschede, with a nominal resolution of 1.5μm and a minimum feature size of 2μm. Initial pattern transfer was carried out using a Quintel Q7000 mid-UV contact mask aligner, with a typical resolution of 1μm. A 0.4μm layer of Shipley S1805 photo resist was spin coated on the entire wafer surface to pattern the initial microscale mesas. The wafer was then etched in a Surface Technology Systems inductively coupled Single-chamber Multiplex DRIE system based on a cyclic process with $SF_6$ and $O_2$ for etching and $C_4F_8$ for passivation. The height of the initial etched mesa was 0.6μm which was chosen to make the height of the sidewall masks significantly ($>$ 8 times) less than the overall depth of the Si beams, and hence reduce the deformation resulting from any residual stress in the sidewall mask. The resist was then

stripped off thoroughly in acetone and Microposit remover 1165.

Figure 3.4 shows the details of the etched silicon mesas. It was found that the etched feature quality could be high if the etching cycle time of the DRIE was minimized and sufficient passivation was deposited to protect the sidewalls during subsequent etching cycles. However, it was also found that excessive passivation leads to a residual layer of $C_4F_8$ on the wafer surface after etching. This polymer layer could cause other problems in the following DRIE steps to form HAR Si suspensions, as described later. Thus, the initial etching step was modified carefully to start and end with etching cycles so that most of the passivation was removed in the last etching cycle, especially on the horizontal Si surface. As shown in Figure 3.4a, high-quality mesas were formed with both the top and bottom corners almost right-angled in a cross-sectional view. However, in the enlarged view of Figure 3.4b, evidence of the sidewall scallops formed in a 6-step cyclic process can clearly be seen in the mesa sidewall.



(a)                                                                 (b)
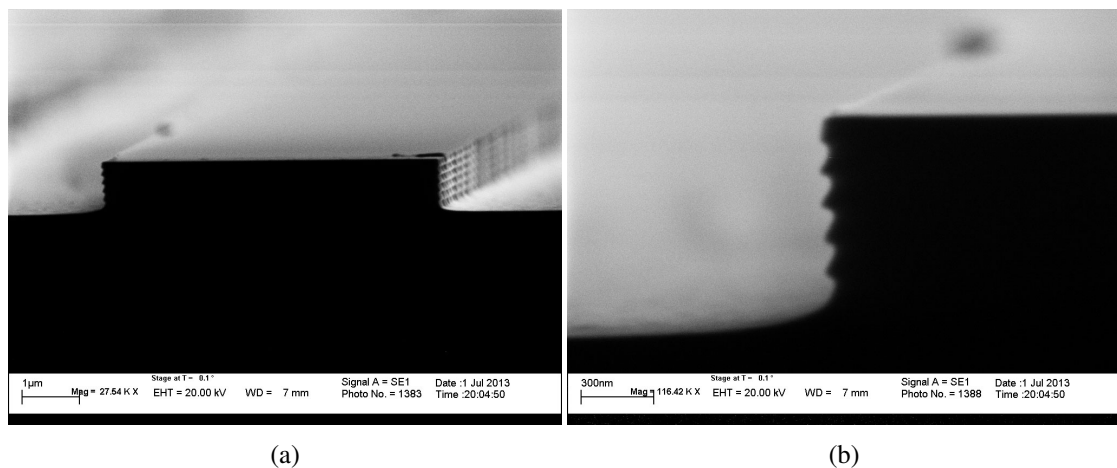
Figure 3.4: SEM views of (a) a silicon mesa etched in the cyclic Bosch DRIE process and (b) close-up sidewall scallops formed in a 6-step etch.

Sputter deposition and Ar plasma etching were chosen to form the Cr/Au sidewall masks following the perimeter of the patterned Si mesas as the next fabrication step. Among many candidate metals and dielectrics, gold was finally selected as a malleable material with low intrinsic stress to form a conformal layer over the whole wafer surface. However, to ensure adhesion, a thin Cr layer had to be deposited. This layer normally introduced higher stress. The sidewall mask was therefore deposited as a bilayer with total width of 100nm (90nm Au and 10nm Cr). The sidewall material was deposited at high pressure ($1.5 \times 10^{-2}$mbar) and then etched at relatively low pressure ($2 \times 10^{-3}$mbar) using in a Nordiko RF sputtering system. To further reduce intrinsic stress, both processes were carried out at low enough power (100W) to

maintain a low temperature.

Figure 3.5a shows a completed Cr/Au sidewall mask layer attached to the original Si mesa after selective sputter etching. The metal mask clearly follows the perimeter of the initial Si mesa. The appearance of scallops inherited from the cyclic etching process shows good attachment of the metal layer. The cross-sectional view in Figure 3.5b shows the height of the etched metal masks was only 2/3 of the original mesa, possibly due to over-etching. It can also be seen that the upper corner of the silicon mesa is rounded, possibly due to a concentration of the Ar plasma during sputter etching.



(a)                                                (b)
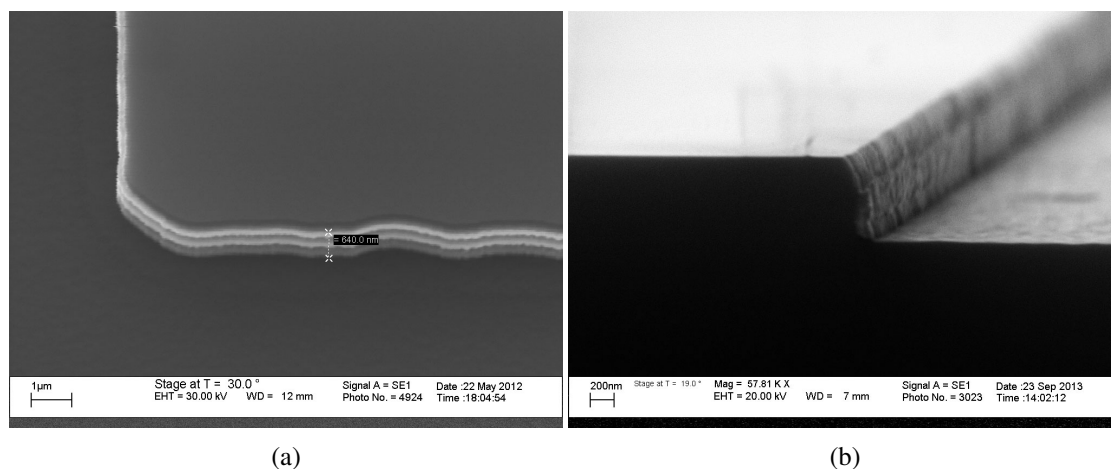
Figure 3.5: SEM views of Cr/Au sidewall masks attached to Si mesas after selective sputter etching.

As the sidewall mask formation is the most critical step of the STL process, further experiments were carried out to characterize this structure. A shallow silicon mesa with a height of approx. 450nm was etched on a single-crystal silicon wafer. A 150nm $SiO_2$ layer was then thermally grown on the entire wafer surface, to provide an interlayer between the original mesa and metal sidewall. After similar sputter deposition and etching steps to those described above, the oxide layer was partially removed from the vertical section in HF vapour. The introduction of this feature inserts contrast into subsequent SEM images, setting the sidewall mask apart from the silicon substrate. In Figure 3.6a, it can be seen that the thickness of the sputter-deposited Au on the horizontal surface (approx. 300nm) is almost three times that on the vertical sidewall (approx. 100nm). It can also be seen that the metal layer conformally covers the silicon mesa, despite the degradation of the mesa due to oxidation. In Figure 3.6b, the coated feature is etched to half of the etching time used before. A similar selectivity can be found in sputter etching, as the metal on horizontal surface is almost removed while a thinner ($< 100nm$) side-

64

wall feature now has almost the same height as the the Si mesa. Lack of thickness uniformity and over-etching are therefore the explanations for the previous results.
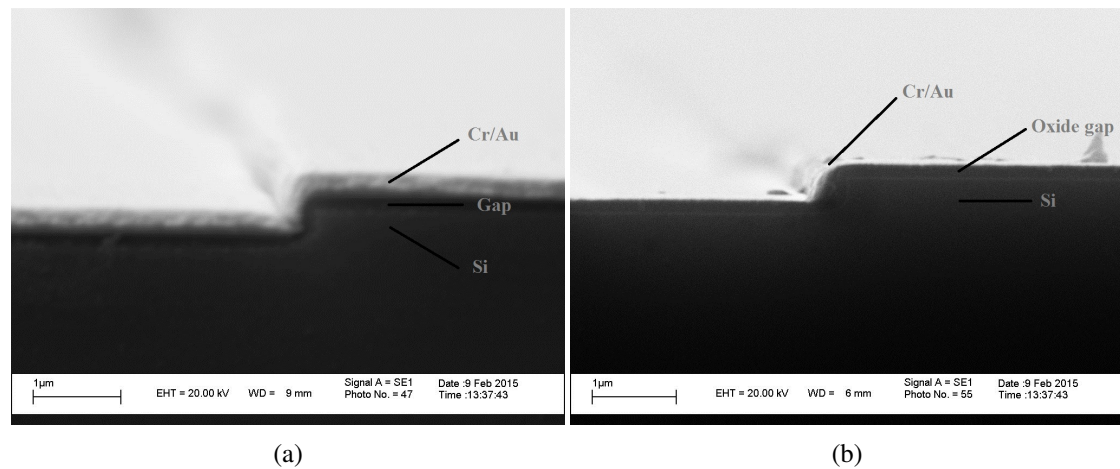


Figure 3.6: Cross-sectional SEM views to characterize sidewall mask formation obtained after (a) deposition of Cr/Au and (b) half selective sputter etching.

A final Cr wet etching step was used to remove any residual metal specks after sputter etching. The etchant is a mixture containing 22% ceric ammonium nitride, 9% acetic acid and 69% water. This etching step prevents Si grass being formed in the DRIE process used to form nanoscale features.

The second optical lithography was then used to pattern the microscale features including the anchors and the crossbeams. A thicker resist (Shipley S1813) was chosen this time, to maintain a good planarization of the existing mesa features. Figure 3.7 shows a 2μm crossbeam patterned over a set of parallel mesas; this feature will tie together the resulting nanoscale beam array. The thickness of the second resist is approx. 1.6μm, which is thick enough to cover the 0.6μm step of the initial mesa. With sufficient resist flow, a good planarization of the mesa array can be achieved. The combined features were then transferred into the Si substrate using the Bosch DRIE process, and then undercut.

As stated in Chapter 2, the standard Bosch process can be further developed to form HAR NEMS features. Although the process itself is quite well understood, special care is needed to prevent any possible lateral erosion of such narrow structures. Firstly, very short etching cycles must be used to minimize the depth of any scallops, preventing two scallops etched from opposite sides of the Si nanobeams meeting each other. Secondly, sufficient passivation must be deposited between etching cycles to maintain anisotropic etching. Here, 350W coil power and 11W platen power were chosen with a 4s during time for both the etching and passivation
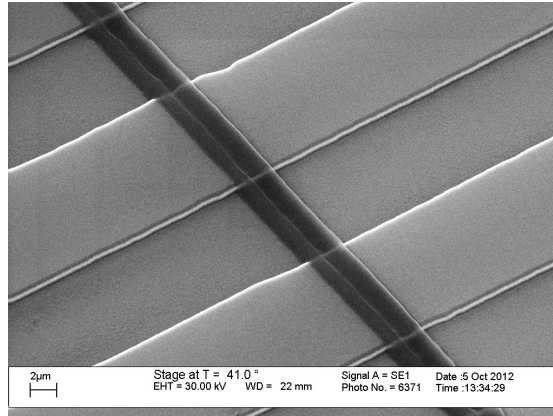
Figure 3.7: SEM views showing resist planarization on the pattern of a crossbeam after the second optical lithography.

cycles.

Figure 3.8a shows a SEM photograph obtained by cleaving across a nanobeam after DRIE. The cleaving results in the Si nanobeam and sidewall mask breaking at different positions. Here the nanobeam has a depth of approximately 3μm and width of < 100nm. The nanobeam is highly vertical and the adhesion of the sidewall mask is excellent. Large scallops inherited from the rear of the Si mesa can be seen in the sidewall mask in the enlarged view. Figure 3.8b shows a similar view of multiple nanobeams with 5μm suspension separation. The location of the original mesa can easily be identified from the position of the higher Si horizontal surface, and the step between the two Si surfaces is the same as the mesa height (0.6μm). The vertical Si sheets were etched further to 4μm enclosing both sides of the mesa. The vertical striations on the nano sheets are typical results obtained from the mid-UV contact optical lithography.



(a)                                                    (b)
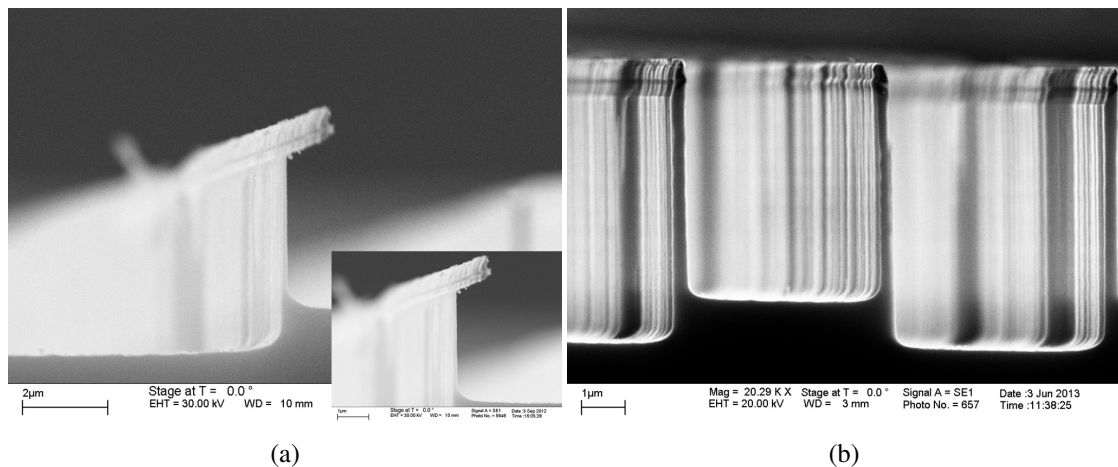
Figure 3.8: Cross-sectional SEM views of nanoscale silicon beams after DRIE.

Figure 3.9 shows an etched structure obtained after using two-step lithography to combine

microscale and nanoscale features. Multiple nanoscale Si beams with a microscale crossbeam tying them together at the centre are shown in Figure 3.9a. Enlarged views then show details of different positions of the structure: micro-to-nano joints on the crossbeam (Figure 3.9b) and buried ends of nanoscale beams near the anchor (Figure 3.9c) show solid connection of the structure. In Figure 3.9d, etched nanoscale beams show extremely high quality with a translucent view under SEM illumination. The height difference between the two horizontal Si surfaces can again be verified by the dark bottom observed from the outer side of the Si sheets. In all cases, resist in the second optical lithography remains on top of all the microscale features as evidence of the use of two different levels of lithography. Some minor misalignment resulting from the second lithography can also be seen.



(a)

(b)

(c)

(d)
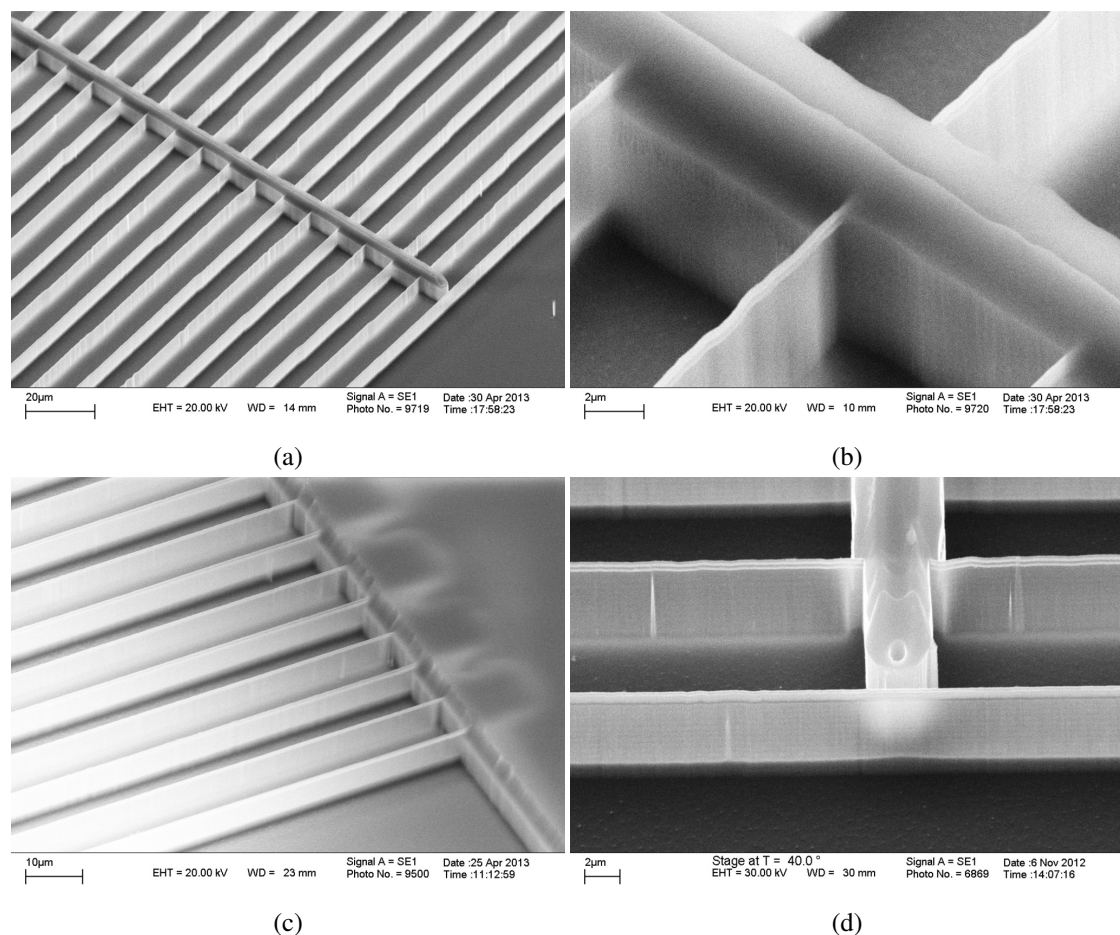
Figure 3.9: SEM views of etched HAR structures showing: (a) and (b) multiple nanoscale beams tied by a microscale crossbeam; (c) solid connection near the anchor; (d) combined micro- and nanoscale features with high quality.

The whole structure was then undercut in a continuous SF$_6$ plasma etching step to release the moveable parts. Nanoscale features were firstly released in a modified Bosch DRIE process with increased etching cycle time. The increased scallops now should meet beneath the nanobeams,

thus undercutting the nanoscale suspension. The modified process starts with a passivation cycle to deposit a passivation layer order to prevent lateral erosion of the suspension itself. To release the microscale crossbeams, a thin layer of $C_4F_8$ polymer was deposited, followed by a short, high-power $SF_6$ plasma to punch through the horizontal surface. This step effectively removes the deposited polymer on the Si substrate but keeps the polymer on the vertical feature as a passivation layer in the following step. A final isotropic $SF_6$ plasma etching step was then used to undercut the microscale crossbeams. The RF power in the final etching step was deliberately be kept low to avoid over-heating the nano suspensions.

Figure 3.10a shows partially undercut nanobeams. A clear gap at the bottom of the Si sheets shows where effective undercutting has occurred. Further undercutting will then gradually release the nanobeams as shown in Figure 3.10b. Figure 3.10c shows cleaved nanobeam before completing undercut. Here, part of the nano suspensions has been formed without any sign of erosion. Figure 3.10d shows fully released nano suspensions in a single-ended actuator. The nanoscale beams are thoroughly released from the Si substrate. This can be confirmed from the identifiable remnant of the original mesa feature underneath (a closed cross-sectional view can also be found in Figure 3.10c). This behaviour greatly assists assessment of the distortion of released structures, which otherwise can be difficult. A further isotropic etching step is then necessary to undercut the crossbeam. Details of a fully released device will be shown in the following section.

(a)                      (b)





(c)                      (d)
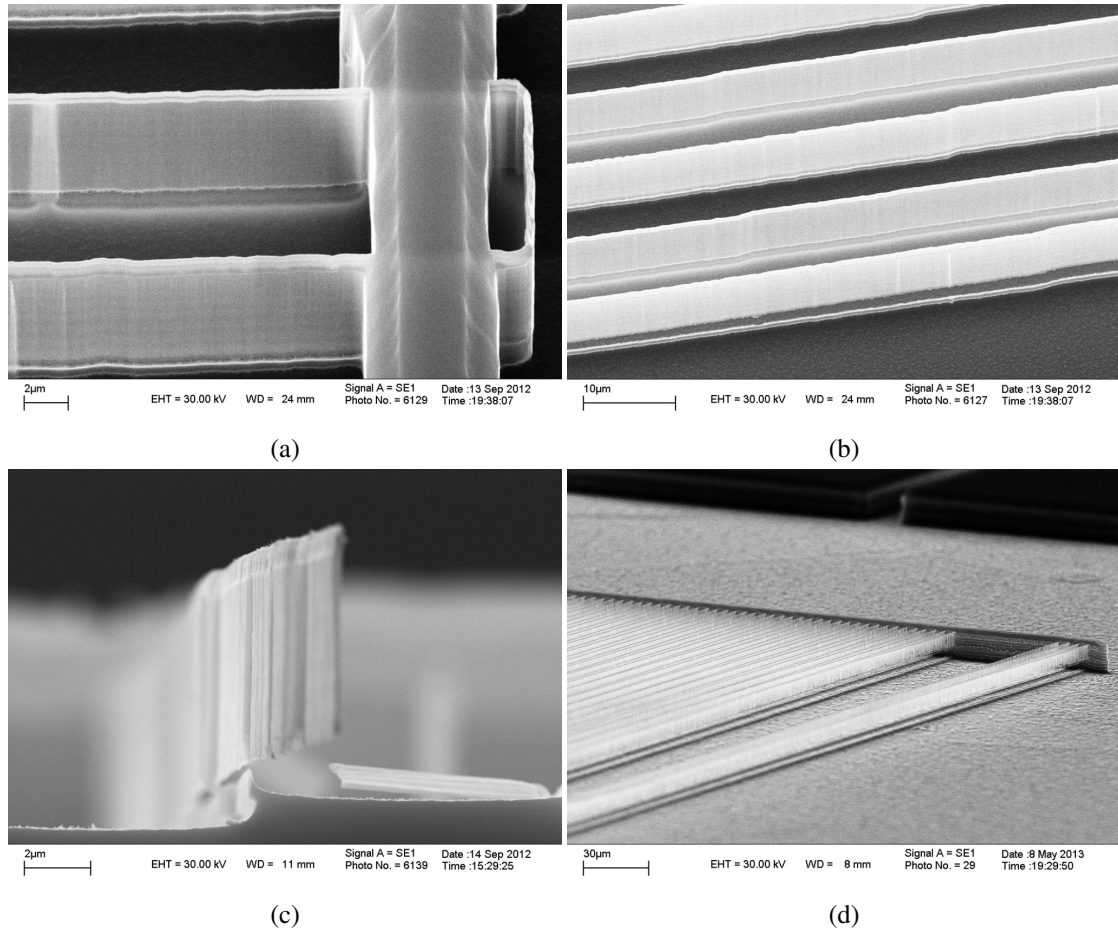
Figure 3.10: SEM views showing: (a) partially and (b) completely undercut nanobeams; (c) cross-sectional view before completing undercut; (d) released nanoscale beam arrays.

### 3.2.2 Prototype devices

Prototype devices based on bulk silicon wafers are described in this section. As shown in Figure 3.11 all devices here are thoroughly released for approx. $4\mu m$ by $SF_6$ plasma undercut. Figure 3.11a and 3.11b show the released central crossbeam on a double-ended actuator. In each case, an etched remnant can be seen in the silicon substrate beneath both the micro- and nanoscale features after release. Similarly, released single-ended NEMS actuators are shown in Figure 3.11c and 3.11d. At the end of the single-ended crossbeams, continuous 3D Si sidewalls can be seen as a supplementary feature. All features show robust connections between microscale and nano-scale features, with little sign of residual stress and erosion.
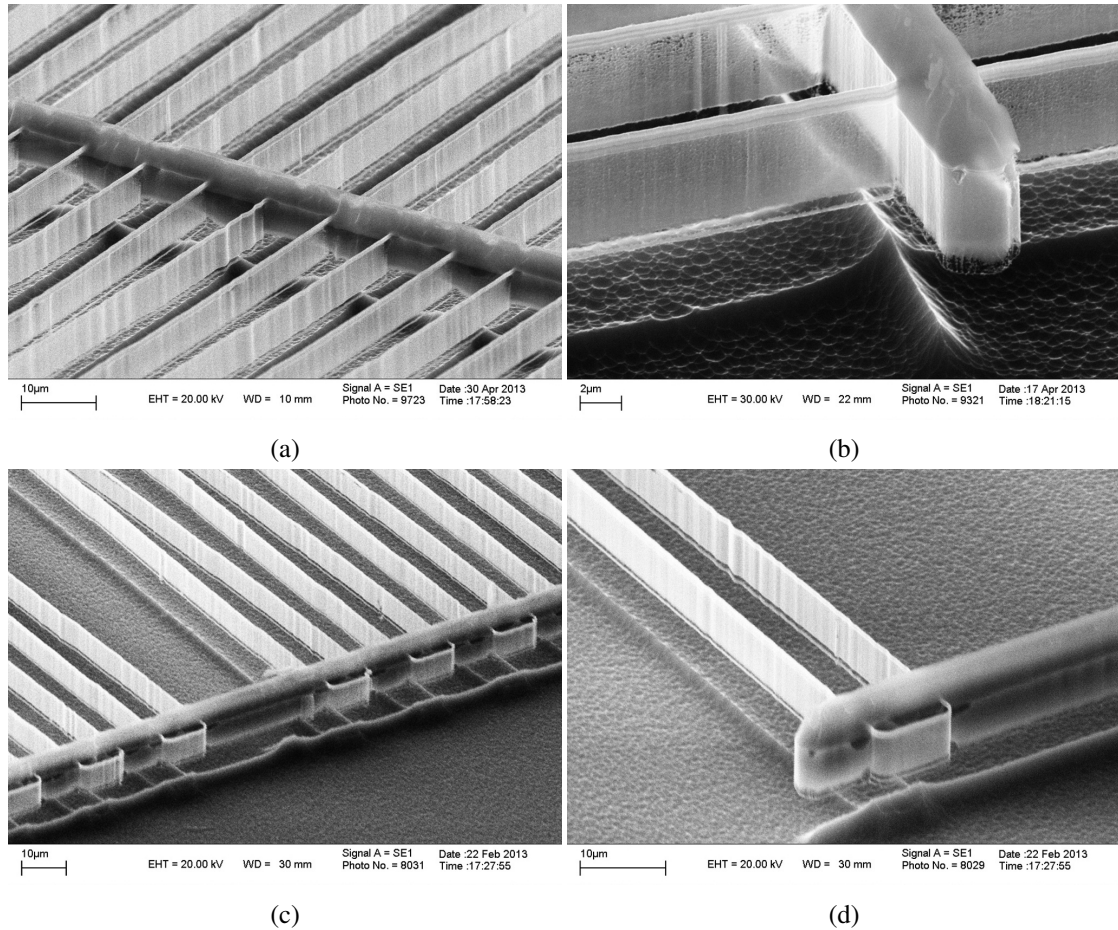
Figure 3.11: SEM views of completely released double-ended ((a) and (b)) and single-ended ((c) and (d)) actuators by plasma undercut.

The prototype devices here prove the viability of the STL NEMS process, and have demonstrated a satisfactory yield over 70%. Verification of mechanical movement can now be investigated. However, in order to analyse the mechanical performance of any electrothermal actuator, it is necessary to drive the device electrically. Using bare Si, however, there will be a considerable current leakage through the silicon substrate. Hence, it is necessary to extend the STL process to BSOI wafers (which contain an oxide interlayer than can be used as an insulator) as described in the next section.

## 3.3 NEMS actuators on BSOI wafers

The process details and fabrication results of the single-layer STL process based on BSOI wafers will be described in this section. In addition to electrical insulation, BSOI wafers allow a much more control of the depth of any mechanical parts, and consequently much better control of mechanical performance. Here, prototype devices were fabricated in 100mm diameter BSOI

wafers, obtained commercially from Icemos Technology, Belfast, with a 2µm thick buried oxide layer and a 5µm thick device layer.

### 3.3.1 Fabrication steps

A modified STL process was developed to fabricate NEMS on BSOI wafers as shown in Figure 3.12 [125]. As before, a first conventional lithography step is used to pattern the initial mesas, which are then etched by DRIE (steps 1, 2). The resist is then stripped (step 3). A conformal metal coating is then deposited, and horizontal surfaces of this metal are removed by directional etching (steps 4, 5). The result is a surface mask defining the nanoscale features. The second conventional lithography step is then carried out to add microscale parts (step 6). The process steps, so far, are the same as that used for a bulk silicon device. However, to transfer the combined pattern into the substrate, the final DRIE step must be extended to reach the buried oxide layer everywhere (step 7). After stripping the resist (step 8), suspended parts are now freed by etching of sacrificial oxide in HF vapour (step 9) and metal is deposited over the entire structure to provide electrical contact (step 10). Alternatively, the final metal layer may be localized to the anchors by depositing and patterning the metal after step 5, before the final etching.
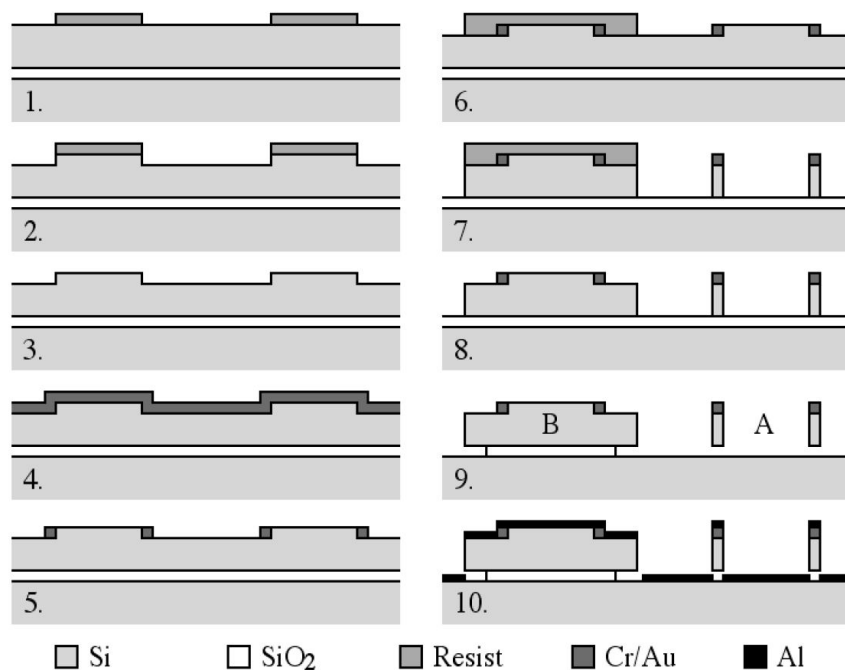


Figure 3.12: Schematic diagram of BSOI STL process developed for NEMS.

The mask set as previously described for the bulk device (Figure 3.1) was used. Similar

results were obtained for the early fabrication steps until final etching down to the buried oxide layer. To transfer the combined pattern into the Si substrate, the same fine etching Bosch DRIE process was also used. However, as shown Figure 3-12, the initial mesa pattern led to terracing of the wafer surface, so that the final etching would reach the buried oxide layer in some regions before others. Hence over-etching had to be carried to ensure all features etched down to the oxide. A dry process was used afterwards to strip the resist off with $O_2$ plasma asher.

Figure 3.13a shows a SEM image of a combined feature immediately after the final DRIE (step 7). The resist from the second optical lithography can be seen remaining on top of the central crossbeam; clearly, this resist has planarized the metal sidewall mask well. After stripping the resist (step 8), the top of the crossbeams shows a stepped nature inherited from the initial mesa pattern (Figure 3.13b). The metal sidewall mask can also be found continuously extending to the Si nano sheets. In both figures, it is very clear that etching has been sufficient, and has been correctly stopped by the buried oxide layer since now there is no height difference between the two horizontal surfaces of the mesa and the slot.



(a)                                        (b)
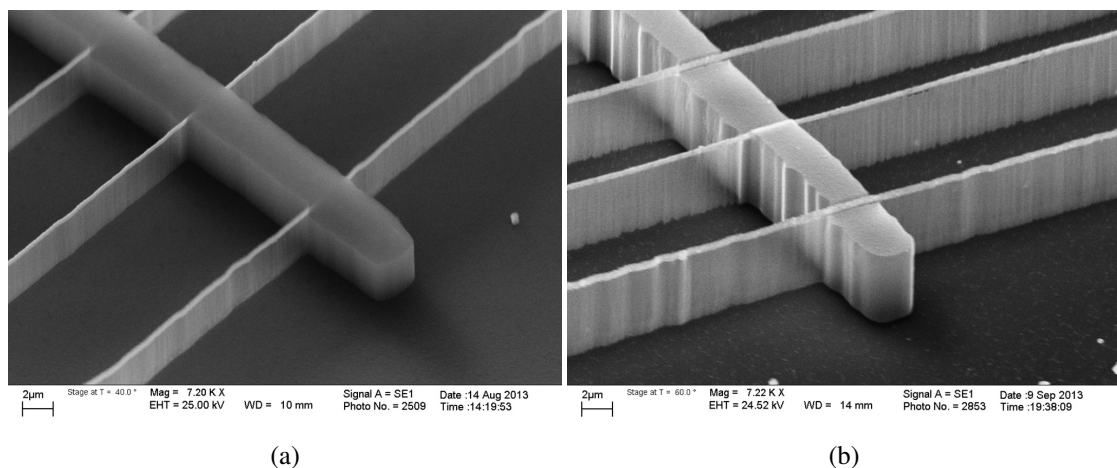
Figure 3.13: SEM views of etched double-ended actuators (a) before and (b) after removing the resist.

Figure 3.14a shows a cross-sectional view of the nanoscale beam obtained by cleaving across a fully etched but unreleased device. Once again, it is clear that the silicon etching has bottomed on the oxide layer since the surfaces on either side of the beam are at the same level. The etching follows the gap width at the bottom defined by the original mesa pattern in the first conventional lithography. This beam has 100nm width and 4.5μm depth, and shows that a very high aspect ratio ($> 45 : 1$) can be obtained, with only minor variations in the vertical direction. An enlarged view of the top of the beam in Figure 3.14b shows the bilayer (Cr/Au) sidewall mask is still in

place.

Adhesion of the sidewall mask is quite good, thus it requires some extra effort to detach it. More detailed information is shown in Figure 3.14c and 3.14d in a closed view. Here, parts the Si nanoscale beams has been broken and become detached from the metal masks by the cleaving. The sidewall masks keep continuous with the two layers peeled apart. These two figures shows two beams on each side of a mesa (c) left and d) right) so that the bilayer structure are symmetrical as two sidewall features. Scalloped shape of the rear of the original mesas also reflects on a similar profile of the mask inter layer.



(a)

(b)

(c)

(d)
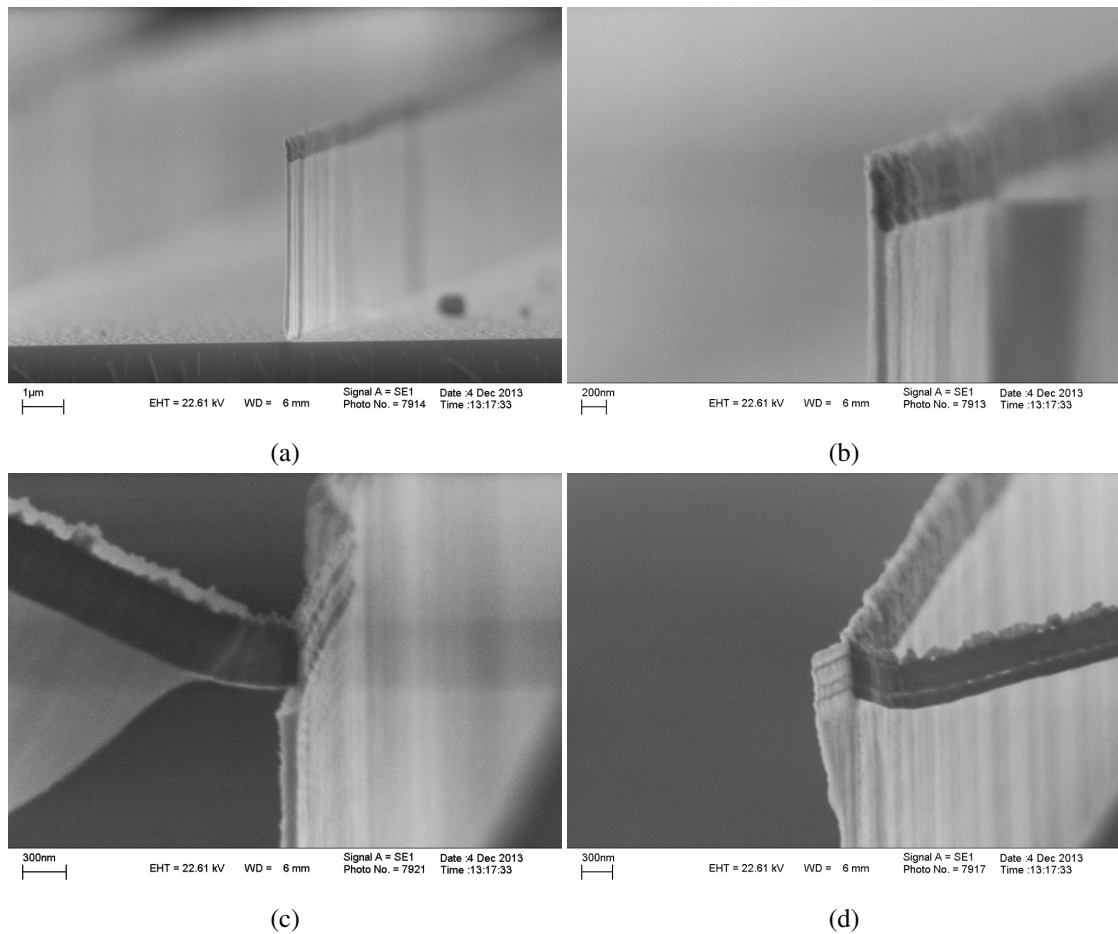
Figure 3.14: Cross-sectional SEM views of etched nanoscale beams highlighting the sidewall masks.

Devices were then released in an Idonus HF VPE (vapour phase etch) system to remove the buried oxide layer. The process was chosen as a dry process thus to avoid any structure collapse due to surface tension in drying step. 40% HF was chosen to achieve a rapid undercutting. However, the rate of undercutting really depended on various experimental factors, such as the substrate temperature, etching area, window size, etc. A typical rate measured in experiment for

a single-ended actuator is approx. $10 - 15nm/min$.

Figure 3.15 shows a partially released single-ended actuator. As can be seen, nanoscale suspensions are fully undercut, and show little sign of stress-induced distortion. Any small redundant features due to artefacts in processing will also be removed in this step. The process has been found to be much less aggressive than the plasma undercut used for bulk silicon devices. The whole device will then be freed by further etching of the residual oxide beneath the crossbeams,as described in the next section.
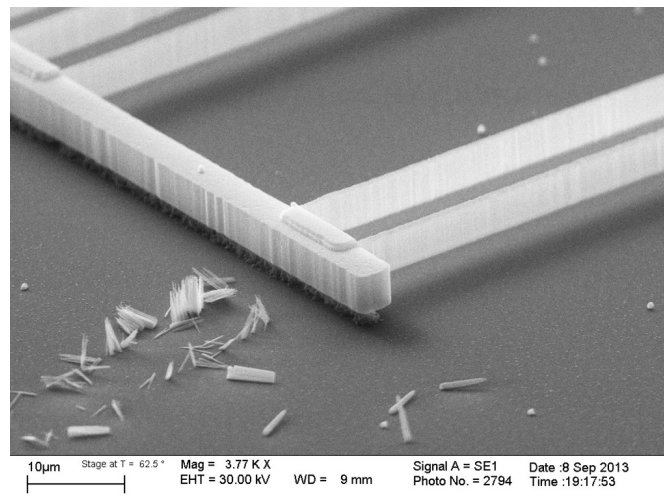


Figure 3.15: SEM views of a partially released BSOI single-ended actuator.

### 3.3.2 Prototype devices

In this section, completed BSOI device structures are demonstrated with SEM photographs. Figure 3.16shows double-ended (a) and single-ended (b) electrothermal actuators. There are 58 unbroken nanoscale beams in each with a beams separation of $10\mu m$. In both devices, the beam arrays are uniform and parallel with little sign of stress buckling. Due to the accurate control of device layer thickness and the low temperature release step, fabrication results show that BSOI provides a more reliable wafer-scale process, with a higher yield.

Details of fully released devices are shown in Figure 3.17. Figure 3.17a shows a close-up of the central crossbeam of the double-ended actuator. The microscale crossbeam has now been fully released from the Si substrate, together with the nanoscale suspensions. Etching quality for both structures are extremely high without any lateral erosion, especially on the nanobeams. The suspended beams have highly vertical walls, with little sign of twisting or lateral deflection caused by residual stress possibly contained in the Cr/Au sidewall masks.

Although devices with suspensions built in at both ends might be expected to show limited
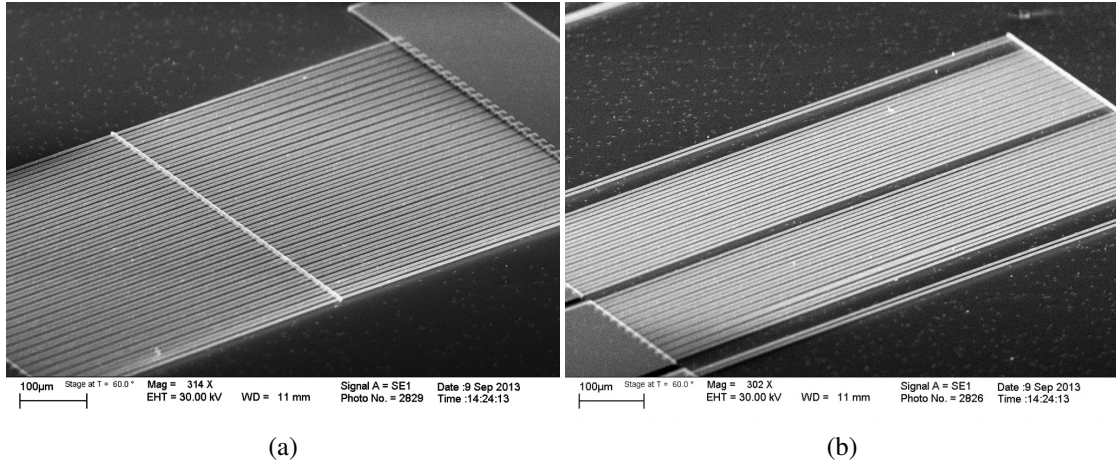
Figure 3.16: Full SEM views of completed BSOI devices: (a) double-ended and (b) single-ended actuators.

stress distortion, similar good results are obtained on the released single-ended device as shown in Figure 3.17b. With the length of the nanobeams doubled, the structures at the free end still show similar high quality as above.

Details of the anchors are shown in Figure 3.17c followed by a close-up view in Figure 3.17d. The micro-to-nano joints between the Si microscale anchors and nanoscale suspensions are solid and robust. The metal masks continuously follow the initial mesa patterns, which can be tracked from the overlaid ends at the anchor rear. The anchors are clearly undercut in the HF vapour, thus eliminating a tracking path to the Si substrate for metallization as shown in Figure 3.12 step 10. This will help to avoid short circuit in device electrical characterization. All devices presented here are entirely released from the handle layer without noticeable deformation.

To drive the device electrically, a 300nm thick aluminium layer was deposited afterwards on the entire surface to provide an electrical contact. As shown in Figure 3.18, the trace of the Al layer below the nanoscale beams also confirms complete release of the suspended structure.
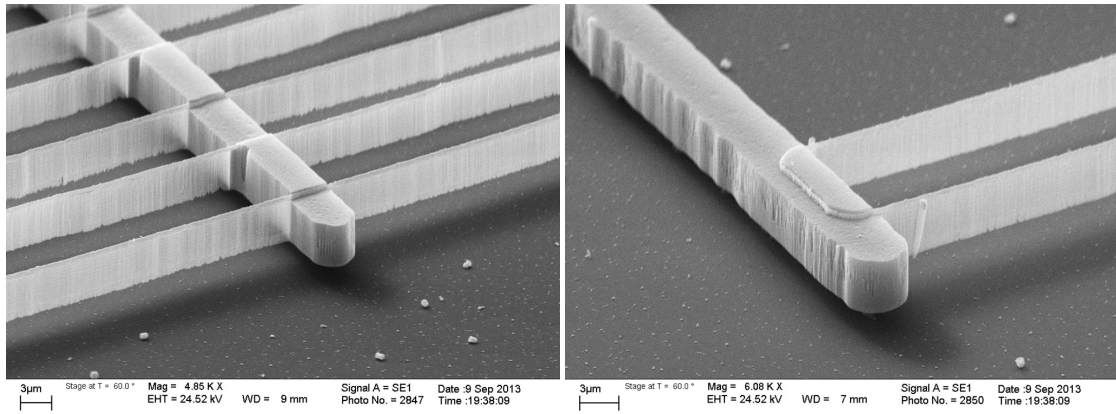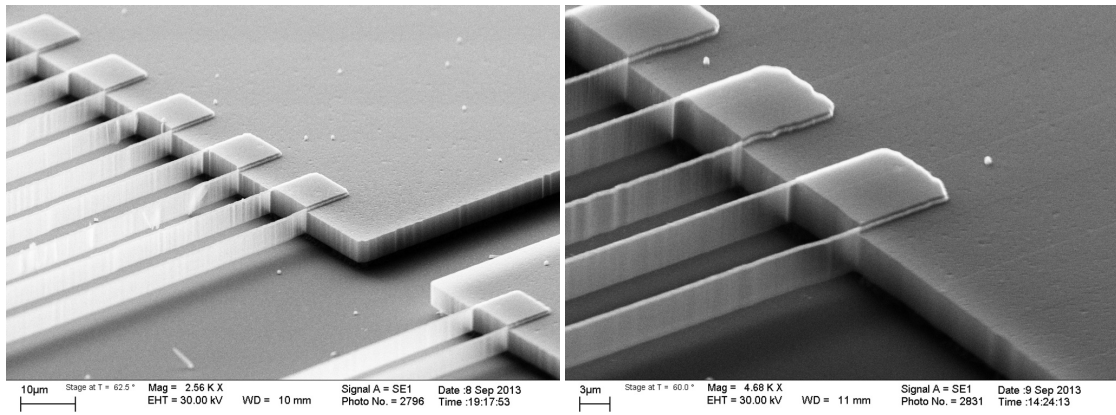
Figure 3.17: SEM views of completely released BSOI devices showing details of: crossbeam for (a) double-ended and (b) single-ended actuators; (c) and (d) features near anchors.
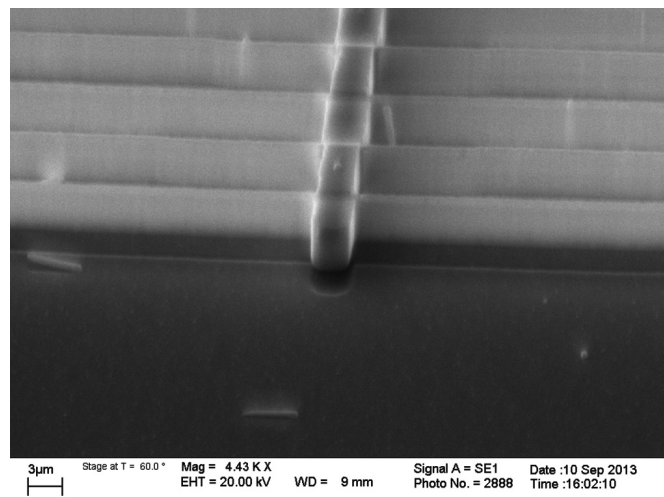


Figure 3.18: SEM views of a double-ended actuator after metallization.

## 3.4 Processing Issues

In this section, processing issues encountered in the fabrication of the prototype devices will be discussed. Following appropriate failure analysis, many of the problems have been overcome by adjusting the relevant parameters of single fabrication steps. Other difficulties can be eliminated by adopting alternative processing methods, such as changing the sidewall material and adding extra conventional lithography steps. However, analysing these problems offers a deep understanding of the STL process and reveals potential problems in future NEMS applications.

### 3.4.1 Lithography planarization

The second conventional lithography step does suffer from minor difficulties of resist planarization. During spin coat, care is needed to ensure sufficient coverage of all the original mesas; failure to do so results in the creation of voids during the long DRIE step. For example, Figure 3.19a shows an SEM view of the central crossbeam of a double-ended actuator after developing the second resist layer. Here, a thin resist (Shipley 1805) was being evaluated, in an attempt to achieve higher resolution. Although the resist has filled in the slots between the etched silicon mesas, it has a poor coverage over the mesas themselves. These would result in a deep slot on the crossbeam, which is supposed to provide a rigid link between the nanoscale beams.

Figure 3.19b shows another typical failure of planarization. Here a thicker resist (Shipley S1813) is used to obtain sufficient coverage. However, the stepped nature of the patterned mesas causes different thickness of the resist on different surfaces, leading to different sizes. A dentate shaped crossbeam can then be predicted after the final deep etching, and the exposure and development of the second resist layer must be carried out with special care to minimize such differences.

(a) (b)
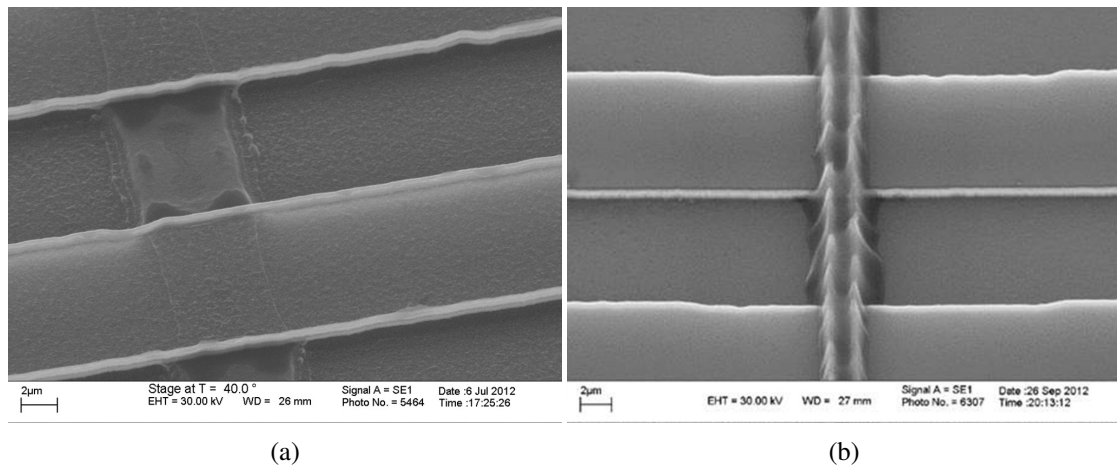
Figure 3.19: SEM views obtained after the second photolithography showing failure of (a) planarization and (b) pattern transfer.

Effective planarization is therefore required, and a thick resist must be used to ensure full coverage of the stepped surface. Care is then needed to ensure complete exposure and appropriate development; failure to do so results in notched beam shape and creation of additional artefacts. These difficulties may be minimized by reducing the mesa height as far as possible.

### 3.4.2 Sidewall mask in deep etching

The quality of the sidewall masks is one of the key elements of the STL process. To begin with, the adhesion between the sidewall mask and the Si mesa must be good enough to survive the final DRIE step. Figure 3.20a shows a typical example of mask detachment occurring during etching. Here, a single-layer Au sidewall has been used as the hard mask for etching nanoscale features. However, this has detached from the original mesa in the plasma DRIE due to the lack of a suitable adhesion layer. Hence, the use of an additional Cr layer is essential, despite the fact that a bilayer Cr/Au sidewall mask is likely to suffer from increased residual stress, as will shortly be described.

Figure 3.20b shows an obvious distortion of the sidewall masks after DRIE with high plasma power. Here, a bilayer Cr/Au layer has been used as the sidewall mask, but has been severely damaged by the high power $SF_6$ plasma etching and melted into localized metal balls. An appropriate low etching power is therefore needed to prevent sidewall mask deformation and to maintain it vertical through the complete etching process.

The initial mesa shape is another key to obtaining high quality sidewall masks. Since its shape will be inherited by the sidewall mask, the mesa edge must be vertical. For example, Figure

3.20c shows a trapezoidal mesa cross-section with the metal sidewalls leaning inward from both sides. The trapezoidal mesa shape results from the isotropic etching in the first conventional lithography. The sidewall shape has been caused by etching occurring simultaneously on two different Si surfaces, combined with an undercut near the bottom of the sidewall masks. Figure 3.20d shows a similar view of the metal masks peeling off from the mesa as etching proceeds, well before any HAR nano-structure can be formed.



(a)                                                          (b)

(c)                                                          (d)
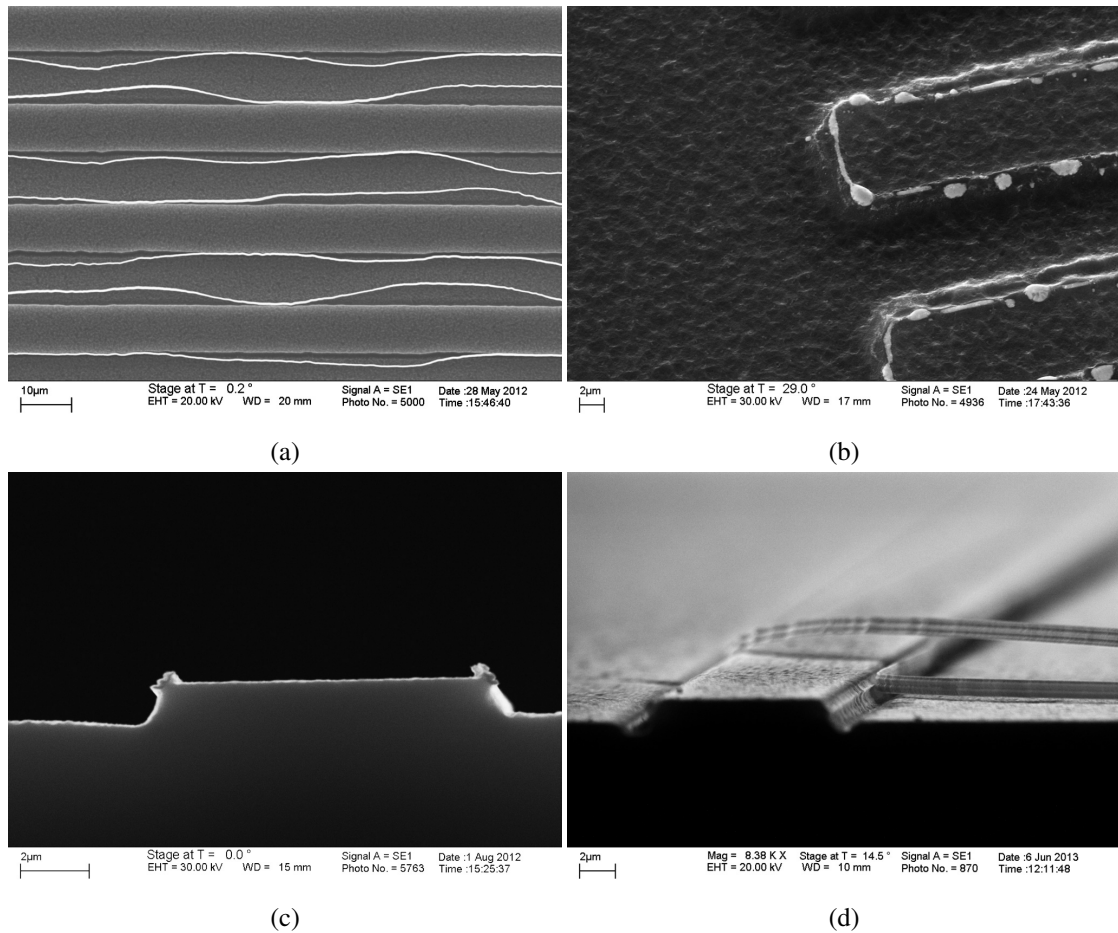
Figure 3.20: SEM views showing: metal masks (a) detachment, (b) distortion and (d) peeling off during DRIE; (c) cross-sectional view of metal masks on a trapezoidal mesa.

### 3.4.3 Erosion

The main difficulty in deep etching and plasma undercut is to control scalloping and passivation. Based on the aspects mentioned in Chapter 2, the erosion effect in device fabrication can now be fully understood. For example, Figure 3.21 shows two typical erosion effects occurring at the micro-to-nano joints near the anchor (a) and crossbeam (b). In both cases, the combined structure has been suspended far (almost 5μm) above the Si substrate by plasma undercut. It is noticeable that most parts of the nanobeams are intact, except the joints. A possible explanation

is that after the nano suspensions formed, cooling through conductive heat transfer becomes available only from the anchors and the large crossbeams, which still sit on the substrate. Localised temperature rises might then increase the etching rate; additionally, the the plasma might be concentrated at concave corners in the structure.
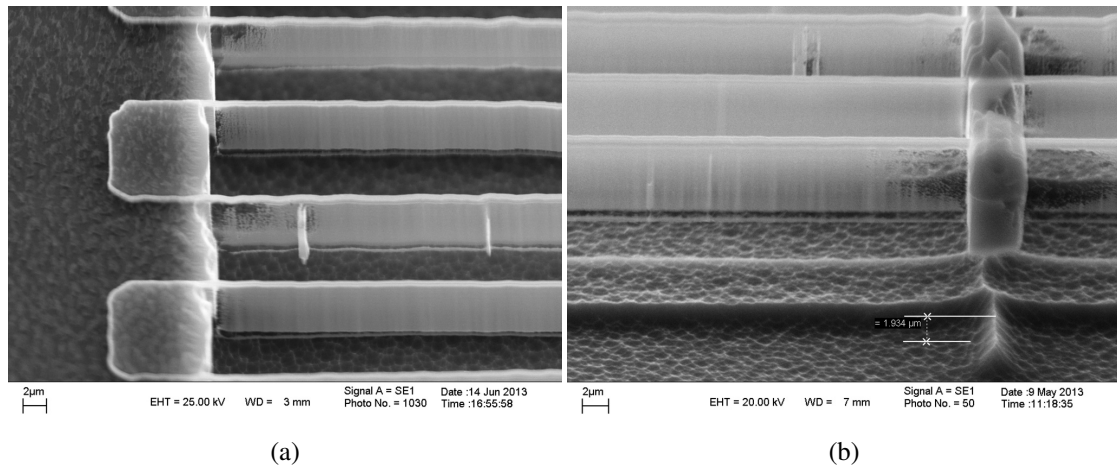


Figure 3.21: SEM views of double-ended actuators with erosion occurring near the (a) anchor and (b) crossbeam.

Most of the erosion effects stem from oversized scallops in nanoscale deep etching. For example, Figure 3.22a shows erosion occurring at the joints to the central crossbeam of a double-ended actuator. Once again, it is at the corners that the erosion is concentrated. However, the damaged parts here appear to be completely different from those in Figure 3.21, presenting a scalloped outlook arising from the cyclic nature of the DRIE process. This is because the DRIE process used to undercut the nanobeams is designed to etch with much larger scallops, and the concentrated plasma again causes unexpected erosion on the joints.

Similarly, Figure 3.22b shown a nanobeam eroded by large scallops from both sides, so that the damage meets in the middle. Here the bilayer Cr/Au sidewall mask at the top of the structure is intact, but large scallops and severe erosion can be observed underneath. The erosion has also led to a poor support for the structures above, with a potential for further collapse in subsequent deep etching.

In addition to the joints, erosion can also occur along the nanobeams due to the lack of passivation. As shown in Figure 3.22c, over-etch clearly starts right under the metal sidewall masks, and once any notches have been formed, the remainder of the Si nanobeam will then be eroded very quickly. An isotropic etching step in $SF_6$ plasma was therefore developed to undercut all the silicon features beneath deliberately and leave only the mask metal as a free

standing structure, as shown in Figure 3.22d. Using this method, suspended Cr/Au beams can now be realised as nano-structures. These can be used to carry out further analysis of the stress contained in the metal sidewall masks, as detailed in the next section.



(a)

(b)

(c)

(d)
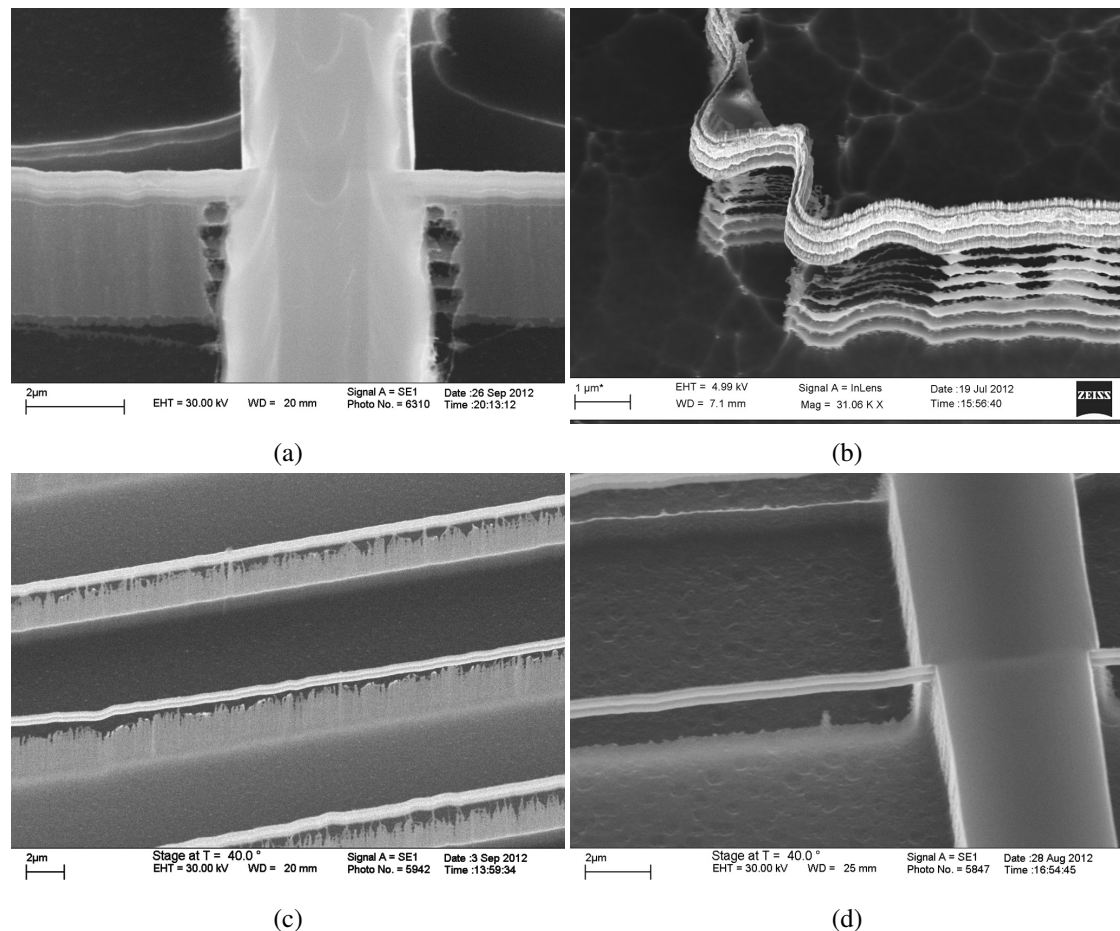
Figure 3.22: SEM views of different erosion occurring along the nanobeams.

To conclude, erosion can be fatal in the formation of NEMS structures since there is little margin for lateral error. However, based on a good knowledge of the Bosch process, most of the erosion can be overcome by either reducing the scallop size or depositing sufficient passivation material between two etch cycles. Scalloping may make it difficult to preserve nanoscale feature width in structures narrower than 100nm. However, modern cyclic DRIE equipment allows extremely rapid gas switching to minimize scallop formation. Consequently it is likely that the 45 : 1 aspect ratio achieved here can be exceeded.

### 3.4.4 Stress

The main difficulty with the STL NEMS process is to avoid intrinsic stress in the sidewall masks. The cause of the effect is most likely the stress formed during the deposition of the two

sputtered metal layers, due to the large difference between the thermal expansion coefficients of the two materials (Cr $6.2 \times 10^{-6} K^{-1}$ and Au $14 \times 10^{-6} K^{-1}$). Various types of distortion have been observed experimentally in fabrication.

For example, Figures 3.23a and 3.23b show double- and single-ended actuators deformed by residual stress in the sidewall mask. Obviously, the device with built-in beams at both ends shows less stress distortion, especially with the use of a central crossbeam to tie all the beams in the array together. Without this constraint, and with a longer beam length, a much more significant out-of-plane curvature can also be observed in the single-ended device. In this case, the residual stress in the sidewall mask has clearly overcome the suspension after HF vapour release.

Figure 3.23c shows the SEM photograph of buckled and broken sidewall masks on a bulk silicon device. The metal sidewalls are now clearly detached from the silicon sheets underneath by the stress. The stress is clearly large, as the force is sufficient to fracture the nano sheets as well. Freed mask metal and adherent silicon sheets also show sign of twisting, which might suggest the presence of residual stress in both horizontal and vertical parts of the metal mask layers.

To investigate this effect, a set of free-ended nanoscale suspensions was formed by cleaving, to assess the lateral deflection of the beams. The separation between each beam was 10μm, while their length was reduced to 50μm to prevent excessive deflection. As shown in Figure 3.23d, the nanoscale Si suspensions have clearly bent towards the side with the Au layer for each pair undercut from the same mesa. This directionality can be confirmed by locating the higher Si surface in the vicinity of each original mesa.

The existence and nature of such stress can then be revealed using alternative processing that effectively forms gauges for the sidewall stress, as we now show. For example, Figure 3.24 shows the sidewall mask for double- ((a) and b)) and single-ended ((c) and (d)) actuators, which has been deliberately undercut by isotropic etching in $SF_6$ plasma to remove the silicon and leave only the sidewall masks in place. In this way, the stiffness of the nanoscale suspensions is significantly reduced for both in-plane and out-of-plane motion, allowing the deformation to be magnified. In Figure 3.24a, suspended metal beams from either side of the same mesa have clearly bunched together, bending towards the outer Au layer in agreement with previous results. This result indicates differential stress between the Cr and Au layer in vertical parts of the bilayer metal sidewalls. Figure 3.24b shows a close-up of the structures near the anchor.

| | |
|---|---|
| (a) | (b) |
| (c) | (d) |
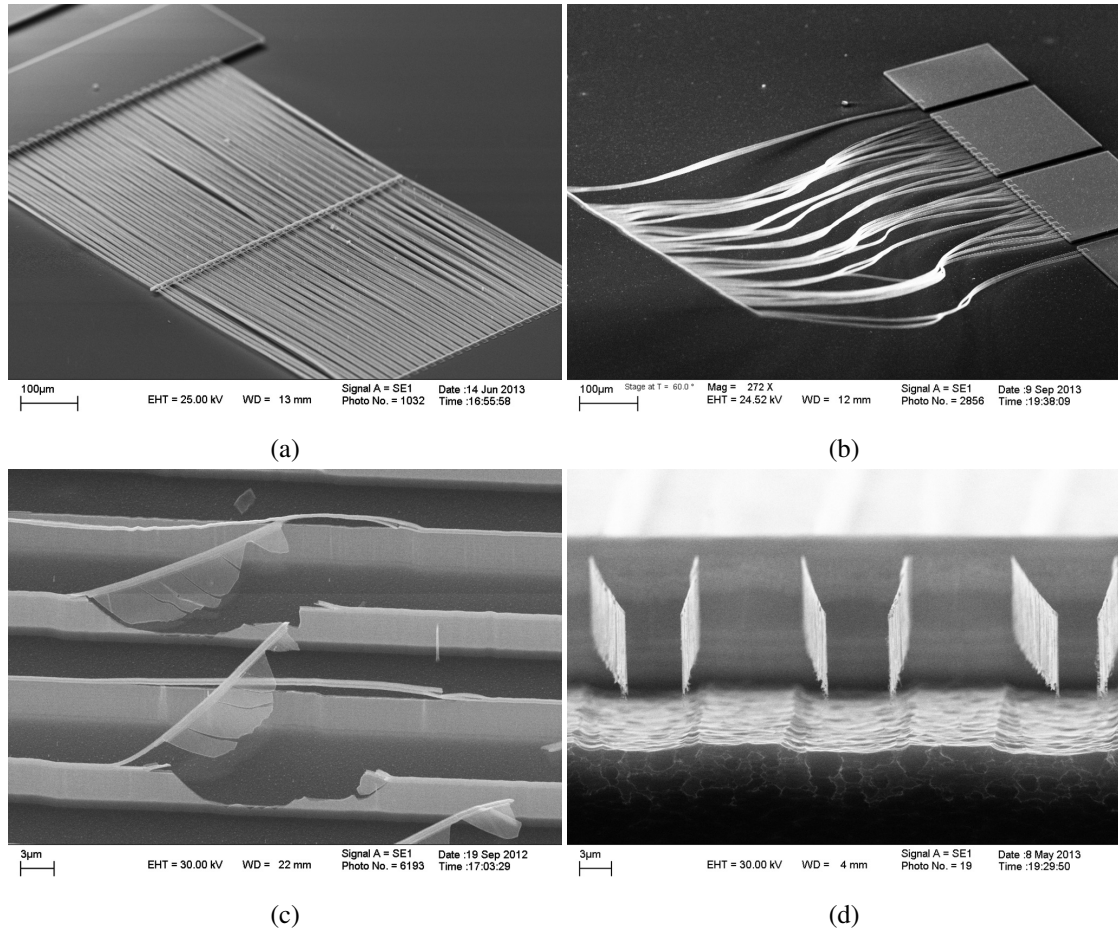
Figure 3.23: SEM views showing: deformed (a) double-ended and (b) single-ended actuators; (c) buckled and broken sidewall masks; (d) deformed free-ended nanoscale suspensions.

The original 10μm separation is retained only at the anchors, and the stress is large enough to force the beams together in pairs away from these points.

Figure 3.24c and 3.24d show single-ended metal sidewall suspensions that have been released using a similar isotropic etching process, but with lower power. Although the beam length is almost double that of the double-ended one, much less deformation is found, with only a minor out-of-plane deflection at the far free ends. Despite the presence of some minor silicon grass, the conclusion is clear: etching with higher power plasma may increase the stress in the metal sidewalls.

The out-of-plane deflection of the single-ended actuators are demonstrated in Figure 3.25. Figure 3.25a shows the SEM photograph of a BSOI device obtained after HF vapour releasing. Due to the silicon suspensions under the metal masks, a comparably small out-of-plane deflection ($< 30°$) is found on the free end. This result is then used to compare with the freed bilayer sidewall masks only in Figure 3.25b: the metal masks have curled out-of-plane by more than
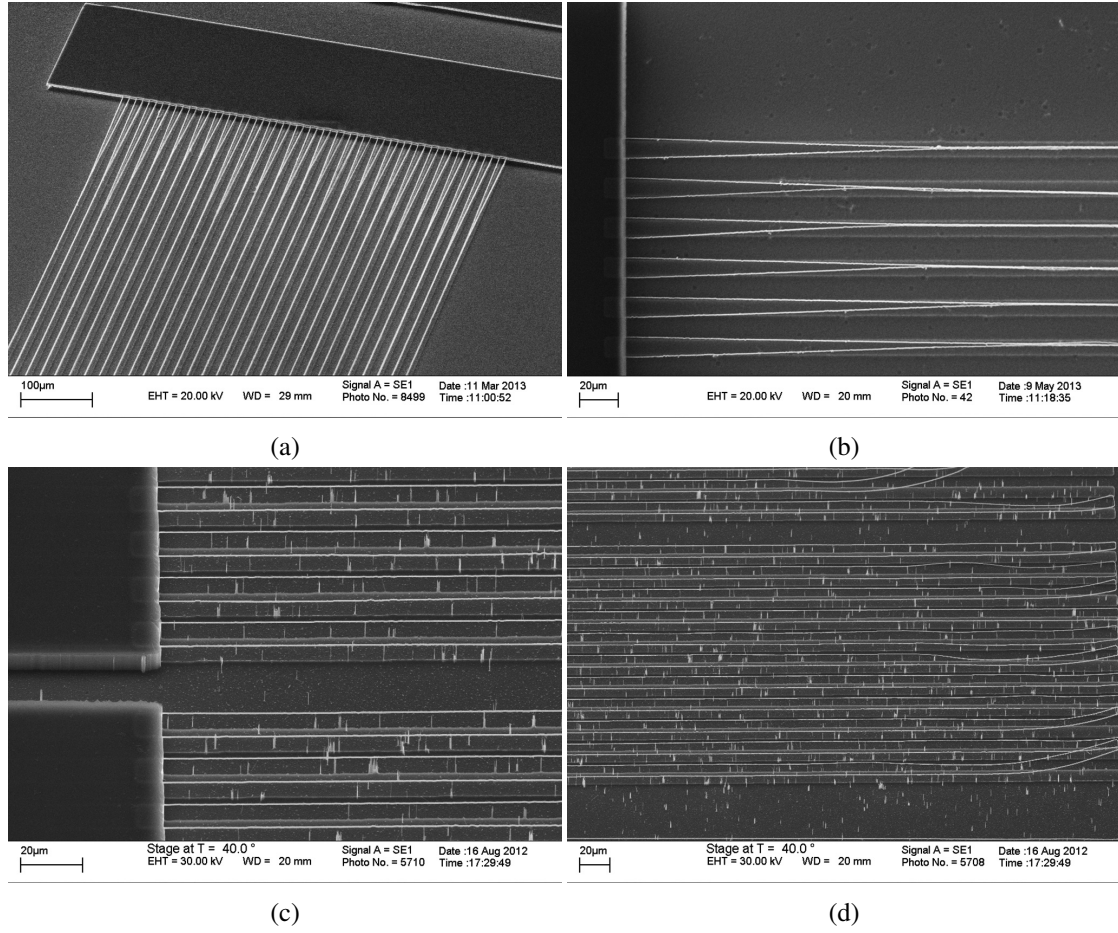
Figure 3.24: SEM views of suspended metal sidewall masks for double-ended ((a) and (b)) and single-ended ((c) and (d)) actuators showing residual stress.

180°, confirming the existence of differential stress between horizontal mesa layers. This effect is attributed to a vestigial layer of Cr beneath the foot of the sidewall masks.

The stress contained in the Cr/Au sidewall masks can now be estimated by using Stoney's film-substrate system model published in 1909 [126–128]. The film stress ($\sigma_f$) in a bimorph system (film on substrate) can be estimated using the following equation:

$$\sigma_f = \frac{1}{6Rt_f} \left[ \left( \frac{E_f}{1-v_f} \right) \frac{t_f^3}{t_f+t_s} + \left( \frac{E_s}{1-v_s} \right) \frac{t_s^3}{t_f+t_s} \right] \tag{3.1}$$

where $R$ is the radius of the curvature, $E_f$ and $E_s$ are the Young's modulus, $v_f$ and $v_s$ are the Poisson's ratio and $t_f$ and $t_s$ are the layer thickness of the films and substrate, respectively. When the film is much thinner than the substrate, the first term in the brackets can then be neglected. Thus, the film stress can be calculated as:

$$\sigma_f = \frac{1}{6R} \left[ \frac{E_s t_s^2}{(1-v_s)t_f} \right] \tag{3.2}$$

84

In the case shown in Figure 3.25b, as all the silicon has been removed deliberately, the bi-layer sidewall masks hence consist of a layer of Cr ($t_f = 10$nm) and a layer of Au ($t_s = 500$nm). The radius of curvature $R$ is measured as 475.1μm. And the following substrate material constants were assumed: Young's modulus $E_s = 79 \times 10^9 \text{N/m}^2$ and Poisson's ratio $v_s = 0.4$. The estimated stress $\sigma_f$ is hence $1.15 \times 10^9 \text{N/m}^2$.

The third example of stress effects is shown in Figure 3.25c: here, the Si nano sheets have again been undercut, but this time leaving the microscale crossbeam remaining at the free end. This now results in a larger out-of-plane curvature, since the free end now is much heavier than that shown in Figure 3.25b. A close-up of the crossbeam is shown in Figure 3.25d. Clearly, all the Si nanobeams have been etched to leave only the metal mask and the supporting crossbeam. The underside of the crossbeam shows new microscale features formed by undercut in $SF_6$ plasma.



(a)

(b)

(c)

(d)
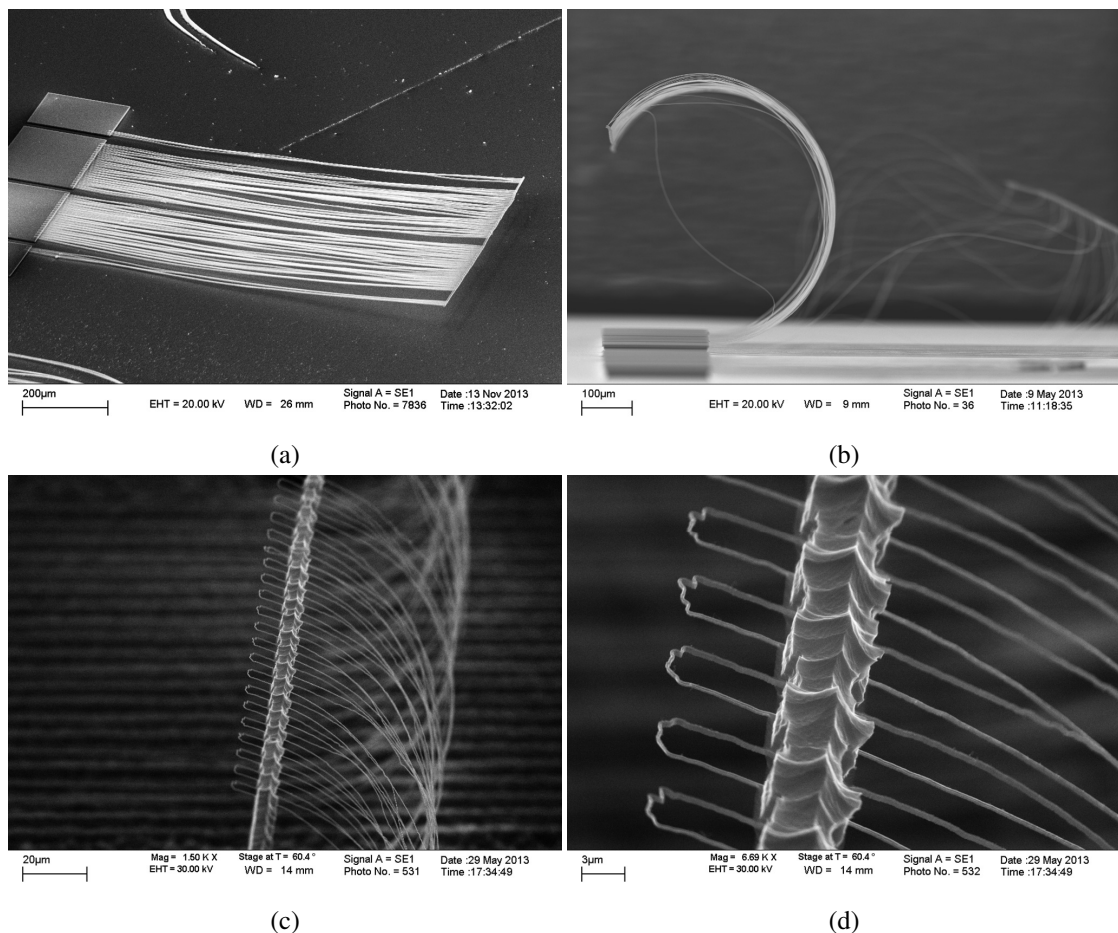
Figure 3.25: SEM views showing the out-of-plane deflection of single-ended actuators.

In most cases, in-plane and out-of-plane deflections are observed at the same time as shown in Figure 3.23b. Of course, both effects could be eliminated with an obvious solution: remove the

mask before sacrificial undercut using wet chemical etching. However, this can cause a variant of surface tension collapse in which the fragile suspension is twisted down onto the substrate during the drying step as shown in Figure 3.26. The approach used here - to leave the mask in place over a deep silicon structure - does allow fabrication of operating devices. However, a better solution would be to use a single layer $SO_2$ mask, since this can be removed together with the oxide interlayer during HF vapour undercut.
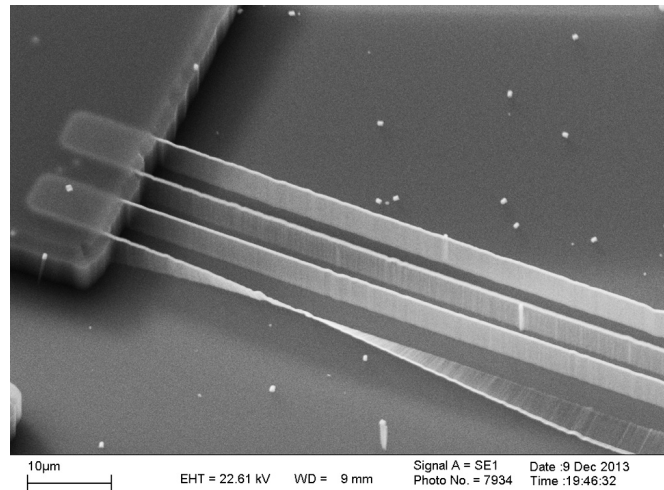


Figure 3.26: SEM views of nanoscale beams showing surface tension collapse.

### 3.4.5 Grass

Silicon grass is a common phenomenon in MEMS fabrication. In the STL process, there are two main reasons for grass formation after the final deep etching. One is the residual specks of metal on the silicon substrate remaining from previous processes, which in most cases have been proven to be residual Cr. These specks might be caused by re-deposition during the selective sputter etching in Ar plasma. However, lengthy wet Cr etching afterwards can remove these specks successfully.

The other cause is excessive passivation deposited in the final deep etching step. If the passivation layer on the horizontal surface is not consumed in the next etching cycle, residual specks of polymer will act as micromasks, causing silicon grass all over the wafer. For our NEMS process, this is more severe than usual. Since the Bosch DRIE process has been deliberately modified to protect nanoscale structures from lateral erosion, any similar-sized artefacts and grass will also be protected. As shown in Figure 3.27a, silicon grass can be formed almost everywhere as a result [129]. A cross-sectional view of the sample is shown in Figure 3.27b. Here, the length of the grass is almost the same as the nanoscale Si sheets, suggesting that the

formation of the grass most likely starts at the same time as the final deep etching.
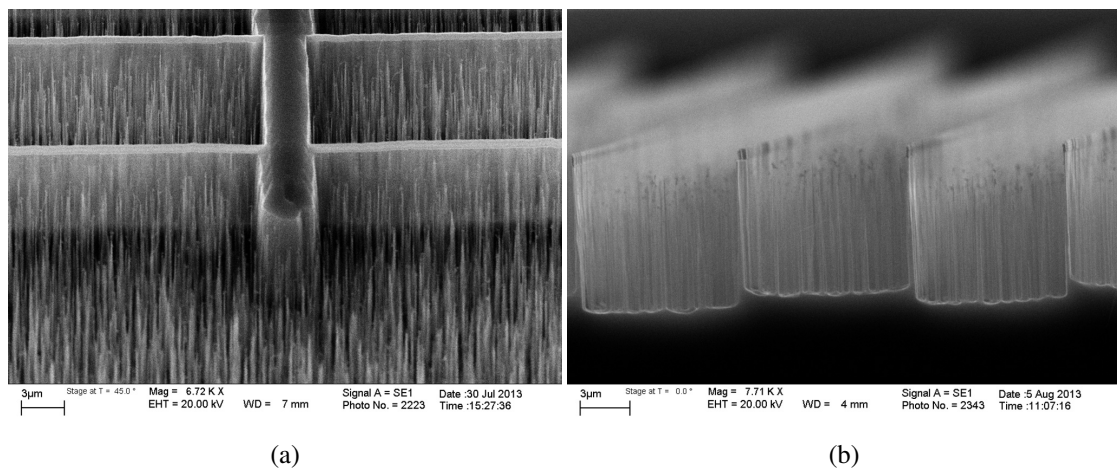


Figure 3.27: (a) Top and (b) cross-sectional view of silicon grass formed after DRIE.

In the examples above, the devices are fabricated on bulk silicon wafers and the images are taken after the final etching step. In the following plasma undercut process, most of the grass will then be cut and fall onto the silicon substrate, which would not be helpful to solve the problem. Nevertheless, a much better result can be obtained when similar BSOI devices are released in HF vapour. Since the wafer is mounted upside down in the etcher, the grass simply falls away when the oxide layer is removed. However, the best solution is to prevent the formation of grass in the first place, which requires further adjustment of the etching process.

## 3.5 Discussion

In this chapter, a single-layer STL process has been designed and developed for mass parallel fabrication of NEMS. The nanoscale features are formed by depositing a conformal layer of metal mask which is then selective etched on the horizontal surfaces, leaving the vertical surfaces as a sidewall mask. The defined pattern is then transferred into silicon by DRIE to form extremely HAR features. Fabricated nanoscale structures have been successfully combined with microscale parts patterned by a second lithography step before final DRIE. Structure suspensions can be achieved by either plasma undercut for bulk devices or HF vapour undercut for BSOI. The typical in-plane dimension of the nanostructures obtained is 100nm with an aspect ratio of 45 : 1.

Two device lay-outs have been designed and fabricated based on the developed single-layer STL including double-ended and single-ended electrothermal actuators. Fabrication results

show success on both bulk silicon and BSOI substrates. Prototype devices have been demonstrated with excellent feature quality. However, the process still suffers from a number of processing issues, mainly in optical lithography, DRIE and residual stress in sidewall masks. Possible approaches to solutions have been proposed including optimising existing or adding additional process steps. Also, the process is still limited by typical topological constrains inherited from general STL, as it cannot form single cantilevers and all nanoscale features must have the same in-plane width.

Apart from these, good results have been obtained for NEMS devices with combined structures of microscale and nanoscale parts. Hence a wider range of NEMS devices with various potential applications [130, 131] can be designed based on STL later.

# 4 Characterization of single-layer NEMS actuators

In this chapter, models and initial performance characterizations are presented for the NEMS electrothermal actuators fabricated in Chapter 3. In Section 4.1, surface profiles of double-ended BSOI electrothermal actuators are acquired using a non-contact interferometric optical profilometer, to evaluate the condition of the completed device and investigate any distortions due to stress. Experimental characteristics of a complete device are then presented. The equipment and experimental set-up are introduced, and electro-mechanical performance is characterized by actuating the device using DC and AC drive currents, and static and dynamic performance is presented. Difficulties with measuring nanoscale devices are highlighted. Finite element analysis (FEA) is then used to provide numerical models for device performance. Problems with numerical simulation and the general inadequacy of this approach for devices with ultra-thin beams are also highlighted.

In Section 4.2, single-ended shape bimorph actuators which can also act as stress gauges are characterized experimentally using similar methods to show the diversity of the device types that can be fabricated by STL. Experimental data and FEA analysis are both presented once again. In Section 7.6, the difficulties encountered in designing and testing NEMS devices are further discussed based on practical experience of experimental measurement and numerical modelling.

## 4.1 Buckling-mode actuator

Figure 4.1a shows the lay-out of a double-ended V-beam actuator fabricated by the single-layer STL process. The actuator has $S$ parallel chevron-shaped nanoscale beams with length $L$ tied by a cross beam with in-plane width $W_C$ at the center. All the hot arms have a common slope angle of $\theta$ and are anchored at either end. The device can therefore be actuated electrothermally by

passing a current between the anchors and through the nanoscale beam array. Figure 4.1b shows SEM view of the overall structure of a prototype device after fabrication.
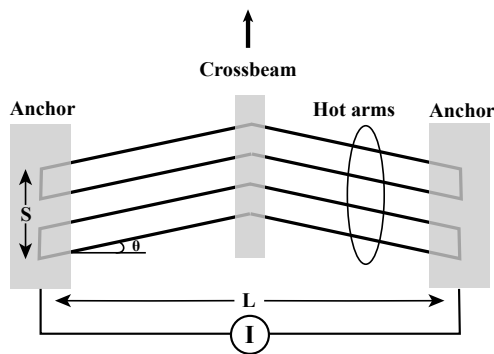


(a)
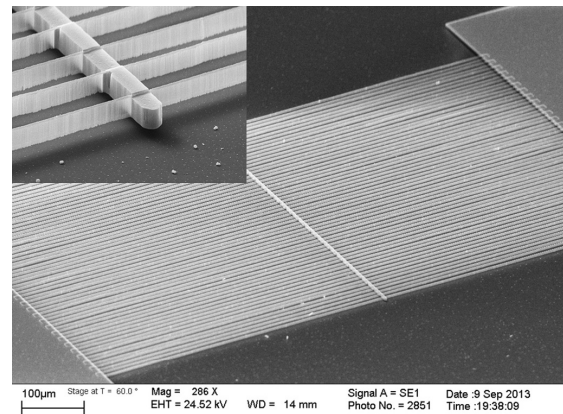


(b)

Figure 4.1: (a) Lay-out of a double-ended buckling-mode V-beam actuator; SEM vies of the overall view and close-up of a prototype device after fabrication.

### 4.1.1 Surface profile

Surface profiles of completed devices were characterized using a scanning white light interferometric profilometer (Wyko NT9100, Veeco Inc.) as shown in Figure 4.2a. The non-contact imaging system is mounted on a vibration isolation table. It measures surface topography from nanometre-scale roughness through millimetre-scale steps, providing 3D surface metrology for device development and failure analysis. A typical resolution for roughness analysis is below 10nm depending on the surface condition.
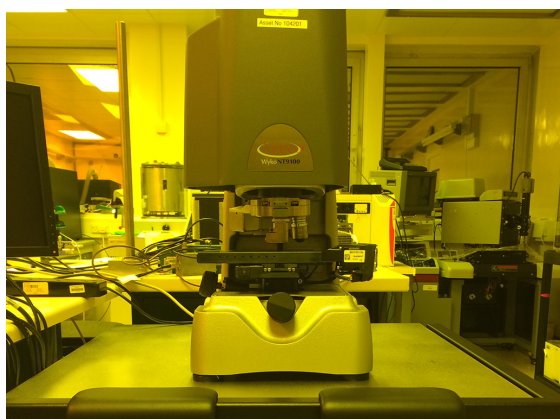


(a)
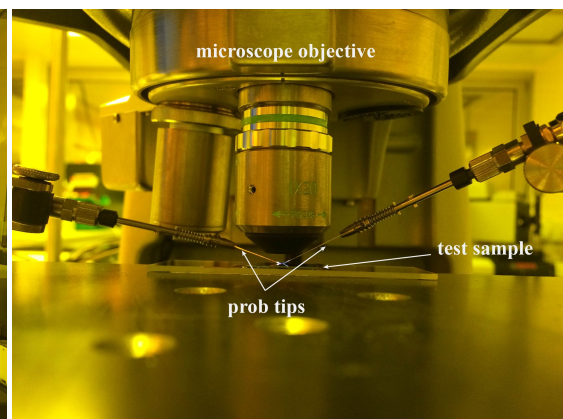


(b)

Figure 4.2: (a) Wyko NT9100 white light interferometric profilometer; (b) the general arrangement for electrothermal actuation using probe tips positioned by 3-axis micro-manipulators.

Figure 4.3 shows the reconstructed surface profiles of a double-ended electrothermal actuator. The device is fabricated on a 5μm device layer on BSOI with a beam separation of 10μm. The combined structure of a nanoscale beam array and a microscale crossbeam is fully undercut and released from the substrate using HF vapour. However, the gaps between the suspensions and the Si substrate cannot be seen using the top-down optical inspection system. Although the dimensions of the nanoscale beams (100nm) are clearly below the in-plane resolution of the imaging system, there is sufficient reflection to generate the complete 3D structure as shown.

Figure 4.3a shows an oblique view near the crossbeam. The stepped surface of the crossbeam follows the mesas used to define the sidewalls. This effect could be eliminated by replacing the Si mesas by sacrificial layer such as silica. The nanoscale beams are parallel and highly vertical, with an almost perpendicular connection to the crossbeam without any tilting or twisting due to stress, despite the fact that the sidewall mask is still in place. The exposed wafer surface is extremely clean, and lacking in particulate debris. The oblique view shows the solid joints at the corner of intersections. Figure 4.3b shows a similar 3D image near the anchors. After stripping the resist, terracing can be seen on the top of the anchors, where the original mesa array intersects the anchors. The vertical striations on the nanobeams are typical results from optical lithography. The 3D reconstructions verify the high structural integrity and quality of the completed device, especially the multiple nanoscale suspensions.



(a)                                    (b)
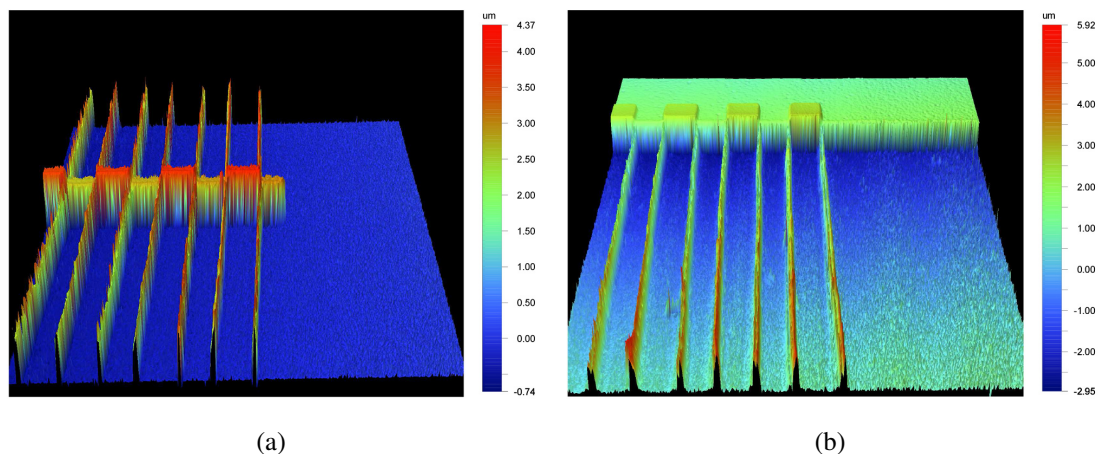
Figure 4.3: Reconstructed 3D surface profiles of a double-ended electrothermal actuator showing regions near the (a) crossbeam and (b) anchors.

Figure 4.4a shows a line-scan profile extracted from the 3D data above, measured along the crossbeam. The feature height corresponds well to the original device layer thickness and its consistency shows that the structure has been released without any significant out-of-plane

deflection.

Figure 4.4b shows a line scan profile measured at $\frac{1}{4}$ of the beam span, where the spacing between the beams is unconstrained. The spacing of the nanoscale beams accurately reflects the original mesa width (10µm), again confirming a lack of stress-induced distortion. However, since the beam width lies below the resolution of the imaging system, there is insufficient reflection from the top surfaces of the nanoscale beams and some variation in apparent height. The reconstructed 3D images confirm the surface profiles of the double-ended actuator shown in the SEM photographs in Chapter 3. To evaluate realistic performance, mechanical performance of prototype devices was then characterized experimentally.





(a)                    (b)
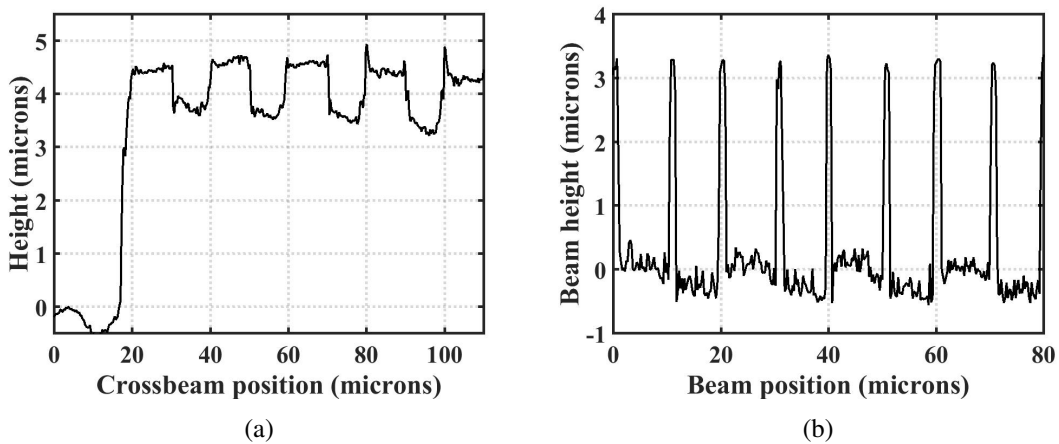
Figure 4.4: Line-scan profiles extracted from 3D surface profiles measured (a) along the top of the crossbeam and (b) across the nanoscale beam span.

## 4.1.2 Mechanical performance

Mechanical motion was first confirmed using a vibration stage, to ensure the suspended structure was thoroughly released from the substrate. The device was then actuated by electrothermal heating, and the corresponding static and dynamic performance was characterized.

After removing the oxide interlayer using HF vapour phase etching, it is important to verify the mechanical motion of the device prior to further quantitative characterization, as it is easy for the suspended structure to remain fixed by any residual oxide underneath. Verification of mechanical motion was carried using a piezoelectrically driven vibration stage, which consisted of a right-angled stainless steel mount and a ceramic disc piezoelectric element (RS 7243166). A double-ended device was mounted on the stage and vibrated in plane. Motion was then verified using an optical microscope equipped with a ×50 objective. In principle, evidence of collective

resonance could then be obtained by sweeping the drive frequency. However, the very small in-plane dimensions of both the beams themselves and the resulting displacements lay below the resolution of the instrument. Other testing methods were therefore investigated to improve the metrology.

For electrothermal characterization, a thin layer of aluminium was deposited over the whole structure to form electrical contacts. The device was then mounted on a substrate, placed under the microscope of an optical metrology system, and electrical contact was made using probe tips positioned using two 3-axis micro-manipulators. To characterize the static performance, a DC current was passed between the anchors. The in-plane deflection could then be monitored using a top-down optical imaging system as illustrated in Figure 4.5a. It was generally difficult to measure deflections, because of the nanoscale feature size, the transparency of the supporting beams and the small in-plane displacement. In the end, the Veeco interferometer was found to give the most useful results with improved in-plane resolution. Figure 4.2b shows the general arrangement for testing with this equipment.



(a)                                          (b)
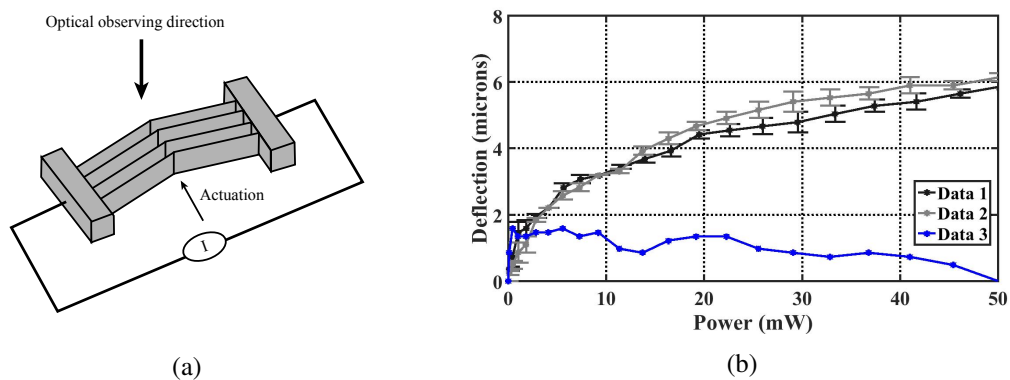
Figure 4.5: (a) Schematic diagram of static in-plane deflection measurement using a top-down optical imaging system; (b) variation of static electrothermal deflection with drive power.

Figure 4.5b shows the variation of deflection with drive power extracted from the difference between the thermally relaxed and distorted states of multiple suspension beams using image analysis software (Vision 4.20, Veeco Inc.). The points of Data 1 and 2 show two sets of data, together with error bars, obtained from different chevron actuators($S = 58$ multibeams with 110nm width, $D = 5\mu$m depth, $L = 1$mm length, 10$\mu$m separation and $W_C = 2\mu$m crossbeam width). The drive powers were calculated from the drive voltage (up to 21V) and the resistance (approx. 8.8k$\Omega$) measured between the anchor points. The variation of deflection with drive power follows a quasi-linear characteristic, which will be compared with the initial numerical

predictions described below and the theoretical predictions in Chapter 5 later. The device then suffered from obvious thermal damage with drive power over 50mW, where the measurement stopped. Data 3 shows the unreasonable behaviour of a device due to thermal damage after a few measurements.

The experimental results shows that very low powers are needed to achieve a microscale displacement, compared with a similar MEMS chevron actuator described in [35]. In particular, for a displacement of approx. 5μm, only 25mW is needed for the NEMS actuator, in other words, 0.43mW for a single nanoscale beam compared with 180mW for a microscale beam.

A number of attempts were made to characterise dynamic performance. Initially a measurement system consisting of an optical microscope equipped with an $\times 100$ objective, a video camera and a calibrated on-screen cursor was used to measure the displacement of the cross-beam tip when driving the actuator at different frequencies. Dark-field microscopy was used to visualise the motion of the nanoscale beams, whose in-plane dimensions otherwise lie below the resolution of the instrument. Figure 4.6 shows images obtained near the central crossbeam, with the device (a) fixed and (b) moving at resonance. For a double-ended electrothermal actuator with a 58-beam array ($W = 110$nm width, $D = 5$μm depth and $L$1mm length) and a $W_C = 2$μm crossbeam, a maximum in-plane displacement of approx. 10μm was observed at a resonant frequency near 1kHz. However it was difficult to measure frequency responses quantitatively this way since the displacement was generally too small except near resonance.
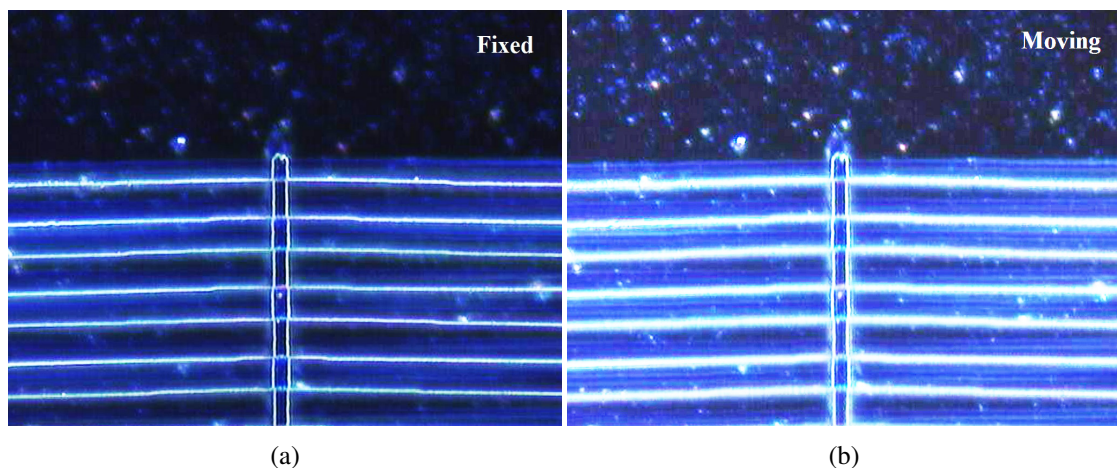


Figure 4.6: Dark-field microscope views of (a) fixed and (b) moving double-ended actuators.

A fibre-based confocal microscope system was then used to measure the scattering from a driven device. Figure 4.7a shows the general arrangement for testing. Light was generated from a laser diode and then coupled into a fiber, whose tip was placed near the crossbeam

of the actuator. Backscattered light from the device was coupled into the fiber, and detected using a mode-stripping photodiode. The output from the photodiode was then further analysed using an oscilloscope or PC. The device was actuated with a sinusoidal drive and electrical contacts were made using probe contacts as before. As with all electrothermal actuators, the mechanical response was at twice of the driving frequency. Once again, experiments were extremely difficult to perform.

Figure 4.7b shows the measured variation of deflection with drive frequency. The deflection clearly falls slowly at low ($< 1$kHz) frequency and more rapidly at high ($> 5$kHz) frequency. The former effect is ascribed to the well-known first-order roll-off of an electrothermal transducer, and the latter to the second-order roll-off of a resonant system above the resonant frequency. There is some evidence of resonance at around 1kHz; however, it was difficult to distinguish the collective resonance from uncorrelated vibration of individual nanoscale beam. Hence, to achieve more accurate characterization, it is worth developing a suitable measuring system with higher resolution for NEMS device.



(a)

(b)
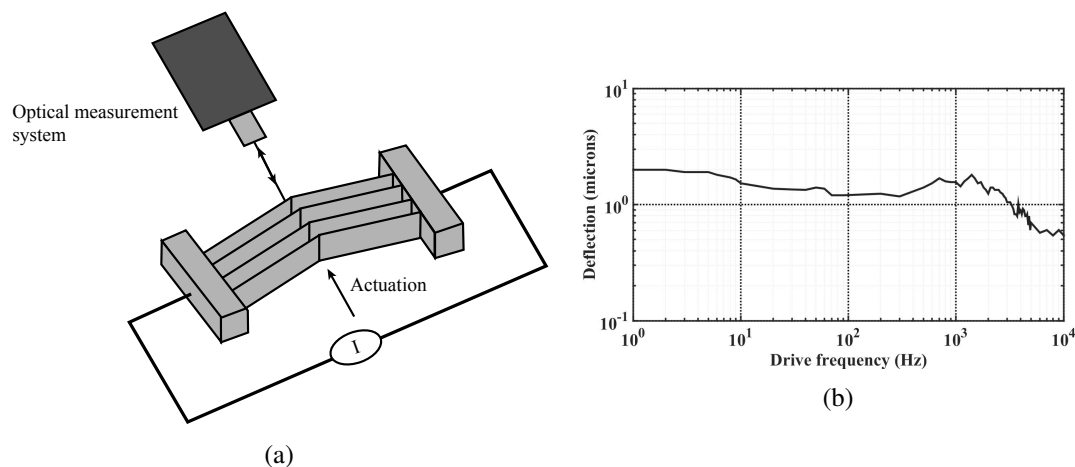
Figure 4.7: (a) Schematic diagram of dynamic performance characterization using an optical measurement system; (b) variation of deflection with drive frequency.

### 4.1.3 Finite element analysis

Finite element analysis (FEA) was used to build numerical models of device performance. The simulation environment here is the MEMS module of COMSOL® Multiphysics 4.4.

To provide an FEA estimation of the performance of a pre-buckled V-beam actuator, a 2-D model of the actuator was built in the X-Y plane. Three physics modules were then used to analyse the structure, namely the Electrical Currents, Heat Transfer in Solids and Solid Me-

95

chanics modules. The first module was used to calculate the local current density and power dissipation when a heater current is passed through the structure. The second module calculates the resulting temperature rise after solving the heat conduction equation for solids. The third module then calculates the deflections caused by constrained thermal expansion. In each case, appropriate material constants and boundary conditions are defined.

Single crystal silicon was the default material for the whole structure, which is united and converted to solid in the model. The following material constants were assumed: coefficient of thermal expansion $\alpha = 2.6 \times 10^{-6} \mathrm{K}^{-1}$, thermal conductivity $k_{th} = 130 \mathrm{W \cdot m^{-1} \cdot K^{-1}}$, Young's modulus $E = 170 \times 10^9 \mathrm{N/m^2}$, Poisson's ratio $\nu = 0.28$, density $\rho = 2329 \mathrm{kg/m^3}$ and electrical resistivity $\rho = 20 \Omega \cdot \mathrm{cm}$. The boundary conditions assumed at either end of the device were a voltage difference between $DV$ and zero, zero temperature rise, zero deflection and zero rotation.

Meshing parameters are critical for accurate simulation, and these must generally be chosen according to experience. Since the geometries of NEMS devices here generally involve high aspect ratios ($100 \leqslant L : W \leqslant 10000$), there must be enough elements in the narrow regions to ensure the accuracy of the numerical calculation. However increasing the number of elements leads to a rapid rise of the memory and time required for simulation. For very narrow (0.1μm) beams, it was often the case that no solution was achieved, due to a failure in convergence and the maximum allowable iteration number (50) was reached without tolerable errors. A customised mesh size was therefore used depending on the beam width. For example, the mesh parameters used for the 0.1μm beam were as follows: maximum element size $1 \times 10^{-5} \mathrm{m}$, minimum element size $5 \times 10^{-9} \mathrm{m}$, maximum element growth rate of 1.05, curvature factor of 0.2, resolution of narrow regions of 10.

A number of different beam widths were considered, namely 0.1μm, 0.5μm, 1μm, 5μm and 10μm. All structures had a beam length of 1mm and an initial pre-buckle of 10μm at the midpoint, structured for the 2D model with multi-physics analysis.

To verify the accuracy of each physics module, analysis results were generated separately. Figure 4.8 shows the current density distribution and temperature distribution for beam width $W = 10$μm and 0.1μm respectively, calculated by the Electrical Currents and Heat Transfer in Solids modules. As shown in Figure 4.8a and 4.8b, the 2D surface plots for $W = 10$μm beam show good agreement with the boundary conditions of fixed voltage difference and fixed temperature at both ends. Hence the current density is almost uniform along the arc length except small changes due to the pre-buckled V-shape, for a voltage sweep from 1 to 20V as

shown in Figure 4.8c. In Figure 4.8d, the temperature change clearly follows the solution of a classic heat conduction equation with zero change at ends and a parabolic variation with a maximum temperature rise at the midpoint of the span, which will be detailed in Chapter 5 later. For $W = 10\mu m$, the peak temperature rise is approx. 8K. Similar results for beam width $W = 0.1\mu m$ have also been plotted in Figure 4.8e and 4.8f for comparison. Here, the simulated voltage ranges again from 1 to 20V to match the parameters in previous experiments. Thus the current density increases linearly and the peak temperature rise reaches the similar value as that of the 10$\mu$m beam, indicating the analysis of both electrical and thermal modules are valid.
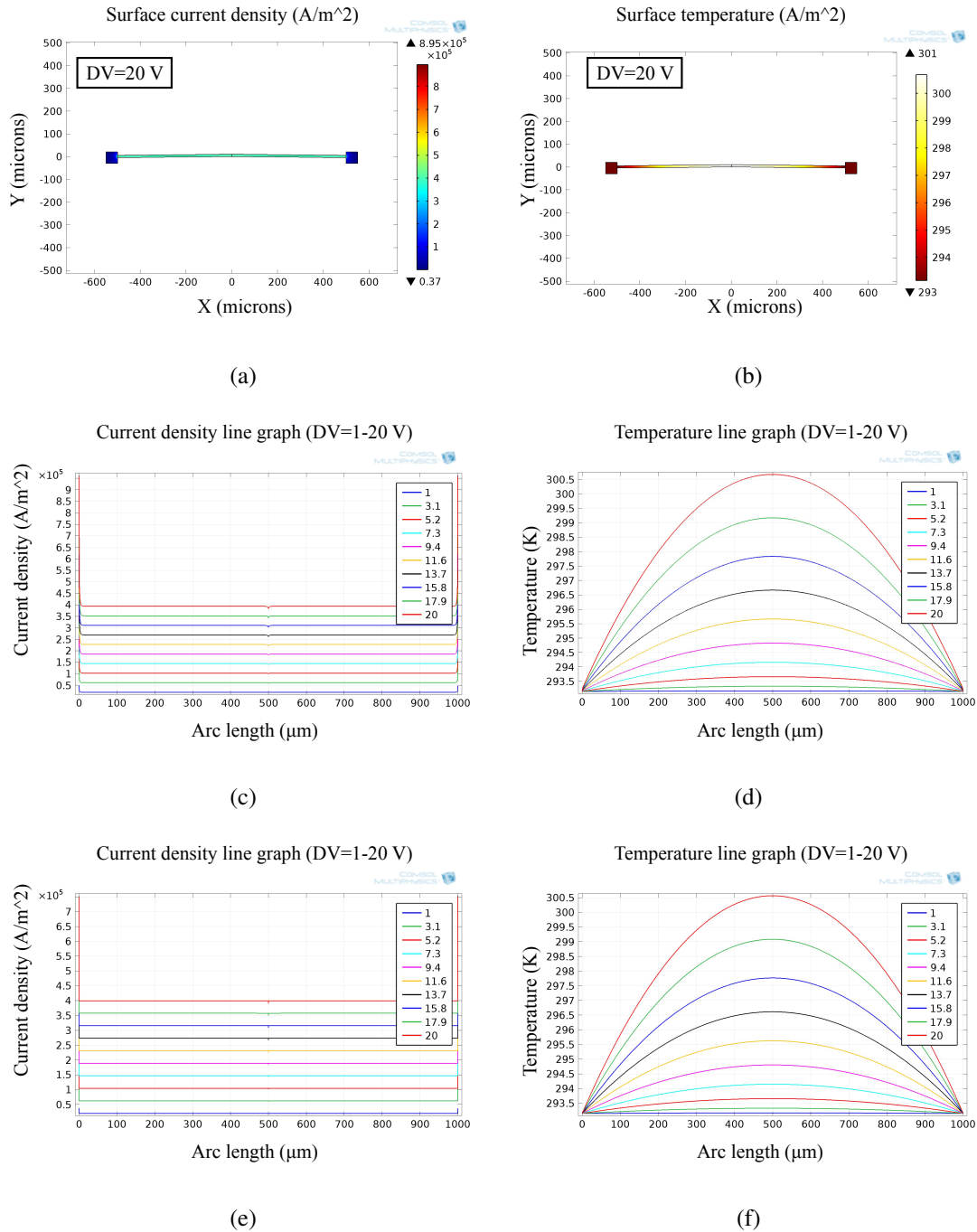
Figure 4.8: FEA simulation results of V-beam actuators showing: (a) surface current density distribution and (b) temperature distribution for a 2D model with beam width $W = 10\mu$m; line graphs of variation of (c) current density and (d) temperature with arc length ($W = 10\mu$m); line graphs of variation of (d) current density and (f) temperature with arc length ($W = 0.1\mu$m).

Although the FEA analysis shows convincing results in both electrical and thermal analysis, practical experience shows that the next stage in the calculation (namely, application of the Solid Mechanics module) is very likely to give erroneous results due to a failure in convergence. For

example, a 2D thermal expansion model was build with a uniform temperature rise applied to the whole structure to monitor the buckling deformation. Figure 4.9a shows the deflected beam shape for a 10μm beam with a temperature change of 350°C. Here, the deflection in the y-direction has been exaggerated.

At first sight, this result appears reasonable. However, all three modules were then used together for the complete evaluation of electrothermal performance. Electrical heating was applied using a parametric sweep in input voltage for beam widths from 0.1 to 10μm. Power consumption was then calculated as the product of the applied current and corresponding voltage. The y-deflection of the midpoint of the beams was then monitored for all structures, and plotted as a function of drive power. Figure 4.9b compares the FEA simulation results (points) with the predictions of an analytic theory (full lines) which will be developed in Chapter 5. Obviously, good agreement is obtained for wide beams ($w > 1$μm). However, for thinner beams the FEA results differs significantly from the analytic results, and the scatter in the data for a beam width $W = 0.1$μm indicates that it is the FEA result that is erroneous.



<div align="center">(a)           (b)</div>
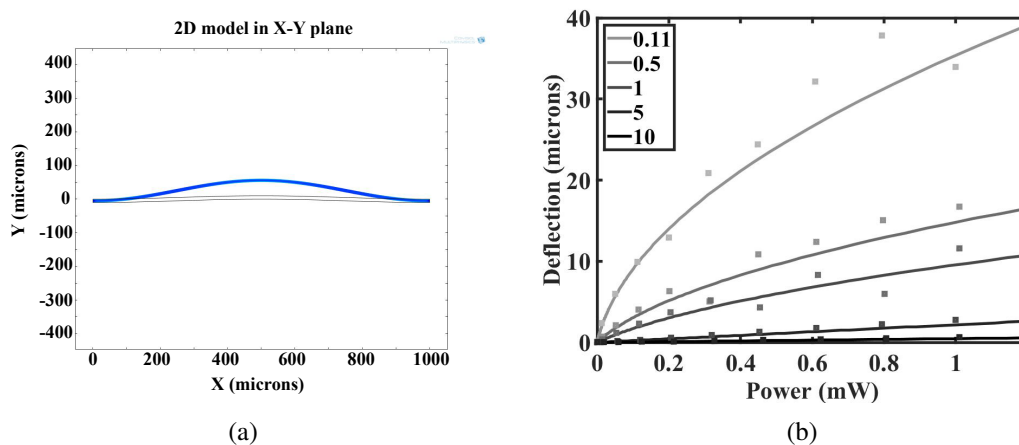
Figure 4.9: (a) 2D FEA model showing the deflected beam shape for a $W = 10$μm V-beam actuator; variation of deflection with power consumption for a V-beam actuator with different values of $W$ in microns, points showing the FEA simulation results and full lines showing the analytic theory predictions.

The results above suggest that FEA simulation is a suitable method to gaining insight and estimating device performance. However it is less appropriate for high-aspect-ratio NEMS with slender beams due to the requirement for very fine meshing to achieve sufficient accuracy.

## 4.2 Shape bimorph actuator

Single-ended shape bimorph actuators that can also act as stress gauges were also fabricated using the single-layer STL process. The original aim was to monitor any deformation caused by intrinsic stress inherited from the process. These devices were fabricated with a wide arrange of geometries, based on those of standard MEMS shape bimorph actuators. Figure 4.10a shows the lay-out of example devices, which typically contain a pointer supported on a set of long arms and a set of short arms, each of different length ($L_C$ and $L_H$) and with a variable number of hot arms (typically, 2 or 4). The dimensions of the link unit and pointer are indicated as shown in Figure 4.10a(i) and 4.10a(ii). Strain with respect to the substrate would result in an observable deflection of the pointer. However, similar deflections could be achieved mechanically and electrothermally, either by applying a displacement to the pointer tip (Figure 4.10a(iii)) or using a heater current to generate the strain (Figure 4.10a(iv)).

Figure 4.10b shows a SEM view of the overall structure of a pair of prototype devices after fabrication. Here two released devices have been designed with a cold beam length of $L_C = 100\mu m$, hot beam length of $L_H = 200\mu m$ and different beam separations of $10\mu m$ and $5\mu m$ respectively. Both have the same in-plane nanoscale beam width of $W = 100nm$. However, little sign of deformation has been observed in either case. As a result, we can conclude that the intrinsic stresses inherited from the STL process (for example, due to the presence of residual mask material) are very small.
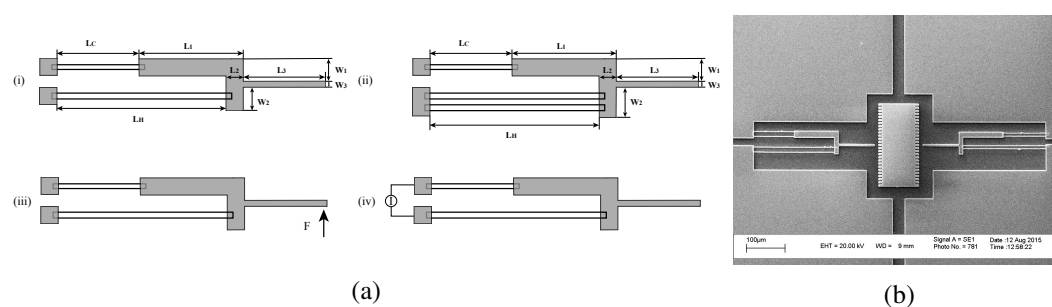


Figure 4.10: (a) Lay-outs of single-ended shape bimorph actuators with 2 (i) and 4 (ii) hot arms with testing diagrams showing mechanical (iii) and electrothermal (iv) actuation.

### 4.2.1 Surface profile

Surface profiles of completed devices were again obtained using the Veeco interferometric profilometer. Figures 4.11 shows the reconstructed surface profiles of a released device fabricated on BSOI with a nanoscale beam separation of $10\mu m$. Again, the gaps between the suspensions

and the Si substrate cannot be seen using the top-down optical inspection system. However, the 3D reconstruction presents a clear picture of the completed device, showing great difference of in-plane dimension magnitude between the microscale and nanoscale features.

Figure 4.11a shows lateral view of the nanoscale beams connecting to the microscale link unit. The two sets of nanoscale beams (which are initially parallel to each other) have each buckled slightly. This effect possibly results from the intrinsic stress in the sidewall masks, which are still in place after release. Any localised defects and imperfection in material or structure arising from optical lithography might magnify such phenomena. Apart from that, the connections between the micro- and nano-scale parts are excellent, with an almost perpendicular intersection and overlap at the joints.

Figure 4.11b shows the oblique view of link unit and the pointer. Intersecting features have clearly resulted in solid joints. The vertical striations on the nanobeams are typical results from optical lithography. The etched structures show highly HAR features from micro- to nano-scale with nearly vertical edges down to the substrate.



(a)      (b)
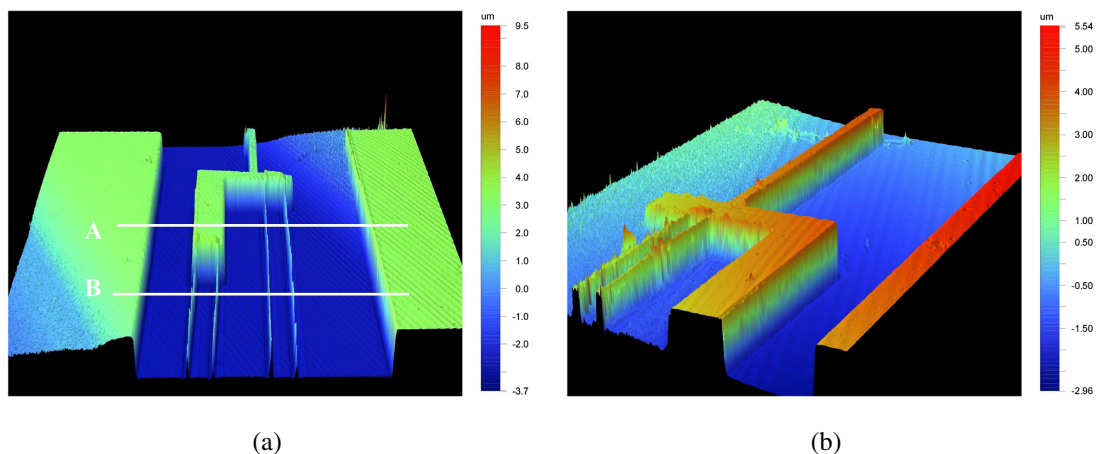
Figure 4.11: Reconstructed 3D surface profiles of a single-ended shape bimorph actuator showing (a) nanoscale beams with perpendicular intersection and (b) link unit and pointer.

Figure 4.12 shows line-scan profiles extracted from the 3D data above, measured along region A (blue line) and B (black and red lines) as shown in Figure 4.11a. All line-scans again clearly show the combined features from microscale to nanoscale of the demonstrated device. Region A shows a line-scan across a set of hot arms and the link unit while region B shows that across a set of hot and cold arms. The spacing of the nanoscale beams is 10μm which reflects the original mesa width. However, presented nanoscale beam height is less than the microscale parts due to insufficient reflection from the top surfaces. In region B, the two line-scans (black and red lines)

of different positions confirm that buckling of the hot arms has occurred due to larger intrinsic stress on the long beams.



(a)
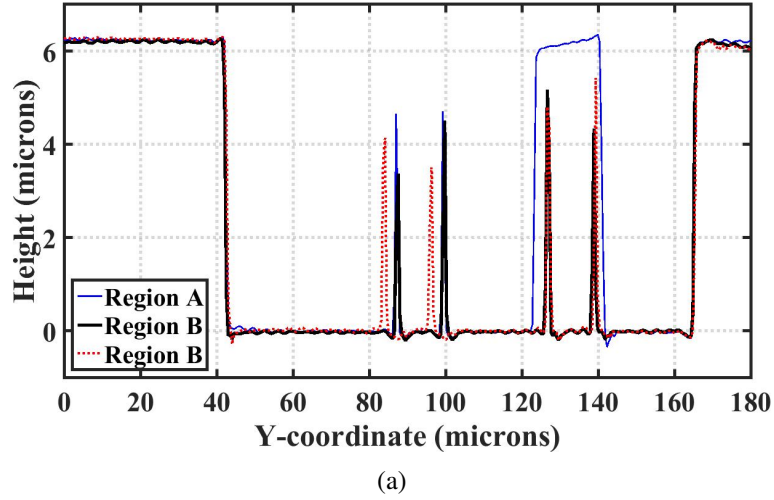
Figure 4.12: Line-scan profiles extracted from 3D surface profiles measured along region A (blue line) and different positions in region B (black and red lines) in Figure 4.11a.

### 4.2.2 Mechanical performance

Displacement can easily be applied to the released device using a probe tip, and the corresponding deflection can then be observed under an optical microscope. For example, Figure 4.13 shows a deflected device before and after applying a transverse deflection to the pointer. The cold and hot beams have two length ($L_C = 100\mu$m and $L_H = 200\mu$m respectively) and the same in-plane width of $W = 100$nm. The following lay-out dimensions as illustrated in Figure 4.10a(i) are used: $L_1 = 110\mu$m$\times$, $L_2 = 10\mu$m$\times$, $L_3 = 90\mu$m$\times$, $W_1 = 33\mu$m$\times$, $W_2 = 21\mu$m$\times$ and $W_3 = 4\mu$m$\times$. Surprisingly, large displacements (approximately 16$\mu$m here) could be imposed on the structure by external actuation without any destructive effects. In addition, the deflection returned back to zero after removal of external actuation, showing good linearity.

<div align="center">(a)             (b)</div>
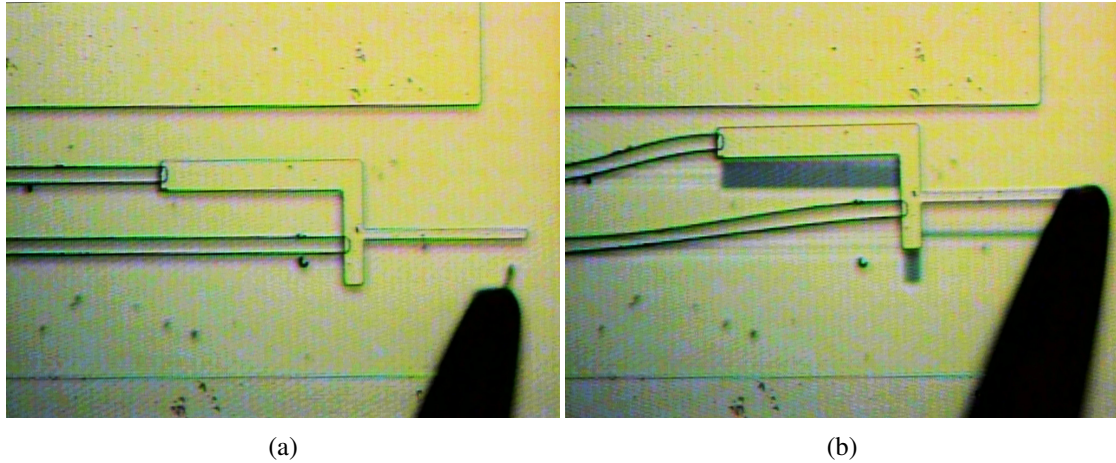
Figure 4.13: Optical microscope photographs of single-ended shape bimorph actuators (a) be-fore and (b) after application of a transverse deflection to the pointer.

To evaluate the electrothermal performance, a current was passed between the anchors to achieve electrothermal actuation (as shown in Figure 4.10a(iv)). The device was again mounted on a substrate under the microscope of an optical metrology system. A DC current was applied by probe tips positioned using two 3-axis micro-manipulators and the in-plane deflection of the pointer was then characterized. This time, deflection measurement should have been easier than before, as the pointer dimension is now microscale. However, the displacement achieved was still small $< 2\mu$m, and special care had to be taken of the amount of applied current. Since there were fewer beams in the structure (which could easily be damaged by extensive thermal heating), it was often found that unpredictable behaviour was obtained with a combination of buckling and thermal runaway.

Figure 4.14 shows the experimental variation of the in-plane y-deflection versus the square of applied voltage ($V^2$) of a complete device with 2 cold arms and 4 hot arms. The following lay-out dimensions as illustrated in Figure 4.10a(ii) are used: $L_C = 105\mu$m, $L_H = 205\mu$m, $L_1 = 110\mu$m, $L_2 = 10\mu$m, $L_3 = 90\mu$m, $W_1 = 31.5\mu$m, $W_2 = 21\mu$m and $W_3 = 4\mu$m. The plotted data is an average of 10 data sets extracted from the tip of the moving pointing arm. The variation of deflection follows a quasi-linear characteristic, in reasonable agreement with the trend predicted by FEA simulations that follow. The maximum deflection is approximately 1.73$\mu$m at a voltage of 3V.
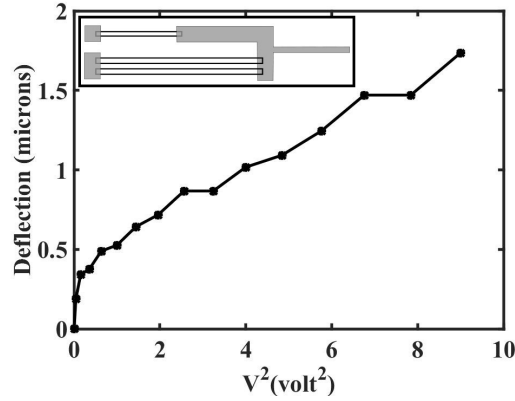
Figure 4.14: Variation of in-plane pointer deflection with the square of applied voltage for a single-ended actuator.

### 4.2.3 Finite element analysis

FEA analysis has also been used to simulate single-ended actuators by 2D models of the complete device built in COMSOL® using a similar method as before. Single crystal silicon was again selected as the mechanical material with the same material constants assumed. In contrast to the buckling mode devices, these structures do have some modes of linear operation, but some difficulties were still experienced.

Firstly, a 2D model of a 2-2-arm actuator was built in the X-Y plane to estimate the deflection obtained when a force was applied in y-direction at the free end of the pointer, mimicking the experiment of Figure 4.13. A fixed constraint was applied at the LHS of each nanoscale beam as boundary condition, since these attached to the anchors. Meshing parameters were carefully chosen based on structure dimensions with previous experience. The following lay-out dimensions as illustrated in Figure 4.10a(i) were used: $L_C = 100\mu m$, $L_H = 200\mu m$, $L_1 = 110\mu m$, $L_2 = 10\mu m$, $L_3 = 90\mu m$, $W_1 = 33\mu m$, $W_2 = 21\mu m$ and $W_3 = 4\mu m$. The in-plane widths of the nanoscale beams covered a range from $0.05\mu m$ to $1\mu m$. A point load of 1N/m was applied at the free end of the pointer in each case.

Figure 4.15a shows the deflected device shape estimated by FEA with a $W = 0.5\mu m$ nanoscale beam width. Using the resulting deflection, the equivalent transverse stiffness $k_{eq}$ of the structure was then calculated as shown in Column 2 of Table 4.1.

Despite the slight rotation of the microscale link unit (which can almost certainly be neglected), the nanoscale beams must deflect under this load much like a conventional beam with one end fixed and one end guided. A free body diagram can then be drawn for each individual
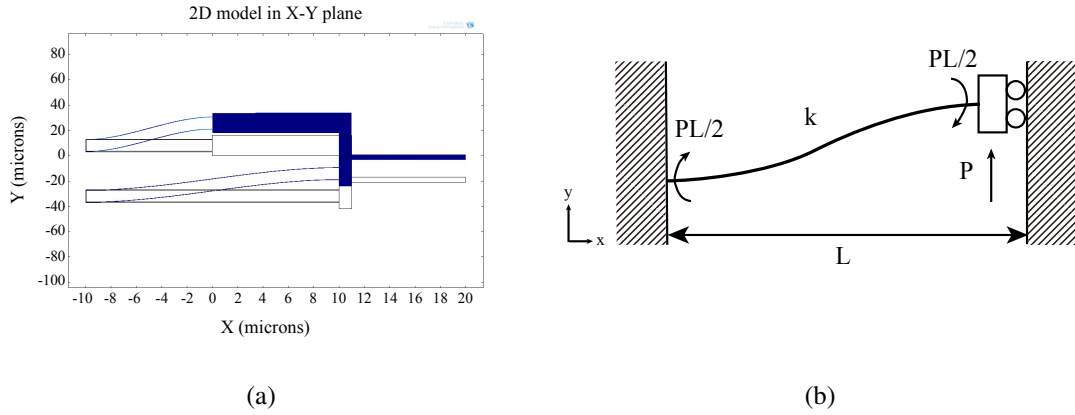
Figure 4.15: (a) 2D FEA model showing the deflected device shape of a single-ended actuator for nanoscale beam width $W = 0.5\mu$m; (b) free body diagram of a loaded single beam with one end fixed and one end guided.

| Beam width $W$ (µm) | FEM $k_eq$ (N/m) | Analytic $k_eq$ (N/m) | Relative error |
|---|---|---|---|
| 1 | 1.9650 | 1.9125 | 2.74% |
| 0.8 | 1.0280 | 0.9792 | 4.98% |
| 0.5 | 0.2559 | 0.2391 | 7.05% |
| 0.2 | 0.0164 | 0.0153 | 7.06% |
| 0.1 | 0.0014 | 0.0019 | 27.32% |
| 0.08 | 0.0001 | 0.0010 | 80.88% |
| 0.05 | 0.0020 | 0.0002 | 740.78% |

Table 4.1: Comparison between FEA and analytic calculations of the transverse stiffness of a single-ended shape bimorph actuator.

beam as shown in Figure 4.15b. For a point end load, the beam should undergo a transverse deflection of $\triangle y = \frac{PL^3}{12EI}$, where $P$ is the applied load, $E$ is Young's modulus of the material and $I$ is the second moment of area of the beam as $I = \frac{W^3 D}{12}$. Thus, the transverse stiffness $k$ of a single beam should be:

$$k = \frac{P}{\triangle y} = \frac{12EI}{L^3} \tag{4.1}$$

For two pairs of nanoscale beams of different length arranged in parallel, the equivalent stiffness $k_eq$ can be estimated as:

$$k = 2 \times (k_1 + k_2) \tag{4.2}$$

where $k_1$ and $k_2$ are the stiffnesses of the hot and cold arms respectively.

Numerical predictions obtained from this analytic theory are presented in Column 3 of Table 4.1. For beam widths $W$ between 0.2 µm and 1 µm, good agreement is obtained with the previous FEA simulation. However, the relative error gradually increases as $W$ decreases, indicating

that simulation in COMSOL® again starts to require considerable time and memory to achieve accurate estimates for very slender beams. For beam widths $W < 0.1\mu$m, there is a rapid rise in error with current mesh parameters, suggesting that numerical estimates from the FEA model must once again be invalid.

To model the electrothermal performance, two types of device lay-outs were considered for evaluation of electrothermal performance, namely the 2-2-arm and 2-4-arm single-ended actuators as shown in Figure 4.10a(i) and (ii). The lay-out dimensions were kept the same as corresponding devices tested experimentally described in Section 4.2.2. 2D models of the complete devices were build in the X-Y plane with all three physics modules applied to the structures as before. A voltage difference of *DV* was applied between the fixed ends of the cold and hot arms to form electrical heating, where the boundary conditions assumed were zero temperature rise, zero deflection and zero rotation.

Since the structure considered here has a combined feature of micro-to-nanoscale, meshing parameters have to be carefully chosen to ensure the accuracy of the calculation. Also, in-plane beam width $W = 1\mu$m was finally chosen for the cold and hot arms due to the failure of convergence when solving models with thinner beams. After practice, the following mesh parameters are used: maximum element size $4.24 \times 10^{-7}$m, minimum element size $8.49 \times 10^{-10}$m, maximum element growth rate of 1.05, curvature factor of 0.2, resolution of narrow regions of 6.

Figure 4.16 shows the FEA results of a 2-2-arm device. Figure 4.16a shows the deflected actuator shape predicted by the 2D model. Clearly the deformed shape could be obtained matching the experiment results when applying a fixed displacement on the pointer as before. This proves that the slight rotation of the microscale link unit can almost be neglected when applying electrothermal heating on such structures. Figure 4.16b and 4.16c shows the current density and temperature distribution for the cold (points) and hot arms (full lines) respectively along the arc length, calculated by the Electrical Currents and Heat Transfer in Solids modules. Both two plots show good agreement with the boundary conditions of the same current density in each arm and fixed temperature at the fixed ends. The temperature change along the cold arms matches the variation of the front part of the hot arms, whose later shows a trend of rise first then falls due to cooling from the link unit at the RHS. The end temperature on the moving ends of both arms are found to be close, showing the temperature rise on the microscale link unit are minor. However, with *DV* ranging from 1 to 3000V, the peak temperature rise has been

enormous and unrealistic. Figure 4.16d shows the y-deflection of the pointer with the square of applied voltage ($DV^2$). Here, the variation is clearly linear, however reasonable displacement (14μm) is achieved by a large voltage (3000V). Considering the enormous temperature rise obtained before, we should then believe the prediction of deflection is erroneous. Hence FEA simulation is very likely to be wrong when coupling the third mechanical module with the first two as before.
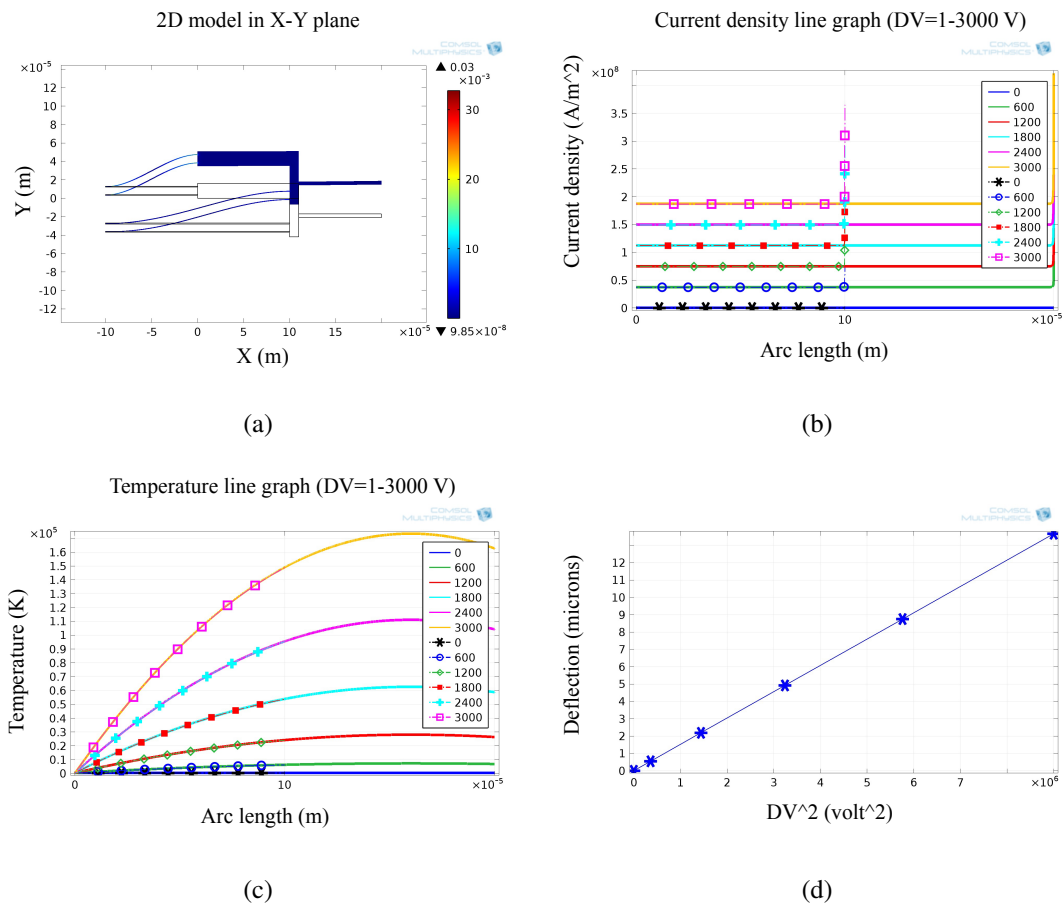


Figure 4.16: (a) 2D FEA model showing the deflected actuator shape for $W = 1$μm; (b) surface current density distribution and (c) temperature distribution predicted by FEA simulations; (c) variation of deflection with the square of applied voltage predicted by FEA.

Other factors that might lead to the failure of the model should also be considered, due on the special combination of the micro- and nanoscale features here. Firstly, the extra cooling cooling such as convection may occur due to the small cross-sections and large surface area of this NEMS beams. This might result in an increase in the power needed to obtain a given deflection. Secondly, with the experimentally observed pre-buckled shape, the deflection of single-ended actuator is to some extent less controllable than the V-beam actuators above. Thirdly, all there

physics module have been applied on the combined structure of micro-to-nanoscale, hence requiring a higher standard of meshing especially on the joint parts.

## 4.3 Discussion

Completed nanoscale devices have been shown to be fully released from the Si substrate without significant distortion. However, it is difficult to carry out any electro-mechanical performance characterization because (a) the width of the nanoscale beams lies below the resolution of the available measurement systems, (b) the displacement is very small and (c) the roll-off of the electrothermal transducer disturbs the observation of the collective resonance in dynamic operation. Thus the corresponding parameters should be adjusted in future designs for ease of testing, for example, a larger displacement might be achieved by changing the beam parameters $W, D, L$. Alternatively, characterization could be performed in an electron microscope equipped with suitable feed-throughs.

In addition, the experimental results that have been obtained show large deviations from the performance predicted using commercial FEA software. The obvious explanation is that the structure of the nanoscale beams here involves an extremely high aspect ratio ($L : W : D = 10000 : 1 : 50$), which requires large number of elements in meshing, especially in the narrow regions. Customized fine meshing helps to solve the problem to some extent, however the rapid rise in the number of elements generated still greatly increases the memory requirements and simulation time in practical use. Thus it is necessary to construct an analytic model for the behaviour of the NEMS actuator to further analyse the mechanical performance. For the buckling mode actuator, a suitable theory will be developed in Chapter 5.

# 5 Theoretical model for NEMS actuators

In this chapter, we consider the design of pre-buckled electrothermal actuators. As shown in Figure 5.1a, in plane motion of the device is achieved by passing a current through an array of beams anchored at both ends. The beams have a pre-buckled shape to ensure motion in the desired direction, and a central crossbeam is provided to force collective motion. Two well-known lay-outs have been studied in literature. The first is the actuator with a raised cosine pre-buckle shown in Figure 5.1b. The second is chevron or V-beam actuator shown in Figure 5.1c. In each case the basis of actuation has been investigated using Euler buckling theory and FEA, typically using a simplified single-beam model.
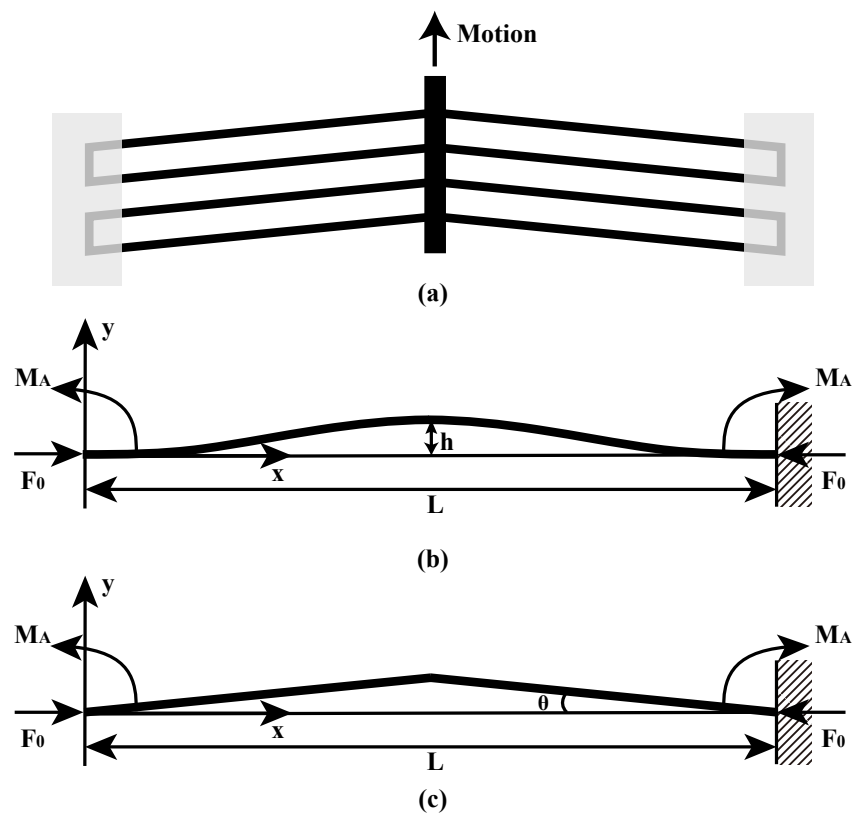


Figure 5.1: (a) Schematic diagram of a double-ended actuator; geometry of a single (b) actuator with raised cosine pre-buckle and (c) V-beam actuator.

However, neither the analytic nor the finite element model of the elastic deformation is very satisfactory. The former does not provide closed form expressions, while the latter often fails when the beams are very long and narrow, which increases the required number of elements rapidly so that the memory and run time quickly become large. An exception is an analytic approximation for deflection in [33] which is purely derived from geometric arguments.

In this chapter, analytic single-beam models are developed for the two actuator types above. The aim is to remedy the deficiency of existing work by developing approximations with closed-form solutions. Particular solutions are found for very slender beams (valid in the double-ended NEMS actuator in Chapter 3), in which the bending dominates over axial compression. Actuators with a raised cosine pre-buckle are investigated in Section 5.1 and V-beam actuators are discussed in Section 5.2. A number of additional considerations (alternative approximations, intrinsic stress, the relation between deflection and power, and the transverse stiffness) are also included. Conclusions are drawn in Section 5.3.

## 5.1 Buckling actuator with raised cosine pre-buckle

We begin with the raised cosine pre-buckle, following the general approach used in [35] (an extension of earlier work on strain sensors [34]). Figure 5.1(b) shows a double-ended single beam of length L and central offset h with a raised cosine pre-buckle. The cross-section has in-plane width $W$ and depth $D$. The initial shape $y_{00}(x)$ of the beam is described by the static variation:

$$y_{00}(x) = h\sin^2\left(\frac{\pi x}{L}\right) \tag{5.1}$$

### 5.1.1 Analytic model

Buckling is achieved by applying an axial force $F_0$ which generates a corresponding bending moment $M(x)$. The shape of the loaded beam $y_0(x)$ is described by solving the Euler buckling equation:

$$EI\frac{\mathrm{d}^2(y_0 - y_{00})}{\mathrm{d}x^2} = M(x) \tag{5.2}$$

Here $I = \frac{W^3 D}{12}$ is the second moment of area of the beam, and $E$ is Young's modulus for the beam material used. In this case, we have $M(x) = M_A - F_0 y_0$, where $M_A$ is an unknown end-moment.

The analysis is then best carried out by substituting $y_0 = y_{00} + u_0$, yielding:

$$\frac{d^2 u_0}{dx^2} + \left(\frac{F_0}{EI}\right) u_0 = \frac{M_A}{EI} - \frac{F_0}{EI} y_{00} \tag{5.3}$$

Equation (5.3) can be solved in terms of the sum of a complementary function (CF) and particular integral (PI). Applying the boundary conditions of:

$$\left.\begin{array}{ll} ① & u_0(0) = 0 \\[1mm] ② & u_0(L) = 0 \\[1mm] ③ & \left.\dfrac{du_0(x)}{dx}\right|_{x=0} = 0 \\[1mm] ④ & \left.\dfrac{du_0(x)}{dx}\right|_{x=L} = 0 \end{array}\right\} \quad \text{Boundary conditions} \tag{5.4}$$

the result is:

$$u_0(x) = h\left(\frac{k_0^2 L^2}{4\pi^2 - k_0^2 L^2}\right) \sin^2\left(\frac{\pi x}{L}\right) \tag{5.5}$$

where $k_0 = \sqrt{\frac{F_0}{EI}}$.

This result demonstrates a special quality of the raised cosine pre-buckle: only the amplitude of the deflection changes during actuation, not the deflected shape. The midpoint deflection $d_{max0}$ is:

$$d_{max0} = u_0\left(\frac{L}{2}\right) = h\left(\frac{k_0^2 L^2}{4\pi^2 - k_0^2 L^2}\right) \tag{5.6}$$

Equation (5.6) implies that $d_{max0}$ will be infinite when $k_0 L = 2\pi$, which is the Euler buckling condition.

The axial force $F_0$ is due to constrained thermal expansion and can be found by calculating the total length of the deflected beam along its length. The total length is approximately:

$$\int_0^L \sqrt{1 + \left(\frac{dy}{dx}\right)^2}\, dx \approx \int_0^L \left[1 + \frac{1}{2}\left(\frac{dy}{dx}\right)^2\right] dx \tag{5.7}$$

Integrating the deflected beam shape allows the change in length due to bending to be found as $\triangle L = \delta L - \delta L_0$, where $\delta L$ is the difference from the horizontal length and $\delta L_0$ is the integral in the unloaded case:

$$\delta L = \int_0^L \left[1 + \frac{1}{2}\left(\frac{dy}{dx}\right)^2\right] dx - L = \frac{1}{2}\int_0^L \left(\frac{dy}{dx}\right)^2 dx \tag{5.8}$$

Hence, the fractional change in length $\frac{\triangle L}{L}$ is:

$$\frac{\triangle L}{L} = \frac{\pi^2 h^2 k_0^2 (8\pi^2 - k_0^2 L^2)}{4(4\pi^2 - k_0^2 L^2)^2} \tag{5.9}$$

We now assume that buckling has induced a constrained thermal expansion following from an average temperature rise $\triangle T_{avg}$. The compatibility condition can be written as:

$$\frac{F_0}{EWD} = \triangle T_{avg}\alpha - \frac{\triangle L}{L} \tag{5.10}$$

Here $\alpha$ is the linear thermal expansion coefficient of the beam material. The three terms in Equation (5.10) describe change in length due to axial compression, thermal expansion and bending, respectively. Substituting for $F_0$, the result can be written in the alternative form:

$$\triangle T_{avg}\alpha = \frac{\triangle L}{L} + \beta^2 k_0^2 L^2 \tag{5.11}$$

where $\beta = \frac{W}{\sqrt{12L}}$.

Since $\frac{\triangle L}{L}$ is a function of $k_0 L$, and $d_{max0}$ is also a function of $k_0 L$, it should be possible to plot $d_{max0}$ as a function of $\triangle T_{avg}$. For example, Figure 5.2a shows the variation of $d_{max0}$ with $\triangle T_{avg}$ based on the analytic model built (full lines), for a silicon beam with the following assumed parameters: $E = 170 \times 10^9 \text{N/m}^2$, $\alpha = 2.6 \times 10^{-6} \text{K}^{-1}$, $L = 1 \times 10^{-3}\text{m}$, $h = 5 \times 10^{-6}\text{m}$, $D = 5 \times 10^{-6}\text{m}$ and different values of $W$ ranging from 0.1μm to 10μm. In each case, the variation is generally similar. When the temperature rise $\triangle T_{avg}$ is negative (so the beam is being artificially cooled, and hence is under tension) the deflection $d_{max0}$ is negative, rapidly tending to $-h$. This result implies that a negative temperature rise tends to straighten the beam, as might be expected. When the temperature rise is positive (so the beam is under compression) the deflection rises monotonically as the beam buckles. For values of $W$ above 1μm, the variations differ significantly; however, for values below 1μm they tend to one another. These results generally correspond to the predictions of FEA (points) and experimental measurements.
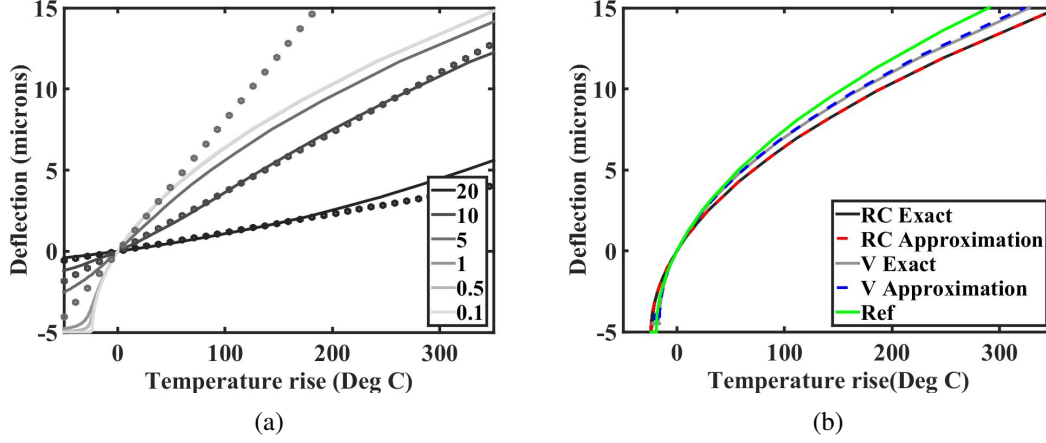
Figure 5.2: (a) Variation of deflection $d_{max0}$ with average temperature rise $\triangle T_{avg}$ for a raised cosine actuator, assuming different values of $W$ in microns (full lines show analytic theory, points show FEA results); (b) Comparison of the exact and approximate variations of $d_{max0}$ with $\triangle T_{avg}$ for a raised cosine (RC) and V-beam actuators (V), assuming $W = 0.1\mu\text{m}$. Also shown are the reference predictions (M. J. Sinclair, "A high force low area mems thermal actuator," in *7th Intersociety Conf. on Thermal and Thermomechanical Phenomena in Electron. Syst. ITHERM 2000.*, Las Vegas, USA, May 2000.)

Although complete, this solution is somewhat unsatisfactory, since it requires numerical evaluation. It would be a considerable advantage to have an analytic solution for $d_{max0}$ in terms of $\triangle T_{avg}$, so that performance could be estimated directly from geometric parameters.

For very slender beams, as $W/L \ll 1$, $\beta \approx 0$. In this case, we may neglect the second term on the RHS of Equation (5.11). This approximation amounts to neglecting the effects of axial compression. In this case, we have:

$$\frac{\triangle L}{L} = \triangle T_{avg}\alpha \tag{5.12}$$

To obtain a suitable solution for $d_{max0}$, we then combine Equation (5.6) and Equation (5.9), to obtain the quadratic:

$$d_{max0}^2 + 2hd_{max0} - \frac{4L^2 \triangle T_{avg}\alpha}{\pi^2} = 0 \tag{5.13}$$

Equation (5.13) has two solutions. Retaining only the positive one, the following expression for the deflection may be obtained:

$$d_{max0} = h\left(\sqrt{1 + \frac{4L^2}{\pi^2 h^2}\triangle T_{avg}\alpha} - 1\right) \tag{5.14}$$

Equation (5.14) is the desired analytic solution. It should be noted that it yields a real re-

sult even when $\triangle T_{avg}$ is negative, until $\triangle T_{avg} = -\frac{\pi^2 h^2}{4\alpha L^2}$. Figure 5.2b compares the exact and approximate variation of the deflection with the average temperature rise for the same parameters as Figure 5.2a, but only the smallest beam width ($W = 0.1 \mu m$, for which $W/L = 10^{-4}$). This agreement is excellent, and the approximate analytic formula tracks the full solution exactly even when the deflection is large. Other curves are superimposed on this figure; these are discussed in the following sections.

We now consider alternative approximation that might be viable for less slender beams, when the axial compression term in Equation (5.11) cannot be neglected. Retaining this term, it is simple to show that:

$$d_{max0}^2 + 2hd_{max0} - \frac{4L^2}{\pi^2}\triangle T_{avg}\alpha + \left(\frac{4W^2}{3}\right)\frac{d_{max0}}{h+d_{max0}} = 0 \qquad (5.15)$$

Equation (5.15) is a cubic function of $d_{max0}$, which clearly has an exact numerical solution. However, focusing again on solutions that yield insight, we now derive an analytic approximation. We simply assume that the solution $d_{max0}$ to this cubic function is close to the earlier quadratic solution and can be written as:

$$d_{max0c} = d_{max0q} + \varepsilon \qquad (5.16)$$

where $d_{max0q}$ is the solution to Equation (5.13) given in Equation (5.14) and $\varepsilon$ is a perturbation. By substituting, it is simple to obtain:

$$2\varepsilon(d_{max0q}+h) + \varepsilon^2 + \left(\frac{4W^2}{3}\right)\frac{d_{max0q}+\varepsilon}{h+d_{max0q}+\varepsilon} = 0 \qquad (5.17)$$

At this point, it might be accurate enough to neglect the term $\varepsilon^2$ and the two $\varepsilon$ terms in the fraction, to get:

$$\varepsilon_1 = -\left(\frac{2W^2}{3}\right)\frac{d_{max0q}}{(h+d_{max0q})^2} \qquad (5.18)$$

Alternatively, by keeping the two $\varepsilon$ terms in the fraction in Equation (5.17), $\varepsilon$ can be obtained as:

$$\varepsilon_2 = -\left(\frac{2W^2}{3}\right)\frac{d_{max0q}}{(d_{max0q}+h)^2 + \left(\frac{2W^2}{3}\right)\frac{h}{d_{max0q}+h}} \qquad (5.19)$$

114

Thus, the effect of axial compression is to reduce the deflection, by an amount that depends on $W$, and (at least for small deflections) $\varepsilon$ is proportional to $d_{max0q}$. Consequently, the initial slope of the deflection characteristic must reduce for wider beams. To illustrate this, we now compare the full solution with the three approximations $A_1$ (Equation (5.14)), $A_2 = A_1 + \varepsilon_1$ (5.18) and $A_3 = A_1 + \varepsilon_2$ (Equation (5.19)) in Figure 5.3. The exact variation for the maximum deflection $d_{max0}$ with temperature change $\triangle T_{avg}$ is shown black and the three approximations $A_1$ (blue), $A_2$ (green) and $A_3$ (red) are shown in colour. The assumed parameters are as before, but the beam width $W$ is increased up to 5μm (so that $W/L = 2 \times 10^{-3}$) to highlight the differences.
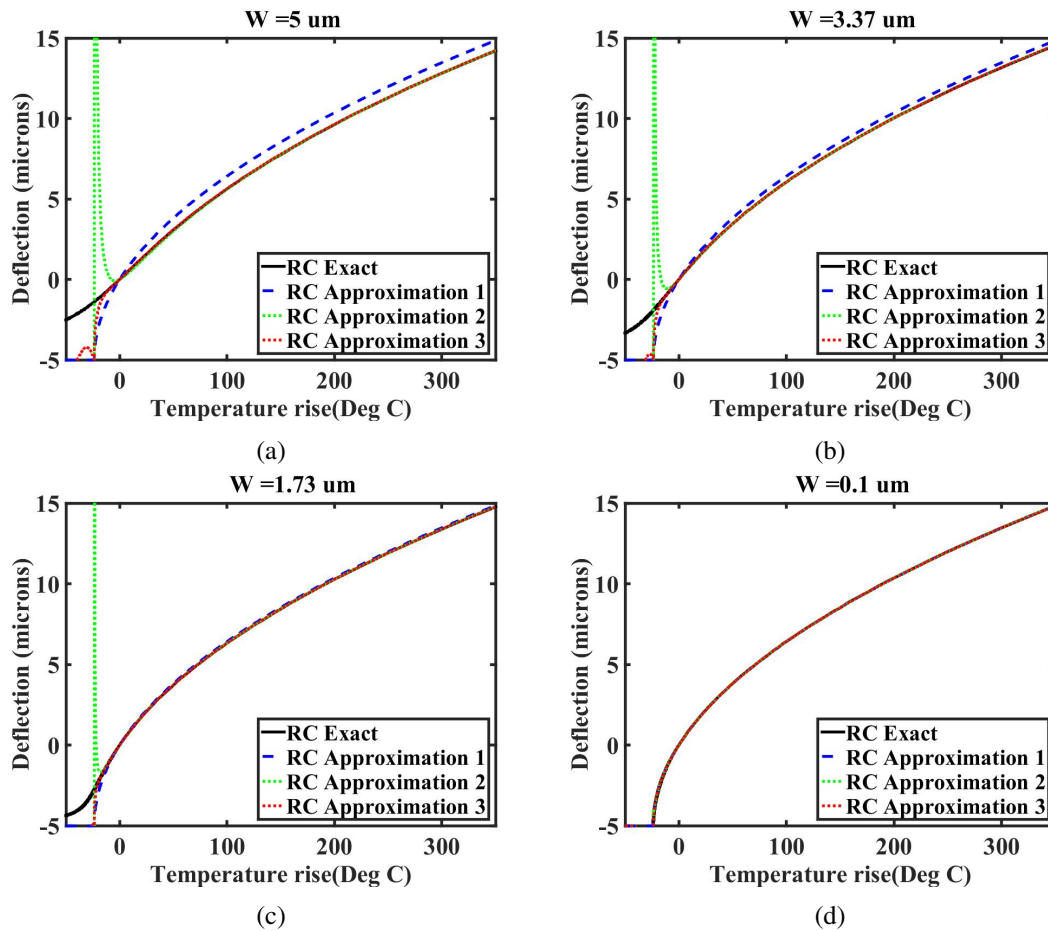


Figure 5.3: Comparison of the exact and three approximate variations of deflection with the average temperature rise for a raised cosine actuators with beam width of (a) 5μm, (b) 3.37μm, (c) 1.73μm and (d) 0.1μm respectively.

The results show that for a temperatures up to 350°C ($W = 0.1$μm), all three approximations agree with the exact solution for very slender beams (Figure 5.3d). As $W$ rises, the simplest approximation $A_1$ becomes increasingly inaccurate. However $A_2$ and $A_3$ are both good matches to the exact solution with $W$ increasing up to 5μm, although both lose efficacy when $d_{max0}$ tends to $-h$. This behaviour is expected from the form of Equation (5.16), but is unimportant for

practical applications when positive temperature rises are norm. The best approximation is $A_3$ for a better performance under negative temperature change compared with $A_2$.

## 5.1.2 Transverse stiffness

We now evaluate the maximum force that can be generated by the raised cosine actuator. We start by considering the case of a structure with an axial force $F_0$ and an additional transverse force $F$ at the midpoint as shown in Figure 5.4. The beam bending equation is Equation (5.2), but the bending moment variation is now:

$$M(x) = M_A - F_0 y + F \frac{x}{2} \qquad\qquad 0 \le x \le \frac{L}{2} \qquad\qquad (5.20)$$

Here $M_A$ is an unknown end-moment. To solve the equations, we substitute $y = y_{00} + u$, yielding:

$$\frac{\mathrm{d}^2 u}{\mathrm{d}x^2} + \frac{F_0}{EI}u = \frac{M_A}{EI} - \frac{F_0}{EI}y_{00} + \frac{F}{2EI}x \qquad\qquad 0 \le x \le \frac{L}{2} \qquad\qquad (5.21)$$
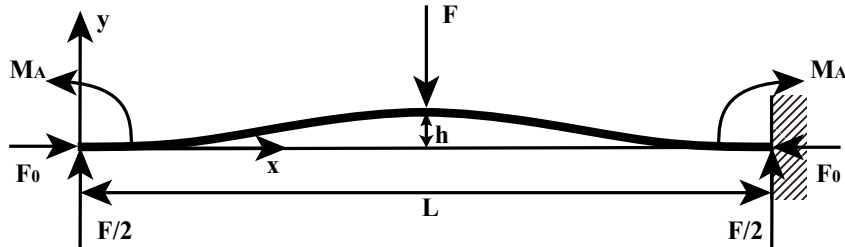


Figure 5.4: A combined loading on a buckling actuator with raised cosine pre-buckle.

Note that the bending moment is a discontinuous function. Thus the bending must be analysed in two separate parts. However, since the structure is symmetric, it should be sufficient to assume a symmetric deflection, satisfying the boundary conditions in the left-hand half of the structure alone.

Equation (5.21) can again be solved in terms of a sum of CF and PI again. By applying the

boundary conditions, namely:

$$
\left.\begin{array}{ll}
① & u(0) = 0 \\[2mm]
② & \dfrac{\mathrm{d}u(x)}{\mathrm{d}x}\bigg|_{x=0} = 0 \\[2mm]
③ & \dfrac{\mathrm{d}u(x)}{\mathrm{d}x}\bigg|_{x=L/2} = 0
\end{array}\right\} \quad \text{Boundary conditions} \tag{5.22}
$$

the result is:

$$
u = \left(\frac{F}{EI}\right)\left(\frac{1}{2k^3}\right)\{kx - \sin(kx) + G[\cos(kx) - 1]\} + u_0 \tag{5.23}
$$

And the deflected beam shape is $y = u + y_{00}$. The midpoint deflection is then:

$$
d_{max} = u\left(\frac{L}{2}\right) = \left(\frac{F}{EI}\right)\left(\frac{1}{2k^3}\right)\left(\frac{kL}{2} - 2G\right) + d_{max0} \tag{5.24}
$$

Clearly the first term above is due to the transverse load, while the second term is due to the axial compression. Note that the value of $k$ is not fixed, but will change when the transverse force $F$ is applied. To find out how it change, we must examine the strain compatibility condition (Equation (5.10)). However, for very slender beams, we may again neglect the term $\frac{F_0}{EWD}$ on the LHS.

Calculation of $\frac{\triangle L}{L}$ follows the method previously used. Using the deflected shape in Equation (5.23). Also, from the strain compatibility condition, we must again have $\frac{\triangle L}{L} = \triangle T_{avg}\alpha$. However, the temperature has not changed, so that:

$$
\frac{\triangle L_0}{L} = \frac{\triangle L}{L} = \triangle A + \triangle B + \triangle C \tag{5.25}
$$

where $\triangle A$, $\triangle B$ and $\triangle C$ are three separate terms composing the calculated results of $\frac{\triangle L}{L}$.

Unfortunately, evaluation of Equation (5.25) is likely to be very difficult, unless we make appropriate approximations. If $kL$ is small, we can expand the results as power series, giving:

$$
\triangle A = -\pi^2 h^2 \frac{768k^2}{(4\pi^2 - k^2 L^2)^3} \tag{5.26}
$$

$$
\triangle B = \pi^2 h^2 \frac{k^2(8\pi^2 - k^2 L^2)}{4(4\pi^2 - k^2 L^2)^2} \tag{5.27}
$$

$$
\triangle C = h^2 \frac{12k^4 L^2}{5(4\pi^2 - k^2 L^2)^2} \tag{5.28}
$$

$$
\tag{5.29}
$$

Re-arranging, we then get:

$$\frac{\triangle L}{L} = \pi^2 h^2 \frac{k^2}{4(4\pi^2 - k^2 L^2)^3} \left[ \left(1 - \frac{48}{5\pi^2}\right) k^4 L^4 + \left(\frac{192}{5} - 12\pi^2\right) k^2 L^2 + (32\pi^4 - 3072) \right]$$

(5.30)

This yields the value of $\frac{\triangle L}{L}$ needed in Equation (5.9). Substituting, we get:

$$\frac{k^2}{k_0^2} = \left(\frac{4\pi^2 - k^2 L^2}{4\pi^2 - k_0^2 L^2}\right)^3 \frac{k_0^4 L^4 - 12\pi^2 k_0^2 L^2 + 32\pi^4}{\left(1 - \frac{48}{5\pi^2}\right) k^4 L^4 + \left(\frac{192}{5} - 12\pi^2\right) k^2 L^2 + (32\pi^4 - 3072)}$$

(5.31)

When both $k_0 L$ and $kL$ are small, we get:

$$\frac{k^2}{k_0^2} \approx \frac{32\pi^4}{32\pi^4 - 3072} = \frac{1}{1 - \frac{96}{\pi^4}} \approx 69.13$$

(5.32)

The stiffness of the actuator is defined as the force needed to return the transverse deflection to zero. Clearly, the deflection $d_{max}$ in Equation (5.24) can be eliminated if:

$$F = \frac{4k^5 h L^2}{(4G - kL)(4\pi^2 - k^2 L^2)} EI$$

(5.33)

To evaluate the stiffness, the results above now need to be related to the deflection $d_{max0}$ in Equation (5.6). Combining the necessary results we obtain:

$$k_T = \frac{F}{d_{max0}} = f\left(\frac{EI}{L^3}\right)$$

(5.34)

where,

$$f = \frac{k^2}{k_0^2} \cdot \frac{4k^3 L^3}{4G - kL} \cdot \frac{4\pi^2 - k_0^2 L^2}{4\pi^2 - k^2 L^2}$$

(5.35)

When $k_0 L$ and $kL$ are small, we can expand $G$ as a power series, to get $f \approx \frac{k^2}{k_0^2} \times 192$. Consequently, the stiffness of the actuator is:

$$k_T = f\left(\frac{EI}{L^3}\right) \approx 69.13 \times 192 \left(\frac{EI}{L^3}\right)$$
$$\approx 1.33 \times 10^4 \left(\frac{EI}{L^3}\right)$$

(5.36)

The term $192\left(\frac{EI}{L^3}\right)$ is the transverse stiffness of a centrally loaded built-in beam. The action of shaping the beam and adding an axial restraint at either end therefore raises the stiffness by considerable amount, the factor $\frac{1}{1 - \frac{96}{\pi^4}} \approx 69.13$ previously found.

The results above are valid only for small $kL$. For comparison, we need an accurate calculation. Earlier work suggests that we must perform two calculations, firstly with axial force alone (to find the transverse displacement caused by buckling), and secondly with both axial force and transverse force (to find the transverse force needed to restore the transverse displacement to zero).

Clearly, all that is needed are values for $k_0L$ and $kL$, which should satisfy the strain compatibility condition Equation (5.25). A MATLAB program was written to implement the above algorithm, using Newton's method to find $kL$ for 100 values of $k_0L$ between 0 and $2\pi$. Convergence is easily achievable, even when $k_0L$ approaches $2\pi$, and the relative error is less than $10^{-8}$.

Using these values, the deflected beam shapes can be found. Figure 5.5 shows typical shapes, for $k_0L = 0\pi$, $0.39\pi$, $0.79\pi$, $1.18\pi$, $1.57\pi$ and $1.96\pi$. The black line shows the original beam shape, a raised cosine peaking at $y_{00} = h$. The blue line shows the shape after applying the axial load. Once again, this is a raised cosine, but with a much larger peak amplitude. The red line shows the shape after applying a transverse force $F_T$ to return the beam to its initial position at the midpoint. Clearly the final shape now incorporates higher order buckling modes. However, it appears to satisfy all the boundary conditions (position and slope at $x = 0$ and $x = \frac{L}{2}$) correctly.
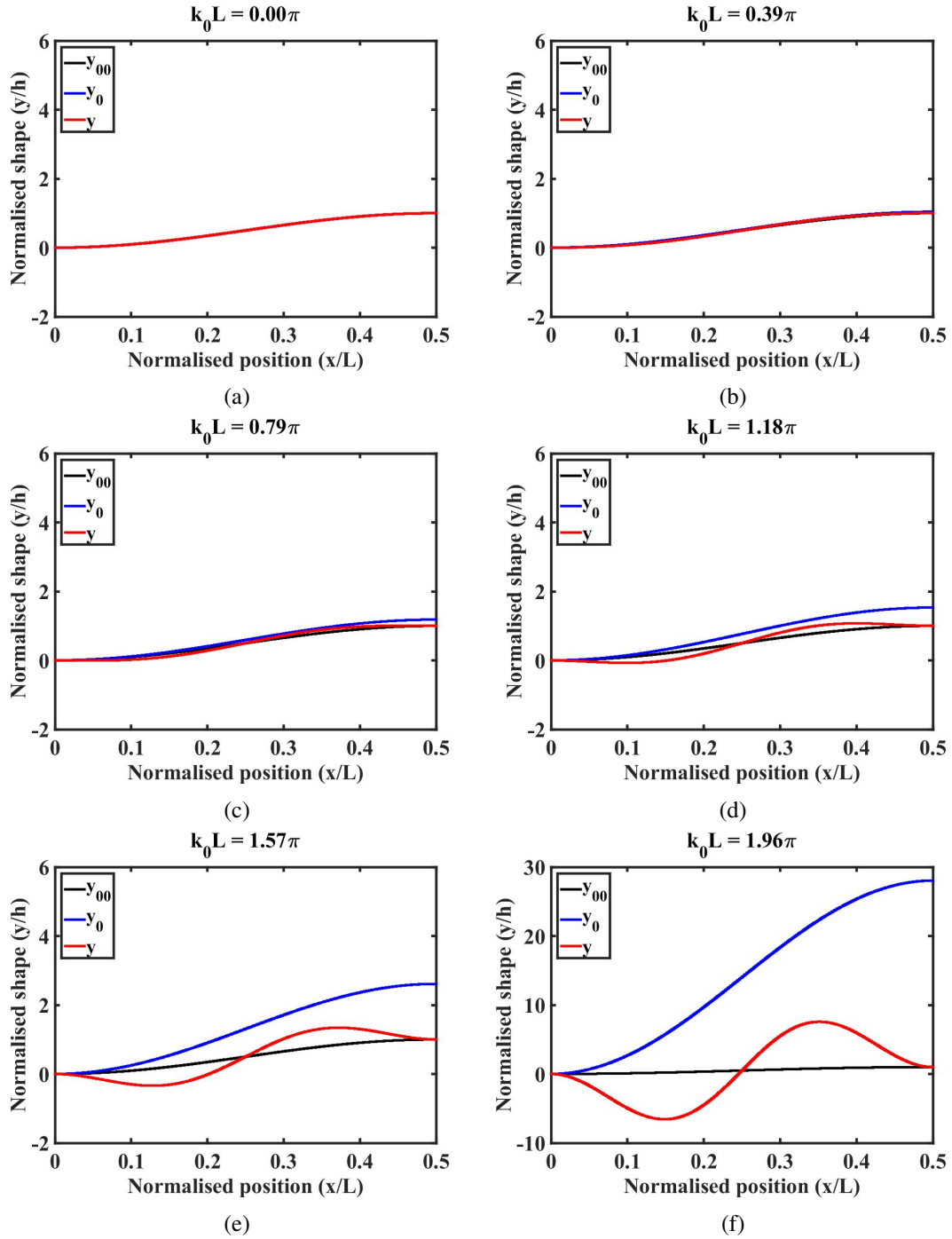
Figure 5.5: Variations of $y_{00}/h$, $y_0/h$, $y/h$ with $x/L$, for $k_0L = 0\pi$, $0.39\pi$, $0.79\pi$, $1.18\pi$, $1.57\pi$ and $1.96\pi$.

A second MATLAB program was used to compare results for the transverse stiffness. Newton' method was again used to find $kL$ values for each $k_0L$ based on Equation (5.25). Figure 5.6 shows the variation of the accurate and approximate scaling factors with $k_0L$. The black line shows the accurate scaling factor (Equation (5.35)), while the blue line shows the approximate factor (Equation (5.36)). The largest value ($1.33 \times 10^4$) is obtained when $k_0L$ tends to zero. This

is in good agreement with the approximate theory, and implies that the transverse stiffness is very high at low deflections (approximately 69 times that of a centrally loaded built-in beam). However, the value falls rapidly as $k_0L$ increases, implying that this increase is quickly lost. Furthermore, the approximate theory is only valid over a very restricted range (for $k_0L$ up to $0.5\pi$), since the addition of a transverse load must increase the axial load.
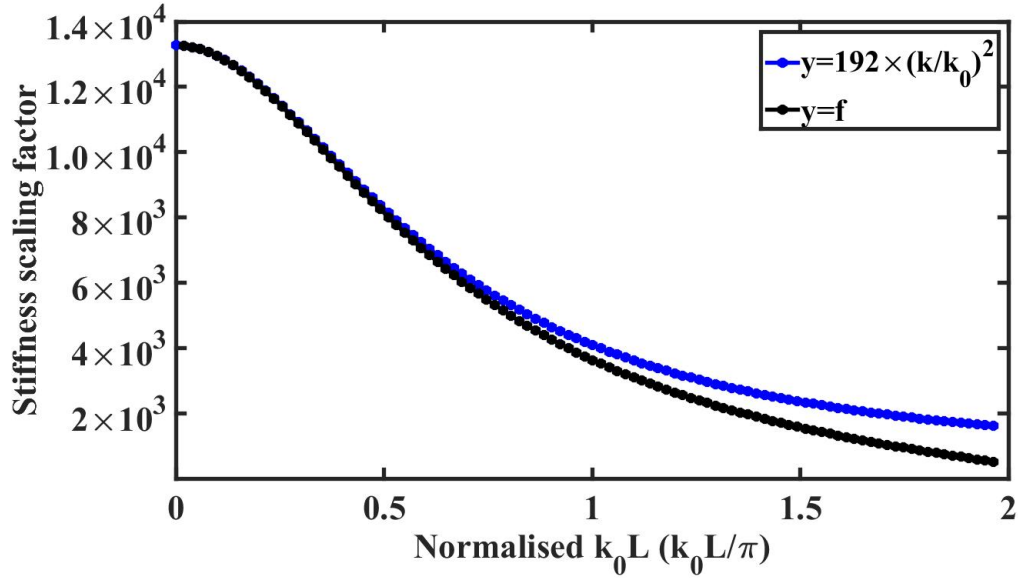


Figure 5.6: Variations of stiffness scaling factor with $k_0L/\pi$.

## 5.2 Buckling actuator with chevron pre-buckle

We now repeat the analysis for the V-beam actuator shown in Figure 5.1(c). The beam has length $L$ and tilt angle $\theta$, so the central offset is $h = \frac{L}{2}\tan\theta$. As before, the beam cross-section has in-plane width $W$ and depth $D$. The initial beam shape $y_{00}(x)$ is described by the static variation:

$$\begin{cases} y_{00}(x) = \dfrac{h}{2}\tan\theta \cdot x & 0 \le x \le \dfrac{L}{2} \\ y_{00}(x) = \dfrac{h}{2}\tan\theta \cdot (L-x) & 0 \le x \le \dfrac{L}{2} \end{cases} \tag{5.37}$$

### 5.2.1 Analytic model

Buckling is again achieved by applying an axial force $F_0$. Since $y_{00}$ is a linear function of $x$ when $0 \le x \le \frac{L}{2}$, Equation (5.2) can be written in the form:

$$\frac{d^2 y_0}{dx^2} + \frac{F_0}{EI}y_0 = \frac{M_A}{EI} \tag{5.38}$$

121

Here $M_A$ is an unknown moment, $I = \frac{DW^3}{12}$ is the second moment of area, and $E$ is Young's modulus.

The boundary conditions are:

$$
\left.\begin{array}{ll}
\textcircled{1} & y_0(0) = 0 \\[2mm]
\textcircled{2} & \left.\dfrac{\mathrm{d}y_0(x)}{\mathrm{d}x}\right|_{x=0} = \tan\theta \\[2mm]
\textcircled{3} & \left.\dfrac{\mathrm{d}y_0(x)}{\mathrm{d}x}\right|_{x=L/2} = \tan\theta
\end{array}\right\} \quad \text{Boundary conditions} \quad (5.39)
$$

Using the PI and CF method, the general solution of the deflected beam shape can be found as [34]:

$$
y_0(x) = \frac{\tan\theta}{k_0}\left\{ \sin(k_0 x) + \tan\left(\frac{k_0 L}{4}\right)[1 - \cos(k_0 x)] \right\} \tag{5.40}
$$

This result implies that the beam changes shape significantly as it deflects in contrast to the raised cosine actuator. The maximum deflection is:

$$
d_{max0} = \frac{2\tan\theta}{k_0}\tan\left(\frac{k_0 L}{4}\right) - \left(\frac{L}{2}\right)\tan\theta \tag{5.41}
$$

Similar to the analysis in the case of raised cosine beam, Equation (5.41) can be easily evaluated as a function of $k_0 L$.

Integrating the deflected beam shape again following the method previous used, the fractional change in length $\frac{\triangle L}{L}$ can be found by calculating the difference from the horizontal length $\delta L$ and the corresponding value $\delta L_0$ in the unloaded case. The result is:

$$
\frac{\triangle L}{L} = \frac{\tan^2\theta}{4k_0 L}\left\{ 2G[1 - \cos(k_0 L)] + (1 - G^2)[\sin(k_0 L) - k_0 L] \right\} \tag{5.42}
$$

where $G = \tan\left(\frac{k_0 L}{4}\right)$ and $\delta L_0 = \frac{L}{2}\tan^2\theta$.

These results then allow $\triangle T_{avg}$ to be found as a function of $k_0 L$ as before, and consequently, $d_{max0}$ may be plotted in terms of $\triangle T_{avg}$. Assumption of the same parameters as those used for Figure 5.2a yields remarkably similar results, suggesting that the overall deflection in a V-beam actuator is dominated by excitation of the lowest-order buckling mode.

As before, we now explore possible approximations to the above that might yield a closed-form solution. A similar approach - relating $d_{max0}$ to $\frac{\triangle L}{L}$ and then solving an approximate compatibility equation - should work. However, this time, there are difficulties caused by the

trigonometric functions in (5.41) and (5.42). These can be circumvented using power series approximations. We first make the substitution $\lambda = \frac{k_0 L}{4}$. Considering two functions $f(\lambda)$ and $g(\lambda)$, Equation (5.41) and Equation (5.42)can be written as:

$$\frac{d_{max0}}{L} = f(\lambda)\tan\theta$$
$$f(\lambda) = \frac{1}{2\lambda}[\tan\lambda - \lambda] \tag{5.43}$$

$$\frac{\triangle L}{L} = g(\lambda)\tan^2\theta$$
$$g(\lambda) = \frac{1}{4\lambda}\left\{\tan\lambda - \lambda[1 - \tan^2\lambda]\right\} \tag{5.44}$$

Since $\tan(x)$ can be expanded as a power series as $\tan x = x + \frac{1}{3}x^3 + \frac{2}{15}x^5 + \cdots$, we can now obtain a power series for $f(\lambda)$ valid to order $\lambda^4$, as:

$$f_1(\lambda) \approx \frac{1}{2}\left(\frac{1}{3}\lambda^2 + \frac{2}{15}\lambda^4\right) \tag{5.45}$$

Similarly, we can obtain a power series for $g(\lambda)$ as:

$$g_1(\lambda) = \frac{1}{3}\lambda^2 + \frac{3}{15}\lambda^4 \tag{5.46}$$

In Figure 5.7, we compare the variations of $f_1$ and $f$ with $k_0 L$ (Figure 5.7a), and $g_1$ and $g$ with $k_0 L$ (Figure 5.7b). The approximations are quite reasonable up to $k_0 L = \pi$, but clearly cannot predict the exact variations beyond this when both $f$ and $g$ tend to infinity.

Despite this, by combining Equation (5.45) and (5.46), we can now write $g$ in terms of $f$ as:

$$g_2(\lambda) = 2f(\lambda) + \frac{12}{5}f^2(\lambda) \tag{5.47}$$

In Figure 5.7c, we compare the variation of the functions $g_2$ and $g$ with $k_0 L$. This time, despite the obvious inaccuracy in the functions $f_1$ and $g_1$, $g_2$ appears to be accurate even for values of $k_0 L$ approaching $2\pi$. A possible explanation is that the errors in the two expansions of power series have cancelled out.
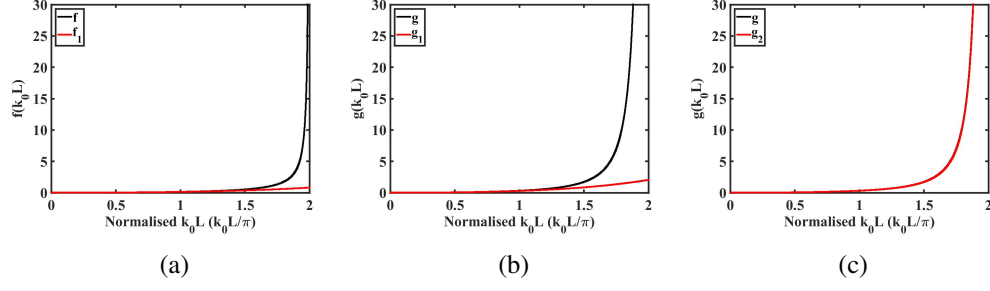
Figure 5.7: Comparison of functions (a) $f$ (blue) and $f_1$ (red); (b) $g$ (blue) and $g_1$ (red); (c)$g$ (blue) and $g_2$ (red).

Generally, we would prefer to have $f$ expressed in terms of $g$. Rearranging Equation (5.47), we get a standard quadratic equation which clearly has two roots; retaining only the positive root, we obtain:

$$f = \frac{5}{12} \left( \sqrt{1 + \frac{12}{5}g} - 1 \right) \tag{5.48}$$

Noting our original definitions of $f$ and $g$, we can then obtain an analytic expression for the midpoint deflection $d_{max0}$ as:

$$d_{max0} = \frac{5L\tan\theta}{12} \left[ \sqrt{1 + \frac{12}{5\tan^2\theta} \cdot \frac{\triangle L}{L}} - 1 \right] \tag{5.49}$$

Neglecting the second term on the LHS of Equation (5.10) as before (assuming a very slender beam), we then have $\frac{\triangle L}{L} = \triangle T_{avg}\alpha$. Thus:

$$d_{max0} = \frac{5L\tan\theta}{12} \left[ \sqrt{1 + \frac{12}{5\tan^2\theta} \triangle T_{avg}\alpha} - 1 \right] \tag{5.50}$$

This result can of course be written in the alternative form:

$$d_{max0} = \frac{5h}{6} \left[ \sqrt{1 + \frac{3L^2}{5h^2} \triangle T_{avg}\alpha} - 1 \right] \tag{5.51}$$

This result is the desired analytic expression for $d_{max0}$ in terms of $\triangle T_{avg}$. Note that $d_{max0}$ is only a function of the beam length $L$, central offset $h$ (namely angle $\theta$), and the average temperature change $\triangle T_{avg}$; the other beam parameters such as $W$ and $D$ have disappeared.

Compared with previous results, the performances of the two actuators are very similar. Clearly, the analytic expressions Equation (5.14) and (5.51) can both be written in the form

$d_{max0} = A\sqrt{1 + B\triangle T_{avg}} - 1$. Consequently, the initial sensitivity of deflection to temperature change $S = \frac{\mathrm{d}d_{max0}}{\mathrm{d}\triangle T_{avg}}\Big|_0$ is $S = \frac{1}{2}AB$. We can then obtain the sensitivities $S_V$ and $S_{RC}$ of the two types of actuator, as:

$$S_{RC} = \frac{2}{\pi^2}\left(\alpha\frac{L^2}{h}\right)$$
$$S_V = \frac{1}{4}\left(\alpha\frac{L^2}{h}\right)$$
(5.52)

Thus, the sensitivity is always proportional to $L^2$ and inversely proportional to $h$; for a common geometry, the ratio $\frac{S_v}{S_{RC}} = \frac{\pi^2}{8} \approx 1.2337$.

If $\theta$ is very small, we can approximate the results in Equation (5.50) further as:

$$d_{max0} = L\sqrt{\frac{5\triangle T_{avg}\alpha}{12}}$$
(5.53)

In these circumstances, the deflection is only a function of the beam length and the temperature rise.

To evaluate the approximations, we assume the same numerical parameters as before. Figure 5.8 shows the variation of midpoint deflection with average temperature change predicted by the exact model (black), and the approximation (red) in Equation (5.50) for beam width $W$ ranging from 0.1μm to 5μm. The results are very similar to those obtained in the raised cosine case earlier. For $W$ up to about 1.5μm, the agreement between the exact and approximate model is good, even for large deflections. The approximation then loses its efficacy as $W$ increases further.
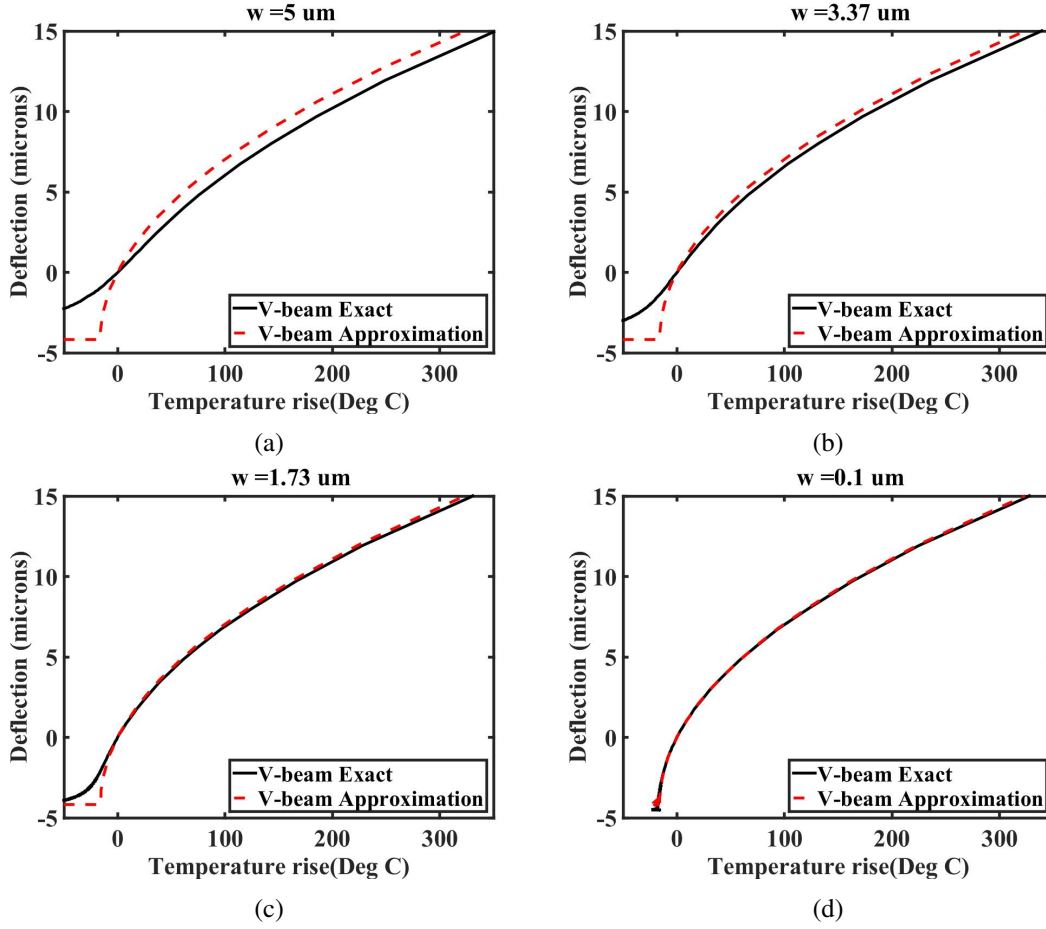
Figure 5.8: V-beam actuator deflection comparison between analytic model (black) and approximation (red) for beam width of (a) 5μm, (b) 3.37μm, (c) 1.73μm and (d) 0.1μm respectively.

Equation (5.51) is clearly analogous to the similar Equation (5.14) for the raised cosine prebuckle. Its predictions are shown superimposed on the earlier Figure 5.2b for the same parameters as before, together with the exact solution (for $W = 0.1$μm). Once again there is good agreement between the exact and approximate models, despite the apparent inaccuracy of the functions $f$ and $g$. In fact, we have constructed higher-order approximations to both these functions, and find that Equation (5.47) is generally an excellent approximation despite the addition of extra terms in the power series. However, the V-beam actuator gives a slightly larger deflection for a given temperature rise.

We now compare the results above with the well-known formula for the deflection of a V-beam actuator in [33] which simply considers the two beam sections to remain straight but increase in length by an amount $\triangle L_h$ due to thermal expansion:

$$d_{max0} = \sqrt{L_h^2 + 2L_h \triangle L_h - L_h^2 \cos^2 \theta} - L_h \sin \theta \tag{5.54}$$

126

Where $L_h = \frac{L}{2}$. Re-arranging, and substituting $h$ for $L_h \cdot \tan\theta$ and $\triangle T_{avg}\alpha$ for $\frac{\triangle L_h}{L_h}$, we get:

$$d_{max0} = h \left[ \sqrt{1 + \frac{L^2}{2h^2}\triangle T_{avg}\alpha} - 1 \right] \tag{5.55}$$

Equation (5.55) clearly has a similar form to our new expressions for raised cosine and V-beam actuators. Its predictions are also superimposed on the earlier Figure 5.2b. It is clearly a worse approximation than Equation (5.51); however, its prediction is remarkable considering the crudity of the model.

Figure 5.9 shows the variation of the deflection with average temperature change for different beam angles, as predicted by the analytic model (full lines) and Equation (5.53) (points). The variation clearly tends to the limit predicted by Equation (5.53) when $\theta$ decreases.
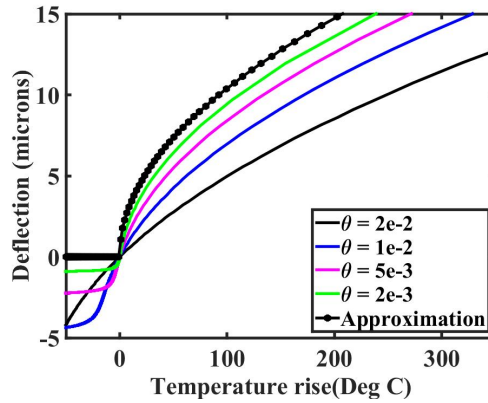


Figure 5.9: Variation of a V-beam actuator deflection with average temperature change for different beam angles $\theta$, as predicted by the analytic model (full lines) and Equation (5.53) (points).

We now consider briefly the additional effect of intrinsic stress, which can arise in many processes used for depositing the mechanical layers in MEMS and NEMS. The analysis starts with the strain compatibility condition in Equation (5.10). The effect of tensile intrinsic stress $\sigma_{int}$ is to insert an axial strain term $-\frac{\sigma_{int}}{E}$, so that $\triangle T_{avg}\alpha$ can be replaced with $\triangle T_{avg}\alpha - \frac{\sigma_{int}}{E}$ in any subsequent expression. The effect of intrinsic stress is therefore to shift deflection characteristics of the form presented here to the right. If deflection measurements are then made from the rest position, the general effect will be to reduce the apparent deflection.

Finally, we consider the relation between average temperature and power, which is of course well-known (see e.g. [132] [133]). Assuming that the beam is heated along its length by a power $P$, and cooled by conduction through the solid, the steady state temperature rise $\triangle T(x)$ is the

solution to heat conduction equation:

$$k_{th}WD\frac{d^2 \triangle T}{dx^2} + \frac{P}{L} = 0 \qquad (5.56)$$

Here $k_{th}$ is the thermal conductivity of the beam material. Hence,

$$P = -k_{th}WDL\frac{d^2 \triangle T}{dx^2} \qquad (5.57)$$

Now the solution to the ordinary differential equation Equation (5.56) subject to the boundary conditions of

$$\left.\begin{array}{ll} ① & \triangle T(0) = 0 \\[2mm] ② & \triangle T(L) = 0 \end{array}\right\} \quad \text{Boundary conditions} \qquad (5.58)$$

is

$$\triangle T = 4 \triangle T_{max}\frac{xL - x^2}{L^2} \qquad (5.59)$$

Here $\triangle T_{max}$ is the temperature at $x = \frac{L}{2}$. Differentiating, we obtain:

$$\triangle T_{max} = \frac{PL}{8k_{th}WD} \qquad (5.60)$$

The peak temperature change $\triangle T_{max}$ and the drive power $P$ are therefore linearly proportional to each other.

The average temperature rise may then be found by integration as:

$$\triangle T_{avg} = \frac{1}{L}\int_0^L \triangle T(x)\,dx = \frac{2}{3}\triangle T_{max} \qquad (5.61)$$

So that $\triangle T_{avg}$ is related to the drive power by:

$$P = \triangle T_{avg} \cdot \frac{12k_{th}WD}{L} \qquad (5.62)$$

All the previous expressions for deflection may be converted into variations with power by making this substitution. For an actuator with $N$ beams, the total drive power is simply $P_T = NP$. If other forms of cooling such as convection occur, a higher power will be required to achieve

the same average temperature. This effect can be modelled by writing:

$$P_T = \beta N P \tag{5.63}$$

where $\beta > 1$ is a factor that models thermal inefficiency (the higher the value of $\beta$, the greater the cooling effect should be). We cannot easily calculate $\beta$, but because the cross-sections of NEMS beams are so small and their surface area is so large, we might expect its value to be quite large.

We now compare the predictions of our V-beam actuator model with our previous experimental results for a BSOI NEMS actuator. To begin with, the following model parameters are assumed: $N = 58, W = 110 \times 10^{-9}\text{m}, D = 5 \times 10^{-6}\text{m}, L = 1 \times 10^{-3}\text{m}, \theta = 0.01\text{rad}, \alpha = 2.6 \times 10^{-6}\text{K}^{-1}, E = 170 \times 10^{9}\text{N/m}^2, k_{th} = 130\text{W} \cdot \text{m}^{-1} \cdot \text{K}^{-1}, \rho = 2330\text{kg m}^{-3}$.

Model predictions (full lines) are compared with experimental data (points) in Figure 5.10. Figure 5.10a shows results obtained with the thermal inefficiency term set to $\beta = 1$. Clearly, the theory predicts much larger displacements than are observed experimentally. The initial slope of the characteristic can be better predicted by assuming an increased value of $\beta$. For example, Figure 5.10b shows the results obtained with $\beta = 6$. However, the model still cannot predict the experimental displacement at large power, but if $\beta$ is increased further, the agreement becomes much worse at low power. Much better agreement overall is obtained when a tensile residual stress of $\sigma_{int} = 8 \times 10^6\text{N/m}^2$ is combined with a $\beta$ value of 22, as shown in 5.10c. This figure also shows the result obtained when $\sigma_{int} = 0\text{N/m}^2$ and $\beta = 22$. The residual stress seems consistent with experimental observation, and the large value of $\beta$ implies that cooling is dominated by effects other than solid conduction.
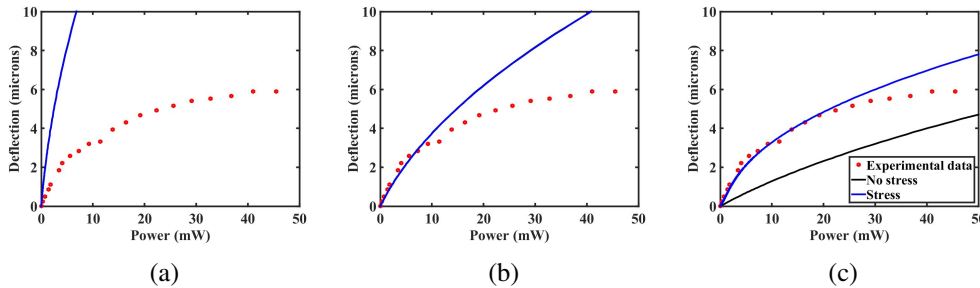


Figure 5.10: Comparison of deflection between analytic model and experimental data with assumption of (a) $\beta = 1$, $\sigma_{int} = 0\text{N/m}^2$; (b) $\beta = 6$, $\sigma_{int} = 0\text{N/m}^2$; c) $\beta = 22$, $\sigma_{int} = 8 \times 10^6\text{N/m}^2$ (blue) and 0 (black).

## 5.2.2 Transverse stiffness

As before, we now evaluate the force and stiffness of a V-beam actuator. The stiffness can again be estimated from the transverse force needed to eliminate the deflection caused by actuation. We consider the case of a V-beam with an axial force $F_0$ and a transverse force $F$ at the midpoint as shown in Figure 5.11a.
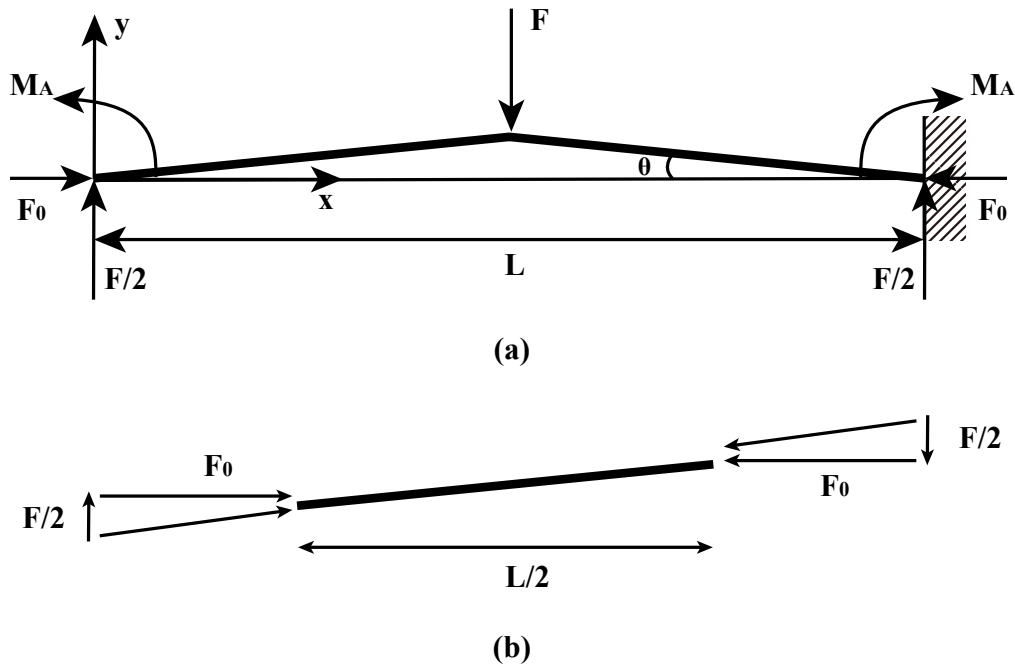


Figure 5.11: (a) A V-beam actuator actuator with combined loading; (b) force involved when there is no bending for a V-beam structure.

The beam bending equation and bending moment are defined in Equations (5.2) and (5.20). Since the V-beam is symmetric, it should be sufficient to assume a symmetric deflection. Hence, we must solve:

$$\frac{\mathrm{d}^2 y}{\mathrm{d}x^2} + \frac{F_0}{EI} y = \frac{M_A}{EI} + \frac{F}{2EI} x \qquad 0 \leq x \leq \frac{L}{2} \tag{5.64}$$

With the boundary conditions as:

$$
\left.
\begin{array}{ll}
① & y(0) = 0 \\[2mm]
② & \dfrac{dy(x)}{dx}\bigg|_{x=0} = \tan\theta \\[2mm]
③ & \dfrac{dy(x)}{dx}\bigg|_{x=L/2} = \tan\theta
\end{array}
\right\} \quad \text{Boundary conditions} \qquad (5.65)
$$

Using the PI and CF method, the solution of Equation (5.64)for the deflected beam shape is:

$$
y(x) = \frac{1}{k}\left(\tan\theta - \frac{F}{2F_0}\right)\left\{\sin(kx) + \tan\left(\frac{kL}{4}\right)[1 - \cos(kx)]\right\} + \frac{F}{2F_0}x \qquad (5.66)
$$

And the midpoint deflection $d_{max}$ is:

$$
d_{max} = \left(\tan\theta - \frac{F}{2F_0}\right)\left[\frac{2}{k}\tan\left(\frac{kL}{4}\right) - \frac{L}{2}\right] \qquad (5.67)
$$

The stiffness of the actuator is defined as the force needed to return the transverse deflection to zero. Clearly, according to Equation (5.67), $d_{max}$ can be reduced to zero if

$$
F = 2F_0\tan\theta \qquad (5.68)
$$

At this point, the end moment $M_A$ is zero, and the vector sum of the forces at either end of each half-beam must yield a force that is entirely axial, as shown in Figure 5.11b, so there can be no bending. The net axial force $F_{axial}$ must equal the axial force induced by constrained thermal expansion as:

$$
F_{axial} = F_0\sqrt{1 + \tan^2\theta} = \triangle T_{avg}\alpha EWD \qquad (5.69)
$$

Substituting $F_0$ back to Equation (5.68), the transverse force $F$ needed to reduce the deflection to zero is:

$$
F = 2\triangle T_{avg}\alpha EWD\sin\theta \qquad (5.70)
$$

To evaluate the transverse stiffness, the results must now be related to the deflection $d_{max0}$ without a transverse load $F$. Provided that bending dominates over axial compression in the

strain compatibility condition, we can write $\frac{\triangle L}{L} = \triangle T_{avg}\alpha$. Since the temperature has not changed, the previous analysis of $\frac{\triangle L_0}{L}$ is still valid. Simplifying Equation (5.42) and expanding $\triangle L$ as a power series, we then get:

$$
\begin{aligned}
\frac{\triangle L}{L} = \frac{\triangle L_0}{L} &= \triangle T_{avg}\alpha \\
&\approx \tan^2\theta \left[ \frac{k_0^2 L^2}{48} + \frac{k_0^4 L^4}{1280} \right]
\end{aligned}
\tag{5.71}
$$

Retaining only the first term, we have:

$$
k_0^2 L^2 = \frac{48\triangle T_{avg}\alpha}{\tan^2\theta}
\tag{5.72}
$$

We can also make a power series approximation for $d_{max0}$ based on Equation (5.41) as:

$$
d_{max0} \approx \tan\theta \frac{k_0^2 L^3}{96} = \frac{\triangle T_{avg}\alpha L}{2\tan\theta}
\tag{5.73}
$$

By combining $d_{max0}$ (Equation (5.73)) and $F$ (Equation (5.70)), the transverse stiffness of the V-beam actuator can be found as:

$$
k_T = \frac{F}{d_{max0}} = \frac{4EWD}{L}\sin\theta\tan\theta \approx \frac{4EWD}{L}\sin^2\theta
\tag{5.74}
$$

This result corresponds well to an expression derived using the complementary energy method in [34].

## 5.3 Conclusion

In this chapter, the analytic approximations to the results of Euler theory have been presented which allow the response of buckling-mode electrothermal actuators to be obtained in closed form for the first time. Similar deflection characteristics are obtained for actuators with raised cosine and chevron pre-buckles, suggesting that deflection is dominated by excitation of the lowest order buckling mode. For both types of actuators, the transverse stiffness is also evaluated with the analytic model built, to estimate the maximum force that can be generated. The approximations made are valid for actuators with slender beams, when the effects of bending dominate over those of axial compression. However, we have compared the approximations with nu-

merical solutions and shown them to be surprisingly accurate, and have presented higher-order corrections for less slender beams. These results should be useful in future designs of buckling actuators.

# 6 Multi-layer STL for NEMS

In this chapter, a multi-layer sidewall transfer lithography (STL) process is introduced and presented based on fabrication results of a collection of mechanical NEMS devices with different structures. This process is an extension of the single-layer STL with three pattern transfer steps, each only requiring optical lithography, making the method suitable for low-cost, wafer scale fabrication. However, the main advantage now is to allow nanostructures intersecting with each other, breaking an important restriction of the single-layer STL.

Process concept and design for the multi-layer STL are introduced in Section 6.1 with illustrated principles. In Section 6.2, pattern transfer and fabrication results obtained in different process stages are demonstrated. A number of devices with variable functions are then presented with fabrication results based on the introduced process in Section 6.3. In Section 6.4, typical processing issues encountered in the multi-layer process are discussed and analysed, possible improvements are suggested compared with the single-layer process. In the end, a conclusion is draw n in Section 6.5.

## 6.1 Process concept and design

As introduced previously, the sidewall transfer lithography is a set of process that can transform the perimeter of a microscale feature into nanoscale only with facilities and techniques needed for conventional lithography, making the method suitable for low-cost, wafer scale fabrication. The general approach is to coat an etched mesa with a conformal layer of material that may be selectively removed from horizontal surfaces, leaving the vertical surfaces to provide a mask whose width is determined by the coating thickness. Conventional lithography is used to add microscale features such as the anchors, and the combined pattern is transferred into silicon using DRIE. Suspended parts are then freed by etching of a sacrificial oxide interlayer. As stated in Chapter 3 and 4, two kinds of typical electrothermal actuators have been designed, fabricated and tested based on such process. In each case, the nanoscale features are generally

one-dimensional.

Although such processes are potentially attractive for mass production of NEMS, they suffer from key topological constraints, and overcoming these limitations should extend the range of applications. For example, additional patterning steps can be easily added to the single-layer STL process to interrupt the polygons to generate more complex designs. Here, a multi-layer STL process is developed which provides intersecting nanoscale features. The three-layer process involves two STL steps to form the nanoscale suspensions in addition to one conventional lithography to form the microscale parts [134].

Figure 6.1 shows the design of an example two-axis electrothermal stage based on the multi-layer STL process. The central stage is actuated in two directions (X and Y) by two chevron-shaped double-ended actuators in each. The layer 1 and 2 STL steps produce nanoscale features in two directions separately, allowing them to intersect with each other. The layer 3 optical lithography step is then used to add microscale patterns of anchors and central stage. This structure represents a useful target, since it contains regions where two of the STL patterns must overlay (A), regions where each STL pattern overlays a conventional pattern (B) and a region where all three layers are present (C).
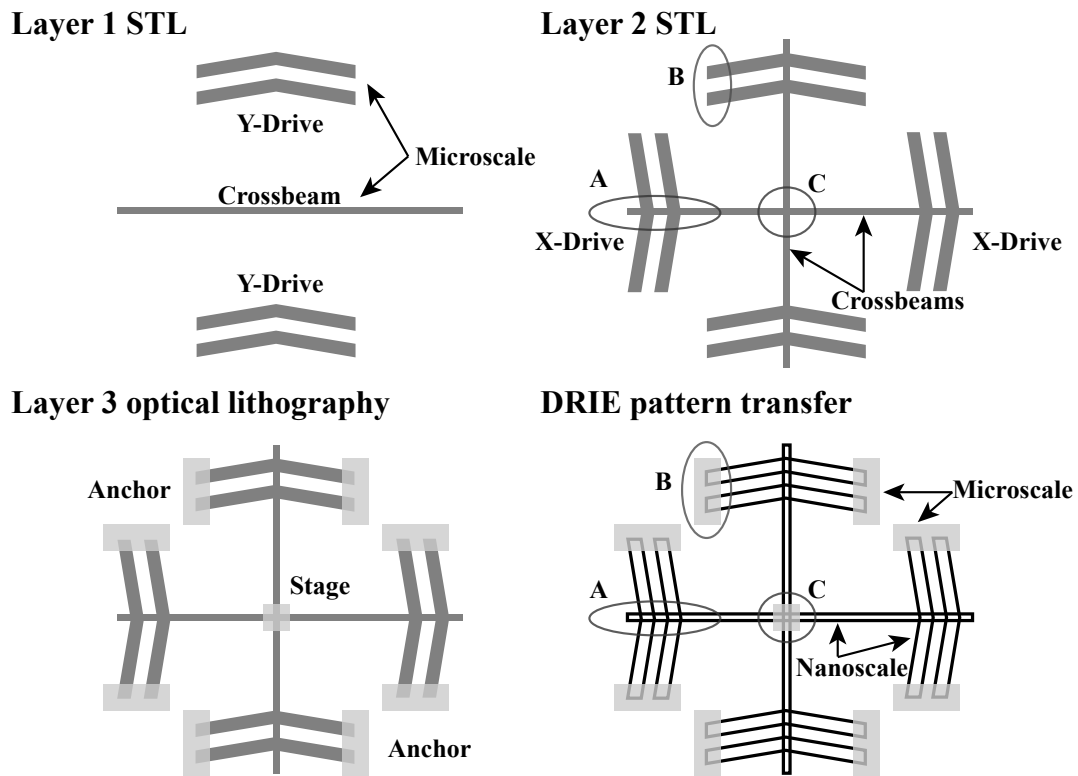
Figure 6.1: Design and lay-out of a two-axis electrothermal stage based on multi-layer STL process.

Figure 6.2 shows 3D schematic diagram of the formation of overlaid sidewall mask features. All that is required to form intersecting nanoscale features is the repetition of a process based on conventional lithography and DRIE to form a shallow mesa, followed by common deposition of a conformal coating whose horizontal surfaces are removed. The remaining vertical surfaces form a sidewall mask that follows the combined perimeter of the overlaid mesa patterns. The repetition of single-layer STL can now fabricate two-dimensional nanoscale lay-outs. A final conventional lithography step can again be used to add microscale features, and the whole pattern can be transferred into the silicon as before, using DRIE. The detailed information of each fabrication step is demonstrated in section 6.2.
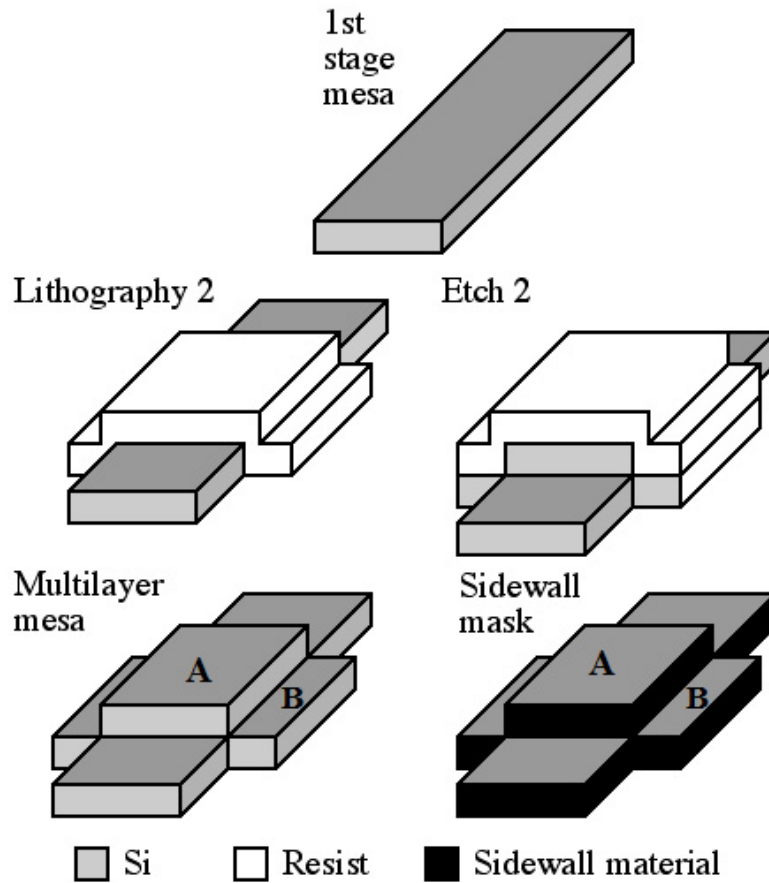
Figure 6.2: 3D schematic diagram of the overlaid sidewall masks formed by the multi-layer STL.

## 6.2 Fabrication steps

Although the fabrication process can be easily modified to be adapted to both bulk silicon and BSOI wafers, demonstrator devices are initially fabricated on 100mm diameter bulk silicon wafers (P-type, $< 100 >$ *orientation*, with a resistivity of $1 - 5\Omega\cdot$cm) for diagnostic purposes.

Here structures were evaluated by SEM using a LEO 1450VP variable pressure instrument, and by optical surface profilometer using a Wyko NT9100. The latter instrument lacks the in-plane resolution to visualise 100nm features fully, but nonetheless yields 3D images that aid structural interpretation.

### 6.2.1 Process flow

Figure 6.3 shows a suitable process for fabricating suspended NEMS using BSOI wafers. Here, for simplicity, overlaid nanoscale features are shown side by side. Two different structures correspond to regions A and B in Figure 6.2 respectively; however, they may clearly intersect

one another. The two STL steps are carried out by patterning and etching a first set of mesas (steps 1-3), and then patterning and etching a second set (steps 4, 5). A low-stress conformal metal coating is then deposited, and horizontal surfaces of this metal are removed by directional etching (steps 6, 7). The result is a surface mask defining overlaid nanoscale features. A third conventional lithography step is then carried out to add any microscale parts (step 8). The combined pattern is transferred into the silicon substrate by deep reactive ion etching (steps 9, 10). Suspended mechanical parts are freed by etching of sacrificial oxide (step 11) and metal is deposited over the entire structure to provide electrical contact (step 12). Alternatively, the final metal layer may be localized to the anchors by depositing and patterning the metal after step 7, before the final deep etching. A similar process may be developed for bulk Si wafer, on which the suspensions are undercut by $SF_6$ isotropic plasma undercut.
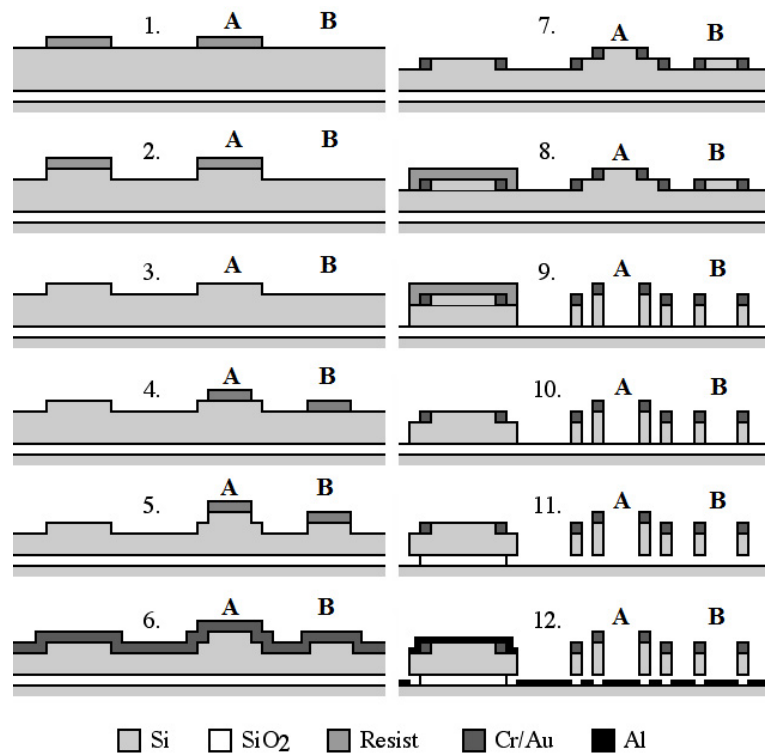


Figure 6.3: Schematic diagram of multi-layer STL based on BSOI.

The process has been firstly used to form NEMS for diagnostic purposes using bulk silicon in place of BSOI. The masks were a low-cost three-layer chrome-on-glass set fabricated by laser writing from Delta Mask B.V., Enschede. The nominal resolution is 1.5μm with a minimum feature size of 2μm. Pattern transfer was carried out using a Quintel Q7000 mid-UV contact mask aligner, with a typical resolution of 1μm. A 0.4μm thick layer of Shipley S1805 optical photoresist was used for patterning the first STL layer; 1.6μm of Shipley S1813 resist was used

for the second, and a thicker resist S1828 of 3μm was used to define the anchors to achieve planarization. Development was carried out using Microposit MF-319, followed by an $O_2$ plasma descum.

Mesa etching was carried out using a STS single chamber multiplex ICP deep reactive ion etcher, using a cyclic process based on $SF_6$ and $C_4F_8$. The DRIE parameters were 6.8mtorr pressure, 350W coil RF power and 11W platen power, with a 10s etch cycle using 50sccm $SF_6$ and 5sccm $O_2$ followed by a 5.2s passivation cycle using 80sccm $C_4F_8$. Here a short passivation cycle was chosen to avoid any residual $C_4F_8$ layer remaining after each etching step, which might lead to grass in the final deep etching.

Figure 6.4a shows an SEM view of 10μm wide overlaid mesas formed by two consecutive cycles of patterning a layer of photoresist and then transferring the resulting features into bare Si to a depth of approx. 1μm by DRIE. The terraced nature of the compound mesa may clearly be seen. Figure 6.4b shows the corresponding optical surface profile, which demonstrates that two sets of mesas with comparable height have been formed. The central block of the nine patch is the parts of the overlaid mesa from the two-step STL, surrounded by four blocks in a cross shape which have been through only one DRIE step. And the remaining four blocks in the corners are etched twice thus being the lowest surfaces.



| (a) | (b) |
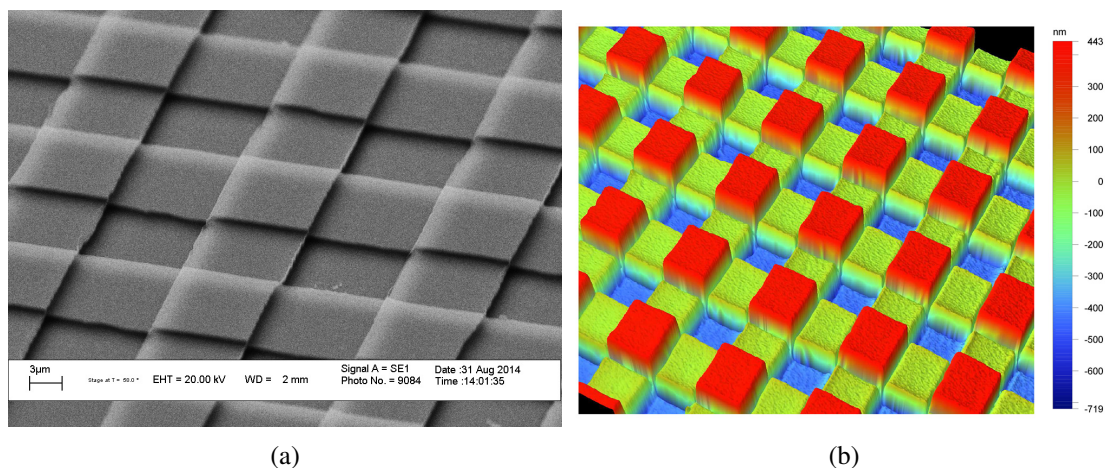
Figure 6.4: (a) SEM view and (b) surface profile of overlaid mesas.

Sputter deposition and etching were carried out using a Nordiko RF sputter coater. A conformal layer of 10nm Cr and 90nm Au was first deposited, and horizontal layers of this material were then etched away by RF sputtering in Ar gas at $2 \times 10^{-3}$ mbar pressure. The Au layer was used to form a low-stress metal sidewall mask, while the higher-stress Cr was used to ensure adhesion.

Figure 6.5 shows details of the mesas after deposition of Cr/Au and sputter etching. Figure 6.5a and 6.5b show different views of the terraced mesas with the sidewall mask formed. The sidewall has a stepped structure that follows the original mesa pattern. Its horizontal surfaces have been completely removed and vertical surfaces eroded to roughly half the original mesa height by sputter etching, as has the edge of the Si mesa. However, continuous joints are clearly formed between the two layers of metal in both views. Figure 6.5c and 6.5d shows SEM photographs obtained in region A (c) and C (d) of the two-axis electrothermal stage illustrated in Figure 6.1. Similarly, metal sidewall mask joints are found following the perimeters of the combined mesa pattern, indicating the intersecting features to be formed.



(a)

(b)

(c)

(d)
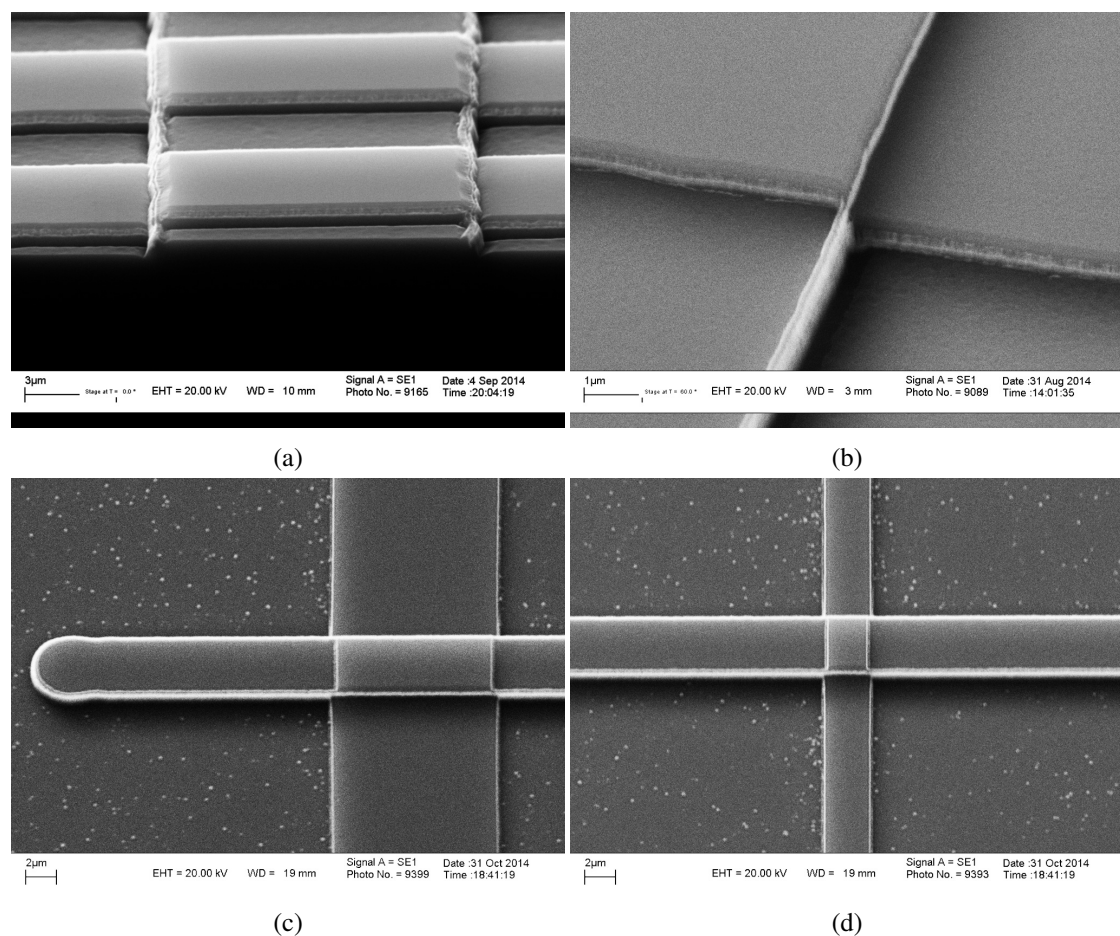
Figure 6.5: SEM views of sidewall masks formed after sputter etching.

Sputter etching can lead to re-deposition of chromium spots; however, this can be removed using an additional wet etch in ceric ammonium nitrate/HCl as explained before.

The following deep silicon etching was again carried out using ICP DRIE. However, the cycle time of the etching step was reduced to 4s to prevent erosion of the nanoscale beam by scalloping. Similarly, the cycle time of the passivation step was reduced to hold the width of the

beam close to 100nm for the full feature height. To reach a depth over 5μm, at least 70 cycles were required in DRIE. Undercut of suspended structures, if needed, could be carried out using a single cycle with a passivation time of 11s and an etch time of 19s.

Figure 6.6 shows the details of the HAR nanoscale features formed after the combined pattern has been transferred into the silicon substrate by deep etching for diagnostic purposes. As shown in Figure 6.6a, the nanoscale features are again continuous from layer-to-layer. A large area of latticed pattern is fenced up by the nanoscale silicon sheets. Figure 6.6b is the corresponding optical surface profile, showing that the depth of the cellar is approx. 8μm with an aspect ratio of 80 : 1.

Figure 6.6c shows a close-up of the top parts of the combined features. The remaining sidewall masks can be seen at the top. The stepped appearance indicates that they are formed in two different levels of the STL process. However, if the original height of the mesas are lowered, or the sidewall masks are over-etched by sputter etching, the thickness of the sidewall masks can be further reduced. As shown in Figure 6.6d the height difference between the two-level masks is minimized so that they are almost levelled horizontally. Apart from this, the adhesion between the sidewall masks and the silicon sheet is quite good, and the HAR features are not distorted by residual stress in all cases.

(a)

(b)

(c)

(d)
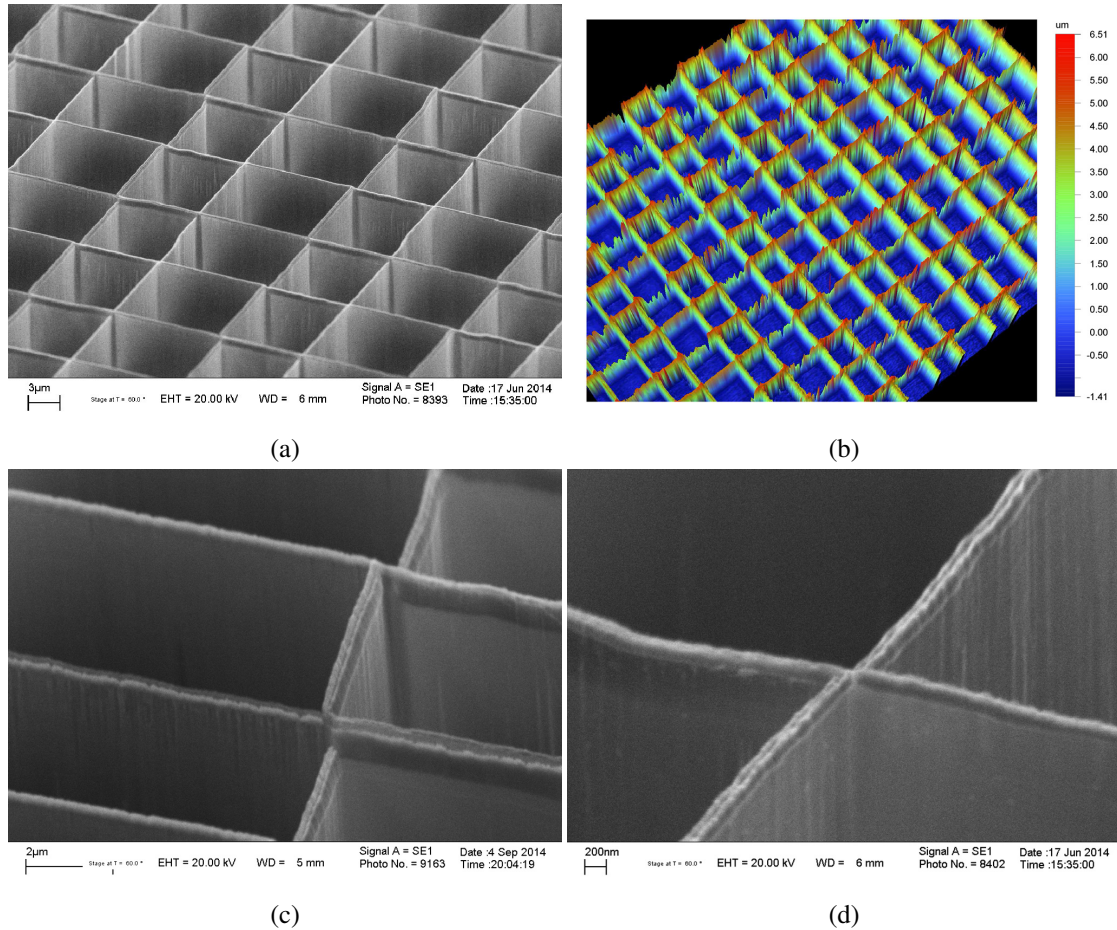
Figure 6.6: (a) SEM view and (b) surface profile of HAR latticed pattern after DRIE; (c) and (d) close-ups of the top parts of the combined features.

### 6.2.2 Test dies

It is now important to verify the quality of the features formed in each STL process. To address this, a series of test dies are designed with features assigned to the two STL layers in reverse orders. Figure 6.7 shows the lay-outs of three sets of test dies containing nested and stacked nanoscale features. All structures are connected to the anchors by overlaying patterned in the layer 3 optical lithography. The feature quality is then characterized at different stages of fabrication process using SEM photographs and reconstruction of surface profiles.

Figure 6.8 shows the fabrication results after the third lithography before deep etching. Figure 6.8a shows the SEM photograph of a pair of dies containing nested features (a square, inside a square border) designed to yield three concentric squire sidewalls with 20µm spacing after completion of pattern. And Figure 6.8b and 6.8c show stacked features with (b) and without (c) intersecting parts designed to yield corresponding nanoscale features with 10µm spacing. The resist remains to show the pattern of the anchors. Figure 6.8d, 6.8e and 6.8f show the surface

**Layer 1 STL**

**Layer 2 STL**

**Layer 3 optical lithography**
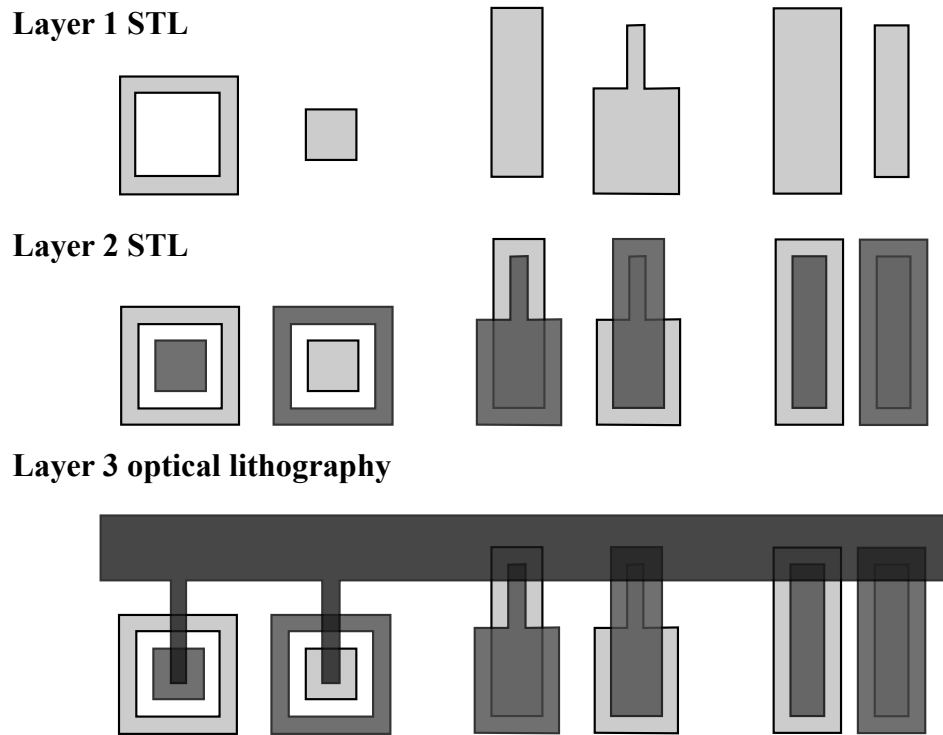
Figure 6.7: Lay-outs of three sets of test dies by multi-layer STL.

profiles. In each case, the difference between the mesas patterned in different STL can barely be seen. However, the planarization of the resist is less satisfied as stepped features can be found in the overlaid regions on the anchors. This will potentially cause problems in the following deep etching, which will be investigated shortly.
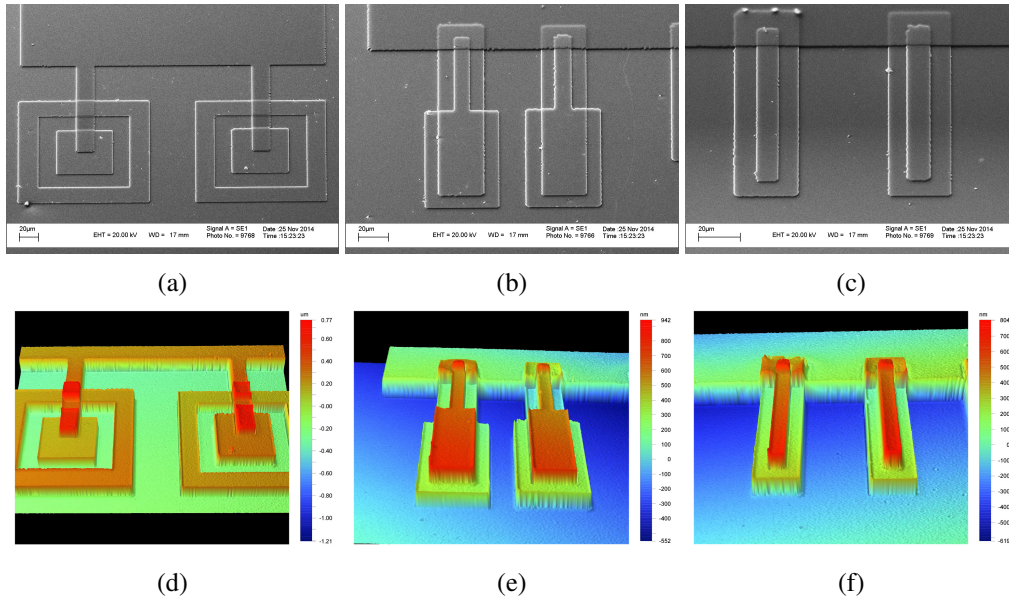
Figure 6.8: SEM views ((a), (b) and (c)) and surface profiles ((d), (e) and (f)) of test dies after the third lithography.

Figure 6.9 shows the corresponding results for the three test dies obtained after the final etching. Resist are stripped off to characterized the overlaid features. As shown with the SEM photographs in Figure 6.9a, 6.9b and 6.9c, the HAR nanoscale features are formed following the perimeters of all mesas as designed. The feature width here is clearly far below that of the original mesas patterned in the optical lithography process. As expected, the following 3D surface profiles shows the same depth of nanoscale Si sheets are formed in all cases. Among these, there are regions where show the joins between the two levels of STL and the anchors are at the same level (Figure 6.9d) and stacked with an intersecting structure (Figure 6.9e), as well as those with a stepped appearance (Figure 6.9f).

144
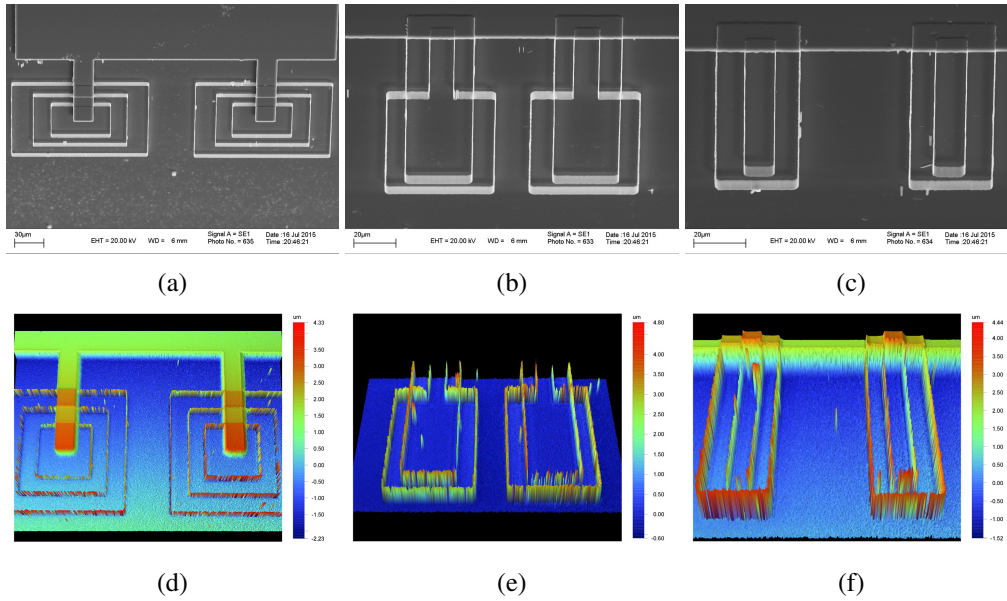
Figure 6.9: SEM views ((a), (b) and (c)) and surface profiles ((d), (e) and (f)) of test dies after final DRIE.

With all the results above, similar features have been clearly achieved for all test dies. It is hence proved that fabrication results of the combined micro- and nanoscale structures are independent of the assignment of features to the two different levels of STL process.

## 6.3 Prototype devices

Using the multi-layer STL process introduced above, a batch of prototype devices with different structures have been fabricated to validate the method and demonstrate a satisfactory yield. A combination of micro- and nanoscale structures have been adapted to demonstrate the better compatibility of the multi-layer STL in more potential applications than a single-layer process. In each case, the main aim is to demonstrate possibilities for patterning rather than investigate device performance.

### 6.3.1 Two-axis electrothermal stage

The detailed lay-outs of two types of two-axis electrothermal stages are shown in Figure 6.10. Figure 6.10a demonstrates the design of type I stage. Four sets of double-ended chevron-shaped buckling actuators are linked by two long crossbeams intersecting in the center. As shown in Figure 6.1, they are split into two groups and patterned in the two STL layers separately to define the nanoscale beams. The intersecting are thus formed after the patterning of the

layer 1 and 2 STL. Microscale anchors at both ends are then defined using the layer 3 optical lithography, as well as the central movable stage supported by the crossbeams. The central stage can then be driven in both X and Y directions by actuating the V-beam actuators linked with the long crossbeams patterned in separated groups, when passing a current between corresponding anchors.

In some cases, similar results may be achieved using alternative lay-outs. For example, as shown in Figure 6.10b, in type II stage the intersections between the crossbeams and the central stage may be achieved by sub-dividing the beams into non-intersecting segments that are linked by the stage itself. Similarly, the intersections between the crossbeams and the actuators may instead be achieved using additional link-bars as well. As the nanoscale features no longer intersect with each other, this design can easily be achieved by using a simpler single-layer STL comparable to the type I stage. However, disadvantages of this approach to design may be a reduction in dynamical performance due to the inertia of the additional microscale components required.



(a) Type I 2-axis Stage          (b) Type II 2-axis Stage
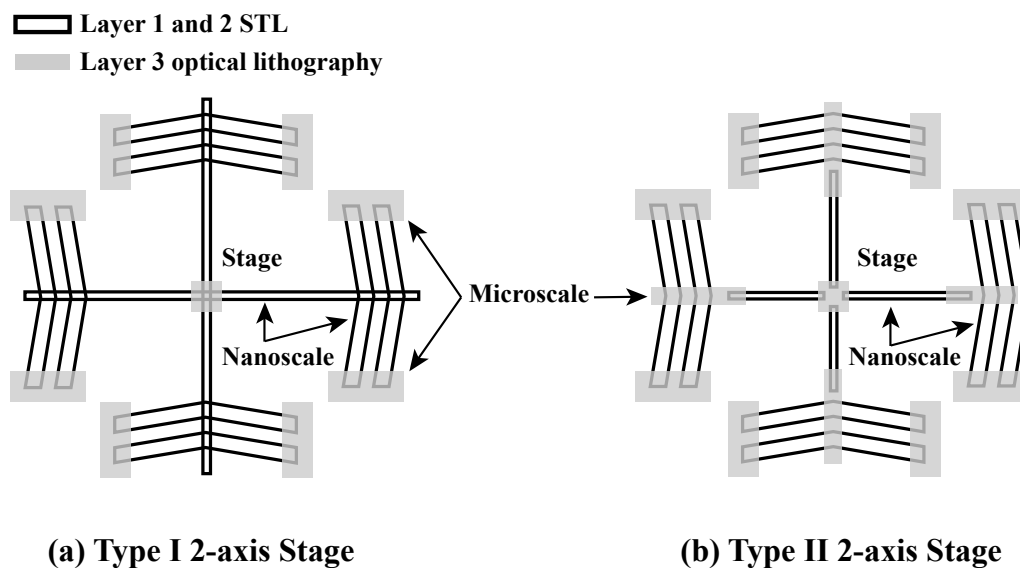
Figure 6.10: Lay-outs of two types of two-axis electrothermal stages by multi-layer STL.

In both designs, the nanoscale beam has two different lengths of 1mm and 500μm with 10μm beam separation and $\theta = 0.01$rad slope. The beam length is shortened to reduce the stress effect

based on previous experience. In both cases, the numbers of actuator beams are much larger than those shown in Figure 6.10, up to 58 for each V-beam actuator. The central stage is also designed to be two different sizes of 10μm and 26μm. In type I stage, the long crossbeam has a total length of 2060μm with a 2μm width, and 10μm of the crossbeam projected beyond the beam array ends. This length is shortened to 820μm in the type II design as the structures are now connected by four link-bars with 10μm width and 770μm length. The final mask contains a mixture of structures with various sizes, and eventually 10 different lay-outs of the two-axis electrothermal stage are designed and fabricated.

Prototype devices were fabricated based on the CAD lay-outs shown in Figure 6.10. Figure 6.11 shows the top view of complete devices on bulk silicon and BSOI. For a mixture 10 different lay-outs of both type I and type II stages, the overall die size is 22951μm × 13575μm. All nano structures were released from the silicon substrate by isotropic plasma undercut or HF vapour.



(a)                                                            (b)
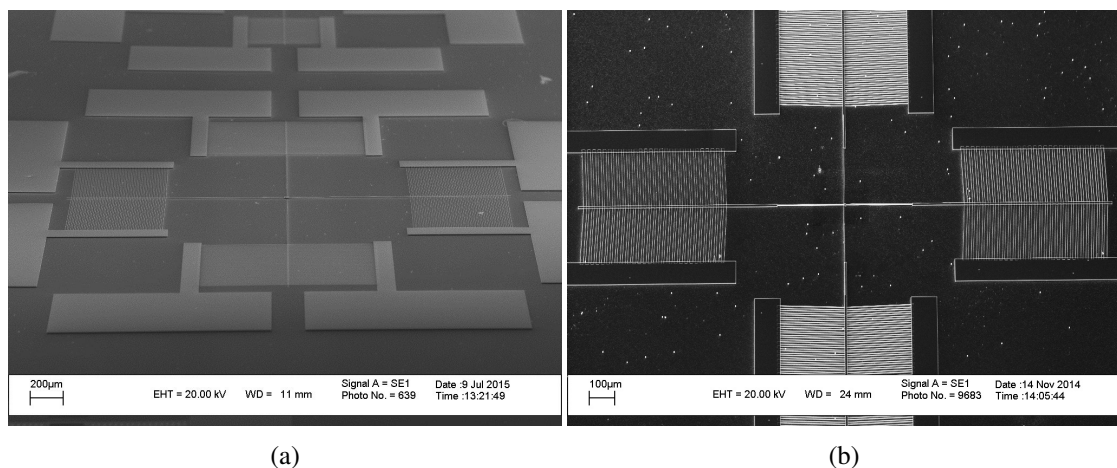
Figure 6.11: SEM views of complete two-axis stages after fabrication.

Figure 6.12 shows SEM photographs of type I stage after completion of deep etching. Figure 6.12a shows supporting structure formed by the two long intersecting crossbeams without patterning the central stage in the third conventional lithography. A solid and robust support is achieved which shows that STL Levels 1 and 2 are combined correctly. Figure 6.12b shows a similar view of the same region, however, this time a 10μm central stage is patterned and formed simultaneously with the crossbeams in the deep etching. Here fabrication results of all three levels of lithography are presented together. The double cross shaped support can still be found after stripping the resist off. A stepped feature can also be found on the top, namely the upper surface of the central stage is slightly lower than the top of the cross beams, which results

from resist planarization in the third lithography.

Figure 6.12c shows the combined pattern of the nanoscale beams, with a crossbeam beam tying the multiple parallel beams together in the middle. Similar to Figure 6.12a, these intersecting structures are also formed in the STL levels 1 and 2. Compared with the single-layer STL process, all beam width here are in nanoscale with a two-dimensional structure.

Figure 6.12d shows a SEM view of half of the V-beam electrothermal actuator after completion of deep etching. The attachment of the actuator beams to their anchors shows the combination of STL level 1 and the conventional lithography level 3. The ends of the polygons defining the beam array are buried in the anchors, so these common features have no effect on the final device.
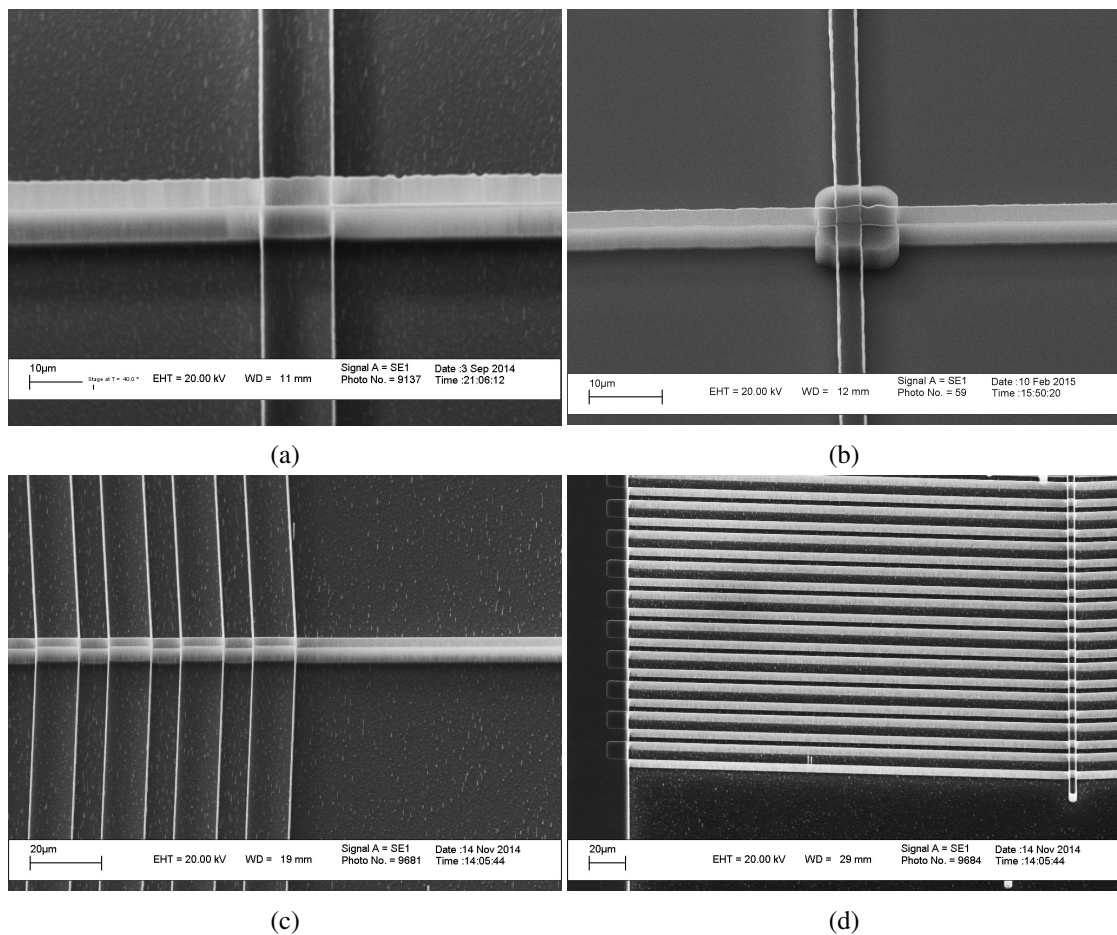


Figure 6.12: SEM views of type I stage after DRIE showing: two long supporting crossbeams intersecting each other with (a) and without (b) patterning the central stage; (c) nanoscale crossbeam tying the multiple beams together; (d) half of the V-beam electrothermal actuator.

Figure 6.13 contains SEM photographs obtained on a type II stage device after completion of deep etching. In Figure 6.13a, the nanoscale intersections are replaced and connections have

been successfully made by the microscale link-bar patterned in the third lithography. The end of the long beam is buried in the link-bar with a long overlay to ensure solid connection, while the other end expected to support the central stage. Figure 6.13b shows a central stage of side 26μm supported on four sets of supporting beams with 4μm overlay. The supporting beams have 2μm separation, which are all patterned in STL lever 1 and transferred into HAR nano structures in the final etching. The distribution of small windows is designed on the stage purposefully for in order to reduce the time needed in undercutting.



(a)                                                                (b)
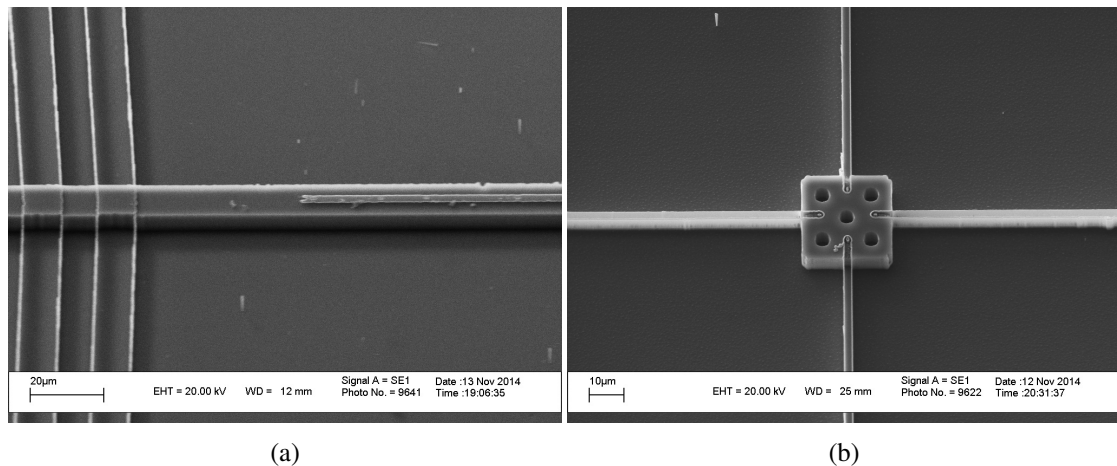
Figure 6.13: SEM views of type I stage after DRIE showing: (a) microscale link-bar connecting nanoscale beams; (b) central stage supported by four nanoscale beams.

Figure 6.14 shows the completed type I device after plasma undercut. The final isotropic plasma etch has sufficient range to undercut nanoscale parts, leaving many structures completely suspended. Since the microscale crossbeam have been replaced by nanoscale intersections, it is now even easer to achieve suspension on movable parts except the central stages. Released structures charged quickly during SEM imaging, unless high pressure or thin sputtered metallization was used; however, in this case high quality images could be obtained. For example, Figure 6.14a shows an SEM view of a chevron actuator from the type I 2-axis stage in Figure 6.10a. Microscale parts remain as anchors fixing the two ends of multiple nanoscale beams in parallel. Figure 6.14b shows a close-up of the intersecting structure, where the crossbeam projects beyond the array. The combined structure including the joints has clearly been undercut which can be told by the remnant beneath following the original features.

|  (a)  |  (b)  |
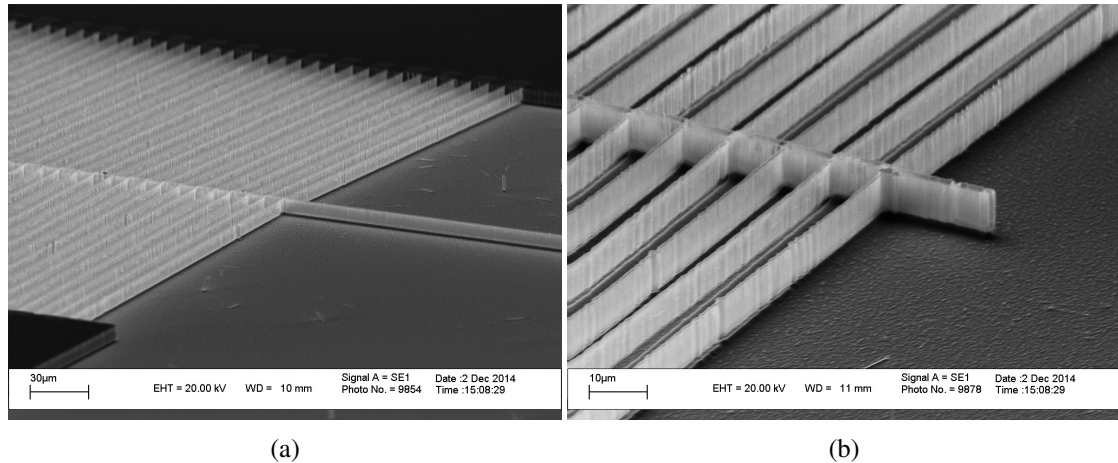
Figure 6.14: SEM views of completed type I stage after plasma undercut.

### 6.3.2 Microgripper

It is also worth noting that functional devices may be fabricated on the same wafer using both single- and double-layer STL patterning simultaneously. For example, Figure 6.15 shows the design of two electrothermal microgripper structures, in which the upper half has deliberately been fabricated in one case using layers 1 and 3 and the lower half using layers 1, 2 and 3. At the fixed ends, anchors are also patterned in layer 3 and subdivided for each half of the gripper to allow a heater current to be passed through all the arms. An in-plane motion of the gripper tip is thus generated due to differential thermal expansion between the hot and cold arms. And the direction of motion is decided by the position of the cold arms as illustrated.

Combined patterns can be achieved in different ways which depends on the feature size. For example, Figure 6.16a shows an SEM view of the designed microgripper obtained after the final deep etching step. The gripper tip consists of two parts with similar shapes but clearly different feature scales: the lower half is made of nanoscale thin walls following a similar shape of the outer border of the upper half in microscale. Gripper arms are nanoscale Si beams patterned in 5µm spacing whose left ends are buried in the upper half but intersecting with the lower ones. Hence, a process combination of either STL layer 1 or 2 with 3 yields micro-to-nano joints, while nanoscale intersecting is achieved by repeating the first two levels of STL process.

Figure 6.16b shows the an optical surface profile of the achieved structure. Feature size in the lower half of the gripper is obviously far below that of the upper half defined by the original mask. The overlaid ends of the nanoscale arms keep the same spacing defined by the original mesas in the lower half, while those regions are protected by photoresist in the upper half. Here,
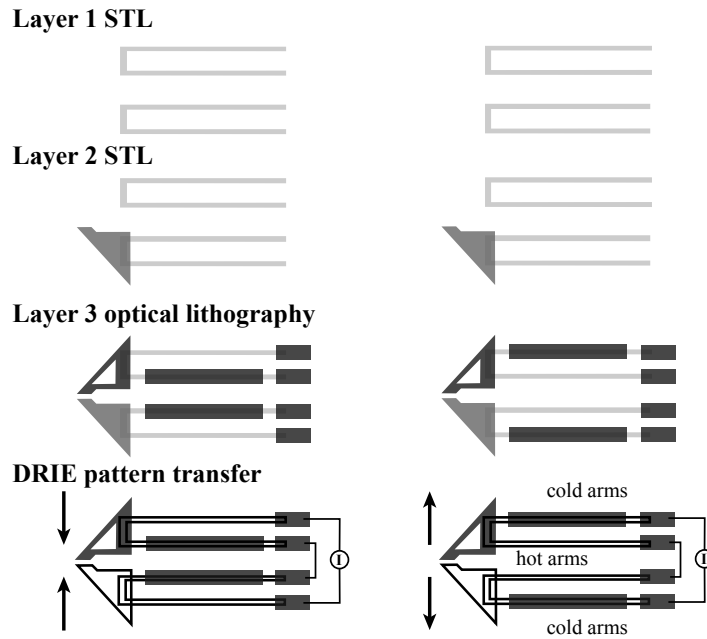
Figure 6.15: Design and lay-outs of microgrippers by multi-layer STL.

all nanoscale features have a similar etch depth as the microscale ones but with a much higher aspect ratio.



(a)                                                    (b)
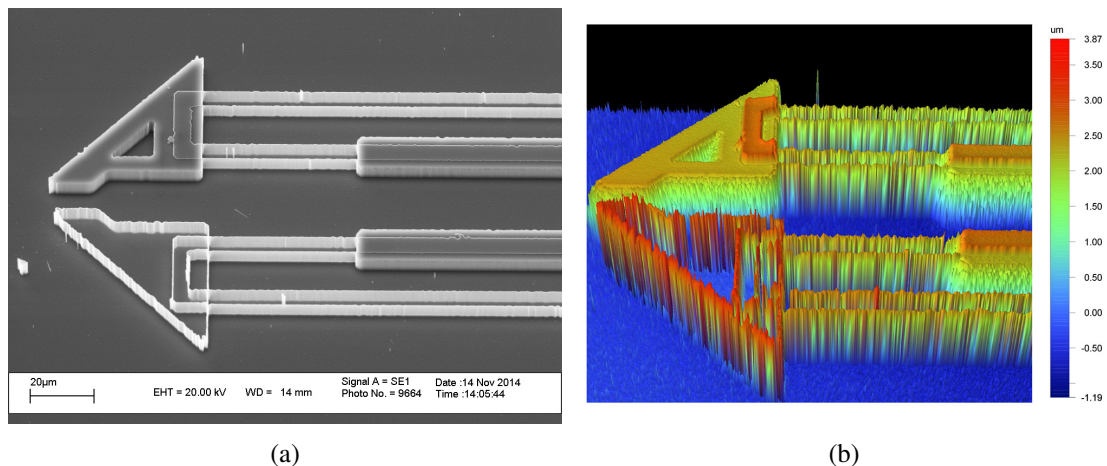
Figure 6.16: (a) SEM view and (b) surface profile of a microgripper after DRIE.

Completed devices then can be realised either by plasma undercut from bulk silicon substrate (Figure 6.17a) or HF vapour for a BSOI device (Figure 6.17b). The main difference is the remnant beneath the released features formed in plasma undercut as mentioned before. Besides, it might also be difficult to undercut large features such as the half microscale tips (up to 15μm) in $SF_6$ plasma due to lateral erosion on the nanoscale features. As shown in Figure 6.17a, the lower half of the structure is completely released, while the upper half remains attached to the substrate in places. With comparison, in Figure 6.17b, a fully released structure is achieved by

removing the interlayer of a BSOI device in HF vapour.



(a)　　　　　　　　　　　　　　　　　　　　　　(b)
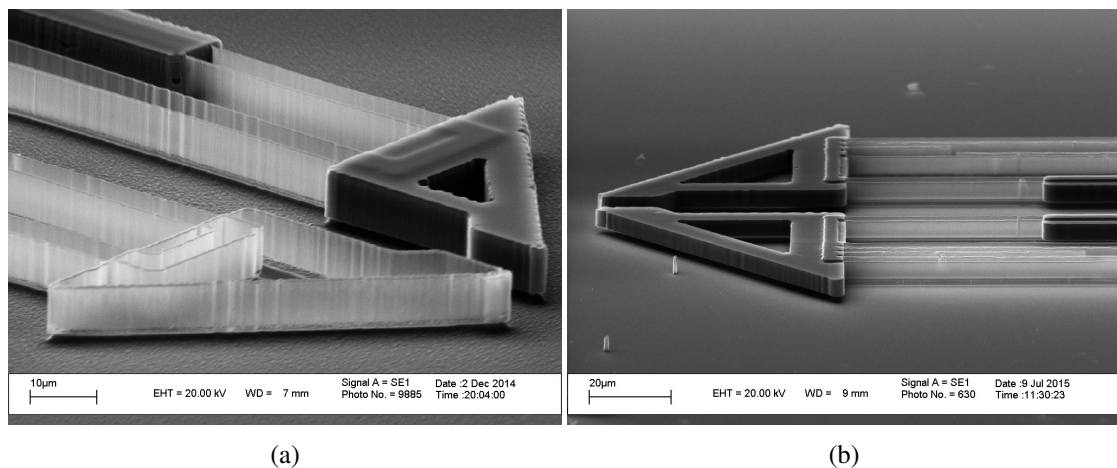
Figure 6.17: SEM views of completed microgrippers released by (a) plasma undercut and (b) HF vapour.

### 6.3.3 Mesh spring

Two-dimensional nanoscale structuring may be used to create surfaces with mechanical anisotropy or other forms of anisotropy. To prove this, meshing springs with different lay-outs are designed and fabricated on the same mask set. Figure 6.18 shows the schematic diagram of a mesh spring based on the two-layer STL process. Two layers of squares in a staggered pattern are defined in the STL lever 1 and 2 separately with overlapping on the corners. A meshed structure is thus formed with microscale anchors and linking block patterned in the third lithography. The effect of structuring has been to create a spring based on a regular mesh of interlocking, flexible square elements, with adjacent elements originally assigned to alternating STL layers.

Figure 6.19 shows structures of the designed mesh spring at different stages during process. Figure 6.19a shows the SEM view of a meshed structure based on overlapping squares with side length 30μm after completion of patterning of all layers 1, 2 and 3. Each square and its adjacent elements are assigned to different STL layers 1 and 2. Figure 6.19b shows the optical surface profile for the same structure. A good planarization is achieved for the overlaid features after patterning the mesa.

Figure 6.19c and 6.19d show the corresponding results of the same device after the final DRIE. HAR features a clearly formed exactly as expected with intersecting corners following the perimeters of defined polygons in previous steps.

Figure 6.20 contains SEM photographs of released structures. As all the movable parts here

**Layer 1 STL**

**Layer 2 STL**

**Layer 3 optical lithography**

**DRIE pattern transfer**
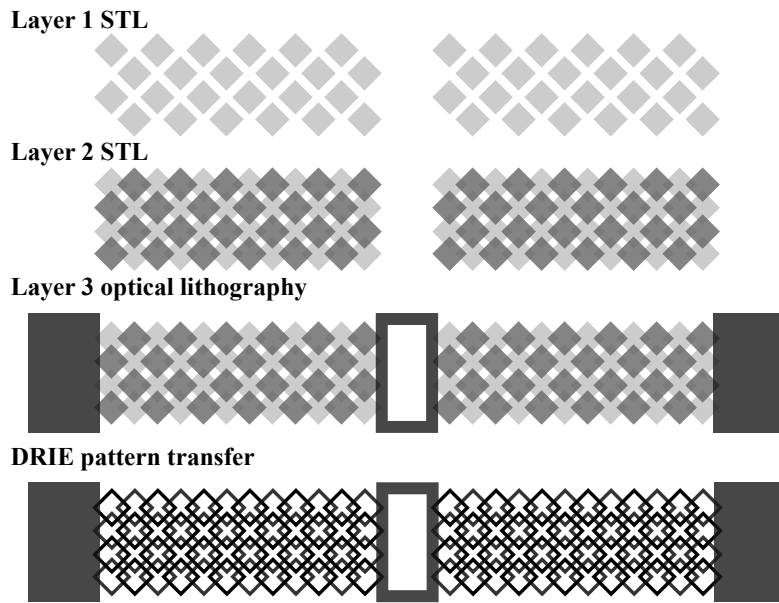
Figure 6.18: Design and lay-outs of mesh springs by multi-layer STL.

are nanoscale Si sheets, interlocking structures are cut thoroughly in a rapid process. Figure 6.20a shows a close-up of the suspended features, which verifies that structural integrity of the interlocking parts has been maintained with good junctions. In Figure 6.20b, a clear gap of approx. 1μm can be observed between the nanoscale suspensions and the silicon substrate by tilting the device in a certain angle. Etching quality in the final DRIE must be high due to the smooth sidewall features for the combined pattern.

It has also been proved that nanoscale parts may easily be combined with common MEMS components. For example, Figure 6.20c shows a SEM view of a nanoscale mesh spring in Figure 6.18 combined with a conventional comb-drive electrostatic actuator based on 5μm wide fingers with 5μm gaps. With this combination, it is now possible to permit reciprocate and flex the spring during operation of the comb-drive, instead of just the heating the nanoscale interlocking elements electro-thermally. Figure 6.20d presents mesh springs with 15μm elements with linking blocks. All structures have been thoroughly released from the substrate without any distortion. These results also proves that all layers of the STL (1, 2, and 3) are compatible with optical lithography patterns in a very wide size range from a few micrometers to millimetres.
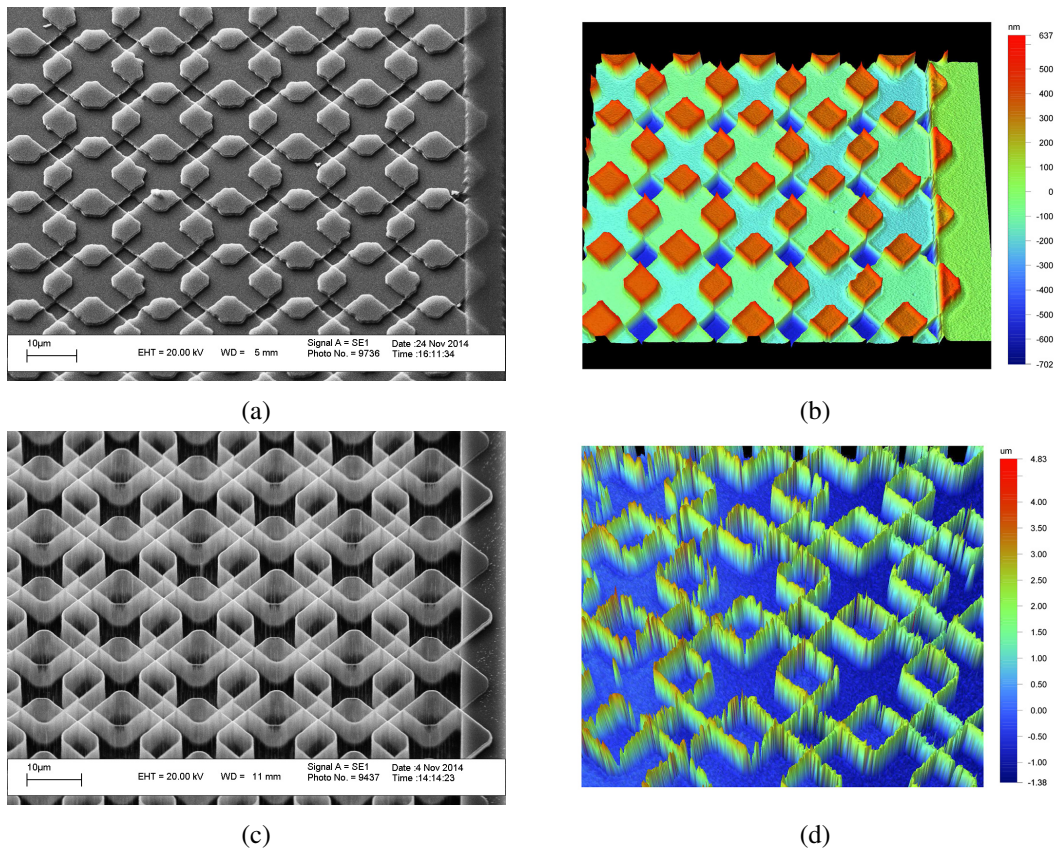
Figure 6.19: (a) SEM view and (b) surface profile of the meshed structure after the third lithography; (c) SEM view and (d) surface profile of the meshed structure after DRIE.
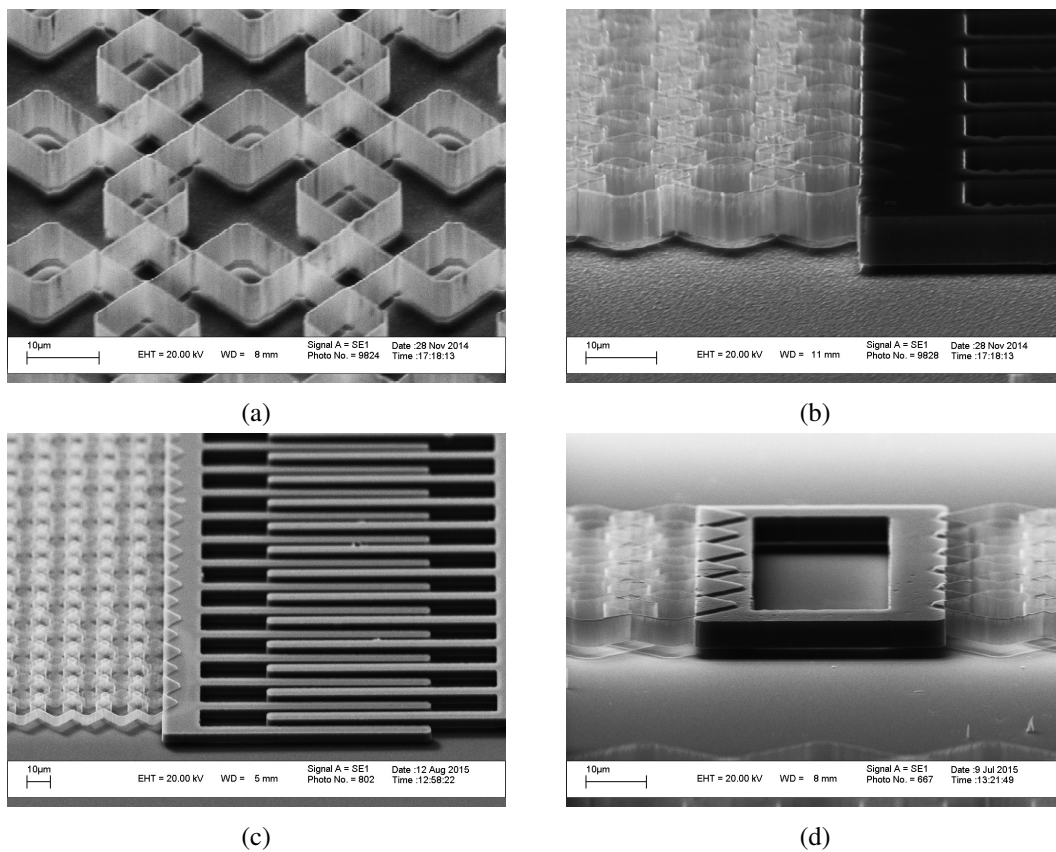


Figure 6.20: SEM views of completed meshed structures released by (a) and (b) plasma undercut and (c) and (d) HF vapour.

## 6.3.4 Other springs

Mechanical springs with variable geometries have been designed on the same mask set to prove the process viability further in different structures. For example, Figure 6.21a illustrates a anchored meander spring defined by a comb-shaped mesa which only requires one STL pattern (either layer 1 or 2) combined with layer 3. Figure 6.21b shows two designs of multi-turn spiral springs, which have two different types of central tables assigned to process layers 3 and 2, respectively.
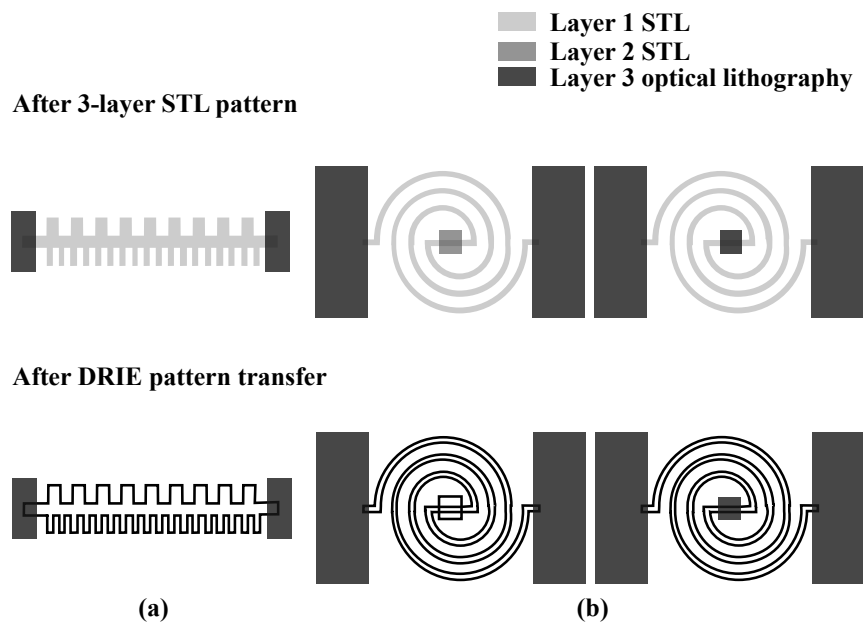


Figure 6.21: Design and lay-outs of (a) meander spring and (b) spiral springs by multi-layer STL.

Figure 6.22 shows the completed meander spring after plasma undercut from different views. In Figure 6.22a, the telltale can be seen as a thin white line indicating the original features with a 1μm gap from the suspended spring. It is then possible to confirm there is minor distortion of the released structures which might be induced by stress contained in the sidewall masks. Similar results can also be found in Figure 6.22b with different spring spacing of 5μm (lower) and 10μm (upper) respectively.

Figure 6.23 shows the SEM photographs of the spiral springs with two types of central tables. Clearly the one in microscale (Figure 6.23a) is patterned in layer 3 and the other in nanoscale (Figure 6.23b) in layer 2. The former yields a solid feature that cannot be undercut using a short-range isotropic plasma etching, while the latter yields a hollow feature that can. Thus, the two structures differ in that the former spring is anchored at its centre while the other is free. Detailed
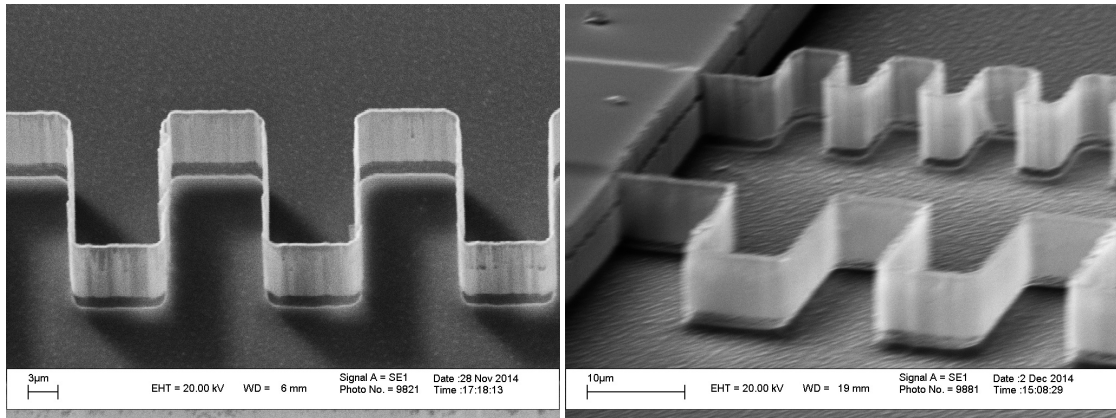
(a)                                    (b)

Figure 6.22: SEM views of completed meander springs released by plasma undercut.

comparison shows little observable difference in the nanoscale features. Results of these devices indicate little stress-induced distortion even for large, complex suspended nanostructures.
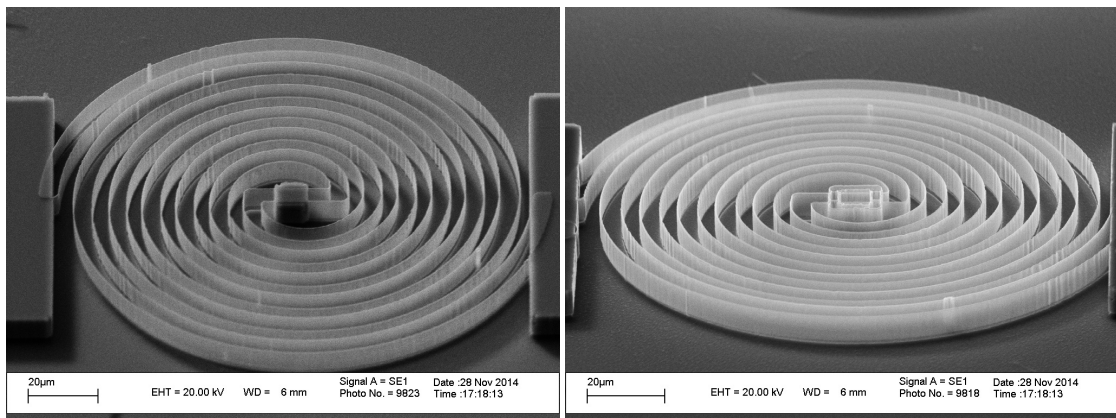


(a)                                    (b)

Figure 6.23: SEM views of completed spiral springs released by plasma undercut.

Verification of mechanical movement can now be investigated on most of the prototype devices by electrothermal heating, in which BSOI devices should surely provide much better performance. However, most behaviour can also be predicted based on previous experience on single-layer devices. Hence, it is now more interesting to investigate processing issues that specifically occurs in the multi-layer STL process, which will be detailed in the next section.

## 6.4 Processing Issues

In this section, processing issues encountered in the fabrication of the multi-layer STL process will be discussed. These issues including the common ones which occurred in the single-layer

STL process, as well as those only found in the multi-layer process. With appropriate failure analysis, many of the problems have been overcome by adjusting the relevant parameters of single fabrication steps. Also, analysing these problems offers a deep understanding of the multi-layer STL process and reveals potential problems in future NEMS applications.

### 6.4.1 General issues

As an extension of the single-layer STL process, the multi-layer STL inherits potential process flaws from the previous generation. These issues includes planarization in optical lithography, erosion in deep etching, stress induced distortion, etc., most of which have been fully analysed and solved previously. Although common causes are shared, the failure presents in variable appearance due to complex structures and the additional STL step in the multi-layer process, which is worth investigating in order to improve device design and yield rate.

Miss alignment is a common problem in MEMS fabrication, which has been observed in the fabrication of the single-ended NEMS actuator in Chapter 3 based on a single-layer STL process. However, this problem can now be fatal in a more complex process as the critical nanoscale features are now in two dimensions. For example, Figure 6.24a show the SEM view of the central part of a miss-aligned two-axis electrothermal stage after deep etching. The nanoscale intersecting beams have 2μm spacing which are supposed to support the central stage with a side length of 10μm. However, clear upward miss alignment ($> 4$μm) can be observed due to failure in the layer 3 conventional pattern as shown.

Effects of diffraction have been found on many patterned features below 4μm. Figure 6.24b shows the fabrication results of conducting only STL layer 1 on 4μm square mesa shapes. The formed mesas have a circular shape in stead of square, with a small hole in the middle in some cases, due to common diffraction effect in optical lithography. Thus HAR nanoscale features after deep etching present a cylindrical shape following the outer border of the circular mesas, where a much smaller cylinder induced by the small holes is enclosed. It is hence noticeable that additional nanoscale features can be formed by defected features due to diffraction, as the sidewall masks are formed on any feature borders. The final structure can thus be complicated and unpredictable. Such common problems existing in optical lithography might be solved by improving the aligning accuracy or compromised with enlarged feature size in mask design.

During the step of undercut, attempts to increase the range of the plasma-based undercut lead to rapid erosion of the nanoscale beams as before. As shown in Figure 6.24c, a large area of

the interlocking structures are eroded on a mesh spring, implying that more selective processes such as HF vapour release are required. Deformation induced by intrinsic stress contained in the sidewall masks are still problems unless an alternative mask material is chosen such as $SiO_2$. However, the structures are found surprisingly robust in some geometric pattern. As shown in Figure 6.24d, parts of the released spiral spring have be coincidentally noticed can do so without breaking due to distortion caused by gas flow during pumping and venting of the vacuum systems.
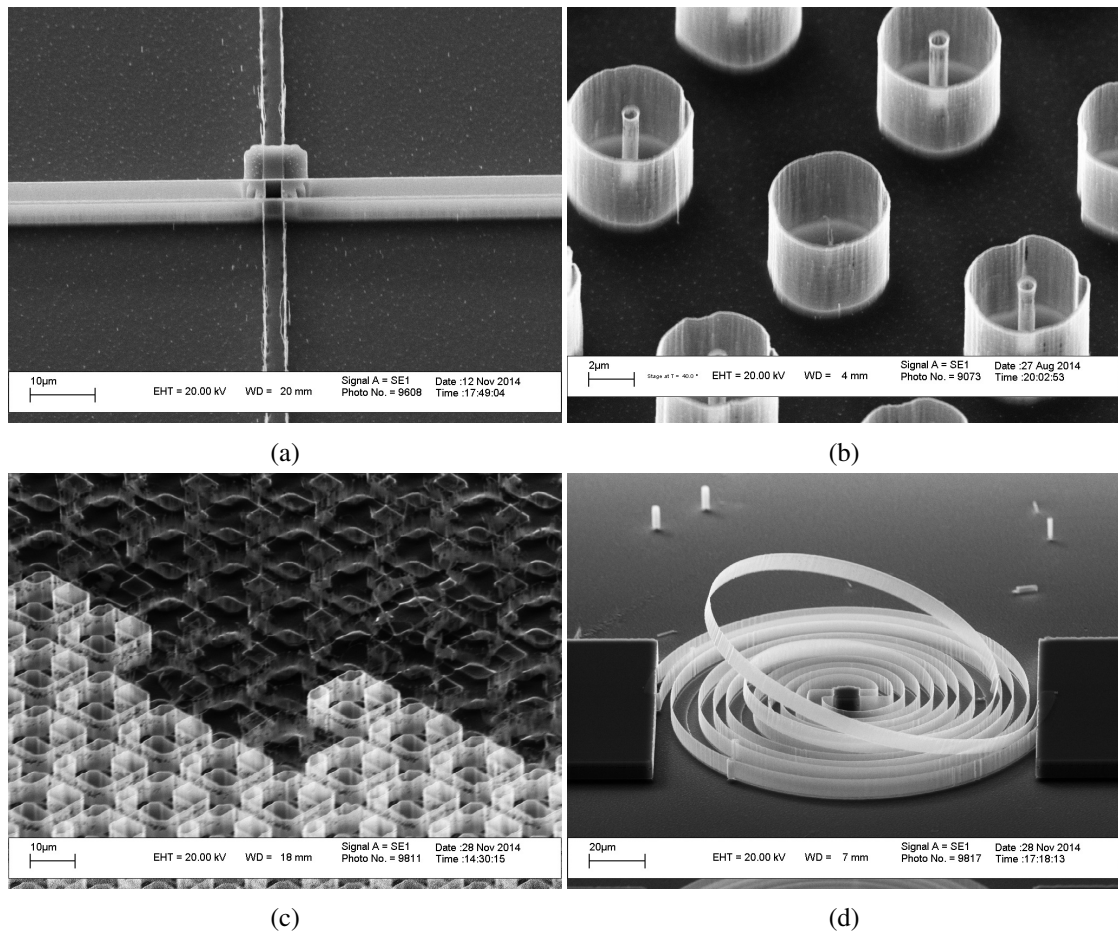


Figure 6.24: SEM views of general process issues showing: (a) miss alignment; (b) diffraction; (c) erosion in plasma undercut; (d) distortion caused by gas flow.

## 6.4.2 Multi-layer planarization

For the multi-layer STL process, the pattern transfer does still suffer from difficulties in planarization between different layers. And the problems may start to occur from the layer 2 pattern, not only in the final conventional lithography step as shown before. Thus special care is needed during lithography to ensure sufficient coverage of all mesas during spin coating of

resist; failure to do so results in the creation of voids during the DRIE step.

For example, failure of planarization is most likely to occur in regions which need all 3 layers of STL. Figure 6.25a shows the SEM photograph of a two-axis electrothermal stage with the overlaid mesas patterned in the first two STL layer (1 and 2) and the central stage in layer 3 after lithography. A similar surface profile in Figure 6.25b shows that the resist thickness in conventional lithography level 3 appears sufficient at the overlay of STL level 1 and 2. However, the enlarged SEM view after deep etching in Figure 6.25c contains a large squared hole in the middle of the intersecting beams. In Figure 6.25d, the corresponding optical surface profile indicates that the hole is quite deep, which means the resist on the top surface of the combined mesas has been exhausted rapidly in the final DRIE step.



|       |       |
|-------|-------|
| (a)   | (b)   |
| (c)   | (d)   |
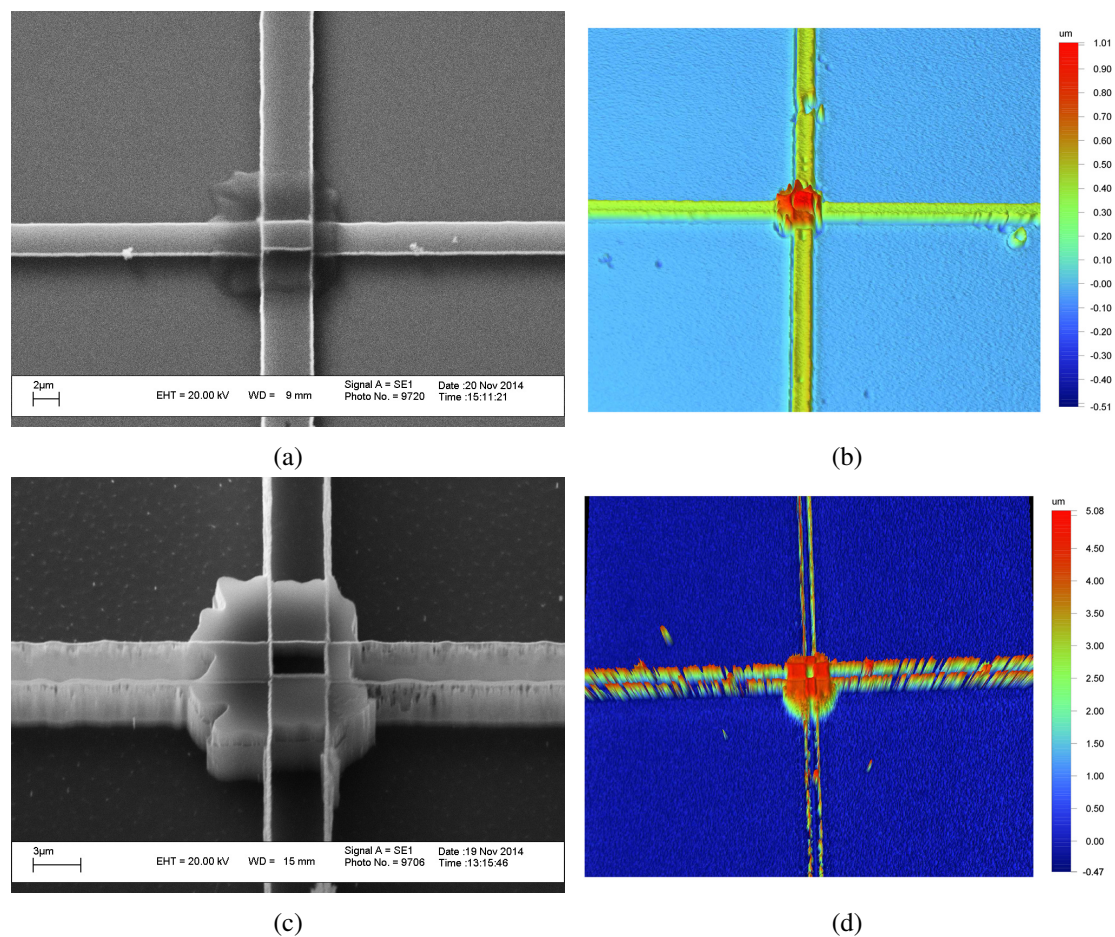
Figure 6.25: SEM views and surface profiles showing failure of planarization in regions patterned by three STL layers before ((a) and (b)) and after ((c) and (d)) final DRIE.

Such problems may exist in regions patterned only in two STL layers as well. Figure 6.26a shows a SEM view of the chevron actuator and suspension link bar after the final deep etching. There is a deep slot between the supposedly buried nanoscale beam ends, which is formed due

to insufficient resist coverage on the polygon shaped mesa in the patterning of layer 3. In Figure 6.26b, another example of the overlaid area near the anchors appears to suffer from similar failure. These results shows that in a multi-layer STL process, attention still needs to be paid to achieving good planarization on features only patterned in one STL layer without intersecting.
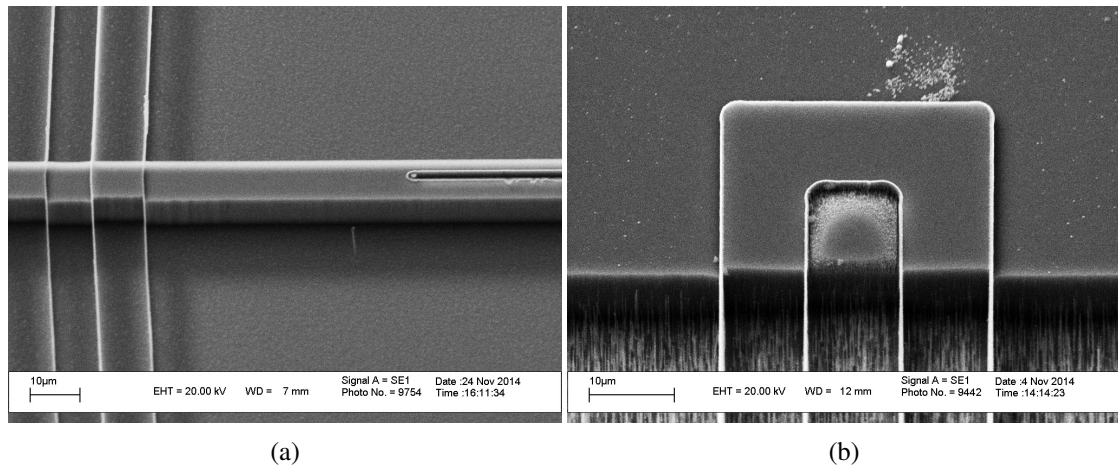


Figure 6.26: SEM views and surface profiles showing failure of planarization in regions patterned by two STL layers.

Full planarization is therefore required in both cases. Thus the thickest photoresist has to be chosen among all three layers and spin coated uniformly over the entire structure during the conventional pattern of layer 3. However, care is then needed to ensure complete exposure of the thickest resist layers; failure to do so results in the creation of additional artefacts. These difficulties may be minimised by reducing the mesa height as far as possible.

### 6.4.3 Degradation

Degradation is another key problem in the multi-layer process. During the initial patterning of the overlaid mesas, edge quality of the first set of mesas is degraded by the DRIE step used to form the second set. In addition, the physical sputtering used to strip the horizontal metal surfaces does also erode the vertical surfaces of the the Si mesas, as well as remove some of attached sidewall masks. All these may result in sidewall masks degradation with poor qualities. As shown in Figure 6.27a, sidewall masks on the higher mesa surface has been over-etched which breaks the links between the two metal layers. Hence, etched HAR features in Figure 6.27b are found discontinuous in these regions which should certainly affect the stability of the two-dimensional mechanical structures. And worse still, the over-etched masks are too thin to protect the Si beam underneath in the deep etching from lateral erosion. Almost 1/3 of the Si

features are eroded as shown in Figure 6.27b.

The degradation effect can be worse if there is a significant quality difference between the two metal layers of the formed sidewall masks. As shown in Figure 6.27c, nanoscale features patterned in only one STL layers manage to survive after the final DRIE step while the remaining all be eroded severely. This must be attributed to degraded layer 1 mesa quality in layer 2 etching. Figure 6.27d shows a similar failure on the mesh spring. However, this time only features derived from the overlaid mesas are eroded, which illustrates that sidewall masks in intersecting regions are initially exhausted in an over-etched case.



| (a) | (b) |
| (c) | (d) |
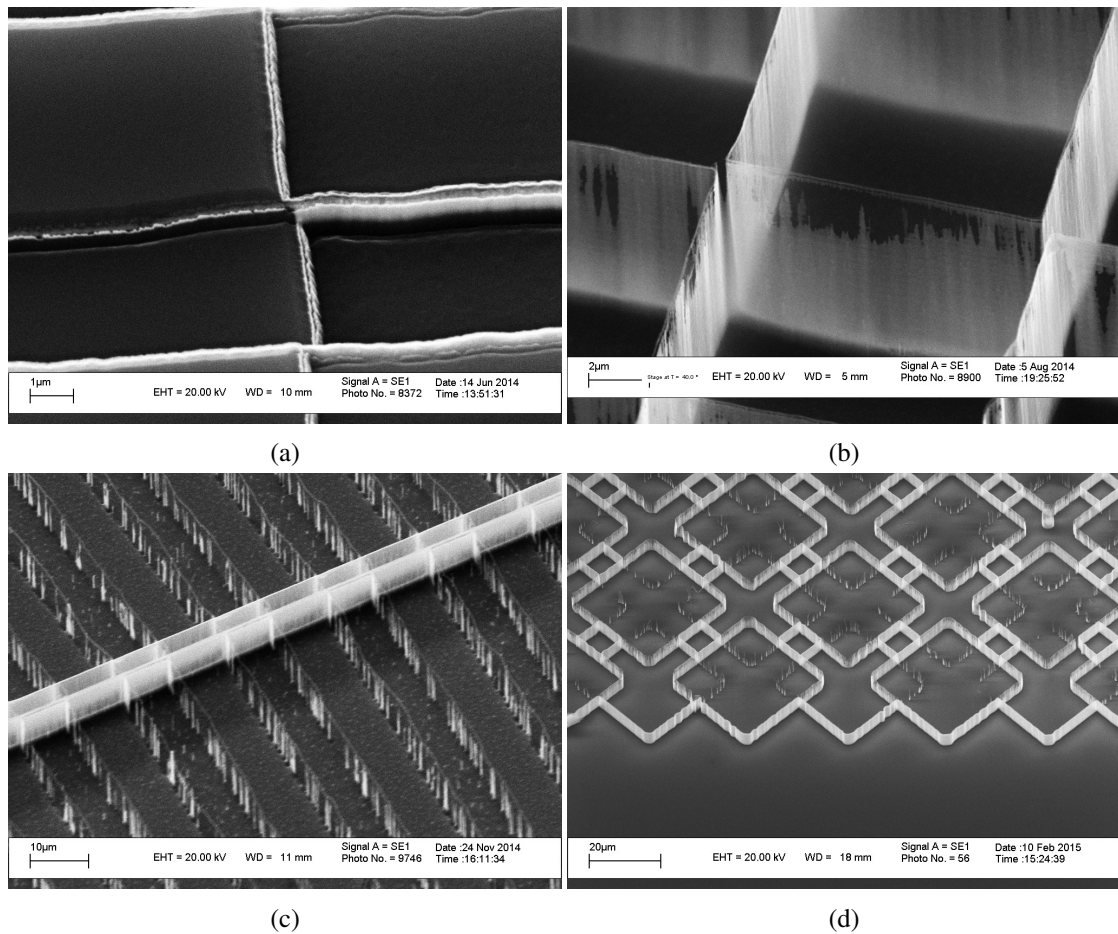
Figure 6.27: SEM views showing the effect of degradation.

To maintain the integrity and continuity of the sidewall masks, special care is needed to prevent over-etching in sputtering, and highly vertical overlaid mesas should surely improve achieved feature quality. Increased mesa height should provide better shading for the sidewall masks thus alleviate the problem somehow, however other processing problems such as planarization should also be taken into comprehensive consideration to balance the effects. Hence, process parameters in a multi-layer STL process need to be chosen carefully depending on dif-

ferent factors in practice.

## 6.5 Discussion

As introduced in this chapter, a multi-layer sidewall transfer lithography process has been designed and developed for mass parallel fabrication of NEMS. Nanoscale features are spread over multiple photomasks, and repetitive cycles of optical lithography and shallow etching are used to transfer these features into a terraced structure. The nanoscale features are formed by depositing a common layer of low stress metal whose vertical surfaces are selectively etched to provide a sidewall mask. The defined pattern is transferred into the silicon as a HAR nanostructure by DRIE, together with other microscale features which can be added in extra conventional lithography steps. The formation of suspended parts is then achieved by either removing the sacrificial layer on a BSOI device or plasma undercut on bulk silicon. Using such processes, multilayer nanoscale structuring of silicon has been demonstrated with a width of 100nm and an aspect ratio of 50 : 1.

Although achieved intersecting nanostructures have broken certain topological constrains and extended the range of applications of previous STL, the process still suffers from a number of limitations. Some of these limitations are inherited from the single-layer STL while the others are initially observe in multi-layer STL. Firstly, additional photomasks are required, since the nanoscale features are spread over multiple layers. Nevertheless, the masks contain relatively large features, and may therefore be low cost. Secondly, overlaid nanoscale features can suffer from microscale alignment errors, and it is important that these do not impact on device operation. Thirdly, overlaid features suffer a gradual degradation in repetitive etching steps, and a thicker resist is required to achieve planarization on mesa features formed in earlier stages. Fourthly, intersecting features contain shallow steps derived from the original mesa pattern. Finally, additional efforts are needed to remove the metal sidewall masks which currently remains in situ. Appropriate mask materials have to be chosen and deposited with special care to avoid stress induced distortion on suspended structures.

Apart from these, surprisingly good results can be obtained. And it is worth noting that the 100nm in plane feature size demonstrated here is limited mainly by the use of a cyclic DRIE process with relatively deep sidewall scallops. Much smaller features are clearly possible using improved etching process and equipment. Current results shows that a wide range of

nanostructures with different potential application aims can be designed and fabricated. And it is likely that the range of possible features can be increased using additional process steps and alternative structure lay-outs.

# 7 Nanoscale metamaterial suspensions

## 7.1 Introduction

In Chapter 6 multi-layer STL has been used to fabricate different types of 2D NEMS suspensions, including nano-scale mesh springs. In this chapter, a simple analysis is developed to allow the mechanical performance of the mesh springs to be compared with the COMSOL$^{\circledR}$ FEA predictions and experimental results. Using this analysis we then show that the 2D lattice can be understood as a material, with equivalent mechanical properties. However, since the structure can become very complicated as the number of repeating units increases, it is difficult to construct an exact analytic theory. Although FEA solvers such as COMSOL$^{\circledR}$ should provide a suitable method of exact analysis, special care must be taken in modelling complicated structures consisting of slender beams, due to the rapid rise of elements in meshing which greatly increases the memory requirements and simulation time.

## 7.2 Mechanical metamaterials

Mechanical metamaterials make use of internal structuring to obtain tailored or new elastic properties [135–137]. Most existing structures are relatively large and made of polymers which cannot be integrated easily in silicon-based MEMS and NEMS. Here we show that multi-layer STL can be used for mechanical metamaterial fabrication, and also for combining nanostructures with microscale parts. Although in comparison with most existing methods, the resulting metamaterials must necessarily be two-dimensional, multi-layer STL still has advantages in terms of its high compatibility and throughput.

Different lattices can be constructed using multi-layer STL, simply by change the patterns used in STL layer 1 and layer 2. For example, Figure 7.1 shows two types of mesh springs considered here. In Figure 7.1a, long, thin rectangles are laid out in two perpendicular directions in the two mask layers, and overlap to form a periodic structure with a square element as a unit

cell (type 1). In Figure 7.1b, an alternative design is demonstrated by overlapping smaller squares, leading to a castellated unit cell (type 2).

Obviously, the two types of material should deflect in different ways, depending on the end loads. For example, if the loads are applied in the x- or y-directions, the structure can distort by bending. However, if the loads are applied in the direction of $x = \pm y$, only axial loads are presented on the individual elements, so no bending can be expected. Thus, it can be expected that the mechanical performance of both types of lattices will be highly anisotropic.
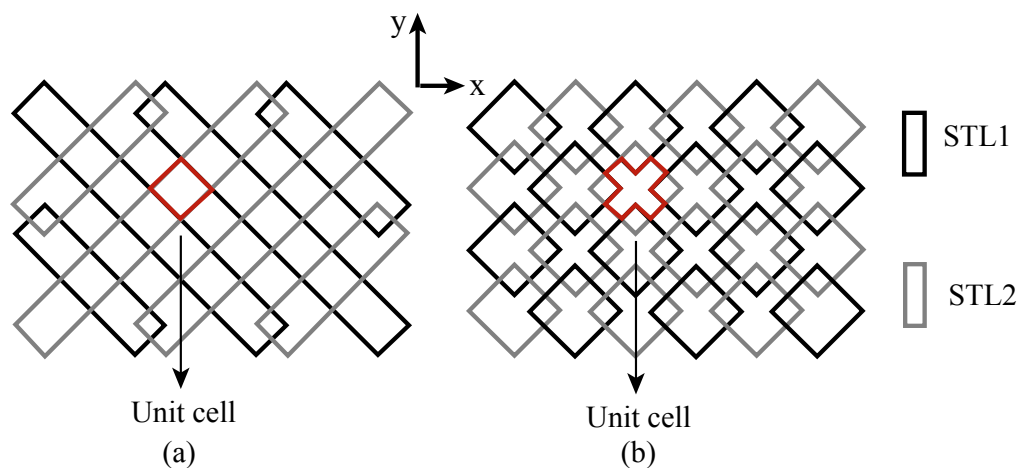


Figure 7.1: Lay-out of (a) type 1 and (b) type 2 nano-mesh suspensions and unit cells fabricated using the multi-layer STL process.

Due to the large open space at the centre of each unit cell, one likely advantage is a large reduction in the effective Young's modulus for the material under axial loads. The other is a larger deflection that can be sustained before the breaking strain of the bulk material is reached.

As known, all crystalline media (e.g. silicon) are really anisotropic, and have different values of Young's modulus in different crystal orientations. The artificial lattice structure constructed using multi-layer STL can introduce an additional mechanical periodicity, which makes the value of Young's modulus controllable and adaptable independently of the crystalline material itself. The new structure hence can be recognised as a new type of mechanical metamaterial.

A number of attempts have already been made to develop suitable techniques for fabricating such materials, including moulding, direct-write laser nanolithography [138], microstereolithography [139] and micro-origami [140]. Some novel properties have been demonstrated and investigated, such as negative Poisson's ratio and negative compressibility. Nonetheless, most of these structures have been made of materials with poor mechanical properties such as polymers. In addition, since most of the processes are not compatible with existing silicon fab-

rication methods, it is also difficult to integrate these structures with other conventional parts in a complete system. Hence, limited progress has been made on investigating the mechanical response of such structures, apart from the case of pure tensile loads. As a low-cost nano fabrication process, multi-layer STL enables 2D silicon structures such as a metamaterials to be combined easily with conventional MEMS parts, allowing more complex loads to be applied [134]. Also, the structures can be integrated with conventional MEMS such as actuators for further investigation.

## 7.3 Analytic model

In this section, analytic models are developed for type 1 and type 2 lattices shown in Figure 7.1 for diagnostic purposes. The analysis begins with a single unit cell and is then extended to complete mesh structures. The response of the material is considered under different types of loads (e.g. axial and transverse). Results are then combined with data from FEA simulation and experiments for comparison in Section 7.4 and 7.5 respectively. For both types of lattice, the new materials have shown different effective mechanical properties. For reason that will become evident, type 2 lattice has been used for experiments. However, the theoretical analysis starts with type 1 since this has a simpler structure.

### 7.3.1 Type 1 lattice

#### 7.3.1.1 Analysis of single cell

Figure 7.2a shows a single unit cell of type 1 lattice with side length of $L$, in-plane width of $w$ and depth of $d$. The corresponding second moment of area for a individual beam is hence $I = \frac{w^3 d}{12}$, and $E$ is the Young's modulus of the material forming the structure. The analysis begins by assuming an in-plane, uni-axial tensile load F along the diagonal.

A free body diagram can then be drawn for each beam of the loaded cell. As show in Figure 7.2b, for the upper half of the cell, the load $\frac{F}{2}$ can be resolved into parallel and perpendicular directions for each beam, resulting in an axial and a transverse force both equal to $\frac{F}{2\sqrt{2}}$, with an additional moment $M$ in each case. Since the beams are likely to be slender (assuming $w = 0.1\mu$ from STL), it is then reasonable to ignore the axial extension compared with the effects of bending. The model is then simplified into the case of bending of a fixed-guided beam, well-known in classical theory.
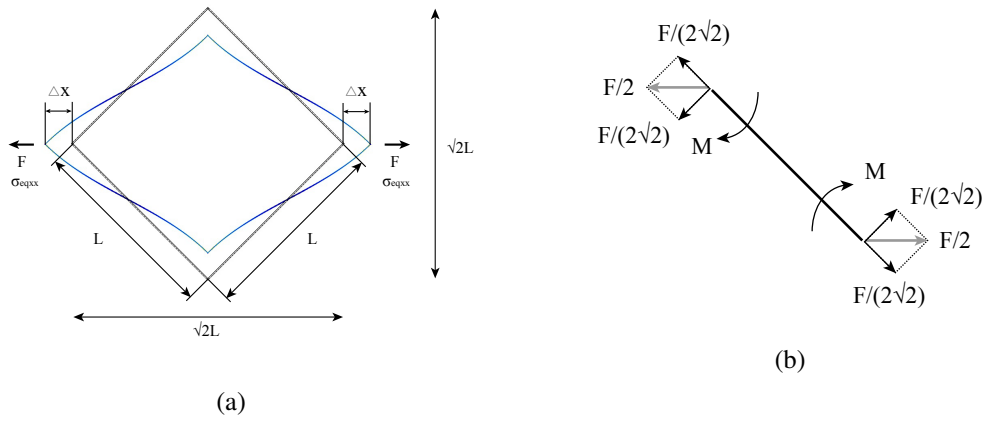
Figure 7.2: (a) Schematic diagram of isolated type 1 unit cell under uni-axial load $F$; (b) free body diagram of a loaded single beam.

For this case, the beam should undergo a transverse deflection $\triangle = \frac{PL^3}{12EI}$, where the load $P = \frac{F}{2\sqrt{2}}$. Considering that a single cell in Figure 7.2a has two sets of beams in series, a net axial extension $\triangle x$ is obtained, which is twice the value of $\triangle$ after projection in the direction of $F$. Thus $\triangle x = \frac{FL^3}{24EI}$, and the stiffness $k$ of a single unit cell is:

$$k = \frac{F}{\triangle x} = 2d \left(\frac{w}{L}\right)^3 E \tag{7.1}$$

However, it should be noted that the beam may deflect in completely different ways under other types of loads as shown Figure 7.3. For example, Figure 7.3a shows a single cell under uniaxial tension in the y-direction; clearly, the analysis here should be exactly the same as the case in Figure 7.2a except that the whole structure is rotated by 90°. However, Figure 7.3b shows a single cell loaded by biaxial tension; in this case there can be be no bending at all, since only axial tensile forces are present. Figure 7.3c shows a single cell loaded by uniaxial compression. The value of $k$ can be calculated in a similar analysis above. Again the distorted pattern should be the same as shown in Figure 7.2a although rotated by 90°. Finally, Figure 7.3d shows a single cell loaded by biaxial compression. With only axial compressive force on each beam, the elements must buckle after the bukling load is reached.
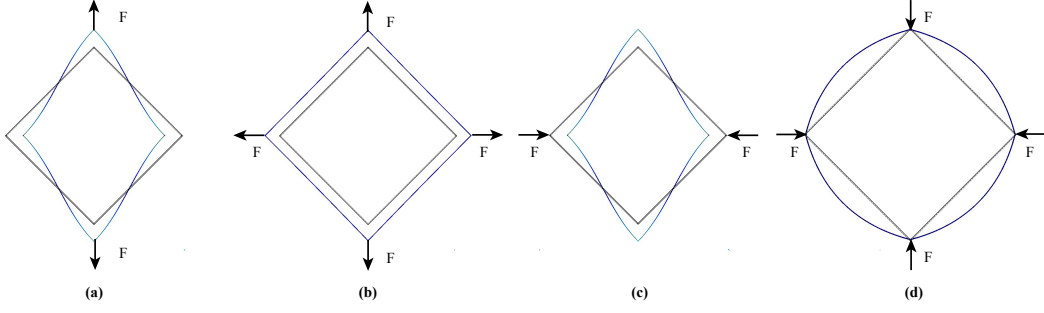
Figure 7.3: Schematic diagrams of type 1 cell under different types of loads: (a) uniaxial tension in y-direction; (b) biaxial tension; (c) uniaxial compression in x-direction; (d) biaxial compression.

### 7.3.1.2 Equivalent bulk parameters

As a novel type of mechanical metamaterial, one advantage is that it is now possible to derive the equivalent bulk parameters of the lattice from the structural parameters and constituent materials. As shown in Figure 7.2a, with a uniaxial load $F$ applied over the cell, the equivalent cross-sectional area is $A = \sqrt{2}Ld$. Hence, the equivalent normal stress is $\sigma_{eqxx} = \frac{F}{\sqrt{2}Ld}$. Considering that the change in length occurs over a span of $\sqrt{2}L$, the equivalent normal strain $\varepsilon_{eqxx}$ is hence $\frac{\triangle x}{\sqrt{2}L}$. Thus we can obtain the equivalent Young's modulus of the material as:

$$E_{eq} = \frac{\sigma_{eqxx}}{\varepsilon_{eqxx}} = \frac{F}{d \triangle x} \tag{7.2}$$

Knowing that $\triangle x = \frac{FL^3}{24EI}$ and substituting $I = \frac{w^3 d}{12}$, we then obtain the effective Young's modulus as:

$$E_{eq} = 2 \left(\frac{w}{L}\right)^3 E \tag{7.3}$$

It thus appears that the value of Young's modulus is reduced by a factor of $2\left(\frac{w}{L}\right)^3$ by constructing a latticed structure using the bulk material (i.e. silicon). In actual experiments, the factor can be very small due to $w \ll L$ ($w = 0.1\mu$, $L = 30\mu$, $2\left(\frac{w}{L}\right)^3 \le 7.41 \times 10^{-8}$). Moreover, it is now possible to change the value of $E_{eq}$ of the material simply by varying the value of $w$ and $L$, which is comparably easy from a design point of view. Also, from the analytic model of a single cell above, it is easy to obtain the corresponding contraction $\triangle y$ in y direction, which clearly has the same value as $\triangle x$. Thus the structure should have a Poisson's ratio of $v = 1$ as a 2D material. Although this value may be too large for most of the applications, it is also possible to change the value of $v$ by varying the angle of the beams. With an angle $\theta$, the corresponding

Poisson's ratio should be $v = \cot\theta$. However, this may change the value of $E_{eq}$ as well.

### 7.3.1.3 Effect of boundaries

The method to analyse a loaded free mesh with multiple cells should be similar as above. As shown in Figure 7.4b, a $3 \times 2$ mesh is attached to a rigid boundary on one end and free on the other. However, due to the boundaries of the practical structure, there is expected to be small departures from the exact periodicity at the edges of the repeated pattern. Although such effects also occur in a crystalline lattice, they are less noteworthy since the size of each unit cell is much smaller.

However, there should be additional differences between the boundary cells rigidly attached to the anchor and those on the free end. It is again less noticeable in a crystalline medium since the Poisson's ratio is smaller than here. If the mesh structure has a sufficiently large number of cells, these effects could be ignored for similar reasons as conventional media. But the increased size of the whole structure may be difficult to integrate into MEMS/NEMS devices of realistic size.

The analysis begins with the simplest case with a $2 \times 1$ mesh attached to a rigid boundary, as shown in Figure 7.4a. Here the boundary span $S$ cannot change between fixed nodes B and C. Similarly, node A cannot move if the axial forces are neglected for thin beams. Thus it is impossible for the structure to distort in the same way as a free cell. Instead, if nodes D and E on the free end are constrained from rotating, the structure should deflect as a portal frame under shear as shown in Figure 7.4a.

In this case, a similar analysis of the distorted structure can be drawn as before. A shearing force $F$ is applied on each portal with two single beams. Projected in the transverse direction, the transverse load is hence $\frac{F}{2\sqrt{2}}$ on each beam, leading to a transverse deflection $\triangle = \frac{PL^3}{12EI}$ according to classical theory. Substituting $P = \frac{F}{2\sqrt{2}}$ and projecting in the direction of $F$ as before, the final axial extension is $\triangle x = \frac{FL^3}{48EI}$. Although $\triangle x$ is half the value in the case of a free cell, we shall still obtain $\triangle y = \frac{FL^3}{24EI}$ for two portals in parallel. Hence the deformed span $S\prime$ for the portal frames is exactly the same as that of a set of free cells as shown in Figure 7.4b. Consequently, there is no need to repeat the analysis for the attached mesh, since we can simply attach the set of free cells directly to the boundary cells without any discontinuity in span. It is therefore convenient to do the analysis separately for boundary and free cells and combine the results together.
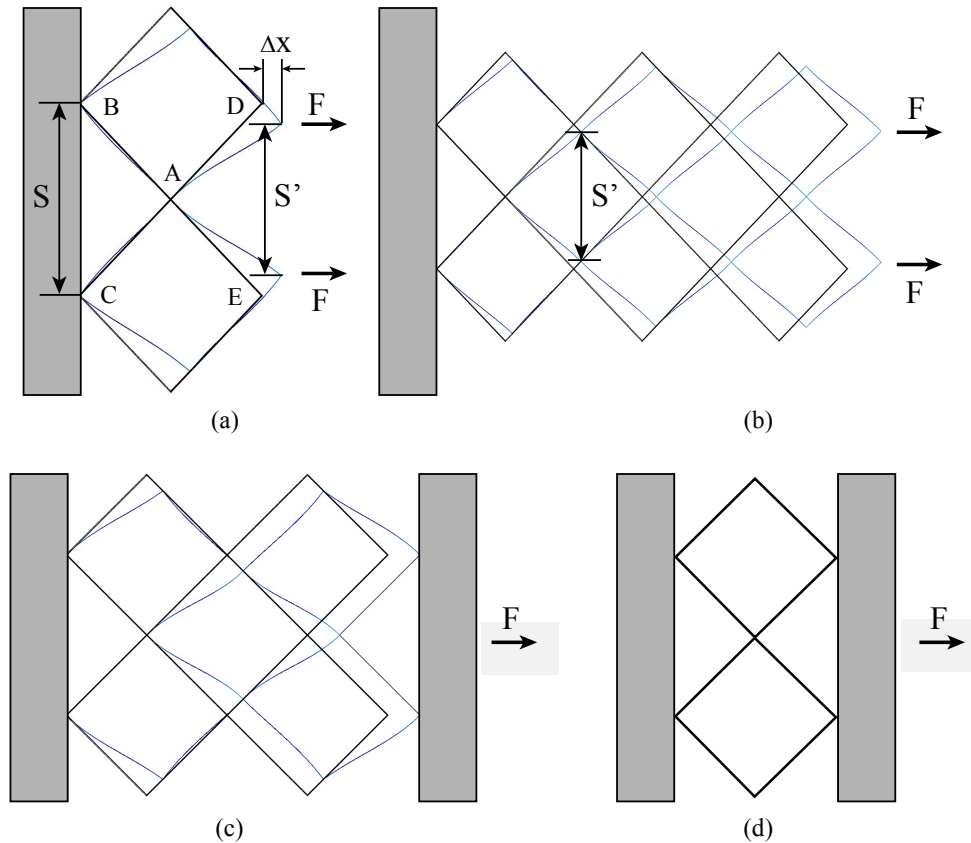
Figure 7.4: Schematic diagrams of: (a) attachment of two type 1 cells to a fixed boundary; (b) continuation to a free lattice; (c) $2 \times 2$ and (d) $1 \times 2$ lattice with both ends constrained.

However, it is noticeable that these results are obtained on the assumption that there is no rotation of the cells on the free ends. Such artificial constraint may be invalid in the realistic case. Nevertheless, for individual cells fully surrounded by other elements, the rotation on each corner should be constrained by the other three elements. Consequently, limited rotation should be expected.

The same principle can be easily adapted to analyse meshes with rigid constraints at both ends. For example, as shown in Figure 7.4c, a $2 \times 2$ mesh is fixed at one end and linked with a rigid connector on the other. Obviously, only the single cell in the middle can distort as a free cell while the other four surrounding it should deflect as portal frames. Figure 7.4d shows a $1 \times 2$ mesh, where the structure cannot move at all.

The next step is to extend the analysis to meshes with an increased number of cells attached to a boundary. As shown in Figure 7.5, a $10 \times 4$ mesh spring with rigid constraints are loaded with axial tensile force. On both ends near the boundaries, there must be a triangular region where the beams cannot deflect at all. The two adjacent regions should contain cells that distort

as portal frames. Beyond these, the rest of the cells, particularly in the middle of the spring, then behave as free structures. The deformed shape of the mesh spring is shown by the lines at the edge. The width of the spring should taper gradually and then reach a constant value in the middle, where the cells are unconstrained. Based on the analytic model above, it is then reasonable to expect a linear decrease of the spring width from the boundary, until it reaches the width of a stretched free mesh in the middle. As shown, to reach this 'free width', the symmetric regions on both ends cannot overlap. As a result, a general $M \times N$ mesh must satisfy the constraint that $M \geq 2N$. Also, the elements near the boundaries cannot relax as much as the free cells, which should make the spring stiffer. If the spring is not long enough, for example as shown in Figure 7.5b, where the portal frame regions at each end overlap, new regions of fixed cells will be generated, with less free cells. Consequently, if the spring is extremely short and wide, the two fixed regions will overlap completely and the whole structure will be unable to move.
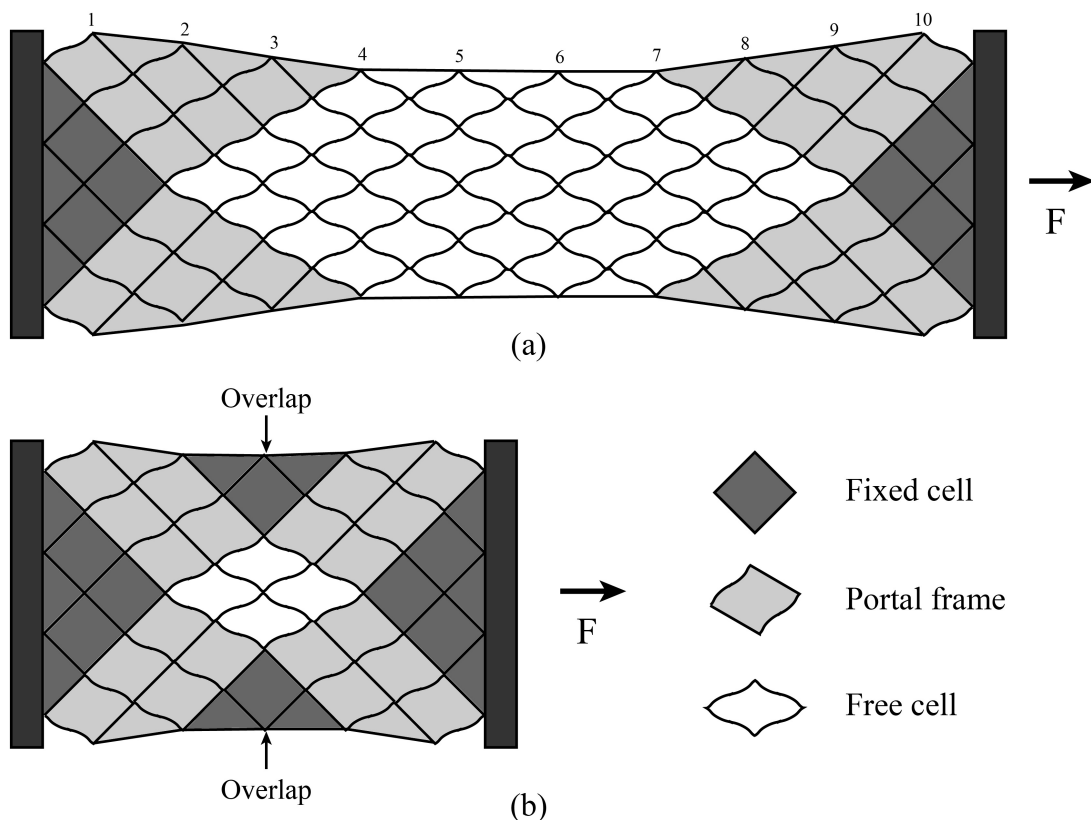


Figure 7.5: Schematic diagrams of: (a) a $10 \times 4$ and (b) $5 \times 4$ type 1 spring with both ends constrained under axial tensile loads.

### 7.3.1.4 Transverse load

A similar analysis can be made for the deflected mesh under bending. For example, Figure 7.6a shows two parallel cells loaded with equal forces $F$ in the opposite directions (upper cell under tension and lower cell under compression). The horizontal axis of symmetry roughly corresponds to the neutral axis in the conventional bending theory. It is then reasonable to expect bending to occur on the lines $A - A\prime$ and $B - B\prime$ under $F$. For a cascaded mesh with more elements, the structures are expected to curve into a circular arc, much as a uniformly bent beam.
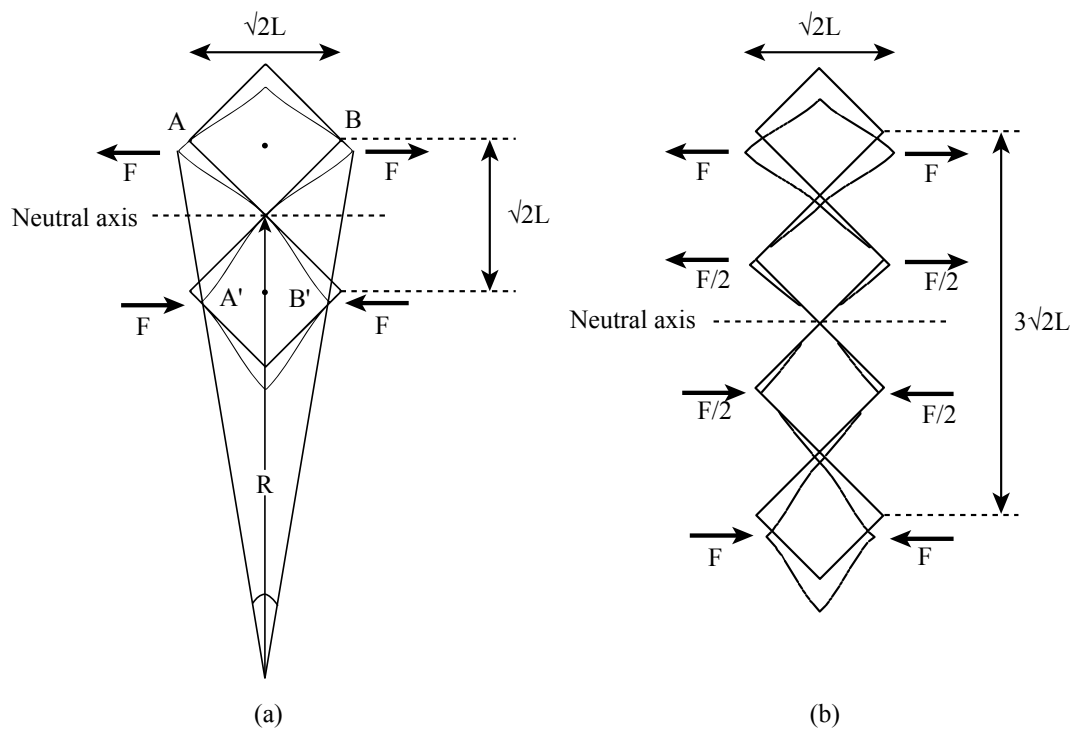


Figure 7.6: Schematic geometries for calculating relation between applied loads band bending of (a) two-cell and (b)four-cell beam.

In this case, the analysis can follow the general approach of classic beam bending theory. Figure 7.6a shows two cells that have been bent into an arc of a radius of $R$. Based on previous analysis, the axial deflection of both cells are $\triangle x = \frac{FL^3}{24EI}$, when the upper cell extends and the lower cell contracts. The two cells are $\sqrt{2}L$ apart (the distance between the two centres). Thus, the subtended angle $\theta$ can be approximated as $\theta = \frac{2\triangle x}{\sqrt{2}L}$. Considering the cell width is $\sqrt{2}L$, we

also have $\theta = \frac{\sqrt{2}L}{R}$. Eliminating $\theta$ from the two equations above, we then obtain:

$$\theta = \frac{\sqrt{2}L}{R} = \frac{2\triangle x}{\sqrt{2}L}$$
$$\frac{1}{R} = \frac{FL}{24EI}$$

(7.4)

The bending moment $M$ of $F$ on the structure is $M = \sqrt{2}FL$. Considering the equivalent Young's modulus obtained in Equation (7.3), it is then possible to combine these results and achieve:

$$\frac{1}{R} = \frac{M}{\sqrt{2}E_{eq}dL^3}$$

(7.5)

Assuming the equivalent second moment of area $I_{eq}$ of the structure in Figure 7.6a as $I_{eq} = \sqrt{2}dL^3$, we can then get:

$$\frac{1}{R} = \frac{M}{E_{eq}I_{eq}}$$

(7.6)

Obviously, this result agrees with the beam bending equation in the conventional theory. With the approximation that $\frac{1}{R} \approx \frac{d^2y}{dx^2}$ where $y$ is the transverse deflection, Equation (7.6) should be a standard Euler beam bending equation. It is then reasonable to expect the metamaterial beams to bend in plane like conventional beams, with suitable values of $E_{eq}$ and $I_{eq}$ chosen.

The analysis then should be extended to beams with more cells across the equivalent beam width. Figure 7.6b shows a four-cell structure loaded in the same way as before, assuming that the axial load changes linearly towards the neutral axis as in the conventional theory. Again, the top cell should extend and the bottom cell should contract by the same amount of $\triangle x = \frac{FL^3}{24EI}$. Now the effective width of the beam is $3\sqrt{2}L$, we shall have $\theta = \frac{2\triangle x}{3\sqrt{2}L}$. Since the width of the individual cell remains the same ($\sqrt{2}L$) we can obtain:

$$\theta = \frac{\sqrt{2}L}{R} = \frac{2\triangle x}{3\sqrt{2}L}$$
$$\frac{1}{R} = \frac{1}{3} \cdot \frac{FL}{24EI}$$

(7.7)

Considering that the new moment due to the loading is now $M = \frac{7}{2}\sqrt{2}FL$, we can again combine the above results with the equivalent Young's modulus as before, to obtain:

$$\frac{1}{R} = \frac{M}{3 \times \frac{7}{2}\sqrt{2}dL^3}$$

(7.8)

Thus, the value of $I_{eq}$ in the four-cell structure is $I_{eq} = 3 \times \frac{7}{2}\sqrt{2}dL^3$. The same method can then be used to find the value of $I_{eq}$ for even wider beams. The results are shown in Table 7.1. Here, the first column shows the number $N$ of cells across the beam width. The second column shows the values of $I_{eq}$ calculated using the method above. These results are re-arranged for in the third column. Using this column, an exact induction formula for the variation on $I_{eq}$ with N can then be extracted as:

$$I_{eq} = \left(N^3 + \frac{1}{2}N^2 - \frac{5}{2}N + 1\right)\frac{d(\sqrt{2}L)^3}{12} \qquad (7.9)$$

Clearly, $I_{eq}$ follows the form of the standard result for a rectangular beam, namely $I = \frac{dw^3}{12}$, with a factor $f = N^3 + \frac{1}{2}N^2 - \frac{5}{2}N + 1$. As the value of $N$ increases, it is clear that the factor $f \approx N^3$. In this regime, $I_{eq}$ can be approximated as $I_{eq} = \frac{d(N\sqrt{2}L)^3}{12}$, as shown in the fourth column.

There is clearly close agreement between the third and fourth columns in Table I, implying that the equivalent second moment of area of the metamaterial beam can be predicted from the equivalent beam width $N\sqrt{2}L$ and depth $d$. Departures from the conventional formula can be understood in terms of weakened edge effects of the meshed structure. In other words, the deflection of a metamaterial beam during bending should approach that of a conventional beam as the beam becomes wider, even though the internal structure may be complex.

| $N$ | $I_{eq}$ | | $\frac{N^3}{12}d(\sqrt{2}L)^3$ |
|---|---|---|---|
| 2 | $\sqrt{2}dL^3$ | $\frac{6}{12}d(\sqrt{2}L)^3$ | $\frac{8}{12}d(\sqrt{2}L)^3$ |
| 4 | $3 \times \frac{7}{2}\sqrt{2}dL^3$ | $\frac{63}{12}d(\sqrt{2}L)^3$ | $\frac{64}{12}d(\sqrt{2}L)^3$ |
| 6 | $5 \times \frac{22}{3}\sqrt{2}dL^3$ | $\frac{220}{12}d(\sqrt{2}L)^3$ | $\frac{216}{12}d(\sqrt{2}L)^3$ |
| 8 | $7 \times \frac{50}{4}\sqrt{2}dL^3$ | $\frac{525}{12}d(\sqrt{2}L)^3$ | $\frac{512}{12}d(\sqrt{2}L)^3$ |
| 10 | $9 \times \frac{95}{5}\sqrt{2}dL^3$ | $\frac{1026}{12}d(\sqrt{2}L)^3$ | $\frac{1000}{12}d(\sqrt{2}L)^3$ |

Table 7.1: Equivalent second moments of area for type 1 metamaterial beams with different numbers of cell.

However, for a cascaded set of meshed structures curved into a circular arc, it is worth noting that the cells in series on both the top and bottom edges should contain a series of discrete steps due to the tensile and compressive loads. Thus there should be additional rotations of the beams expected to join the cells together without discontinuities. FEA has also been used to investigate the deflection in a realistic case to prove the estimation made above. These details will be shown in Section 7.4.

### 7.3.2 Type 2 lattice

We now consider the development of a similar analytic model for the type 2 lattice. Figure 7.7a shows a unit cell consisting of 12 individual beams of length $\frac{1}{3}L$, loaded with an axial tensile forces $F$. Obviously, only the four beams at the top and bottom of the cell are loaded, with a transverse load $\frac{F}{2\sqrt{2}}$. Using the textbook transverse deflection $\triangle = \frac{PL^3}{12EI}$ where $P = \frac{F}{2\sqrt{2}}$, we shall have $\triangle = \frac{F}{648\sqrt{2}EI}$ for each beam. However, the structure in Figure 7.7a has four beams in series for each half cell. Consequently, projected in the axial direction, the net axial extension is $\triangle x = \frac{FL^3}{324EI}$. As a result, the stiffness $k$ of a single type 2 cell can be found as:

$$k = \frac{F}{\triangle x} = 27d \left(\frac{w}{L}\right)^3 E \tag{7.10}$$

Comparing the above result with the type 1 cell in Equation (7.10), the stiffness of type 2 cell is $\frac{27}{2}$ times larger. This result can be understood as the effects of reducing the beam length $L$ by a factor of 3 (the numerator $27 = 3^3$) and doubling the number of beams in series (the denominator 2).

The next step is then derive the equivalent bulk parameters of the type 2 material as before. As shown in Figure 7.7a, with a uniaxial load $F$ applied over the cell, the equivalent cross-sectional area is $A = \frac{4}{3}\sqrt{2}Ld$. Hence, the equivalent normal stress is $\sigma_{eqxx} = \frac{3\sqrt{2}F}{4Ld}$. Considering that the change in length occurs over a span of $A$, the equivalent normal strain is: $\varepsilon_{eqxx} = \frac{3\sqrt{2}\triangle x}{4L}$. Thus we can obtain the equivalent Young's modulus of the material as:

$$E_{eq} = \frac{\sigma_{eqxx}}{\varepsilon_{eqxx}} = \frac{F}{d\triangle x} \tag{7.11}$$

Knowing that $\triangle x = \frac{FL^3}{324EI}$ and substituting $I = \frac{w^3d}{12}$, we can get:

$$E_{eq} = 27 \left(\frac{w}{L}\right)^3 E \tag{7.12}$$

Consequently, the value of Young's modulus for the type 2 metamaterial is also larger by a factor of $\frac{27}{2}$ compared with the type 1 material. It then seems that the type 2 material is stiffer than the type 1 material mechanically. Nevertheless, care must be taken of other mechanical properties for comprehensive comparison of relative performance. For example, as the elements in type 2 structure can also twist, we may expect the structure to be less resistant to out-of-plane bending compared with the type 1. Such prediction has successfully been verified experimentally: most
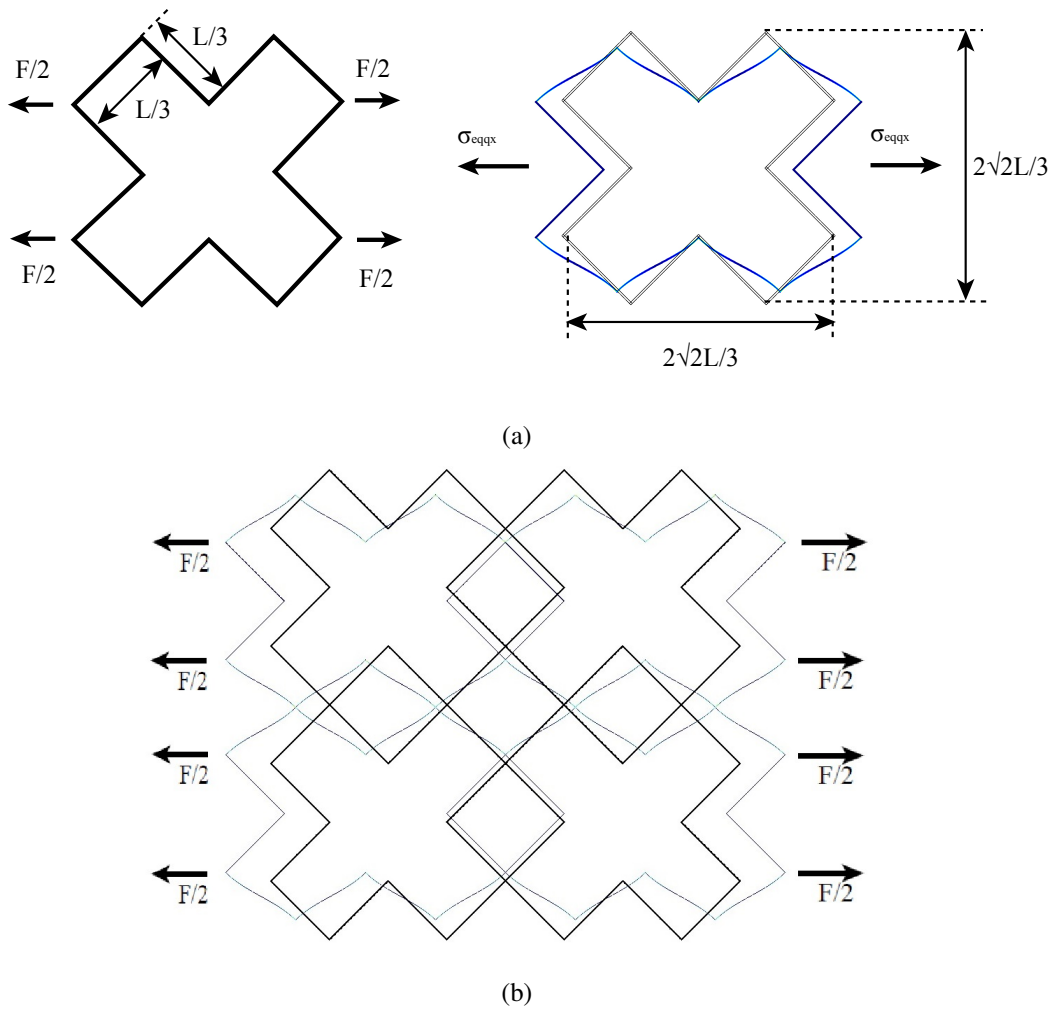
Figure 7.7: Schematic diagrams of: (a) isolated single type 2 cell and (b) $2 \times 2$ mesh under axial tensile loads.

type 2 structures tend to buckle out-of-plane easily under axial compressive loads.

Ideally, the deflection of a free mesh under loads, as shown in Figure 7.7b, should be analysed in the same way as before. Obviously, similar results can be expected that there should be difference between the free cells and those attached to a rigid boundary. However, the analytic model is expected to be much more complicated than before, due to the complexity of the type 2 structure. Considering the above analysis for both type 1 and type 2 lattice has provided a reasonable estimation of the spring performance under different types of end loads, it is now worth investigating the behaviour properly. Hence, numerical methods such as FEA should really be used for comparison. Details of these will be fully explained in the next section.

## 7.4 Finite element model

In this section, FEA is carried out using the 2D solid mechanics module of a finite element modelling software COMSOL® for comparison with the previous analytic results. Different structure geometries have been investigated, including variations of $M \times N$ mesh of both type 1 and type 2 materials. Structures have also been analysed subjected to axial and transverse loads with appropriate boundary conditions. For the mesh structures made of bulk material silicon, the following parameters have been assumed: the Young's modulus $E = 170 \times 10^9 \text{N/m}^2$, the Poisson's ratio $v = 0.28$, the element length $L = 30\mu\text{m}$, the depth $d = 4\mu\text{m}$ and different values of in-plane individual beam width $w$. The parameters are chosen to match those of the devices fabricated on BSOI later experimentally. Although COMSOL® struggles to model HAR structures, the deflected shape of different types of structures have been generated successfully for comparisons. In each case, the simulation generates similar deformed patterns as predicted by the analytic model, showing good agreement with the basic analysis.

To begin with, geometries of single unit cell of both type 1 and type 2 materials are investigated to calculate the axial stiffness $k$ in each case. These results are compared with the analytic theory as shown in Table 7.2. For single beam width $w$ varying from 0.05μm to 0.2μm, good agreement has been obtained between COMSOL® and the analytic model in each case, although the former is approximately 10% larger than the later for type 1 and 15% for type 2. However, the differences gradually reduce as $w$ reduces. Considering that bending should dominate more over axial stresses for thinner single beams, the results again agree with the approximate theory. Although the two predictions match better with smaller values of $w$, it is found difficult to model large arrays with thin elements. Thus, the value $w = 0.2\mu\text{m}$ has been chosen for subsequent simulations.

| Type 1 $w$ (μm) | Analytic $k_1$ (N/m) | FEM $k_1$ (N/m) | Ratio |
|---|---|---|---|
| 0.2 | 0.403 | 0.4535 | 1.125 |
| 0.1 | 0.0504 | 0.0556 | 1.1036 |
| 0.05 | 0.0063 | 0.0069 | 1.0926 |
| Type 2 $w$ (μm) | Analytic $k_2$ (N/m) | FEM $k_2$ (N/m) | Ratio |
| 0.2 | 5.44 | 6.472 | 1.1897 |
| 0.1 | 0.68 | 0.7728 | 1.1364 |
| 0.05 | 0.085 | 0.094 | 1.11 |

Table 7.2: Comparison between analytic and FEM predictions of single cell axial stiffness for type 1 (upper) and 2 (lower) metamaterials.

Metamaterial beams based on $M \times N$ lattices have then been investigated under axial tensile

loads for both type 1 and type 2 materials. For example, Figure 7.8a shows the deflected beam shape of a $10 \times 2$ array of type 1 cells with a total beam length $L_b$. The assumed boundary constraints are that the left end is fixed and the right end is connected by rigid bar. The predicted deflected shape is shown as sketched.

FEA modelling results for loaded type 1 and 2 beams are shown in Figures 7-9a and b respectively. In each case, the applied axial force is $4 \times 10^{-7}$N. The deflections in x- and y-directions have been calculated for all the top and bottom elements. The data is plotted as circles for $10 \times 2$ and crosses for $10 \times 4$ lattices. As shown in Figure 7.9a, for type 1 beams, the dotted lines show analytic predictions obtained using the method stated in Section 7.3. Good agreement has been obtained between the two predictions. Both methods have shown that the boundary elements should behave differently from elements in the center of the beam. The stiffness in this region is approximately twice the value of the free cell, as the deflections in the x- and y-directions vary gradually. The $10 \times 4$ array clearly takes longer to reach a constant 'free' width in the middle. In Figure 7.9b, similar behaviour can be found for type 2 beams, but with much smaller deflections obtained under the same load due to the comparably high value of $k$ for type 2 lattice. Also, the beam now relaxes from the boundary into the centre region much more quickly than the type 1 beam.



(a)

(b)
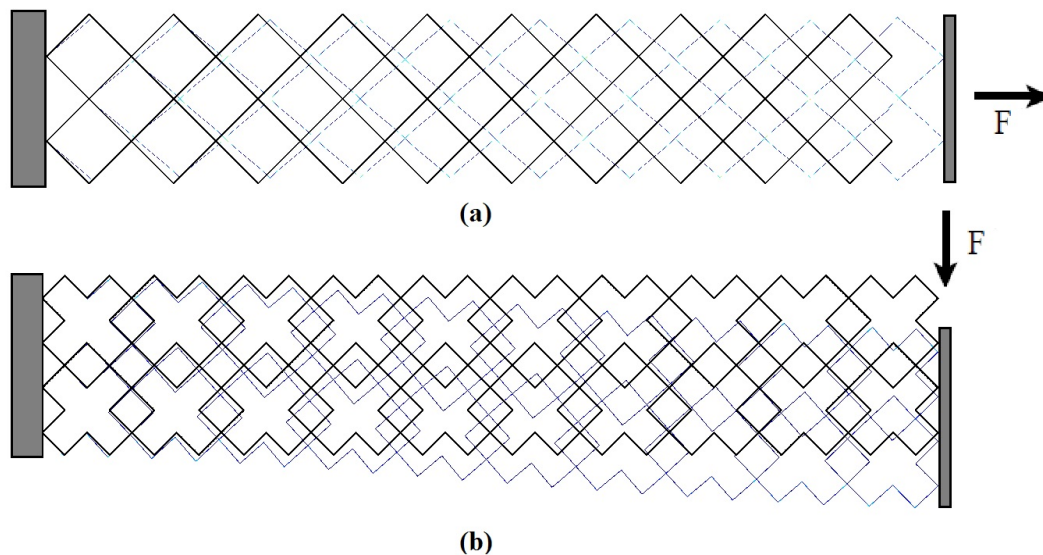
Figure 7.8: Numerical models of loaded metamaterial beams: (a) $10 \times 2$ type 1 beam under axial tensile load; (b) $10 \times 2$ type 2 beam under transverse load.

The same method has also been used to model deflected beams with $M \times N$ lattices under bending. For example, Figure 7.8b shows the deflected beam shape of a $10 \times 2$ array of type 2

cells with a total beam length $L_b$. To mimic conventional boundary conditions, a fixed constraint is applied on the left end, while the right end is tied by a rigid connector and guided. A transverse load of $4 \times 10^{-8}$N is applied on the right, and the predicted deflected shape is shown as sketched. Figure 7.10a and 7.10b shows the predicted results of type 1 and type 2 beams respectively, both with $10 \times 2$ (circles) and $10 \times 4$ (crosses) structures. As before, the deflection of edge elements in the x- and y-directions are plotted. In Figure 7.10a , the dotted lines show the prediction of the analytic theory. For a uniform beam with one end fixed and the other end guided, the transverse deflection along the beam based on the conventional beam bending theory is:

$$y(x) = \frac{F}{12EI}x^2(3L_b - 2x) \tag{7.13}$$

The lines show the deflections obtained by substituting the values of $E_{eq}$ and $I_{eq}$ developed previously. Clearly, the analytic prediction achieved using the effective medium method agrees well with the numerical FEA results, although there is a large axial deflection due to the high value of $v$. In Figure 7.10b, smaller x-deflections can be observed for type 2 beam, which might indicate a greater utility for the type 2 structure.



(a)                                                                 (b)
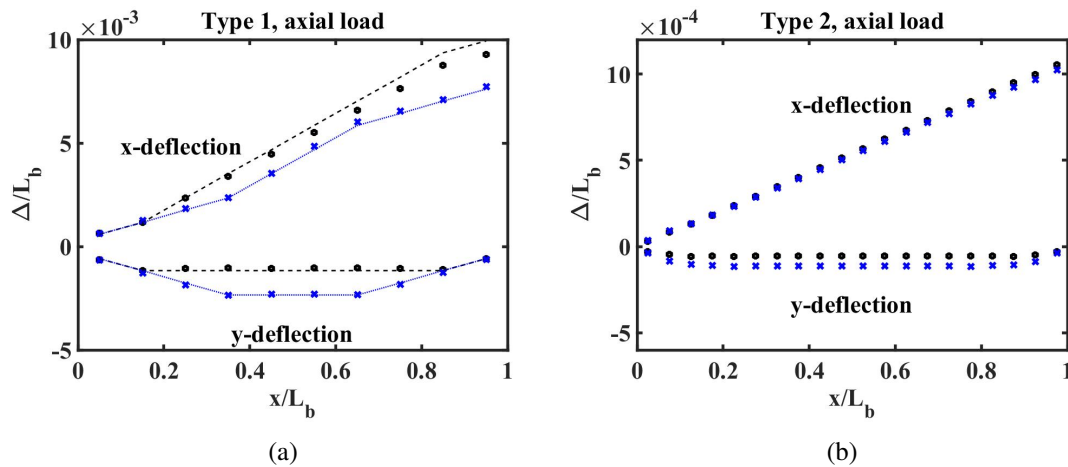
Figure 7.9: Comparisons between analytic (dotted lines) and FEA (points) predictions of x- and y-deflections of edge elements for $10 \times 2$ (black) and $10 \times 4$ (blue) (a) type 1 and (b) type 2 beams under axial tensile loads.

179
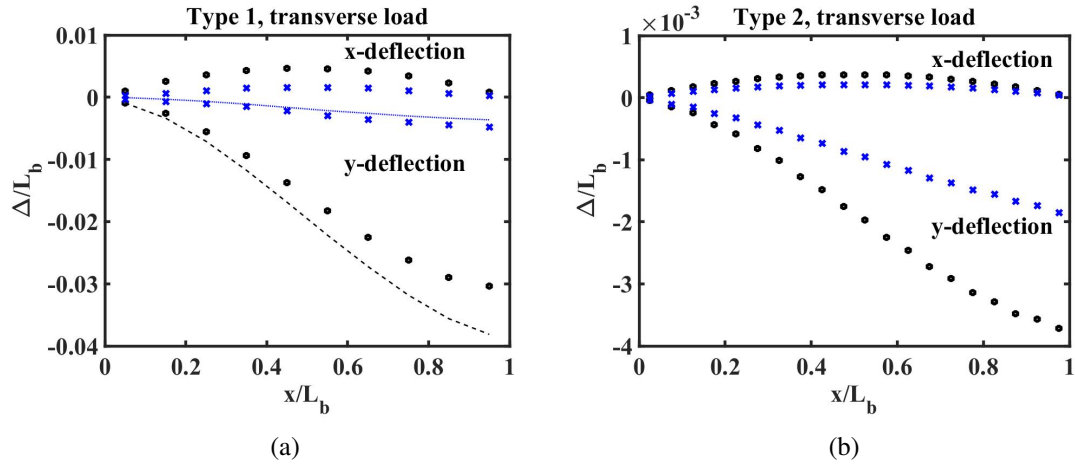
Figure 7.10: Comparisons between analytic (dotted lines) and FEA (points) predictions of x- and y-deflections of edge elements for $10 \times 2$ (black) and $10 \times 4$ (blue) (a) type 1 and (b) type 2 beams under transverse loads.

## 7.5 Experiment results

### 7.5.1 Prototype devices

Fabricated devices have been tested experimentally to compare with the predictions of the analytic models developed above. Devices with a variety of lay-outs have been made on BSOI wafers using the multi-layer STL process described in Chapter (6). As shown in Figure 7.11, test results for two main geometries will be presented. Figure 7.11a shows two sets of mesh springs anchored at one end and connected together by a rectangle linking unit on the other end. This arrangement allows displacements to be applied to the linking unit in both the x- and y-directions using a probe tip. In Figure 7.11b, a mesh spring is fixed at the left-hand end and attached to an electrostatic comb drive on the right, which allows calibrated axial loads to be applied.

However, it is worth noting that the meshed structures in both devices are made of the type 2 instead of type 1 metamaterial. Based on the previous analytic theory, type 1 metamaterial has a number of disadvantages. The effective Poisson's ratio is $v = 1$ which is too large for most applications. In addition, its unit cell can only be sheared in particular ways. These characteristics make it very different from conventional materials, with large unwanted perpendicular displacements and difficulties when attached to boundaries. However, the COMSOL® simulations show that type 2 material can behave much better; it has smaller perpendicular displacements, and matches much more smoothly to boundaries due to an effective Poisson's ratio $v = 0.54$. In addition, its unit cell can easily be distorted. These two facts provide considerably improved
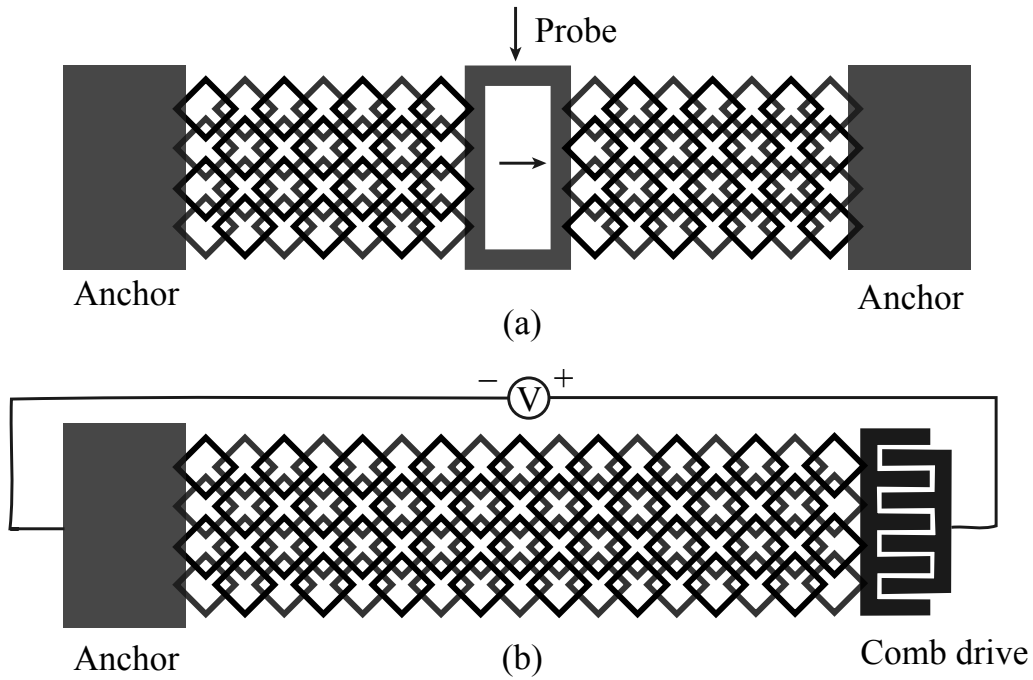
Figure 7.11: Schematic diagrams of test devices: (a) anchored type 2 mesh spring with link unit; (b) mesh spring combined with comb drive.

mechanical performance for the type 2 material.

Figure 7.12 shows SEM views of completed prototype devices before testing. Figure 7.12a shows two metamaterial beams with built-in ends attached to anchors on the left side. The meshes have been built with two different individual cell sizes ($L = 15\mu$m and $L = 30\mu$m). Different beam widths have also been demonstrated with 6 and 2 cells in parallel respectively. Figure 7.12b and 7.12c show metamaterial springs attached to microscale linking units and comb electrodes, respectively. In both cases, suspension has been achieved for released structures including nanoscale and microscale parts, with little sign of deformation due to the residual stress. Figure 7.12d shows a close-up of a metamaterial spring that has been buckled out-of-plane. The curved shape are smooth with the joints of nanostructures intact, showing that the type 2 structure can sustain very large out-of-plane deflection.

Large displacements can easily be applied to fabricated mesh springs using probe tips, and deflections can then be observed under an optical microscope. For example, Figures 7.13 and 7.14 shows the deformed structures of the device in Figure 7.11a after applying an axial tensile and a transverse deflection on the linking unit. The size of the mesh spring is $18 \times 16$ cells with element cell length of $30\mu$m. Microscope views of the device before and after loading have been taken for comparisons.
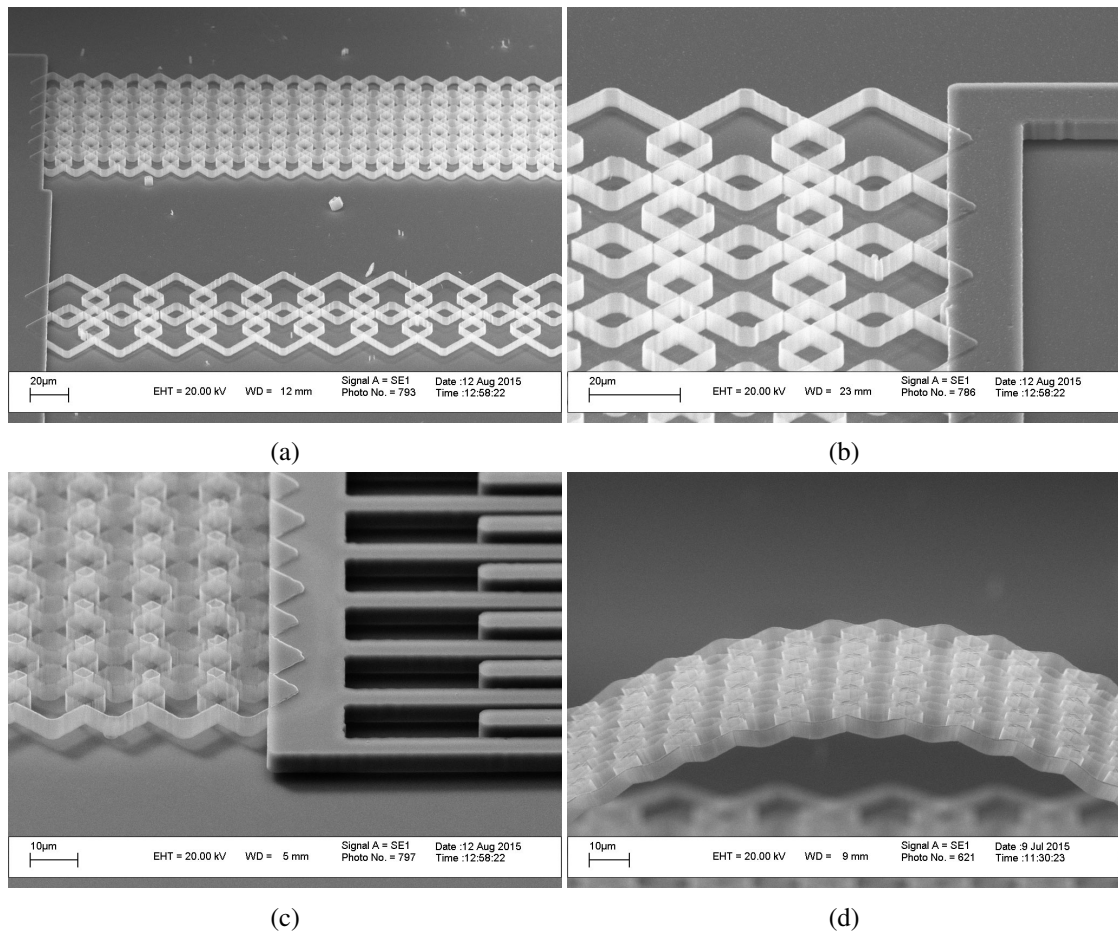
Figure 7.12: SEM views of type 2 metamaterial springs showing: (a) built-in ends attaching to anchors with two different single cell sizes; springs attaching to (c) linking unit and (d) comb electrodes; (d)close-up of out-of-plane buckling.

In Figure 7.13, a significant large tensile strain around 6% has been obtained, although evidence of fracture starts apparently at the bottom right-hand corner. The lattice structure must be broken further more with larger axial extension applied. Similarly, Figure 7.14 shows that a large transverse deflection can be obtained for the same structure.

Figure 7.15 shows the effect of applying a similar axial compressive deflection to a $18 \times 6$ mesh spring. Clearly, the mesh buckles out-of-plane due to the compressive strains. Such behaviour has be observed in experiments for the type 2 metamaterial universally. Thus the structure is expected to be less resistant to out-of-plane bending.

(a)                                    (b)
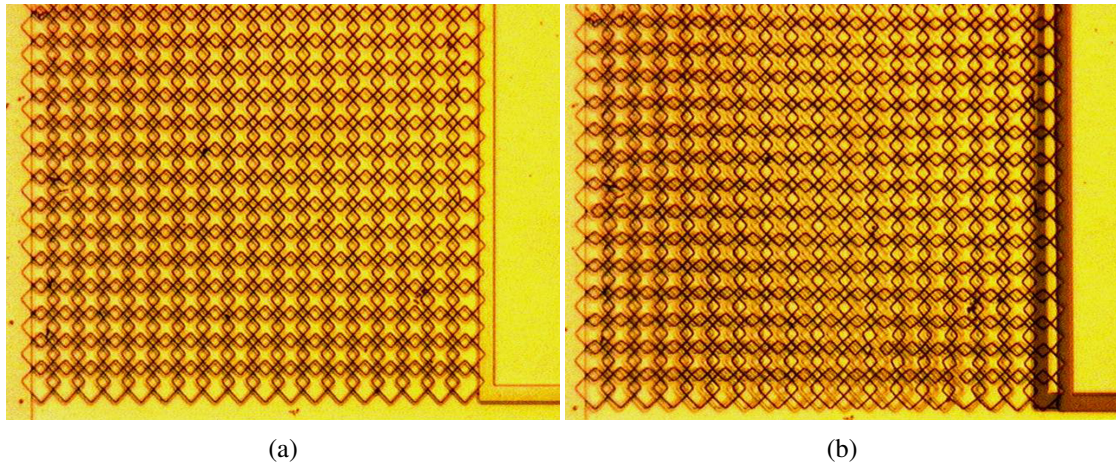
Figure 7.13: Optical microscope photographs of metamaterial springs (a) before and (b) after application of an axial tensile deflection.



(a)                                    (b)
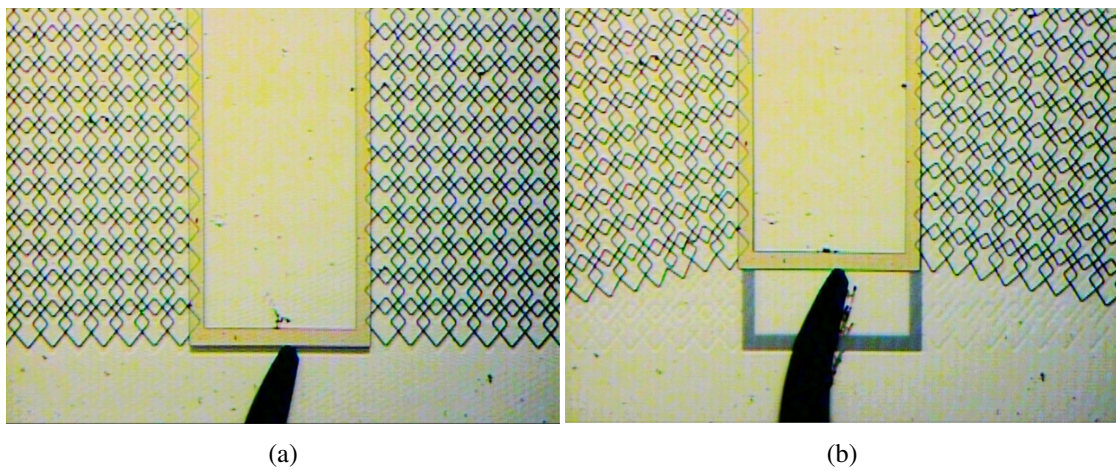
Figure 7.14: Optical microscope photographs of metamaterial springs (a) before and (b) after application of a transverse deflection.



(a)                                    (b)
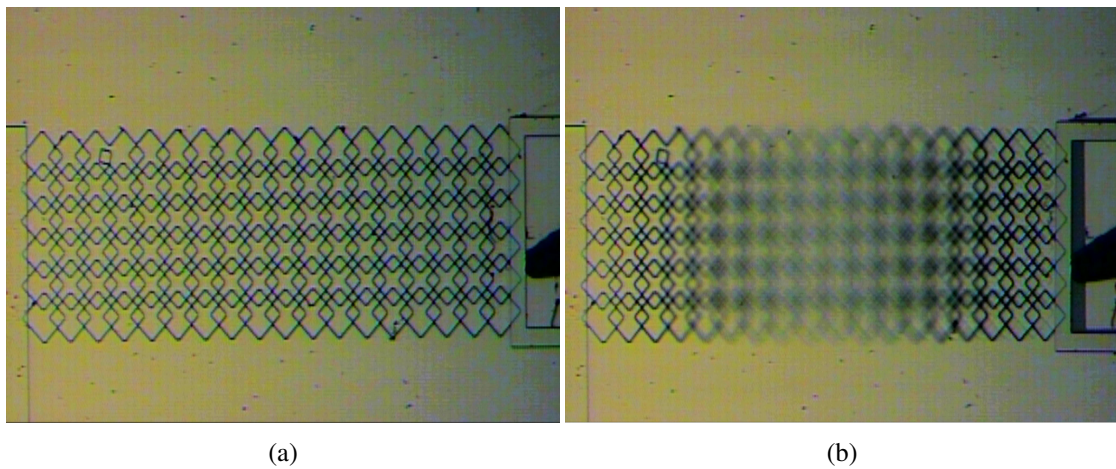
Figure 7.15: Optical microscope photographs of metamaterial springs (a) before and (b) after application of an axial compressive deflection.

### 7.5.2 Fitted shape of deflection

To further investigate the elastic performance of the mesh spring, deflected beam shapes obtained experimentally are compared with the predictions from the analytic model. For example, transverse deflections along the beam are then extracted from the optical microscope views such as Figure 7.16a, and then plotted versus axial position as shown in Figure 7.16b. Four sets of data, obtained with different end-deflections, are compared with the analytic model. The analysis is based on boundary conditions for end-loaded beams with one end fixed and the other guided. Thus the theoretical variation of transverse deflection versus axial position should follow Equation (7.13). The four predictions are then plotted, by matching the peak deflections obtained in the experiments. Clearly the agreement obtained for small deflections is good, but starts to become poorer as the total transverse deflection increases. This suggests that the approximate effective medium theory is valid for small in-plane deflections, but less accurate for large defections, possibly due to the axial tension induced.

A similar analysis has also been made for buckled mesh springs. Figure 7.17a shows an SEM view of an $18 \times 6$ spring that has buckled out-of-plane strongly with one end fixed and the other effectively pinned in position. Clearly, the beam has undergone very significant out-of-plane deflection.

Although we have not so far presented a similar step-by-step analysis for out-of-plane bending of a metamaterial beam, it is reasonable to assume that a similar effective medium theory should also be valid in this case. Namely, the metamaterial beam should behave much as a conventional beam, with suitable value of $E_{eq}$ and $I_{eq}$. The deflection shown above can then be modelled as an axially loaded beam with boundary conditions of one end fixed and the other pinned.

The theoretical variation of transverse deflection should therefore follow standard Euler buckling theory. For a fixed-pinned, buckled beam, the transverse deflection is well known to be given by:

$$y(x) = \frac{V}{kF}\left[\sin\left(kx\right) - kL_b\cos\left(kx\right) + k(L_b - x)\right] \tag{7.14}$$

Here $F$ is the axial force causing the buckling, and $V$ is a support reaction. In addition, $k = \sqrt{\frac{F}{E_{eq}I_{eq}}}$ and $kL$ is the solution of the eigenvalue equation $kL_b\cos\left(kL_b\right) - \sin\left(kL_b\right) = 0$. The first solution is $kL_b = 4.4934$.

The resulting variaton is plotted in Figure 7.17b for comparison. Experiment data extracted from SEM photographs is plotted as circles and the predictions of Equation (7.14) as a dashed
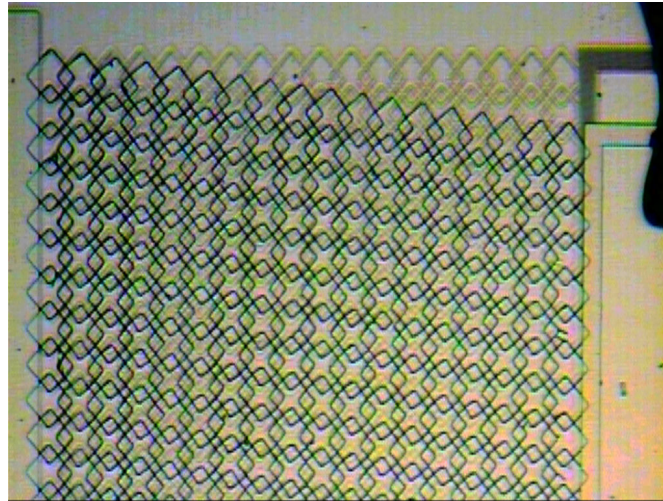
(a)
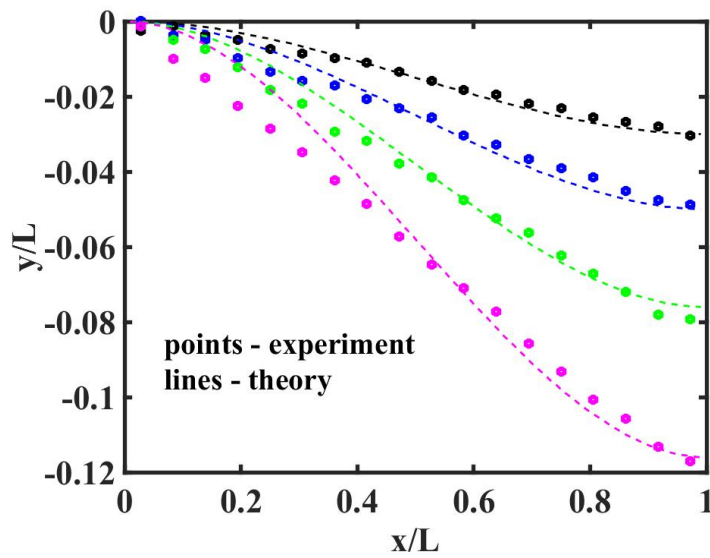


(b)

Figure 7.16

line, with the value of $\frac{V}{kF}$ normalised to match the peak deflection. Clearly, the agreement is not excellent. However, if we adjust the axial coordinate to take the large transverse deflection into consideration, much better agreement can be obtained as shown by the full line. Thus, the above results suggest that the effective medium theory should also be approximately valid within certain limits for out-of-plane buckling of metamaterial structures.
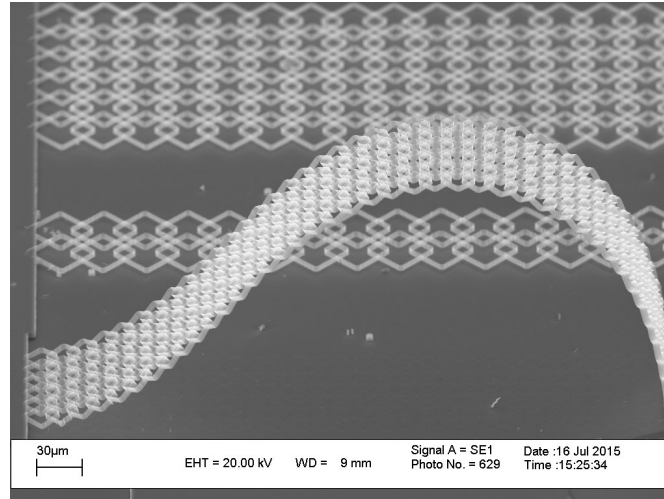
(a)
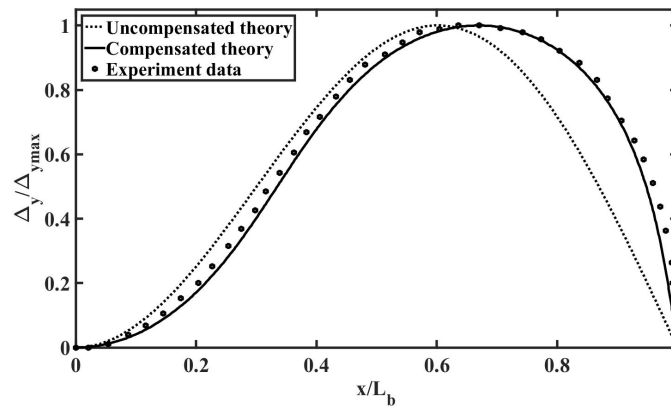


(b)

Figure 7.17: (a) SEM views of a metamaterial beam buckling out-of-plane; (b) comparison of the experimental deflection (points) with theoretical predictions before (dashed line) and after (full line) compensation for axial contraction.

### 7.5.3 Measurement of spring constant

Previously, we have shown in Figure 7.11b a $18 \times 16$ mesh spring combined with a comb-drive actuator to measure the spring constant by applying calibrated axial force. The spring consists of unit cells with side length of 30µm. There are 48 electrode gaps measured as 5µm each for the comb actuator, driven by applied voltage between the spring anchor and fixed part of the comb. The fixed end of the spring and the substrate are both grounded to avoid floating. Both in- and out-of-plane deflection have been measured accurately by using Veeco optical surface profiler. Data obtained from different positions of the device are averaged to produce final deflection versus the square of applied voltage ($V^2$).

Figure 7.18a shows the experimental variation of in-plane x-deflection (circles) and out-of-

plane z-deflection (diamonds) with the square of applied voltage ($V^2$). The x-deflection initially increases rapidly with $V^2$, and then follows a much smaller slope which is approximate linear. The variation of the z-deflection shows that the moving electrode is initially about 0.5μm higher then the fixed electrode, suggesting some initial misalignment (confirmed in Figure 7.18b). As the value of $V^2$ rises, the moving comb is gradually brought into alignment, and the expected linear variation in deflection occurs. Eventually, at very large voltages, the moving electrode collapses onto the substrate (as shown in Figure 7.18c). This behaviour might result from electrostatic attraction towards the substrate due to failure of grounding.

For the x-deflection, the initial rapid rise might be explained by the misalignment of the comb electrodes. The moving electrodes are possibly tilted by curvature of the mesh spring during release, which can be verified in SEM photographs. As the applied voltage increases, the curvature is removed by straightening the spring, resulting in a rapid increase in deflection at small axial force. Once the metamaterial spring has completely straightened, the behaviour of the spring and comb drive should then follow the standard model of an electrostatic actuator.

For a comb drive with electrode capacitance $C$, the force in the moving direction under a DC voltage $V$ is:

$$F = \frac{dC}{2dx}V^2 \qquad (7.15)$$

For a comb drive with $N$ electrode gaps each of width $g$, the capacitance variation can be calculated as $\frac{dC}{dx} = \frac{N\varepsilon_0 d}{g}$. The metamaterial spring should be stretched by the electrostatic force until an equilibrium state is achieved when the spring force equals the electrostatic force, as:

$$F = k_T \triangle x_T = \frac{N\varepsilon_0 d}{2g}V^2$$
$$\triangle x_T = \frac{N\varepsilon_0 d}{2k_T g}V^2 \qquad (7.16)$$

where $\varepsilon_0$ is the permittivity of free space, $k_T$ is the elastic stiffness of the mesh spring and $\triangle x_T$ is the axial displacement. Assuming the axial stiffness of type 2 cell is $k_2$, with a $N_s \times N_p$ mesh spring, the stiffness can be calculated as $k_T = \frac{N_p}{N_s}k_2$. Using the predicted value of $k_2$ from the analytic model in Table 7.2, $k_T = \frac{16}{18} \times 0.68 = 0.604$N/m. Knowing $N = 48$, $d = 4$μm and $g = 5$μm, we can obtain the predicted axial displacement $\triangle x_T$ in microns as:

$$\triangle x_T = 0.28 \times 10^{-3}V^2 \qquad (7.17)$$

Equation (7.17) is plotted as a dashed line in Figure 7.18a for comparison. By assuming an offset of 2.6μm derived from the initial misalignment, good agreement has been achieved between the theoretical predictions and the later experimental data. This is a remarkable result, and proves that the estimated elastic properties of the metamaterial are essentially accurate.



(a)



(b)
(c)
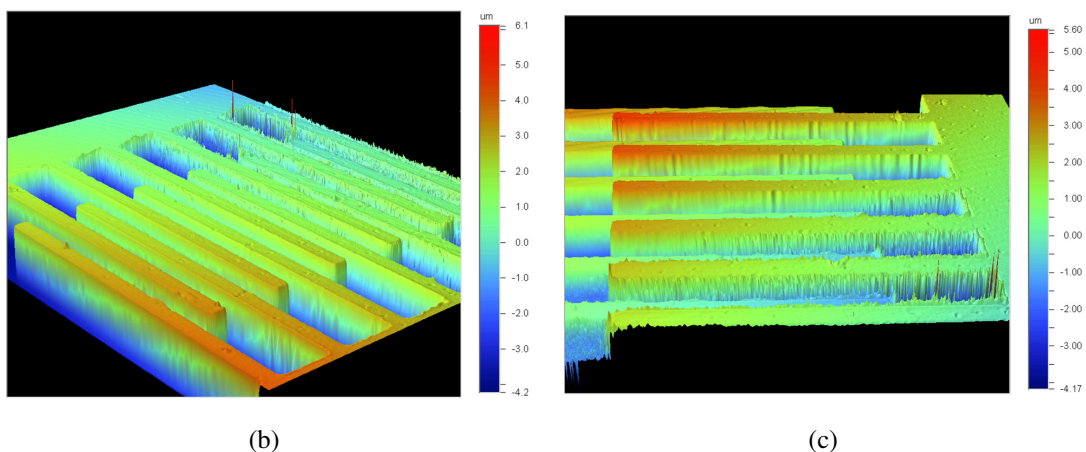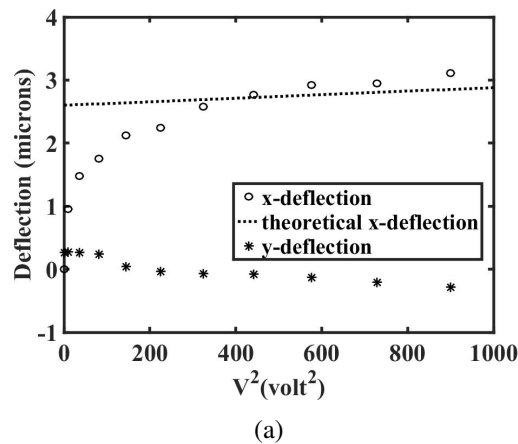
Figure 7.18: (a) Experimental variation of x- (circles) and y-deflections (diamonds) versus voltage for electrostatically driven metamaterial springs, compared with theoretical prediction (dashed line); surface profile of misaligned (b) and collapsed (c) actuator at the beginning and end of characterisation.

## 7.6 Discussion

In this chapter, multi-level STL has been used to fabricate novel 2D nanostructured mechanical metamaterials. The process shows many advantages over the existing techniques as it forms realistic sized metamaterial structures using single crystal silicon, which is fully compatible with today's microelectronics fabrication processes. In addition, it is now possible to combine the new material with other conventional MEMS parts to form a complete device or system. Although the structuring must necessarily be 2D due to the use of a top-down process, the high-

yield, low-cost process has demonstrated its potential for new opportunities in metamaterial development.

Two different types of mesh structures have been proposed to form metamaterials. A simple effective medium analytic theory has been developed. The theory derives from conventional analysis and provides approximate predictions for the metamaterial beams under axial and transverse loads. The behaviour of the metamaterial beams is similar to that of conventional theory but with certain boundary effects. The theory has been compared with the predications of FEA modelling using COMSOL[®], and with the deflection of experimental structures under different loadings. It has been shown that fabricated structures are intact and robust, and can easily undergo large, reversible in-plane and out-of-plane deformations. Good agreement has been achieved between analytic theory, FEA modelling and experiment results, indicating that the theory and model are reasonable and credible. Although these results are preliminary, the excellent combination of the design, fabrication and theory of the metamaterial shows a good potential for developing NEMS with novel properties in the future.

# 8 Conclusion

## 8.1 Summary

In this thesis, a new fabrication process for nano-electro-mechanical systems based on sidewall transfer lithography has been demonstrated. Originally developed for mass-parallel fabrication in microelectronics, STL can realise sub-micron features using only techniques and equipment for microscale fabrication, greatly reducing cost and improving throughput. However, STL was originally targeted at CMOS fabrication and consequently has received limited attention for more general 3D micromachining. Here a wide range of NEMS devices has been designed and fabricated using STL, including actuators, microgrippers and 2D mechanical metamaterials. Analytic and experimental characterizations of the different devices have also been carried out to highlight differences from traditional MEMS devices. A brief overview and summary of the thesis is presented below.

A general introduction introduction is provided in Chapter 1 together with on the literature review. The chapter starts with a brief summary of the current MEMS industry and existing MEMS fabrication techniques, followed by a description of typical mechanical MEMS sensors and actuators. Recent development of NEMS is then reviewed, different methods of fabricating nanoscale devices are introduced, and example NEMS devices are described. The development of STL is then reviewed, together with the original CMOS applications, and the potential application of STL to 3D micromachining is proposed. An outline of the thesis is provided in the end of the chapter.

In Chapter 2, a STL NEMS process for use in general 3D micromachining is introduced. Firstly, the process is presented in a step-by-step fashion based on a common process flow. Then a modified Bosch process for deep reactive ion etching is developed to allow the nanoscale silicon etching needed for NEMS fabrication. A plasma undercut process is also introduced as an extension of the Bosch process to enable dry release of suspended parts. For each process

step, technical details are presented together with the results of experimental fabrication trials. The process constraints and issues are highlighted and discussed.

Chapter 3 covers the design principles of and fabrication results obtained from NEMS electrothermal actuators based on a single-layer STL process. Completed prototype devices are demonstrated in bulk silicon and bonded silicon-on-insulator, confirming that STL has been successfully used to form continuous 3D features with high aspect ratio. In each case, nanoscale lithography and HAR silicon etching are discussed in detail using evidence provided by SEM photographs. Residual issues encountered during the process are highlighted and possible solutions are presented.

Chapter 4 describes the characterization of devices fabricated using the single-layer NEMS process. The devices investigated include double-ended buckling-mode electrothermal actuators and single-ended shape bimorph actuators. In each case, surface profiles obtained using a non-contact interferometric optical profilometer show low residual distortion due to stress. Different approaches are investigated to characterize the mechanical performance experimentally. For example, the devices have been electro-thermally actuated to characterize both static and dynamic performance. Problems with experimental measurement of such small structures are discussed. Finite element analysis is also used to construct 2D models of device performance, whose results are then compared with the analytic estimation and experimental results. The inadequacy of FEA for NEMS design is highlighted, due to its inability to model ultra-thin beams without inaccuracy or convergence failure.

In Chapter 5, an alternative analytic theory is then developed for buckling-mode electrothermal actuators, to address the design problems observed using FEA. Two actuator lay-outs are investigated, with a raised cosine and V-beam pre-buckle, respectively. In each case, the model is based on Euler buckling theory, and closed-form, analytic approximations for deflections are obtained using the assumption that bending dominates over axial compression. The theoretical predictions are compared with FEA predictions and with experimental results. Reasonable agreement is achieved in each case, confirming the validity of the analytic models for the design of NEMS buckling actuators.

In Chapter 6, a more advanced multi-layer STL process is presented. In contrast to single-layer STL NEMS processing, nanoscale features can now intersect with each other, allowing more complex lay-out designs to be realised. The process concept is first introduced, and results obtained at different fabrication stages are then presented using example SEM photographs.

A wide variety of prototype device lay-outs are then demonstrated, showing the diversity of designs that can be realised. Typical issues and constraints of the multi-layer STL are then discussed.

Chapter 7 presents a key new target application for multi-layer STL, namely nanostructured mechanical metamaterials. A brief introduction to mechanical metamaterials is first presented, and existing problems in design and fabrication are highlighted. Two-dimensional analytic models are then developed for two different unit cells arranged as a mesh in a periodic mechanical lattice, by using a simple effective medium analytic theory. Analysis is then presented for the deflected mesh under axial and transverse loads. Finite element analysis is then carried out for comparison. Since the beam elements are much shorter, much better results are now obtained, but this time computational limits are reached when the number of unit cells is too large. Finally, experimental results from prototype devices are presented, which show excellent agreement with the analytic theory. Despite the simplicity of the models, the approach shows a good combination of design, fabrication and characterization of the novel applications of STL, proposing more promising possibilities in the future.

## 8.2 Conclusions and future work

In this thesis, a sidewall transfer lithography process for NEMS fabrication has been introduced. The process uses conventional optical lithography to allow localised nanoscale parts to be combined with supporting microscale features, making the method suitable for low-cost and wafer-scale fabrication. Prototype devices have been designed and fabricated with a minimum in-plane width of 100nm and an aspect ratio of $> 50 : 1$. Device performance has been characterized experimentally, and the results have been compared with FEA simulations and analytic theory. The process has been shown to be particularly suitable for fabricating 2D nanostructured mechanical metamaterials. The thesis has therefore presented a detailed investigation of STL NEMS, covering a diversity of aspects including process development, device design, experimental characterization and analytic theory.

Although STL has been successfully adapted to applications in 3D micromachining, further work is still needed to solve residual process issues. Firstly, there is some evidence of stress in released structures, leading to distortion of nanoscale suspensions. These effects can be eliminated by removing the sidewall masks using extra dry etching steps or by replacing the metal

masks with $SiO_2$ masks, which can be removed using HF vapour phase etching. Secondly, to achieve better nanoscale etching, the Bosch DRIE process should be further optimised to eliminate the erosion and grass caused by excessive etching and passivation respectively. Thirdly, other process issues such as planarization during lithography and degradation of second-layer features must be solved to improve feature quality. However, any such solutions must be compatible with the current process, to retain the advantages of low-cost and mass parallel fabrication.

STL NEMS design is mainly restricted by the geometric constraints of the process. Although multi-layer STL allows nanoscale features to intersect, breaking one key restriction of single-layer STL, nanoscale features must still follow the perimeters of closed polygons and have constant width. Furthermore, it is currently impossible to realise nanoscale features with nanoscale separations. Such restrictions may well be significant in many NEMS designs. However, greater design freedom can be introduced by adding additional patterning steps that interrupt the closed polygons or employ extra sidewall layers that allow feature widths to be varied in discrete steps. If these problems can be successfully addressed, sidewall processing may be a significant enabler for the commercialization of NEMS sensors with enhanced sensitivity arising from (for example) reduced suspension width. In addition, the use of sidewall NEMS processing to fabricate nanostructured metamaterials may have a role in improving sensor properties. This thesis has demonstrated the ease with which effective material properties can be altered by varying simple overlaid patterns, which suffer from none of the lay-out restrictions described above.

Experimental characterization of NEMS has been proved difficult, due to the limited resolution of the available measurement equipment. Thus, it is necessary to develop measuring systems with higher resolution for assessing NEMS performance. There are several possibilities, including electron beam microscopy and optical interferometry; however, the latter must be adapted to in-plane motion. A further possibility is the use of capacitance variations; however, suitable structures must be embedded in the design at the outset.

Due to the general inaccuracy of FEA when simulating slender beams, which form the main elastic elements of many NEMS designs, it is necessary to develop appropriate analytic theories. For linear devices, the best approach is likely to be the stiffness matrix method. The matrix elements are standard results from the Euler theory for linear beam elements, and consequently are inherently accurate for slender beams. The method allows flexure-based devices with moderately complex topology to be analysed easily by inversion of a simple set of matrix equations

that incorporate all necessary boundary conditions and loads. For non-linear devices, such approaches cannot easily be used. However, we have already shown how quasi analytic results can be obtained from suitable modification to the Euler buckling and compatibility equations, and it is possible that this approach can be extended to connected elements.

From the above, we can conclude that STL NEMS processing has been successfully established as a new method of nanoscale device fabrication. There are many applications in sensing and actuation, many possibilities for design and process development, and the future of the method is bright.

## 8.3 List of publications

The following conference and journal papers are published in part to the work described in this work:

1. D. Liu, R. R. A. Syms, "NEMS actuators by sidewall transfer lithography," *39th Int. Conf. on Micro and Nano Eng.*, London, UK, Sept. 16-19, 2013.

2. D. Liu, R. R. A. Syms, "NEMS by sidewall transfer lithography," *J. Microelectromech. Syst.*, vol. 23, pp. 1367-1373, Dec, 2014.

3. D. Liu, R.R.A. Syms and M.M. Ahmad, "NEMS by multilayer sidewall transfer lithography," *28th IEEE Int. Conf. on MEMS*, Estoril, Portugal, Jan. 18-22, 2015.

# Bibliography

[1] R. P. Feynman, "There's plenty of room at the bottom," *Engineering and science*, vol. 23, no. 5, pp. 22–36, 1960.

[2] H. C. Nathanson, W. E. Newell, R. A. Wickstrom, and J. R. Davis Jr., "The resonant gate transistor," *IEEE Trans. Electron Devices*, vol. 14, no. 3, pp. 117–133, 1967.

[3] K. E. Petersen, "Silicon as a mechanical material," *Proceedings of the IEEE*, vol. 70, no. 5, pp. 420–457, 1982.

[4] R. T. Howe and R. S. Muller, "Resonant-microbridge vapor sensor," *IEEE Trans. Electron Devices*, vol. 33, no. 4, pp. 499–506, 1986.

[5] K. S. J. Pister, M. W. Judy, S. R. Burgett, and R. S. Fearing, "Microfabricated hinges," *Sens. Actuators, A*, vol. 33, no. 3, pp. 249–256, 1992.

[6] Yole Development Inc. (2014), "2014 mems market per application [online]," Available: http://www.yole.fr/iso_album/memsmarket_july2014.jpg.

[7] J. W. Judy, "Microelectromechanical systems (mems): fabrication, design and applications," *Smart Mater. Struct.*, vol. 10, no. 6, p. 1115, 2001.

[8] W. Pfann and R. Thurston, "Semiconducting stress transducers utilizing the transverse and shear piezoresistance effects," *J. Appl. Phys.*, vol. 32, no. 10, pp. 2008–2019, 1961.

[9] M.-H. Tsai, Y.-C. Liu, and W. Fang, "A three-axis CMOS-MEMS accelerometer structure with vertically integrated fully differential sensing electrodes," *J. Microelectromech. Syst*, vol. 21, no. 6, pp. 1329–1337, 2012.

[10] R. Amarasinghe, D. Dao, V. Dau, and S. Sugiyama, "Ultra miniature novel three-axis micro accelerometer," in *IEEE Sensors 2009 Conference*, Christchurch, New Zealand, October 2009.

[11] Analog Devices Inc. (2009) Ultralow power digital accelerometer ADXL346 [data sheet]. Available: http://www.analog.com/media/en/technical-documentation/data-sheets/ADXL346.pdf.

[12] L. Wang, D. M. Sipe, Y. Xu, and Q. Lin, "A MEMS thermal biosensor for metabolic monitoring applications," *J. Microelectromech. Syst*, vol. 17, no. 2, pp. 318–327, 2008.

[13] Y. Zhao and T. Cui, "Fabrication of high-aspect-ratio polymer-based electrostatic comb drives using the hot embossing technique," *J. Micromechanics and Microengineering*, vol. 13, no. 3, p. 430, 2003.

[14] R. Legtenberg, A. Groeneveld, and M. Elwenspoek, "Comb-drive actuators for large displacements," *J. Micromechanics and microengineering*, vol. 6, no. 3, p. 320, 1996.

[15] P. Minotti, P. Langlet, G. Bourbon, and T. Masuzawa, "Design and characterization of high-torque/low-speed silicon based electrostatic micromotors using stator/rotor contact interactions," *JPN. J. Appl. Phys.*, vol. 37, no. 3B, p. L359, 1998.

[16] R. Yeh, S. Hollar, and K. S. Pister, "Single mask, large force, and large displacement electrostatic linear inchworm motors," *J. Microelectromech. Syst*, vol. 11, no. 4, pp. 330–336, 2002.

[17] M. Mita, M. Arai, S. Tensaka, D. Kobayashi, and H. Fujita, "A micromachined impact microactuator driven by electrostatic force," *J. Microelectromech. Syst*, vol. 12, no. 1, pp. 37–41, 2003.

[18] K. B. Lee and Y.-H. Cho, "Laterally driven electrostatic repulsive-force microactuators using asymmetric field distribution," *J. Microelectromech. Syst*, vol. 10, no. 1, pp. 128–136, 2001.

[19] R. Legtenberg, J. Gilbert, S. D. Senturia, and M. Elwenspoek, "Electrostatic curved electrode actuators," *J. Microelectromech. Syst*, vol. 6, no. 3, pp. 257–265, 1997.

[20] M. Shikida, K. Sato, and T. Harada, "Fabrication of an s-shaped microactuator," *J. Microelectromech. Syst*, vol. 6, no. 1, pp. 18–24, 1997.

[21] M. Ataka, A. Omodaka, N. Takeshima, and H. Fujita, "Fabrication and operation of polyimide bimorph actuators for a ciliary motion system," *J. Microelectromech. Syst*, vol. 2, no. 4, pp. 146–150, 1993.

[22] H. Sehr, I. Tomlin, B. Huang, S. Beeby, A. Evans, A. Brunnschweiler, G. Ensell, C. Schabmueller, and T. Niblock, "Time constant and lateral resonances of thermal vertical bimorph actuators," *J. Micromechanics and Microengineering*, vol. 12, no. 4, p. 410, 2002.

[23] J. T. Butler, V. M. Bright, and W. D. Cowan, "Average power control and positioning of polysilicon thermal actuators," *Sensors and Actuators A: Physical*, vol. 72, no. 1, pp. 88–97, 1999.

[24] J. M. Noworolski, E. H. Klaassen, J. R. Logan, K. E. Petersen, and N. I. Maluf, "Process for in-plane and out-of-plane single-crystal-silicon thermal microactuators," *Sensors and Actuators A: Physical*, vol. 55, no. 1, pp. 65–69, 1996.

[25] T. Moulton and G. Ananthasuresh, "Micromechanical devices with embedded electro-thermal-compliant actuation," *Sensors and Actuators A: Physical*, vol. 90, no. 1, pp. 38–48, 2001.

[26] T. Lu, J. Hutchinson, and A. Evans, "Optimal design of a flexural actuator," *Journal of the Mechanics and Physics of Solids*, vol. 49, no. 9, pp. 2071–2093, 2001.

[27] I. Roch, P. Bidaud, D. Collard, and L. Buchaillot, "Fabrication and characterization of an su-8 gripper actuated by a shape memory alloy thin film," *J. Micromechanics and Microengineering*, vol. 13, no. 2, p. 330, 2003.

[28] E. T. Carlen and C. H. Mastrangelo, "Electrothermally activated paraffin microactuators," *J. Microelectromech. Syst*, vol. 11, no. 3, pp. 165–174, 2002.

[29] C. S. Pan and W. Hsu, "An electro-thermally and laterally driven polysilicon microactuator," *J. Micromechanics and Microengineering*, vol. 7, no. 1, p. 7, 1997.

[30] J. H. Comtois, M. A. Michalicek, and C. C. Barron, "Electrothermal actuators fabricated in four-level planarized surface micromachined polycrystalline silicon," *Sensors and Actuators A: Physical*, vol. 70, no. 1, pp. 23–31, 1998.

[31] R. Cragun and L. L. Howell, "A constrained thermal expansion micro-actuator," pp. 365–371, 1998.

[32] L. Que, J.-S. Park, and Y. Gianchandani, "Bent-beam electro-thermal actuators for high force applications," in *12th IEEE Int. Conf. on MEMS*, Orlando, USA, January 1999.

[33] M. J. Sinclair, "A high force low area mems thermal actuator," in *7th Intersociety Conf. on Thermal and Thermomechanical Phenomena in Electron. Syst. ITHERM 2000.*, Las Vegas, USA, May 2000.

[34] Y. B. Gianchandani and K. Najafi, "Bent-beam strain sensors," *J. Microelectromech. Syst*, vol. 5, no. 1, pp. 52–58, 1996.

[35] L. Que, J.-S. Park, and Y. B. Gianchandani, "Bent-beam electrothermal actuators-part i: Single beam and cascaded devices," *J. Microelectromech. Syst*, vol. 10, no. 2, pp. 247–254, 2001.

[36] N. Fleck, G. Muller, M. Ashby, and J. Hutchinson, "Strain gradient plasticity: theory and experiment," *Acta Metallurgica et Materialia*, vol. 42, no. 2, pp. 475–487, 1994.

[37] J. Stölken and A. Evans, "A microbend test method for measuring the plasticity length scale," *Acta Materialia*, vol. 46, no. 14, pp. 5109–5115, 1998.

[38] D. Lloyd, "Particle reinforced aluminium and magnesium matrix composites," *International Materials Reviews*, vol. 39, no. 1, pp. 1–23, 1994.

[39] D. Lam, F. Yang, A. Chong, J. Wang, and P. Tong, "Experiments and theory in strain gradient elasticity," *Journal of the Mechanics and Physics of Solids*, vol. 51, no. 8, pp. 1477–1508, 2003.

[40] E. C. Aifantis, "Exploring the applicability of gradient elasticity to certain micro/nano reliability problems," *Microsystem Technologies*, vol. 15, no. 1, pp. 109–115, 2009.

[41] K. Zandi, B. Wong, J. Zou, R. V. Kruzelecky, W. Jamroz, and Y.-A. Peter, "In-plane silicon-on-insulator optical MEMS accelerometer using waveguide fabry-perot microcavity with silicon/air bragg mirrors," in *23rd IEEE Int. Conf. on MEMS*, Wanchai, Hong Kong, January 2010.

[42] A. A. Trusov, I. P. Prikhodko, S. A. Zotov, A. R. Schofield, and A. M. Shkel, "Ultra-high q silicon gyroscopes with interchangeable rate and whole angle modes of operation," in *Sensors, 2010 IEEE.* IEEE, 2010, pp. 864–867.

[43] J. Laine and D. Mougenot, "Benefits of MEMS based seismic accelerometers for oil exploration," in *14th IEEE Int. Conf. on Solid-State Sensors, Actuators and Microsystems, TRANSDUCERS 2007*, Lyon, France, June 2007.

[44] K. C. Schwab and M. L. Roukes, "Putting mechanics into quantum mechanics," *Physics Today*, vol. 58, no. 7, pp. 36–42, 2005.

[45] A. Tseng, K. Chen, C. D. Chen, K. J. Ma *et al.*, "Electron beam lithography in nanoscale fabrication: recent development," *IEEE Trans. Electron. Packag. Manuf.*, vol. 26, no. 2, pp. 141–149, 2003.

[46] W. Chen and H. Ahmed, "Fabrication of 5–7 nm wide etched lines in silicon using 100 kev electron-beam lithography and polymethylmethacrylate resist," *Appl. Phys. Lett.*, vol. 62, no. 13, pp. 1499–1501, 1993.

[47] C. Vieu, F. Carcenac, A. Pepin, Y. Chen, M. Mejias, A. Lebib, L. Manin-Ferlazzo, L. Couraud, and H. Launois, "Electron beam lithography: resolution limits and applications," *Applied Surface Science*, vol. 164, no. 1, pp. 111–117, 2000.

[48] J. Gierak, C. Vieu, M. Schneider, H. Launois, G. B. Assayag, and A. Septier, "Optimization of experimental operating parameters for very high resolution focused ion beam applications," *J. Vac. Sci. Technol. B*, vol. 15, no. 6, pp. 2373–2378, 1997.

[49] J. Fujita, M. Ishida, T. Ichihashi, Y. Ochiai, T. Kaito, and S. Matsui, "Growth of three-dimensional nano-structures using fib-cvd and its mechanical properties," *Nuclear Instruments and Methods in Physics Research Section B: Beam Interactions with Materials and Atoms*, vol. 206, pp. 472–477, 2003.

[50] R. Kometani, T. Hoshino, K. Kanda, Y. Haruyama, T. Kaito, J.-i. Fujita, M. Ishida, Y. Ochiai, and S. Matsui, "Three-dimensional high-performance nano-tools fabricated using focused-ion-beam chemical-vapor-deposition," *Nuclear Instruments and Methods in Physics Research Section B: Beam Interactions with Materials and Atoms*, vol. 232, no. 1, pp. 362–366, 2005.

[51] S. Matsui, T. Kaito, J.-i. Fujita, M. Komuro, K. Kanda, and Y. Haruyama, "Three-dimensional nanostructure fabrication by focused-ion-beam chemical vapor deposition," *J. Vac. Sci. Technol. B*, vol. 18, no. 6, pp. 3181–3184, 2000.

[52] X. Lai, F. Ding, Z. Xu, W. Wu, J. Xu, and Y. Hao, "Suspended nanoscale solenoid metal inductor with tens-nh level inductance," in *21st IEEE Int. Conf. on MEM*, Tucson, USA, 2008.

[53] F. Ding, C. Ni, W. Yu, C. Li, W. Wu, and J. Xu, "Stress-assistant selective etching mechanism for lithography-independent nanofabrication," in *15th IEEE Int. Conf. on Solid-State Sensors, Actuators and Microsystems, TRANSDUCERS 2009*, Denver, USA, June 2009.

[54] L. Xia, W. Wu, J. Xu, Y. Hao, and Y. Wang, "3d nanohelix fabrication and 3d nanometer assembly by focused ion beam stress-introducing technique," in *19th IEEE Int. Conf. on MEMS*, Istanbul, Turkey, January 2006.

[55] Z. J. Davis, G. Abadal, O. Hansen, X. Borise, N. Barniol, F. Perez-Murano, and A. Boisen, "Afm lithography of aluminum for fabrication of nanomechanical systems," *Ultramicroscopy*, vol. 97, no. 1, pp. 467–472, 2003.

[56] S. Y. Chou, P. R. Krauss, and P. J. Renstrom, "Imprint lithography with 25-nanometer resolution," *Science*, vol. 272, no. 5258, p. 85, 1996.

[57] S. Y. Chou, P. R. Krauss *et al.*, "Nanoimprint lithography," *J. Vac. Sci. Technol. B*, vol. 14, no. 6, pp. 4129–4133, 1996.

[58] S. R. Quake and A. Scherer, "From micro-to nanofabrication with soft materials," *Science*, vol. 290, no. 5496, pp. 1536–1540, 2000.

[59] S. Y. Chou, P. R. Krauss, W. Zhang, L. Guo, and L. Zhuang, "Sub-10 nm imprint lithography and applications," *J. Vac. Sci. Technol. B*, vol. 15, no. 6, pp. 2897–2904, 1997.

[60] M. Schvartzman and S. J. Wind, "Robust pattern transfer of nanoimprinted features for sub-5-nm fabrication," *Nano Lett.*, vol. 9, no. 10, pp. 3629–3634, 2009.

[61] C. L. Cheung, R. Nikolić, C. Reinhardt, and T. Wang, "Fabrication of nanopillars by nanosphere lithography," *Nanotechnology*, vol. 17, no. 5, p. 1339, 2006.

[62] A. V. Whitney, B. D. Myers, and R. P. Van Duyne, "Sub-100 nm triangular nanopores fabricated with the reactive ion etching variant of nanosphere lithography and angle-resolved nanosphere lithography," *Nano Lett.*, vol. 4, no. 8, pp. 1507–1511, 2004.

[63] K. Ekinci, "Electromechanical transducers at the nanoscale: actuation and sensing of motion in nanoelectromechanical systems (NEMS)," *small*, vol. 1, no. 8-9, pp. 786–797, 2005.

[64] A. N. Cleland and M. L. Roukes, "Fabrication of high frequency nanometer scale mechanical resonators from bulk si crystals," *Appl. Phys. Lett.*, vol. 69, no. 18, pp. 2653–2655, 1996.

[65] L. Sekaric, J. Parpia, H. Craighead, T. Feygelson, B. Houston, and J. Butler, "Nanomechanical resonant structures in nanocrystalline diamond," *Appl. Phys. Lett.*, vol. 81, no. 23, pp. 4455–4457, 2002.

[66] M. Roukes, "Nanoelectromechanical systems face the future," *Phys. World*, vol. 14, no. 2, pp. 25–31, 2001.

[67] A. N. Cleland and M. L. Roukes, "A nanometre-scale mechanical electrometer," *Nature*, vol. 392, no. 6672, pp. 160–162, 1998.

[68] K. Ekinci, Y. Yang, and M. Roukes, "Ultimate limits to inertial mass sensing based upon nanoelectromechanical systems," *J. Appl. Phys.*, vol. 95, no. 5, pp. 2682–2689, 2004.

[69] B. Ilic, Y. Yang, K. Aubin, R. Reichenbach, S. Krylov, and H. Craighead, "Enumeration of dna molecules bound to a nanomechanical oscillator," *Nano Lett.*, vol. 5, no. 5, pp. 925–929, 2005.

[70] I. Palaci, S. Fedrigo, H. Brune, C. Klinke, M. Chen, and E. Riedo, "Radial elasticity of multiwalled carbon nanotubes," *Phys. Rev. Lett.*, vol. 94, no. 17, p. 175502, 2005.

[71] T. Hertel, R. Martel, and P. Avouris, "Manipulation of individual carbon nanotubes and their interaction with surfaces," *J. Phys. Chem. B*, vol. 102, no. 6, pp. 910–915, 1998.

[72] S.-B. Lee, K. Teo, M. Chhowalla, D. Hasko, G. Amaratunga, W. Milne, and H. Ahmed, "Study of multi-walled carbon nanotube structures fabricated by pmma suspended dispersion," *Microelectronic Eng.*, vol. 61, pp. 475–483, 2002.

[73] J. Che, T. Cagin, and W. A. Goddard III, "Thermal conductivity of carbon nanotubes," *Nanotechnology*, vol. 11, no. 2, p. 65, 2000.

[74] C. L. Cheung, J. H. Hafner, and C. M. Lieber, "Carbon nanotube atomic force microscopy tips: direct growth by chemical vapor deposition and application to high-resolution imaging," *Proc. Nat. Acad. Sci.*, vol. 97, no. 8, pp. 3809–3813, 2000.

[75] S. S. Wong, A. T. Woolley, T. W. Odom, J.-L. Huang, P. Kim, D. V. Vezenov, and C. M. Lieber, "Single-walled carbon nanotube probes for high-resolution nanostructure imaging," *Appl. Phys. Lett.*, vol. 73, no. 23, pp. 3465–3467, 1998.

[76] Q. Zhao, M. D. Frogley, and H. D. Wagner, "Direction-sensitive strain-mapping with carbon nanotube sensors," *Compos. Sci. Tech.*, vol. 62, no. 1, pp. 147–150, 2002.

[77] P. Dharap, Z. Li, S. Nagarajaiah, and E. Barrera, "Nanotube film based on single-wall carbon nanotubes for strain sensing," *Nanotechnology*, vol. 15, no. 3, p. 379, 2004.

[78] J. Stetter and G. Maclay, "Carbon nanotubes and sensors: a review enabling technology for mems and nanodevices," *Enabling technology for MEMS and nanodevices*, pp. 357–382, 2008.

[79] Y.-K. Choi, J. Zhu, J. Grunes, J. Bokor, and G. A. Somorjai, "Fabrication of sub-10-nm silicon nanowire arrays by size reduction lithography," *J. Phys. Chem. B*, vol. 107, no. 15, pp. 3340–3343, 2003.

[80] Y. Zhao, E. Berenschot, H. Jansen, N. Tas, J. Huskens, and M. Elwenspoek, "Sub-10nm silicon ridge nanofabrication by advanced edge lithography for NIL applications," *Microelectronic Eng.*, vol. 86, no. 4, pp. 832–835, 2009.

[81] K. Nicholas, H. Brockman, and I. Stemp, "Fabrication of submicron polysilicon lines by conventional techniques," *Appl. Phys. Lett.*, vol. 26, no. 7, pp. 398–399, 1975.

[82] A. Ipri, "Sub-micron polysilicon gate cmos/sos technology," in *1978 Int. Electron Devices Meeting (IEDM)*, Washington, DC, USA, December 1978.

[83] T. Jackson and N. Masnari, "A novel submicron fabrication technique," in *1979 Int. Electron Devices Meeting (IEDM)*, Washington, DC, USA, December 1979.

[84] W. Hunter, T. Holloway, P. Chatterjee, and A. Tasch Jr, "A new edge-defined approach for submicrometer mosfet fabrication," *Electron Device Lett., IEEE*, vol. 2, no. 1, pp. 4–6, 1981.

[85] D. H. Kim, S.-K. Sung, J. S. Sim, K. R. Kim, J. D. Lee, B.-G. Park, B. H. Choi, S. W. Hwang, and D. Ahn, "Single-electron transistor based on a silicon-on-insulator quantum wire fabricated by a side-wall patterning method," *Appl. Phys. Lett.*, vol. 79, no. 23, pp. 3812–3814, 2001.

[86] Y.-K. Choi, T.-J. King, and C. Hu, "A spacer patterning technology for nanoscale cmos," *Electron Devices, IEEE Transactions on*, vol. 49, no. 3, pp. 436–441, 2002.

[87] J. Horstmann and K. Goser, "New fabrication technique for nano-MOS transistors with w= 25 nm and l= 25 nm using only conventional optical lithography," *Microelectronic Eng.*, vol. 61, pp. 601–605, 2002.

[88] L. Sun, X. Liu, D. Hou, and R. Han, "SOI schottky barrier tunnelling transistors fabricated with spacer technology," *Electronics Lett.*, vol. 40, no. 8, pp. 511–513, 2004.

[89] H.-C. Lin, M.-H. Lee, C.-J. Su, T. Huang, C. Lee, and Y.-S. Yang, "A simple and low-cost method to fabricate tfts with poly-si nanowire channel," *Electron Device Lett., IEEE*, vol. 26, no. 9, pp. 643–645, 2005.

[90] J. Hållstedt, P.-E. Hellström, Z. Zhang, B. G. Malm, J. Edholm, J. Lu, S.-L. Zhang, H. Radamson, and M. Östling, "A robust spacer gate process for deca-nanometer high-frequency MOSFETs," *Microelectronic Eng.*, vol. 83, no. 3, pp. 434–439, 2006.

[91] B. Degroote, R. Rooyackers, T. Vandeweyer, N. Collaert, W. Boullart, E. Kunnen, D. Shamiryan, J. Wouters, J. Van Puymbroeck, A. Dixit *et al.*, "Spacer defined finFET: Active area patterning of sub-20nm fins with high density," *Microelectronic Eng.*, vol. 84, no. 4, pp. 609–618, 2007.

[92] R. Otterbach, U. Hilleringmann, T. Horstmann, and K. Goser, "Structures with a minimum feature size of less than 100 nm in CVD-diamond for sensor applications," *Diamond and related materials*, vol. 10, no. 3, pp. 511–514, 2001.

[93] X.-M. Yan, S. Kwon, A. Contreras, M. Koebel, J. Bokor, and G. Somorjai, "Fabrication of dense arrays of platinum nanowires on silica, alumina, zirconia and ceria surfaces as 2-d model catalysts," *Catalysis Lett.*, vol. 105, no. 3-4, pp. 127–132, 2005.

[94] X.-M. Yan, S. Kwon, A. Contreras, J. Bokor, and G. Somorjai, "Fabrication of large number density platinum nanowire arrays by size reduction lithography and nanoimprint lithography," *Nano Lett.*, vol. 5, no. 4, pp. 745–748, 2005.

[95] Z. Zhang, P.-E. Hellström, J. Lu, M. Östling, and S.-L. Zhang, "A novel self-aligned process for platinum silicide nanowires," *Microelectronic Eng.*, vol. 83, no. 11, pp. 2107–2111, 2006.

[96] Z. Zhang, J. Lu, P.-E. Hellström, M. Östling, and S.-L. Zhang, "Ni2si nanowires of extraordinarily low resistivity," *Appl. Phys. Lett.*, vol. 88, no. 21, p. 3103, 2006.

[97] A. Contreras, X.-M. Yan, S. Kwon, J. Bokor, and G. Somorjai, "Catalytic co oxidation reaction studies on lithographically fabricated platinum nanowire arrays with different oxide supports," *Catalysis lett.*, vol. 111, no. 1-2, pp. 5–13, 2006.

[98] D. S. Hsu and H. F. Gray, "Vertical thin-film-edge field emitters: fabrication by chemical beam deposition, imaging of cathodoluminescence and characterization of emission," *Thin solid films*, vol. 286, no. 1, pp. 92–97, 1996.

[99] D. Hsu and H. Gray, "A low-voltage, low-capacitance, vertical ruthenium–lithium–ruthenium sandwich layer thin-film-edge dispenser field emitter electron source," *Appl. Phys. Lett.*, vol. 75, no. 16, pp. 2497–2499, 1999.

[100] J. C. Yi, "Miniband properties of superlattice quantum dot arrays fabricated by the edge-defined nanowires," *Microelectronics Journal*, vol. 39, no. 3, pp. 369–374, 2008.

[101] J. Yi, "Anisotropic transport properties of quantum dot arrays fabricated by the edge-defined nanowires," *Microelectronics Journal*, vol. 40, no. 3, pp. 473–475, 2009.

[102] F. Gómez-Campos, S. Rodríguez-Bolívar, A. Luque-Rodríguez, J. López-Villanueva, and J. Carceller, "Intraband photon absorption in edge-defined nanowire superlattices for optoelectronic applications," *J. Appl. Phys.*, vol. 108, no. 12, p. 124307, 2010.

[103] L. Q. Chen, M. B. Chan-Park, Y. H. Yan, Q. Zhang, C. M. Li, and J. Zhang, "High aspect ratio silicon nanomoulds for uv embossing fabricated by directional thermal oxidation using an oxidation mask," *Nanotechnology*, vol. 18, no. 35, p. 355307, 2007.

[104] J. Haneveld, E. Berenschot, P. Maury, and H. Jansen, "Nano-ridge fabrication by local oxidation of silicon edges with silicon nitride as a mask," *J. Micromechanics and Microengineering*, vol. 16, no. 6, p. S24, 2006.

[105] J. Rao, H. Zou, R. R. A. Syms, E. Cheng, and C. Liu, "Fabrication of 2d silicon nanomold based on sidewall transfer," *Micro & Nano Lett.*, vol. 6, no. 1, pp. 29–33, 2011.

[106] P. Grabiec, M. Zaborowski, K. Domanski, T. Gotszalk, and I. Rangelow, "Nano-width lines using lateral pattern definition technique for nanoimprint template fabrication," *Microelectronic Eng.*, vol. 73, pp. 599–603, 2004.

[107] S. R. Sonkusale, C. J. Amsinck, D. P. Nackashi, N. H. Di Spigna, D. Barlage, M. Johnson, and P. D. Franzon, "Fabrication of wafer scale, aligned sub-25nm nanowire and nanowire templates using planar edge defined alternate layer process," *Physica E: Low-dimensional Systems and Nanostructures*, vol. 28, no. 2, pp. 107–114, 2005.

[108] Y. Zhao, E. Berenschot, M. De Boer, H. Jansen, N. Tas, J. Huskens, and M. Elwenspoek, "Fabrication of a silicon oxide stamp by edge lithography reinforced with silicon nitride for nanoimprint lithography," *J. Micromechanics and Microengineering*, vol. 18, no. 6, p. 064013, 2008.

[109] K.-S. Park, K.-H. Baik, D.-P. Kim, J.-C. Woo, K.-S. No, K. Lee, and L.-M. Do, "Sub-30 nm gate template fabrication for nanoimprint lithography using spacer patterning technology," *Journal of nanoscience and nanotechnology*, vol. 11, no. 2, pp. 1625–1628, 2011.

[110] University of California, Berkeley, "Thin-body MOSFET's process I [online]," Available: http://www-inst.eecs.berkeley.edu/~ee290d/fa13/LectureNotes/Lecture7.pdf.

[111] D. Flanders and N. Efremow, "Generation of < 50 nm period gratings using edge defined techniques," *J. Vac. Sci. Technol. B*, vol. 1, no. 4, pp. 1105–1108, 1983.

[112] P. Vettiger, P. Buchmann, K. Dätwyler, G. Sasso, and B. VanZeghbroeck, "Nanometer sidewall lithography by resist silylation," *J. Vac. Sci. Technol. B*, vol. 7, no. 6, pp. 1756–1759, 1989.

[113] D. S. Hsu, N. Turner, K. Pierson, and V. Shamamian, "20 nm linewidth platinum pattern fabrication using conformal effusive-source molecular precursor deposition and sidewall lithography," *J. Vac. Sci. Technol. B*, vol. 10, no. 5, pp. 2251–2258, 1992.

[114] U. Hilleringmann, T. Vieregge, and J. Horstmann, "A structure definition technique for 25 nm lines of silicon and related materials," *Microelectronic Eng.*, vol. 53, no. 1, pp. 569–572, 2000.

[115] K.-H. Chung, S.-K. Sung, D. H. Kim, W. Y. Choi, C. A. Lee, J. D. Lee, and B.-G. Park, "Nanoscale multi-line patterning using sidewall structure," *JPN. J. Appl. Phys.*, vol. 41, no. 6S, p. 4410, 2002.

[116] R. R. A. Syms, "Sub-micron structuring at mesa edges," *Microelectronic Eng.*, vol. 73, pp. 295–300, 2004.

[117] A. Carlson and T.-J. K. Liu, "Negative and iterated spacer lithography processes for low variability and ultra-dense integration," *SPIE Advanced Lithography 2008*, p. 69240B, 2008.

[118] J. Sakamoto, H. Kawata, M. Yasuda, and Y. Hirai, "25 nm wide silicon trench fabrication by edge lithography," *JPN. J. Appl. Phys.*, vol. 50, no. 8S2, p. 08KC03, 2011.

[119] K.-H. Chung, W. Y. Choi, S.-K. Sung, D. H. Kim, J. D. Lee, and B.-G. Park, "Pattern multiplication method and the uniformity of nanoscale multiple lines," *J. Vac. Sci. Technol. B*, vol. 21, no. 4, pp. 1491–1495, 2003.

[120] G. Cerofolini, G. Arena, C. Camalleri, C. Galati, S. Reina, L. Renna, and D. Mascolo, "A hybrid approach to nanoelectronics," *Nanotechnology*, vol. 16, no. 8, p. 1040, 2005.

[121] X. Han, H. Luo, W. Wu, J. Xu, G. Yan, Y. Jin, and Y. Hao, "Stacked SiO2/Si nanonail array fabricated by spacer technology for biomedical applications," in *14th IEEE Int. Conf. on Solid-State Sensors, Actuators and Microsystems, TRANSDUCERS 2007*, Lyon, France, June 2007.

[122] Q. Xie, Q. Zhou, F. Xie, J. Sang, W. Wang, H. A. Zhang, W. Wu, and Z. Li, "Wafer-scale fabrication of high-aspect ratio nanochannels based on edge-lithography technique," *Biomicrofluidics*, vol. 6, no. 1, p. 016502, 2012.

[123] R. R. A. Syms, H. Zou, J. Yao, D. Uttamchandani, and J. Stagg, "Scalable electrothermal MEMS actuator for optical fibre alignment," *J. Micromechanics and Microengineering*, vol. 14, no. 12, p. 1633, 2004.

[124] W. Sassen, V. Henneken, M. Tichem, and P. Sarro, "An improved in-plane thermal folded v-beam actuator for optical fibre alignment," *J. Micromechanics and Microengineering*, vol. 18, no. 7, p. 075033, 2008.

[125] D. Liu and R. R. A. Syms, "NEMS by sidewall transfer lithography," *J. Microelectromech. Syst*, vol. 23, no. 6, pp. 1366–1373, 2014.

[126] G. G. Stoney, "The tension of metallic films deposited by electrolysis," *Proceedings of the Royal Society of London. Series A, Containing Papers of a Mathematical and Physical Character*, vol. 82, no. 553, pp. 172–175, 1909.

[127] A. Brenner and S. Senderoff, "Calculation of stress in electrodeposits from the curvature of a plated strip," *J. Res. Natl. Bur. Stand*, vol. 42, no. 105, pp. 105–123, 1949.

[128] G. Moulard, G. Contoux, G. Motyl, G. Gardet, and M. Courbon, "Improvement of the cantilever beam technique for stress measurement during the physical vapor deposition process," *J. Vac. Sci. Technol. A*, vol. 16, no. 2, pp. 736–742, 1998.

[129] D. Liu and R. R. A. Syms, "NEMS actuators by sidewall transfer lithography," in *39th Int. Conf. on Micro and Nano Eng.*, London, UK, September 2013.

[130] R. Wood, V. Dhuler, and E. Hill, "A MEMS variable optical attenuator," in *Optical MEMS, 2000 IEEE/LEOS International Conference on*.   IEEE, 2000, pp. 121–122.

[131] R. R. A. Syms, H. Zou, J. Stagg, and H. Veladi, "Sliding-blade MEMS iris and variable optical attenuator," *J. micromechanics and microengineering*, vol. 14, no. 12, p. 1700, 2004.

[132] C. D. Lott, T. W. McLain, J. N. Harb, and L. L. Howell, "Modeling the thermal behavior of a surface-micromachined linear-displacement thermomechanical microactuator," *Sensors and Actuators A: Physical*, vol. 101, no. 1, pp. 239–250, 2002.

[133] R. Hickey, D. Sameoto, T. Hubbard, and M. Kujath, "Time and frequency response of two-arm micromachined thermal actuators," *J. Micromechanics and Microengineering*, vol. 13, no. 1, p. 40, 2003.

[134] D. Liu, R. R. A. Syms, and M. M. Ahmad, "NEMS by multilayer sidewall transfer lithography," in *28th IEEE Int. Conf. on MEMS*, Estoril, Portugal, January 2015.

[135] B. Xu, F. Arias, S. T. Brittain, X.-M. Zhao, B. Grzybowski, S. Torquato, and G. M. Whitesides, "Making negative poissonâĂŹs ratio microstructures by soft lithography," *Adv. Mater.*, vol. 11, no. 14, p. 1186, 1999.

[136] K. Bertoldi, P. M. Reis, S. Willshaw, and T. Mullin, "Negative poisson's ratio behavior induced by an elastic instability," *Adv. Mater.*, vol. 22, no. 3, pp. 361–366, 2010.

[137] Z. G. Nicolaou and A. E. Motter, "Mechanical metamaterials with negative compressibility transitions," *Nature Mater.*, vol. 11, no. 7, pp. 608–613, 2012.

[138] T. Bückmann, N. Stenger, M. Kadic, J. Kaschke, A. Frölich, T. Kennerknecht, C. Eberl, M. Thiel, and M. Wegener, "Tailored 3d mechanical metamaterials made by dip-in direct-laser-writing optical lithography," *Adv. Mater.*, vol. 24, no. 20, pp. 2710–2714, 2012.

[139] X. Zheng, H. Lee, T. H. Weisgraber, M. Shusteff, J. DeOtte, E. B. Duoss, J. D. Kuntz, M. M. Biener, Q. Ge, J. A. Jackson *et al.*, "Ultralight, ultrastiff mechanical metamaterials," *Science*, vol. 344, no. 6190, pp. 1373–1377, 2014.

[140] J. L. Silverberg, A. A. Evans, L. McLeod, R. C. Hayward, T. Hull, C. D. Santangelo, and I. Cohen, "Using origami design principles to fold reprogrammable mechanical metamaterials," *Science*, vol. 345, no. 6197, pp. 647–650, 2014.